Study of the structure and dynamics of magnetic skyrmions

University of Oxford

A thesis submitted for the degree of

Doctor of Philosophy

Richard Brearton

Lincoln College

August 4, 2021

For Andreea, without whose constant support I would have no hope of completing this great endeavour.

Acknowledgements

The contents of this document represent my microscopic capacity for original thought; my ideas are largely the osmotic result of a decade surrounded by brilliant physicists (although, any mistakes contained within this thesis are of my own invention). While I have always been intrigued by physics, any student of the subject can appreciate that interest alone is insufficient to generate correct answers. The initial tedium one encounters when struggling to make accurate predictions using physical theories undoubtedly deters countless students. Those responsible for maintaining my enthusiasm as I got to grips with physics in school, later encouraging me to apply to Oxford's competitive physics course when others dissuaded me, are Mr. Keith Caulkin and Mr. Bernard Doherty. As an undergraduate, I was lucky enough to be taught by Dr. Graeme Smith, Prof. Roman Walczak, and Prof. Steve Simon. Roman's teachings gave me not only a strong foundation in quantum mechanics, but were crucial in nurturing what little algebraic ability I have. If the efficacy of Graeme's general relativity and vector calculus tutorials are not obvious by the end of chapter 2, then, clearly, I should have used more indices. Steve's fascinating courses in statistical and condensed matter physics ultimately decided my specialization – I may not understand half of it half as well as well as I should like, and I like less than half of it half as well as it deserves, but I've had a fantastic time coming to grips with the bits of condensed matter physics that I am able to comprehend.

I must also thank the people that provided support during the DPhil degree. At Oxford, during his masters year, Robbie Oliver's practical skills were invaluable when setting up the lab; we had a great time synthesizing our first thin film samples together, and continued to have almost daily scientific discussions after he started his DPhil. At Diamond, Dr. David Burn's endless patience is to thank

for my experimental proficiency with the REXS technique. David, as well as Sam Moody and Luke Turnbull from Durham University, kept me great company for many twelve hour shifts at the synchrotron, staying positive even when magnetic signal was nowhere to be found. Michael Hutcheon is solely to blame for my obsession with programming, without which this thesis would be incomplete – throughout the DPhil, we spent hundreds of hours building (and using) miscellaneous software as a proxy for discussing (or venting about) our research. Thanks also to Kenneth Hughes and Tom Langton, for keeping me sane in and out of the various national lockdowns, and for putting up with my regular physical rants. And of course, thanks to Andreea, for being by my side for the whole journey.

It has been an incredible privilege to conduct this research under the supervision of Prof. Gerrit van der Laan and Prof. Thorsten Hesjedal. Gerrit's limitless intuition for magnetism, scattering techniques, and physics in general has been priceless when converting projects into publications. Our many discussions have shaped my theoretical understanding of REXS, and his sage remarks often forced me to re-evaluate the meaning of my own research. Finally, special thanks go to Thorsten: for all our late night discussions of ridiculous magnetic devices, bizarre scattering geometries, needlessly aesthetic figures and unconventional computing techniques; and for the twelve hour days in the lab repairing vacuum equipment, building gas and cooling lines, and looking for skyrmions in dead samples. For this and so much more, thank you; these last four years have been a blast.

Abstract

Magnetic skyrmions (skyrmions hereafter) are recently discovered localized vortex-like magnetic structures, defined by their unit topological winding number. From this nontrivial topology, skyrmions inherit unusual physical properties. They have been shown to be particularly robust to deformation, and so they are often referred to as being "topologically protected". In conductive materials, they appear to source electric and magnetic fields. When driven by an applied force, their topology prevents them from moving collinearly with the direction of the applied force; the angle by which they are deflected is known as the skyrmion Hall angle. Large skyrmion Hall angles are known to decrease the depinning threshold for motion under external drives, and skyrmions are known to be sensitive to ultra-low current density spin-transfer and spin-orbit torques.

These factors, combined with their nano-scale size, have generated excitement around the prospect that skyrmions could find use as a next-generation information carrier. This led to the publication of dozens of skyrmionic device schematics, each more ingenious than the last. Despite this flurry of applied research, magnetic skyrmions are still far from finding technological use. This can be attributed to two key issues. The first is materials problem; while there are dozens of materials systems that host these topological whirls, no material is known to host skyrmions with the three necessary characteristics of having a diameter on the order of 10 nm, stability at room temperature, and stability at remanence (although, FeGe and $\mathrm{Co}_x\mathrm{Zn}_y\mathrm{Mn}_z$ satisfy the first two criteria, and many magnetic multilayers meet the last two). The

second issue is a lack of physical understanding of the structure and dynamics of magnetic skyrmions, which will be the focus of this thesis.

The structural investigation begins with the establishment of the necessary mathematical framework; magnetic skyrmions, and the magnetization textures they coexist with, are first constructed and investigated analytically. Then, the two-dimensional morphology of lattices of these objects is investigated experimentally using resonant elastic x-ray scattering, and the first measurement of the magnetic soliton lattice above room temperature is presented, alongside the first measurement of the skyrmion liquid phase. Following this 2D study, the fascinating three-dimensional structure of skyrmions is probed; a mathematical discussion of the conical modulation of skyrmion strings is followed by an experimental and theoretical study of the surface-pinned nature of skyrmions.

An important model for the description of skyrmion dynamics is Thiele's equation, but this equation suffers from the prerequisite that one must have *a priori* knowledge of the interaction potential between the magnetization structures whose motion it describes, and their environment. To extend the cases in which Thiele's equation can be used, a general form of the interaction potential between any two magnetization configurations is derived and benchmarked. Thiele's equation in the presence of external spin-transfer torque, spin-orbit torque, and magnetic field gradient drives is derived; this is used to show that, when skyrmions are driven by spin-orbit torque down a nanowire, they are only negligibly deflected by the non-uniform magnetic field generated by the current through the wire. Using the knowledge of skyrmion-skyrmion interactions and their coupling to external fields, the properties of large systems of skyrmions are studied numerically by integrating Thiele's equation, revealing the strain and defect driven dynamics of skyrmion crystals. Finally, the first technique that allows for the determination of the all-important skyrmion Hall angle from the skyrmion lattice state is discussed, and used experimentally to perform the first measurement of the skyrmion Hall angle in FeGe.

Publications

The following publications have arisen, in part or in full, as a consequence of this work.

On the three-dimensional structure of skyrmions; R. Brearton, D. M. Burn, G. van der Laan, T. Hesjedal. Manuscript in preparation. Content relevant to chapters 2 and 4.

Observation of the magnetic soliton lattice state above room temperature; R. Brearton, L. Turnbull, J. Barker, G. Balakrishnan, P. Hatton, G. van der Laan, and T. Hesjedal. Manuscript in preparation. Content relevant to chapter 3.

Periodically modulated skyrmion strings in Cu_2OSeO_3; D. M. Burn, R. Brearton, S. L. Zhang, G. van der Laan, T. Hesjedal. *npj Quantum Mater.*, submitted. Content relevant to chapter 4.

Magnetic skyrmion interactions in the micromagnetic framework; R. Brearton, G. van der Laan and T. Hesjedal. *Phys. Rev. B* 101 (2020), p. 134422. Content relevant to chapters 2 and 5.

Diameter-independent skyrmion Hall angle observed in chiral magnetic multilayers; K. Zeissler, S. Finizio, C. Barton, A. J. Huxtable, J. Massey, J. Raabe, A. V. Sadovnikov, S. A. Nikitov, R. Brearton, T. Hesjedal, G. van der Laan, M. C. Rosamond, E. H. Linfield, G. Burnell, C. H. Marrows. *Nat. Commun.* 11 (2020), p. 428. Content relevant to chapter 6.

Skyrmions in anisotropic magnetic fields: strain and defect driven dynamics; R. Brearton, M. Olszewski, S. L. Zhang, M. R. Eskildsen, C. Reichhardt, C. J. O. Reichhardt, G. van der Laan and T. Hesjedal. *MRS Adv.* 4 (2019), pp. 643–650. Content relevant to chapter 7.

Deriving the skyrmion Hall angle from skyrmion lattice dynamics; R. Brearton, L. Turnbull, J. Barker, G. Balakrishnan, P. Hatton, G. van der Laan, and T. Hesjedal. *Nature Communications* 12 (2021), p. 2723. Content relevant to chapter 8.

Contents

1 Introduction **1**

1.1 On magnetism 3

1.1.1 Micromagnetism and magnetic energetics 7

1.1.2 The Landau-Lifshitz-Gilbert equation 10

1.1.3 The topology of magnetization 13

1.2 Structure of the thesis 15

2 Micromagnetism in two dimensions **18**

2.1 The symmetry of micromagnetism 19

2.2 The two-dimensional structure of skyrmions 26

2.3 Neighbouring magnetic textures 35

2.3.1 Helices, cones and solitons 35

2.3.2 Surface twist instabilities 38

3 Measuring 2D magnetic structures **40**

3.1 Studying magnetic order experimentally 41

3.2 REXS from helicoidal structures 48

3.3 Chiral soliton lattice above room temperature 55

3.4 REXS from the skyrmion crystal 58

3.4.1 Additional phases of skyrmion ensembles 63

4 Skyrmions in three dimensions 67

4.1 Conically modulated skyrmion strings 68

4.2 Surface pinning effects 79

5 Interactions in micromagnetism 88

5.1 Thiele's equation 89

5.2 Calculating micromagnetic interaction potentials 92

5.2.1 The interaction between two skyrmions 98

5.2.2 The interaction between a skyrmion and a surface twist 100

5.2.3 Calculating interaction potentials numerically 101

5.3 Interactions between conically modulated skyrmions 108

6 External forces 112

6.1 The skyrmion Hall angle 112

6.2 Current driven motion 113

6.2.1 Spin-transfer torque 114

6.2.2 Spin-orbit torque and the spin Hall effect 116

6.3 Skyrmions in non-uniform magnetic fields 118

6.3.1 Perpetuum mobile 120

6.4 The motion of skyrmions through nanowires 122

7 Magnetically straining the skyrmion crystal 126

7.1 Numerics 127

7.2 Anisotropic magnetic fields 128

7.3 Defects and dislocations 132

8 Measuring the skyrmion Hall angle 138

8.1 Deriving the skyrmion Hall angle from skyrmion lattice dynamics . . 140

8.2 The skyrmion Hall angle in FeGe 143

9 Summary and outlook 149

A Appendix 152

A.1 Details of skyrmion hosting materials 152

A.2 Sample details 152

Chapter 1

Introduction

For many people, knots are an important part of day-to-day life. Sailors rely on them to dock and tow, surgeons use them to close wounds, fishermen need them to secure lines, and tailors use them to hold our clothes together. The bow knot is strong enough to remain tight for hours, but only requires a single tug to untie – millions use this knot every day to fasten their shoes. Given their prevalent utility, one might naively expect that mathematicians have been solving knot-related problems for thousands of years, but careful inspection shows that this field of study is far more complex than one might initially imagine.

For instance, consider the knots on the left of Fig. 1.1(a). Intuitively, it is clear that these two knots are in some sense the same – mathematically, one can say they can be *smoothly deformed* into each other. But what about the knot on the right of Fig. 1.1(a)? Despite its apparent simplicity, the question of how to go about calculating the equivalence of two knots was addressed in 1985 [1]. The idea is to construct an algorithm, which takes as an input a picture of a knot, and outputs some sort of mathematical expression. If the two mathematical expressions are the same, then the knots are the same, regardless of any differences in the twists and turns taken between the pictures. If the expressions differ, then the knots are different, and they can only be made the same if string is cut and the knot is retied.

A series of knots of steadily increasing complexity is shown in Fig. 1.1(b) – each knot in the series is unique, meaning that none could be smoothly deformed into any other.

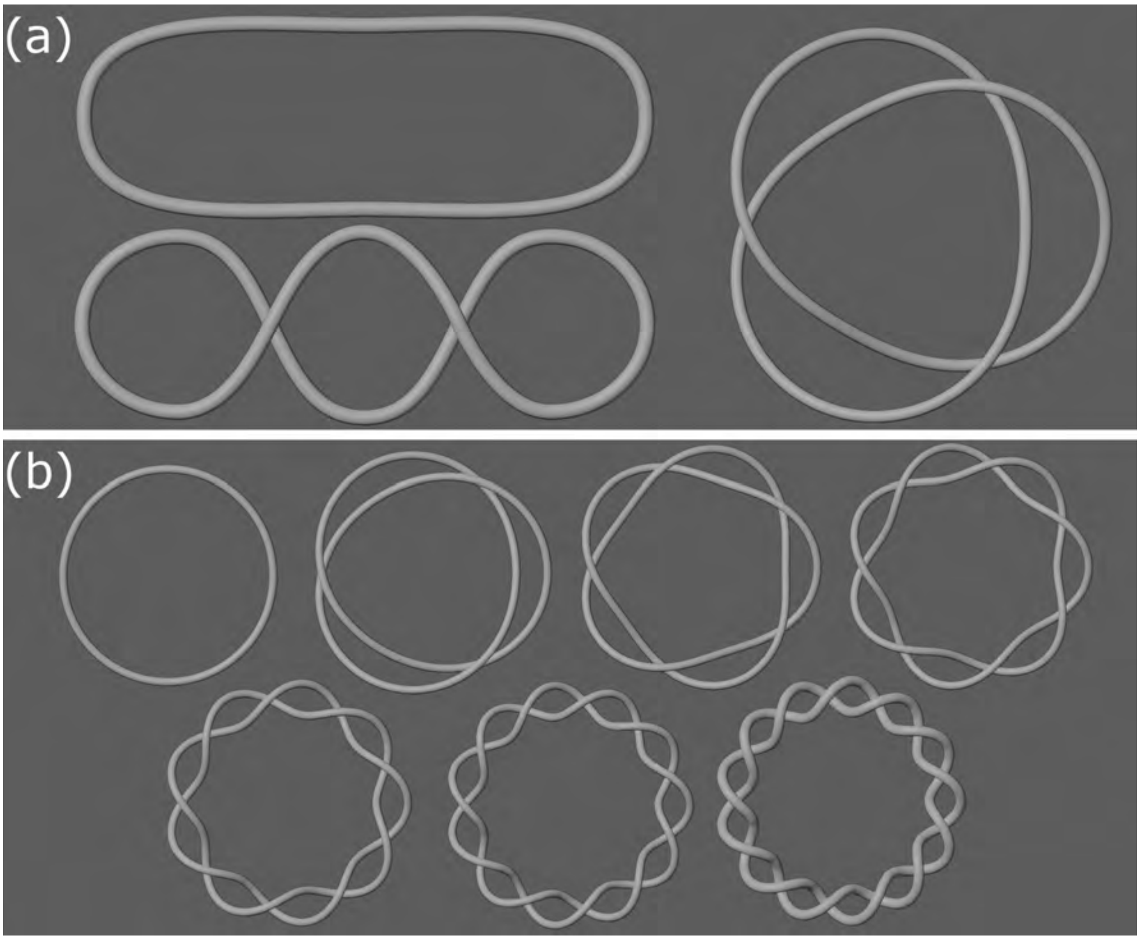

Figure 1.1: Examples of knots. (a) The two knots on the left of this panel are topologically equivalent, as they can be smoothly deformed into each other. The trefoil knot on the right is topologically distinct from the simple loops on the left, and can only be turned into a loop by cutting and retying. (b) A series of knots that cannot be smoothly deformed into one another. These are the (p, q) torus knots, with $p = 2$ and $q = 2n + 1$ for $n = 1, ..., 7$ [2].

A related problem is the question of equivalence of three-dimensional shapes: is it possible to smoothly deform a sphere until it becomes a doughnut? Squeeze as you may, a quick experiment reveals that a football becomes toroidal only if a pair of scissors is involved. Similarly to how knots can be represented by an expression, these shapes can be classified by a number known as a genus, where the genus of a three-dimensional shape is the number of holes needed to poke through a sphere to arrive at something that can be squeezed smoothly into that shape [3].

It is the mathematical field of topology that deals with these classifications. Motivated by topology, in 1962, British physicist and mathematician Tony Skyrme hypothesized that the stability of nuclear particles could be associated with a number [4]. He speculated that this number was related to the twisting of the field configuration of the nucleons, so that nucleons with different degrees of twisting could not be smoothly deformed into one another. While his theory of nucleons has fallen out of favour with the particle physics community, the idea that objects can be stabilized by their topology has flourished over time and such objects came to be known as skyrmions. In the field of condensed matter physics alone, particles that are stabilized by their topology have been theorized to exist in Bose-Einstein condensates and superconductors, and have been found experimentally in liquid crystals and magnetic materials [5–9].

The focus of this work will be on the skyrmions present in magnetic materials, which are characterized by their whirling magnetic moments. Before introducing these magnetic skyrmions and delving into the consequences of their topology, it is necessary to develop a mathematical toolkit that will allow for the analytical investigation of magnetic states. This framework is motivated and developed below.

1.1 On magnetism

The story of magnetism begins in much the same way as a fanciful tale, with a shepherd tending his herd on a remote mountaintop. It is said that the nails of Magnes the shepherd's shoes, and the ferrule of his staff, inexplicably adhered to an ore. The ore borrowed Magnes' name and came to be known as magnetite by the Romans[1].

---

[1] Magnetite's origins are intriguing, and disputed. Pliny the Elder places Magnes the shepherd on Mount Ida, while Isidore of Seville claims that both Magnes and the mountain are Indian [10, 11]. Other authors claim that the name magnetite comes from the ancient province of Magnesia, from which a great quantity of iron was exported [12]. The Greeks knew of magnetite as lodestone at a similar time; the great Greek philosopher Thales of Miletus argued that the attraction of iron to lodestone constituted evidence that lodestones had souls [13].

Ferromagnets can acquire a finite net magnetization in the absence of an external magnetic field. The alignment of magnetic moments on a macro-scale gives rise to physical phenomena that are difficult to miss, such as magnetite ore magnetizing, and then attracting, the iron nails in a shepherd's shoes. Though ferromagnets are simple magnetic structures, mankind tinkered with magnetite for millennia before fully understanding the quantum mechanical nature of its magnetic properties. This was accomplished in 1926, when Heisenberg showed that the energy of a two-atom system decreases when spins align [14]. This interatomic interaction energy is called the Heisenberg exchange interaction after its discoverer, although Heisenberg's name is often omitted in favour of the definite article.

One could argue that the simplest non-uniform configuration of magnetic moments is the antiferromagnet, defined by materials in which nearest neighbour magnetic moments favour antiparallel coordination (where ferromagnets would favour parallel coordination). But, as antiferromagnets have no net magnetization, they are much more difficult to detect. In contrast to the relatively modern magnetite (Fe_3O_4), haematite (Fe_2O_3), an antiferromagnet, has been used by humans for over 70,000 years as a blood-red paint [15]. Despite this staggeringly long history, it was not until 1932, in the PhD thesis of Louis Néel, that the first theoretical steps towards understanding antiferromagnetism were made [16]. In this early work, the possibility of local[1] antiferromagnetic ordering was inferred from signatures in magnetic susceptibility curves. Thanks to the advent of neutron diffraction, the antiferromagnetic states of haematite were finally understood in 1951, in work that won Shull the Nobel Prize in 1994 [18].

In 1958, Igor Dzyaloshinskii showed that the weak ferromagnetism above the Morin transition in haematite can be described by Landau's theory of phase tran-

---

[1] Néel's PhD supervisor was Pierre Weiss, who developed mean field theory to describe ferromagnetic phase transitions [17]. Néel was motivated to consider a local mean field theory after hearing of the short-ranged character of the Heisenberg exchange interaction. At the time of publication of his thesis, Néel did not fully comprehend the nature of the antiferromagnetic states he derived, considering them to be more like a paramagnet made up of fluctuating antiferromagnetic domains [16].

sitions of the second kind, purely on the basis of symmetry arguments [19]. Two years later, Toru Moriya showed that Dzyaloshinskii's new energy terms can be associated with spin-orbit coupling, deriving them quantum mechanically from second order perturbation theory [20]. This interaction energy has the distinctly unusual quality of being minimized when adjacent magnetic moments are mutually orthogonal – thanks to their seminal contributions to the field, the interaction came to be known as the Dzyaloshinskii-Moriya interaction, although to emphasize its contrast with Heisenberg's exchange interaction this term is often referred to as "the antisymmetric exchange interaction".

This interaction was used in 1959 to conjecture that magnetic helices, referred to as a "new type of antiferromagnetism" thanks to their lack of a net moment, are the ground state of MnO_2 [21]. These spirals of magnetic moments were the first example of a stable magnetic lattice that is incommensurate with the underlying atomic lattice, existing on length-scales orders of magnitude larger than the atomic spacing. In the 50 years following the discovery of magnetic helices, advances in experimental techniques led to the discovery of a range of magnetic states, but the only incommensurate lattice states remained the one dimensional helical state and its close relative, the conical state.

This situation was turned on its head in 2009, when the fingerprint of a crystal of two-dimensional whirls of magnetic moments was observed in the small-angle neutron scattering pattern from a crystal of MnSi [9]. Shortly afterwards, these strange vortex-like magnetic structures were measured in direct space in $FeCo_{0.5}Co_{0.5}Si$ using a Lorentz transmission electron microscope, and, excitingly, they were found to respond to ultra-low current densities [22, 23]. These magnetization configurations were also found to have a topological character, as it can be shown to be impossible to smoothly deform them into any of their surrounding states. This topology earns them the name "magnetic skyrmion", but the name is not just for show – it grants these skyrmions a myriad of unusual behaviours along with substantially fortified stability [24].

The commotion brought about by the discovery of magnetic skyrmions has led to a surge of research in the field of topological magnetism, with the decade following their first sighting leading to the publication of articles on antiskyrmions [25], antiferromagnetic skyrmions [26], biskyrmions [27, 28], skyrmion bags [29, 30], skyrmionium [31, 32], merons [33, 34], antiferromagnetic merons [35], and hopfions [36–39], all in the context of magnetism. Of the above, supposed images of biskyrmions have been concretely shown to simply be images of magnetic bubbles [40], observations of antiskyrmions might well be observations of triangular type-II magnetic bubbles [41], antiferromagnetic skyrmions have only been found in synthetic magnets [42], skyrmion bags have only been observed in liquid crystals [29], and merons are essentially topologically trivial (as will be discussed shortly).

One might naively suspect that it is straightforward to ensure that a proposed magnetization state is stable by calculation. The mathematical framework used to study the structure of skyrmions and their neighbouring textures in this work is the simplest model one can use to describe the magnetization of materials with the abovementioned symmetric and antisymmetric exchange interactions, and an externally applied field. More than a decade after the first observation of magnetic skyrmions, using the most symmetric model of a magnetic skyrmion within this simplified framework, a solution for the closed form expression for the magnetization configuration is not known. As the quantity and quality of practical investigations carried out on an ever increasing range of materials systems escalates, it is difficult for theory to keep pace with experiment. This theoretical framework is introduced below, and its exploration is the topic of chapter 2.

Where errors arise from observation, they tend to result from the generally complicated nature of the experimental techniques one can use to investigate magnetic states. While in many respects the resolution (both spatial and temporal) of measurements of the magnetization of materials is remarkable, no technique has the ability to probe the magnetization in its entirety; acquisition of data relating to magnetism is always missing some information, and a brief discussion of what information is missing from each technique can be found in chapter 3.

1.1.1 Micromagnetism and magnetic energetics

As skyrmions are typically large compared to the atomic spacing of their host materials, adjacent magnetic moments within a skyrmion tend to be very nearly aligned. The size of skyrmions is governed by the energetics of the underlying crystal, which sets characteristic length scales for modulations such that any magnetic object that could coexist with a skyrmion should be incommensurate with the atomic lattice. This will be used to describe the magnetization of materials as a vector field $\mathbf{M} = M_S\mathbf{m}$ throughout this work, where $M_S = |\mathbf{M}|$ is the saturation magnetization (which will be assumed to be constant throughout), as opposed to a collection of discrete magnetic moments. This is the underlying assumption of *micromagnetics*, so called because it was originally used to study the behaviour of magnetism on the micrometre-scale, though, assuming that the periodicity of the atomic lattice is on the order of 1 Å, this theory is perfectly valid on the nanoscale [43].

In this micromagnetic regime, the energy of a magnetization field must be a functional of the magnetization $\mathbf{m}(\mathbf{x})$, where $\mathbf{x}$ refers to the spatial coordinates. Throughout this work, functionals will be disambiguated from functions by the use of square brackets, so that $A[b]$ denotes that A is a functional taking the function b as its argument, while $A(b)$ denotes that A is a function taking the number b as its argument. Neglecting external magnetic fields (whose energy density is simply $\mathcal{E}_B = -M_S\mathbf{m}\cdot\mathbf{B}$), using Einstein's summation convention, assuming that the energy density is well described by lowest order couplings between the magnetization field and its derivatives, this takes the general form

$$E[\mathbf{m}(\mathbf{x})] = \iiint \Big[\alpha_{ij}m_im_j + \beta_{ijk}\big(m_i\partial_k m_j - m_j\partial_k m_i\big) + \gamma_{ik}\partial_i m_j\partial_k m_j\Big]d^3x\,, \quad (1.1)$$

where f_i is the ith component of the vector $\mathbf{f}$, $\partial_i = \partial/\partial x_i$, α, β and γ are tensors that dictate coupling magnitudes. In particular, α describes the coupling of the magnetization to itself, which decides the magnitude of crystalline anisotropies, β controls the coupling between the magnetization and its derivatives, which defines the strength and orientation of the antisymmetric exchange interaction, and γ sets the strength of the coupling between derivatives, which becomes the exchange interaction.

The self coupling term $\alpha_{ij}m_im_j$ determines the strength of specifically uniaxial anisotropies, where, for example, an anisotropy along the z-axis would be described by a tensors α_{ij} whose only non-zero component is $\alpha_{zz} = K$. Throughout this work, for simplicity, α_{ij} will be taken to be zero. Other common crystalline anisotropy terms, such as the cubic anisotropy, are fourth order in $\mathbf{m}$ and not considered here.

Intuitively, one would expect the most general form of the β term to read $\beta_{ijk}(\beta^{(a)}m_i\partial_k m_j + \beta^{(b)}m_j\partial_k m_i)$, where $\beta^{(a)}$ and $\beta^{(b)}$ are arbitrary constants, whereas the β term in Eq. (1.1) is totally antisymmetric. This comes from the fact that, as any tensor can be written as a sum of a symmetric and an antisymmetric tensor, the derivative terms can be written $\beta^{\mathrm{A}}(m_i\partial_k m_j - m_j\partial_k m_i) + \beta^{\mathrm{S}}(m_i\partial_k m_j + m_j\partial_k m_i)$, where now β^{A} and β^{S} are the coefficients of the antisymmetric and symmetric parts of the derivative tensor, respectively. But, assuming that the coupling between the magnetization and its derivatives is isotropic, $\beta_{ijk} = \beta_{ijl}$ for any k, l, which allows the symmetric term $\beta_{ijk}\beta^{\mathrm{S}}(m_i\partial_k m_j + m_j\partial_k m_i)$ to be written as a total derivative [44]. So, these symmetric coupling terms only contribute towards an energy offset and can be ignored, leaving only the antisymmetric term shown in Eq. (1.1) [44].

The differences $\mathcal{L}^k_{ij} = m_i\partial_k m_j - m_j\partial_k m_i$ are known as Lifshitz invariants, and the symmetry of the underlying material decides which components of the tensor β_{ijk} are finite (and therefore which Lifshitz invariants are allowed). If the material has a centre of symmetry, then $\beta_{ijk} = 0$. For uniaxial ferromagnets without a centre of symmetry belonging to the crystal classes (nmm), where $n \in \{3, 4, 6\}$, the only non-zero components of β are $\beta_{xzx} = D$ and $\beta_{yzy} = -D$; magnets in the classes (n22) have the additional term $\beta_{yxz} = D'$ [45]. In cubic helimagnets, $D' = D$, so that one can write [46]

$$\beta_{ijk}(m_i \partial_k m_j - m_j \partial_k m_i) = D\mathbf{m} \cdot (\nabla \times \mathbf{m}) \,. \tag{1.2}$$

The exchange term $\gamma_{ik}\partial_i m_j \partial_k m_j$ is not the most general form of a coupling between derivatives (which would be $\gamma_{ik}^{jl}\partial_i m_j \partial_k m_l$, where indices are raised only for notional convenience). Instead it is the first terms in the expansion of the energy density in powers of derivatives of $\mathbf{m}$, which is more easily seen when the term is written $\gamma_{ik}\partial_i \mathbf{m} \cdot \partial_k \mathbf{m}$ [47]. In uniaxial crystals whose special axis is used to orient the z-axis, the finite elements of the γ tensor are the exchange constants $\gamma_{xx} = \gamma_{yy} = J_1$, and $\gamma_{zz} = J_2$ [47]. In cubic crystals, the exchange constants $J_1 = J_2$, so that $\gamma_{ij} = J\delta_{ij}$, where δ_{ij} is the Kronecker delta. In this case, the exchange term can be written very simply using index notation as $J\partial_i m_j \partial_i m_j$, or in vector notation using the shorthand $J(\nabla\mathbf{m})^2$.

The focus of this work will be on the spin structures, particularly skyrmions, found in chiral cubic magnets. In this case, neglecting uniaxial and cubic anisotropies, and considering only the coupling between the magnetization and the externally applied magnetic field, the micromagnetic energy functional can be written as

$$E = \iiint \left[J\left(\nabla\mathbf{m}\right)^2 + D\mathbf{m} \cdot (\nabla \times \mathbf{m}) - M_S \mathbf{m} \cdot \mathbf{B} \right] d^3x \,. \tag{1.3}$$

The coupling between the magnetization and the field it generates is neglected here, which is, in general, not a good idea. This should lead to an additional term $E_{\text{Demag}} = -M_S \iiint \mathbf{m} \cdot \mathbf{B}_{\text{Demag}}$, where $\mathbf{B}_{\text{Demag}}$ is the demagnetizing field and E_{Demag} is its Zeeman energy. This term can be ignored only when $\mathbf{B}_{\text{Demag}}$ is roughly constant, so that it simply rescales the externally applied field. Regardless of its validity, this approximation is born of necessity, as computing the demagnetizing field $\mathbf{B} = -M_S/4\pi \iiint (\nabla \cdot \mathbf{m})\mathbf{r}/r^3 d^3x$ is prohibitively difficult analytically, and time consuming numerically. While some idealized demagnetizing fields have been calculated analytically [48–50], the complex structures studied using Eq. (1.3) in this work would not be well modelled by any simple approximation. Similarly, computing the demagnetizing field for nanoscale structures numerically is possible, but it fast becomes too computationally demanding for calculations on a larger scale.

The approach taken here is simply to use Eq. (1.3) as a toy model. All anisotropies have been ignored, along with the non-negligible demagnetizing field, in favour of deriving results based on the physics of the simplest possible chiral system. While any results derived using Eq. (1.3) are unlikely to yield detailed quantitative information, they can certainly provide invaluable qualitative insight into the magnetic structures inhabiting chiral cubic crystals.

1.1.2 The Landau-Lifshitz-Gilbert equation

The Euler-Lagrange equations of the energy functional derived in Eq. (1.3) can be used to find stable magnetization structures, but cannot be used alone to study magnetization dynamics. The equation of motion for the magnetization can be written down qualitatively by noticing that, to conserve $|\mathbf{m}|$, the equation of motion must take the form [47, 51]

$$\partial_t \mathbf{m} = \boldsymbol{\omega} \times \mathbf{m}\,. \tag{1.4}$$

To derive an expression for $\boldsymbol{\omega}$ and understand the terms that arise, consider the case when the motion of $\mathbf{m}$ dissipates negligibly little energy. This can be shown to the case for long wavelength excitations of the magnetization and at low temperatures; this proof is omitted here, but can be found in Ref. [47]. To find the condition that must be satisfied for dissipation to be absent, it will be assumed that the magnetization is an independent parameter whose equilibrium distributions can be found by solving the Euler-Lagrange equations of the free energy, holding the magnetic field $\mathbf{H}$, temperature T and volume V constant. The Helmholtz function F is the thermodynamic potential that depends on these variables, and its variation for an infinitesimal change of the magnetization $\mathbf{m}$ can be written

$$\delta F = -\mu_0 M_S \iiint \mathbf{H}_{\mathrm{Eff}} \cdot \delta\mathbf{m}\, d^3x\,, \tag{1.5}$$

where $\mathbf{m}(\mathbf{x}) \cdot \mathbf{H}_{\mathrm{Eff}}(\mathbf{x})$ is an effective Zeeman energy density felt by the magnetization at a coordinate $\mathbf{x}$ that results from all of the interactions between the magnetization and its environment at $\mathbf{x}$. The rate at which energy is dissipated by the variation of the magnetization can then be written [47]

$$Q = -\partial_t F\,. \tag{1.6}$$

Carrying out the derivative in Eq. (1.6) on the free energy in Eq. (1.5) at constant temperature, volume and field gives

$$Q = \mu_0 M_S \iiint \mathbf{H}_{\mathrm{Eff}}(\partial_t \mathbf{m}) d^3x = \mu_0 M_S \iiint \mathbf{H}_{\mathrm{Eff}} \cdot (\boldsymbol{\omega} \times \mathbf{m})\, d^3x\,, \tag{1.7}$$

where the equation of motion Eq. (1.4) has been used to replace the time derivative with $\boldsymbol{\omega} \times \mathbf{m}$. So, if the motion of the magnetization is dissipation-less $\boldsymbol{\omega}$ must be parallel to $\mathbf{H}_{\mathrm{Eff}}$, and the equation of motion can be written

$$\partial_t \mathbf{m} = \gamma \mathbf{H}_{\mathrm{Eff}} \times \mathbf{m}\,, \tag{1.8}$$

where γ, the gyromagnetic ratio of the electron, is the constant of proportionality that relates $\boldsymbol{\omega}$ to $\mathbf{H}_{\mathrm{Eff}}$ [47, 51]. If the motion of the magnetization is not conservative, then its time derivative must acquire a component normal to $\mathbf{H}_{\mathrm{Eff}} \times \mathbf{m}$. Continuing to require that $\partial_t |\mathbf{m}| = 0$, then the dissipative term must be normal also to $\mathbf{m}$. The only vector normal to both of these terms is given by $\mathbf{m} \times (\mathbf{H}_{\mathrm{Eff}} \times \mathbf{m})$. Rescaling the constants of proportionality so that the magnitude of $\partial_t \mathbf{m}$ is constant and defining the damping term so that it is different to the non-dissipative term by a factor α_G, where α_G is an arbitrary damping parameter, the Landau-Lifshitz equation becomes

$$\partial_t \mathbf{m} = -\frac{\gamma}{1+\alpha_G^2}\mathbf{m}\times\mathbf{H}_{\text{Eff}} - \frac{\alpha_G\gamma}{1+\alpha_G^2}\mathbf{m}\times(\mathbf{m}\times\mathbf{H}_{\text{Eff}})\,. \tag{1.9}$$

Using the fact that $\mathbf{m}\times(\mathbf{m}\times\partial_t\mathbf{m}) \parallel \partial_t\mathbf{m}$ and rescaling time, this can be arranged into the Landau-Lifshitz-Gilbert (LLG) form [52]

$$\dot{\mathbf{m}} = -\gamma\mathbf{m}\times\mathbf{H}_{\text{Eff}} + \alpha_G\mathbf{m}\times\dot{\mathbf{m}}\,, \tag{1.10}$$

where α_G can now be identified as the Gilbert damping parameter [53].

To use this equation to study the dynamics of the magnetization, it is necessary to identify $\mathbf{H}_{\text{Eff}}$. This can be written in terms of the free energy F using Eq. (1.5), where derivatives with respect to volume and the magnetization give

$$\mathbf{H}_{\text{Eff}} = -\frac{1}{\mu_0 M_S}\frac{d^2F}{d\mathbf{m}dV}\,. \tag{1.11}$$

To find the free energy $F[\mathbf{m}]$, it is necessary to find the functional that is minimized to find the equilibrium state in a system with constant volume and temperature [54]. Sufficiently far from the Curie temperature, terms $\mathcal{O}(M^2)$ arising from Landau's theory of phase transitions can be ignored and the magnetization dependent component of the free energy becomes the energy functional given in Eq. (1.3). So, the effective field $\mathbf{H}_{\text{Eff}}$ can be computed from the energy functional in Eq. (1.3), which can in turn be used to compute the equation of motion of the magnetization. The process of integrating this equation of motion numerically is commonly known as computational micromagnetics, which is a technique used extensively throughout this work. As the magnetization field $\mathbf{m}$ produced by integration of Eq. (1.10) tends towards local minima of $E[\mathbf{m}]$ for any finite value of α_G, this technique can be used both to study magnetization dynamics, and as a method to solve for the minima of $E[\mathbf{m}]$. To solve Eq. (1.10) numerically, the Fidimag package is used, which integrates Eq. (1.10) using the finite differences method [55]. It is worth emphasizing that, as a fundamental assumption in micromagnetism is that the magnetization field is slowly varying, computational micromagnetics can give information only on zero temperature magnetization states. The introduction of a finite temperature would lead to discontinuous variations in the magnetization field, resulting from a non-zero coupling between phonons and magnetic moments.

1.1.3 The topology of magnetization

If skyrmions are defined as being particles that are stabilized by their topology, then before discussing magnetic skyrmions, it is necessary to develop some topological ideas that are relevant to magnetism. The construction of these topological tools is a two-stage process. Firstly, magnetic states must be identified that cannot be smoothly deformed into one another, in a sense analogous to how the loops in Fig. 1.1(b) cannot be smoothly deformed into each other. Secondly, an algorithm $N\left[\mathbf{m}\right]$ must be developed, which takes as an input a magnetization state $\mathbf{m}$, and whose output obeys the rules

- $N\left[\mathbf{m}_1\right] = N\left[\mathbf{m}_2\right] \iff$ the magnetization state $\mathbf{m}_1$ **can** be smoothly deformed into the magnetization state $\mathbf{m}_2$
- $N\left[\mathbf{m}_1\right] \neq N\left[\mathbf{m}_2\right] \iff$ the magnetization state $\mathbf{m}_1$ **cannot** be smoothly deformed into the magnetization state $\mathbf{m}_2$

To succeed, it is useful to consider the case when the moments within a surface S of magnetization $\mathbf{m}$ have an angular span of 4π steradians. Defining the inverse stereographic projection of $\mathbf{m}$ as $\mathbf{m}_P$, the magnetic moments of $\mathbf{m}_P$ are all centred on the origin, and point in every direction on the unit sphere. Now, consider a deformation of $\mathbf{m}$ that results in the angular span of $\mathbf{m}$ decreasing to $4\pi - \Delta$, where Δ is a positive number smaller than 4π. Again applying an inverse stereographic projection, as the angular span of $\mathbf{m}$ is less than 4π, there will be discontinuity in the form of a hole on the spherical surface mapped out by the $\mathbf{m}_P$. As the stereographic projection is a conformal map[1], this hole in $\mathbf{m}_P$ must correspond to a discontinuity in the magnetization $\mathbf{m}$. A discontinuity implies a divergent derivative, which in turn gives a divergent increase in exchange energy $J(\nabla\mathbf{m})^2$. So, a magnetization field $\mathbf{m}$ that has an angular span of 4π steradians cannot be deformed without paying a divergent price in the exchange energy. The above argument generalizes straightforwardly to magnetization fields with an angular span of $4\pi p$ steradians, where $|p| \in \mathbb{N}^+$, and $\mathbb{N}^+$ represents the set of positive natural numbers.

Consequently, a vector field with an angular span of more than (or equal to) $4\pi|p|$ (or, equivalently, a vector field whose inverse stereographic projection wraps the unit sphere one or more times) is, in a sense, "topologically protected", as to deform the vector field to one with an angular span that is less than $4\pi|p|$ involves "cutting" (or, introducing a discontinuity into the magnetization with a divergent energy cost). So, to develop an algorithm that obeys the rules stated above, it is necessary to find an expression known as the topological winding integral $N[\mathbf{m}]$, whose result N counts the number of times the magnetization's inverse stereographic projection $\mathbf{m}_P$ wraps the unit sphere. The angular area spanned by an infinitesimal region of magnetization $d\Omega = \mathbf{m}\cdot(\partial_x\mathbf{m}\times\partial_y\mathbf{m})dxdy$ [56]. Then, the topological winding number of the magnetization enclosed within a surface S is simply $1/4\pi\int_S d\Omega$, or, written as a functional of the magnetization it becomes

$$N[\mathbf{m}(\mathbf{x})] = \frac{1}{4\pi}\iint_S \mathbf{m}\cdot\left(\frac{\partial\mathbf{m}}{\partial x}\times\frac{\partial\mathbf{m}}{\partial y}\right)dx\,dy\,. \tag{1.12}$$

This equation can be used to define magnetization configurations containing skyrmions as being magnetization fields $\mathbf{m}_{\mathrm{Sk}}$ in which $N[\mathbf{m}_{\mathrm{Sk}}]$ is a non-zero integer. As will be found in the following chapter, magnetization fields that locally minimize Eq. (1.3) can be found with $N = 1$. As the original definition of a skyrmion as being a "field configuration stabilized by its topology" is quite generic, any magnetization

---

[1] The conformality of the stereographic projection is almost as old as calculus itself, discovered in 1695 by Edmond Halley, who used it to understand star charts.

field with a non-zero integer winding number N is technically a skyrmion, but for clarity, any state with $N \neq 1$ tends to be given a different name. For example, the antiskyrmion state mentioned previously is a magnetization configuration for which $N = -1$. The comment made about merons being topologically trivial can now also be put into context. Magnetic merons are defined as magnetization configurations $\mathbf{m}_{\text{Meron}}$ for which $N[\mathbf{m}_{\text{Meron}}] = 1/2$. As this number is less than one, the inverse stereographic projection of a meron's magnetization already contains a discontinuity as it only covers a hemisphere. This means that no additional discontinuities need to be created for a meron to be deformed into, for example, a uniformly magnetized state for which $N = 0$. However, merons will inherit some of the other topological properties discussed in this work. For example, merons would also exhibit a finite skyrmion Hall angle, as this angle is a function of the topological winding number – the skyrmion Hall angle will be discussed in detail in chapters 6-8.

1.2 Structure of the thesis

In chapter 2, the complicated symmetry of Eq. (1.3) is investigated. This is used to contextualize the differences between theoretical models and experimental measurements. The Euler Lagrange equations of Eq. (1.3) are then studied in detail, and used to construct a toy model of a skyrmion, as well as study the form of magnetic helices, cones, solitons, and surface twist instabilities.

Chapter 3 provides a discussion of the various techniques that can be used to study the magnetization field $\mathbf{m}$, mentioning the pros and cons of each method. Particular attention is paid to the resonant elastic x-ray scattering (REXS) technique in reflection, due to both its intricacy and its relevance in this work. Standard scattering patterns on the conical state, and helical state, obtained using this technique, are presented, and the implications of magnetic truncation rods on the observed patterns are discussed. Then, the first experimental evidence for a magnetic soliton lattice above room temperature is presented, captured using REXS in a transmission geometry. Finally, REXS patterns obtained on the skyrmion lattice in Cu_2OSeO_3 are presented, as well as the first measurement of the skyrmion liquid phase.

Chapter 4 discusses the three dimensional nature of magnetic skyrmions. First, skyrmions surrounded by the conical state are shown analytically to become conically modulated. The form of this conical modulation is found by solving the LLG equation as a function of applied field. REXS experiments show that, for some magnetic histories, the conical state can coexist with the skyrmion lattice, implying that the skyrmion lattice in that case is conically modulated. Then, a detailed REXS study of the behaviour of skyrmion tubes near the surface of their confining material is carried out. It is shown that one cannot disambiguate a surface pinned skyrmion state from a non-surface-pinned skyrmion state with REXS directly on resonance because of the length of magnetic truncation rods. An off-resonance study then proves that the skyrmion lattice gets pinned to the surfaces of its confining material. This is attributed to the fact that skyrmions cost more energy than surface twist instabilities.

Chapter 5 presents a discussion of Thiele's equation, derived from the LLG equation, which is an equation of motion for localized, robust magnetization configurations. The main drawback of Thiele's equation is that one must have *a priori* knowledge of interparticle interactions to fully leverage its computational power. To solve this problem, a complete theory of micromagnetic interactions, relevant to all magnetization textures whose motion can be described by Thiele's equation, is developed. This theory is used to calculate the skyrmion-skyrmion and skyrmion-surface twist interaction potentials, and benchmarked by computational micromagnetics, using a new technique to accurately obtain interaction potentials numerically. The skyrmion-skyrmion interaction derived is consistent with previously published literature, and the skyrmion-surface twist interaction potential provides a substantial increase in accuracy over previous work. Finally, the attractive interaction between conically modulated skyrmions is reviewed, and used to explain the skyrmion liquid phase discovered in chapter 3.

Chapter 6 is something of an intermezzo, discussing topics widely covered in the literature such as the skyrmion Hall angle, the LLG equation with additional spin-orbit torque and spin-transfer torque terms, the emergent electric field generated by a skyrmion in motion, and the dissipative coupling between a skyrmion and an electron gas. The force that acts on a skyrmion due to a non-uniform magnetic field is derived, and studied micromagnetically to show that the deflection of a skyrmion driven down a nanowire by the spin-orbit torque effect due to the force from the magnetic field gradient (generated by the current in the wire) is negligible.

In chapter 7, Thiele's equation is integrated numerically to study the strain-inducing effects of anisotropic magnetic fields. The origin of these anisotropic fields in real experiments is examined. The numerical results are found to be consistent with experimental data, and the resultant behaviour of the skyrmion lattice is found to be sensitively dependent on its defects and dislocations.

Chapter 8 leverages the results of chapter 7 to derive a new technique that can be used to measure the skyrmion Hall angle from scattering experiments on the skyrmion lattice state. This is used to make the first measurement of the skyrmion Hall angle in the nearly room temperature skyrmion system FeGe. The measured skyrmion Hall angle was 55°, which is largest skyrmion Hall angle ever recorded. The implications of the technique, and of the magnitude of the angle, are reviewed, followed by a brief summary of the thesis and comments on its significance.

Chapter 2

Micromagnetism in two dimensions

The seemingly simple energy functional presented in Eq. (1.3) has fascinating solutions, and is likely minimized by a host of currently unknown magnetization fields. The focus of this chapter is on the one- and two-dimensional solutions to its Euler-Lagrange equations, including skyrmions, helices, cones, solitons, and surface twist instabilities.

Before beginning, the symmetry of the integrand of the energy functional is investigated. This is in no small part motivated by the volume of literature claiming that the rotational and translational symmetry of the typical skyrmion ansatz is in some sense necessitated by nature [24, 57, 58]. Such statements will be found to have absolutely no grounding in reality, as the true translational and rotational symmetry of the micromagnetic energy density is highly non-trivial. Then, the symmetric skyrmion ansatz will be introduced as what it is – a highly simplified, convenient tool with which one can study the property of topological magnetization configurations. Substituting this ansatz into the energy functional will show that its minimum energy configuration is acquired when it has a unit topological winding number and a helicity of $\gamma = \pm\pi/2$. Finding the radial Euler-Lagrange equations leads to a differential equation with no known solution. A simple toy model of the radial profile of this azimuthally symmetric skyrmion ansatz will be derived and discussed.

The helicoidal states hosted by this energy functional will then be derived by inspection of the Euler-Lagrange equations of Eq. (1.3) under a general helicoidal ansatz. This will be used to derive the form of spin helices, cones and solitons. The magnetic solitons arise as, for a particular orientation of the applied field, the helicoidal Euler-Lagrange equations become the time-independent sine-Gordon equation. But, the sine-Gordon equation should also have kink solutions [59]. These kink solutions arise in micromagnetics in the form of surface twist instabilities, and an expression for their profile will be derived.

2.1 The symmetry of micromagnetism

In the following arguments, it will be convenient to refer to individual terms in the integrand of the micromagnetic energy functional given in Eq. (1.3), which can be rewritten as

$$E = \iiint_V \mathcal{E}(\mathbf{m}) d^3x = \iiint_V \Big[\mathcal{E}_J(\mathbf{m}) + \mathcal{E}_D(\mathbf{m}) + \mathcal{E}_B(\mathbf{m})\Big] d^3x \,, \tag{2.1}$$

where $\mathcal{E}_J = J(\nabla\mathbf{m})^2$ is the exchange energy density, $\mathcal{E}_D = D\mathbf{m}\cdot(\nabla\times\mathbf{m})$ is the antisymmetric exchange energy density, $\mathcal{E}_B = -\mathbf{m}\cdot\mathbf{B}$ is the Zeeman energy density, and $\mathcal{E}$ is the total micromagnetic energy density.

To construct an appropriate ansatz to solve any problem in physics, it is necessary to understand the symmetries of the physical system in question. Infinitesimal rotations generated by the arbitrary vector field $\mathbf{a}(\mathbf{x})$ act on any vector $\mathbf{v}$ to produce $\mathbf{v}' = \mathbf{v} + \lim_{\Delta\to 0}\Delta\mathbf{a}\times\mathbf{v}$, where primes denote values in the rotated frame. Rotating

$\mathbf{m}$ in the Zeeman energy density by rotations generated by $\mathbf{a}$ gives

$$\mathcal{E}'_B = \mathcal{E}_B - \lim_{\Delta\to 0} \left(\Delta\mathbf{a}(\mathbf{x}) \times \mathbf{m}(\mathbf{x})\right) \cdot \mathbf{B}(\mathbf{x})\,. \tag{2.2}$$

Clearly, if $\mathbf{a}(\mathbf{x}) \parallel \mathbf{B}(\mathbf{x})$, $\mathcal{E}'_B = \mathcal{E}_B$. This is a statement of the rather obvious result that the Zeeman energy density is symmetric under rotations of the magnetization about $\mathbf{B}$. Now considering the behaviour of the exchange energy density under rotations generated by $\mathbf{a}(\mathbf{x})$, remembering that $|\nabla\mathbf{m}|^2 = (\partial_i m_j)(\partial_i m_j)$ and using Einstein summation convention throughout, gives

$$\mathcal{E}'_J = (\partial_i m'_j)(\partial_i m'_j)\,, \tag{2.3}$$

$$= J \lim_{\Delta\to 0} \left[(\partial_i(m_j + \Delta\epsilon_{jkl}a_k m_l))(\partial_i(m_j + \Delta\epsilon_{jkl}a_k m_l))\right], \tag{2.4}$$

$$= \mathcal{E}_J + J \lim_{\Delta\to 0}(2\Delta\partial_i m_j \partial_i \epsilon_{jkl} a_k m_l) + \mathcal{O}(\Delta^2)\,. \tag{2.5}$$

where ϵ_{ijk} is the Levi-Civita tensor. In order to eliminate the second term in Eq. (2.5), it is necessary to assume that rotations generated by $\mathbf{a}$ are uniform in magnitude and orientation throughout space (so that $\partial_i a_j = 0\ \forall\ i, j$). This allows Eq. (2.5) to be rewritten as

$$\mathcal{E}'_J = \mathcal{E}_J + J \lim_{\Delta\to 0}(2\Delta\partial_i m_j \epsilon_{jkl} a_k \partial_i m_l) + \mathcal{O}(\Delta^2)\,, \tag{2.6}$$

$$= \mathcal{E}_J + \mathcal{O}(\Delta^2)\,, \tag{2.7}$$

where the second term in Eq. (2.6) is zero by symmetry under the exchange of the j and l indices, as $\epsilon_{jkl} = -\epsilon_{lkj}$[1].

Finally, it is necessary to consider the general response of the Dzyaloshinskii-Moriya term $\mathcal{E}_D$ to a rotation. The value of the antisymmetric exchange energy

---

[1] This is entirely analogous to the vector identity $\mathbf{v} \cdot (\mathbf{a} \times \mathbf{v}) = 0$, but here the role of $\mathbf{v}$ is played by the tensor $\partial_i m_j$.

density in the frame rotated by rotations generated by $\mathbf{a}(\mathbf{x})$ is given by

$$\mathcal{E}'_D = \lim_{\Delta\to 0}\Big[D\left(m_i + \Delta\epsilon_{ijk}a_j m_k\right)\epsilon_{ilm}\partial_l\left(m_m + \Delta\epsilon_{mno}a_n m_o\right)\Big]\,. \tag{2.8}$$

This can be rewritten in terms of the energy density in the unrotated frame, which takes the form $\mathcal{E}_D = Dm_i\epsilon_{ijk}\partial_j m_k$ using index notation

$$\mathcal{E}'_D = \mathcal{E}_D + \lim_{\Delta\to 0} D\Delta\big(m_i\epsilon_{ilm}\partial_l\epsilon_{mno}a_n m_o + \epsilon_{ijk}a_j m_k\epsilon_{ilm}\partial_l m_m\big)\,. \tag{2.9}$$

Each product of Levi-Civita tensors in Eq. (2.9) can be substituted by products of Kronecker deltas, giving (to first order in Δ)

$$\mathcal{E}'_D = \mathcal{E}_D + \lim_{\Delta\to 0} D\Delta\big((\delta_{in}\delta_{lo} - \delta_{io}\delta_{ln})m_i\partial_l a_n m_o + (\delta_{jl}\delta_{km} - \delta_{jm}\delta_{kl})a_j m_k\partial_l m_m\big)\,. \tag{2.10}$$

Evaluating the Kronecker deltas and applying the product rule gives

$$\begin{aligned}\mathcal{E}'_D = \mathcal{E}_D + \lim_{\Delta\to 0} D\Delta\big(&m_i m_l\partial_l a_i - m_i m_i\partial_l a_l + m_i a_i\partial_l m_l - a_j m_k\partial_k m_j \\ &a_j m_k\partial_j m_k - m_i a_l\partial_l m_i\big)\,,\end{aligned} \tag{2.11}$$

$$\begin{aligned}= \mathcal{E}_D + \lim_{\Delta\to 0} D\Delta\big(&\mathbf{m}\cdot\left(\left(\mathbf{m}\cdot\nabla\right)\mathbf{a}\right) + \left(\mathbf{m}\cdot\mathbf{m}\right)\left(\nabla\cdot\mathbf{a}\right) + \left(\mathbf{m}\cdot\mathbf{a}\right)\left(\nabla\cdot\mathbf{m}\right) - \\ &\mathbf{a}\cdot\big((\mathbf{m}\cdot\nabla)\mathbf{m}\big)\big)\,,\end{aligned} \tag{2.12}$$

where the final two terms in Eq. (2.11) cancel as $\{ijkl\}$ are dummy variables. The first two terms $\mathcal{O}(\Delta)$ in Eq. (2.12) result from the non-uniformity of the generator of rotations, $\mathbf{a}$; both terms vanish if $\partial_i a_j = 0\ \forall\ i, j$, as was the case for the exchange energy density. The origin of the last two terms is unclear at first glance; they are related to the curl of $\mathbf{m}(\mathbf{x})$. If one requires that $\nabla\times\mathbf{m} \parallel \mathbf{a}$, then

$$\nabla\times\mathbf{m} = \left(\nabla + \mathbf{a}\times\nabla\right)\times\mathbf{m} \tag{2.13}$$

by the associative property of the cross product. In this case, Eq. (2.8) can be rewritten as

$$\mathcal{E}'_D = \lim_{\Delta\to 0}\Big[D\left(m_i + \Delta\epsilon_{ijk}a_j m_k\right)\epsilon_{ilm}\left(\partial_l + \Delta\epsilon_{lno}a_n\partial_o\right)\left(m_m + \Delta\epsilon_{mpq}a_p m_q\right)\Big], \tag{2.14}$$

and repeating the algebra detailed in Eqs. (2.9–2.11) yields

$$\begin{aligned}\mathcal{E}'_D = \mathcal{E}_D + \lim_{\Delta\to 0} D\Delta\big(&m_i m_l\partial_l a_i - m_i m_i\partial_l a_l + m_i a_i\partial_l m_l - m_i a_i\partial_m m_m + \\ &a_j m_k\partial_j m_k - m_i a_l\partial_l m_i + m_i a_m\partial_i m_m - a_j m_k\partial_k m_j\big),\end{aligned} \tag{2.15}$$

$$= \mathcal{E}_D + \lim_{\Delta\to 0} D\Delta\big(\mathbf{m}\cdot\left(\left(\mathbf{m}\cdot\nabla\right)\mathbf{a}\right) + \left(\mathbf{m}\cdot\mathbf{m}\right)\left(\nabla\cdot\mathbf{a}\right)\big), \tag{2.16}$$

where now the only terms $\mathcal{O}(\Delta)$ remaining in Eq. (2.16) vanish under rotations generated by a vector field $\mathbf{a}$ that is constant throughout space.

One might intuitively expect that the Zeeman energy density has translational symmetry along the direction of the external field $\mathbf{B}$. This turns out not to be the case. Consider a spatially varying vector field $\mathbf{b}(\mathbf{x})$. This vector field can generate infinitesimal translations, using $\mathbf{v}' = \mathbf{v} + \lim_{\Delta\to 0}\Delta(\mathbf{b}\cdot\nabla)\mathbf{v}$, where primes now denote vectors in the translated frame. The Zeeman energy density in such a translated frame becomes

$$\mathcal{E}'_B = \mathcal{E}_B - \lim_{\Delta\to 0}\big(\Delta(\mathbf{b}\cdot\nabla)\mathbf{m}\big)\cdot\mathbf{B}. \tag{2.17}$$

The term $\mathcal{O}(\Delta)$ vanishes in two cases. Writing $\mathbf{m}' = \mathbf{m} + \mathcal{T}(\Delta\mathbf{b})\mathbf{m}$, where $\mathcal{T}(\Delta\mathbf{b}) = \lim_{\Delta\to 0}(\Delta\mathbf{b}\cdot\nabla)$ is an operator that maps vectors $\mathbf{v}(\mathbf{x})$ to $\mathbf{v}(\mathbf{x}+\Delta\mathbf{b})$, the first of these cases corresponds to $\mathcal{T}(\Delta\mathbf{b})\mathbf{m}\perp\mathbf{B}$. The second of these cases corresponds to $\mathcal{T}(\Delta\mathbf{b})\mathbf{m} = \mathbf{0}$. Under the same translation, the exchange energy density becomes

$$\mathcal{E}'_J = J\lim_{\Delta\to 0}\partial_i(m_j + \Delta b_k\partial_k m_j)\partial_i(m_j + \Delta b_k\partial_k m_j), \tag{2.18}$$

$$= \mathcal{E}_J + J\lim_{\Delta\to 0} 2\Delta\partial_i m_j\partial_i b_k\partial_k m_j + \mathcal{O}(\Delta^2), \tag{2.19}$$

where $\mathcal{E}'_J = \mathcal{E}_J$ in Eq. (2.19) when the gradient of the magnetization is normal to the gradient in the change in magnetization due to translation; where the gradient is taken along each axis in turn. This is difficult to tell from Eq. (2.19) as it cannot be directly written out in terms of standard vector identities, but this symmetry can be more easily inferred when Eq. (2.19) is written out in the following form

$$\mathcal{E}'_J = \mathcal{E}_J + 2J(\partial_i \mathbf{m}) \cdot (\partial_i \mathcal{T}(\Delta\mathbf{b})\mathbf{m}) + \mathcal{O}(\Delta^2)\,. \tag{2.20}$$

An nontrivial example of this symmetry can be found in a simple spin helix, described by

$$\mathbf{m}_{\text{Helix}} = M_S\big[\cos{(kz+\phi)}, \sin(kz+\phi), 0\big] \tag{2.21}$$

in Cartesian coordinates where M_S is the saturation magnetization, ϕ is a phase factor and $\mathbf{k} = k\hat{\mathbf{z}}$ is the wavevector, aligned along the z-axis without loss of generality. In this case, the derivatives $\partial_i(\Delta\mathbf{b}\cdot\nabla)\mathbf{m}$ and $\partial_i\mathbf{m}$ (with $i \in \{xyz\}$) become

$$\partial_i(\Delta\mathbf{b}\cdot\nabla)\mathbf{m} = -k^2\Delta b_z\delta_{iz}\big[\cos kz, \sin kz, 0\big]\,, \tag{2.22}$$

$$\partial_i\mathbf{m} = k\delta_{iz}\big[-\sin kz, \cos kz, 0\big]\,, \tag{2.23}$$

so that $\mathcal{E}'_J = \mathcal{E}_J$ under arbitrary translations. Finally, the antisymmetric exchange energy density becomes

$$\mathcal{E}'_D = D\lim_{\Delta\to 0}(m_i + \Delta b_l\partial_l m_i)\epsilon_{ijk}\partial_j(m_k + \Delta b_l\partial_l m_k)\,, \tag{2.24}$$

$$= \mathcal{E}_D + D\lim_{\Delta\to 0}\Delta(m_i\epsilon_{ijk}\partial_j b_l(\partial_l m_k) + b_l(\partial_l m_i)\epsilon_{ijk}\partial_j m_k) + \mathcal{O}(\Delta^2)\,, \tag{2.25}$$

$$= \mathcal{E}_D + D\lim_{\Delta\to 0}\Delta\big(\mathbf{m}\cdot(\nabla\times(\mathbf{b}\cdot\nabla)\mathbf{m}) + ((\mathbf{b}\cdot\nabla)\mathbf{m})\cdot(\nabla\times\mathbf{m})\big) + \mathcal{O}(\Delta^2)\,, \tag{2.26}$$

when $\mathbf{m}$ is translated by $\mathcal{T}(\Delta\mathbf{b})$. Ignoring terms $\mathcal{O}(\Delta^2)$, the condition for $\mathcal{E}'_D = \mathcal{E}_D$ in Eq. (2.26) can be expressed as

$$\mathbf{m}\cdot(\nabla\times\mathcal{T}(\Delta\mathbf{b})\mathbf{m}) = -\mathcal{T}(\Delta\mathbf{b})\mathbf{m}\cdot(\nabla\times\mathbf{m})\,. \tag{2.27}$$

This contains the trivial solution $\mathcal{T}(\Delta\mathbf{b})\mathbf{m} = \mathbf{0}$, but could be solved numerically for magnetization configurations that solve it non-trivially.

The key results of this section are the following symmetry constraints placed on $\mathbf{m}(\mathbf{x})$ such that the total energy density $\mathcal{E}' = \mathcal{E}$ is invariant under rotations generated by $\mathbf{a}(\mathbf{x})$ and translations generated by $\mathbf{b}(\mathbf{x})$ in Eqs. (2.2), (2.5), (2.12), (2.17), (2.19) and (2.26). The constraint equation for rotational symmetry is given by

$$\begin{aligned} 0 = -B_i\epsilon_{ijk}a_j m_k + &2J\partial_i m_j \epsilon_{jkl} a_k \partial_i m_l + \\ &D\big(m_i m_l \partial_l a_i - m_i m_i \partial_l a_l + m_i a_i \partial_l m_l - a_j m_k \partial_k m_j\big)\,. \end{aligned} \tag{2.28}$$

The constraint equation for translational symmetry is given by

$$\begin{aligned} 0 = -b_i\partial_i m_j B_j + &2J\partial_i m_j \partial_i b_k \partial_k m_j + \\ &D(m_i\epsilon_{ijk}\partial_j b_l(\partial_l m_k) + b_l(\partial_l m_i)\epsilon_{ijk}\partial_j m_k)\,. \end{aligned} \tag{2.29}$$

Finally, the constraint equation for combined rotational and translational symmetry can be found by summing right-hand side (RHS) of Eq. (2.28) with the RHS of Eq. (2.29) (and by relaxing the constraints of independent rotational and translational symmetry)

$$\begin{aligned} 0 = -B_i\epsilon_{ijk}a_j m_k - b_i\partial_i m_j B_j + 2J\big(\partial_i m_j \epsilon_{jkl} a_k \partial_i m_l + \partial_i m_j \partial_i b_k \partial_k m_j\big) + \\ D\big(m_i m_l \partial_l a_i - m_i m_i \partial_l a_l + m_i a_i \partial_l m_l - a_j m_k \partial_k m_j + \\ m_i\epsilon_{ijk}\partial_j b_l(\partial_l m_k) + b_l(\partial_l m_i)\epsilon_{ijk}\partial_j m_k\big)\,. \end{aligned} \tag{2.30}$$

Non-trivial solutions of Eq. (2.30) would provide the most general form of an ansatz of a magnetization configuration that leaves the total micromagnetic energy density invariant under combined translations and rotations. While no attempts will be made to solve Eq. (2.30) directly, its complexity illustrates that if one constructs a simple ansatz for an $\mathbf{m}(\mathbf{x})$ with a winding number N, one cannot possibly hope to describe all of the configurations available $\mathbf{m}(\mathbf{x})$ with winding number N. So, while the topics of one- and two-dimensional magnetization structures will be addressed in this chapter, it should come as no surprise that magnetic skyrmions are truly three-dimensional structures. Likewise, the rich three-dimensional magnetization textures explored in chapter 4 represent just the tip of the iceberg of what micromagnetics has to offer.

Instead of pondering the case when Eq. (2.30) holds while each of the constituent terms are finite, it may be more practical to consider the eventuality when each of the rotational/translational symmetry constraints hold independently simultaneously.

First considering rotations, from Eq. (2.2), the Zeeman energy density is symmetric under rotations generated by $\mathbf{a}(\mathbf{x}) \propto \mathbf{B}(\mathbf{x})$. According to Eq. (2.5), to satisfy the symmetry of the exchange energy density at the same time further requires that the external magnetic field $\mathbf{B}(\mathbf{x})$ does not change its orientation[1]. Of the four problematic terms in Eq. (2.12), the first two are already zero by the requirements of the exchange interaction, while the last two place the first bound on the magnetization: $(\nabla \times \mathbf{m}) \parallel \mathbf{B}$. So, each of Eqs. (2.2), (2.5) and (2.12) can be simultaneously non-trivially satisfied when $\mathbf{B}$ is uniaxial and $(\nabla \times \mathbf{m}) \parallel \mathbf{B}$.

For the translational symmetries, Eq. (2.17) requires that the change in magnetization due to translation is perpendicular to the external magnetic field, while Eq. (2.19) requires that the partial derivatives of the change in magnetization due to translation are normal to the partial derivatives of the magnetization. The interpretation of non-trivial translational symmetries in the Dzyaloshinskii-Moriya energy density is more difficult. The left hand side of Eq. (2.27) can be read as "the dot product between the curl of the vector field describing the change in magnetization due to translation, and the unperturbed magnetization"; the right hand side is "the dot product between the vector field describing the change in magnetization due to translation, and the curl of the unperturbed magnetization". This is a complex symmetry that will not be explored further here, but it would be possible to solve Eq. (2.27) for magnetization configurations that satisfy this equality so that $\mathcal{E}'_D = \mathcal{E}_D$.

---

[1] It is possible for a magnetic field to be uniaxial and nontrivial without breaking $\nabla \cdot \mathbf{B} = 0$. For example $\mathbf{B} = f(x, y)\hat{\mathbf{z}}$ is non-divergent for any function $f(x, y)$.

2.2 The two-dimensional structure of skyrmions

As previously defined, magnetic skyrmions are characterized by any localized magnetization configuration with a topological winding number $|N| \geq 1$. Throughout this work, magnetization fields with a constant magnitude, satisfying $\mathbf{m} \neq \mathbf{m}(\mathbf{x})$, will be considered. In this regime, the word "localized", when applied to a magnetization field, implicitly denotes that the magnetization field is embedded within some encompassing magnetization configuration. To make this notion precise, consider the localized magnetization configuration $\mathbf{m}_1(r,\theta)$ embedded within $\mathbf{m}_\infty(r,\theta)$, where r is the radial coordinate, and θ is the azimuthal coordinate, in the standard polar coordinate system. Then, if $\mathbf{m}_1$ is centred at the origin, the condition for $\mathbf{m}_1$ to be localized can be written

$$\lim_{r\to\infty} \mathbf{m}_1(r,\theta) = \mathbf{m}_\infty(r,\theta)\,. \tag{2.31}$$

The magnetic flux-density $\mathbf{B}$ appearing in the micromagnetic energy density could, in principle, be an arbitrary non-divergent vector field. Following the rotational symmetry discussion in the previous section, it is lucrative to make the assumption that the external magnetic field is uniaxial. Further to this assumption, the external field will be assumed to be constant, i.e. $\partial_i \mathbf{B} = 0 \ \forall \ i$; while this may appear as a needless oversimplification, it will be possible to consider the validity of this approximation once a skyrmion has been constructed analytically. As such, the magnetic flux density can be used to define our coordinate system such that $\mathbf{B} = B\hat{\mathbf{z}}$.

For any magnetization configuration to be considered 2D, a trivial translational symmetry must be imposed along an axis in 3D. As the external magnetic field has been assumed to be constant, the above symmetry discussion shows that the entire micromagnetic energy density now has a rotational symmetry when $\nabla \times \mathbf{m} \parallel$

B. This information is still insufficient to construct a simple ansatz, as is still not even required that the translational symmetry axis is parallel to the external field[1]. To make analytical progress, it is useful to assume that the magnetization configuration of a skyrmion $\mathbf{m}_1$ is azimuthally symmetric about the translation axis. It is important to appreciate at this point that this ansatz is purely a toy model and far from a symmetry requirement; any physical properties derived using this model should not be expected to hold in general.

It is possible to find the magnetization field $\mathbf{m}_\infty$ that minimizes the energy of $\mathbf{m}_\mathbf{1}$ by evaluating the various energy density terms in Eq. (2.1) in the limit $r \to \infty$. To satisfy Eq. (2.31), it must be possible to write

$$\mathbf{m}_1(r,\theta) = \sin f(r)\mathbf{m}_{\text{int}}(r,\theta) + \cos f(r)\mathbf{m}_\infty(r,\theta)\,, \tag{2.32}$$

where $\mathbf{m}_{\text{int}}$ controls the internal structure of $\mathbf{m}_1$, $\lim_{r\to\infty} f(r) = 0$, and $\mathbf{m}_{\text{int}} \perp \mathbf{m}_\infty$[2]. Using azimuthal and axial symmetry, $\mathbf{m}_\infty$ can be written as

$$\mathbf{m}_\infty = k_\theta(r)\hat{\boldsymbol{\theta}} + k_r(r)\hat{\mathbf{r}} + k_z(r)\hat{\mathbf{z}} \tag{2.33}$$

which, assuming the k_i are well behaved at infinity[3], must tend towards a constant vector. In this case, $\mathcal{E}_D(\lim_{r\to\infty}\mathbf{m}_\infty) = \mathcal{E}_J(\lim_{r\to\infty}\mathbf{m}_\infty) = 0$, and $\mathcal{E}_B(\lim_{r\to\infty}\mathbf{m}_\infty) = -M_S k_z B$, so that the magnetization configuration $\mathbf{m}_\infty$ that minimizes the micromagnetic energy is given simply by the field polarized state, $\mathbf{m}_\infty = M_S\hat{\mathbf{z}}$. The most general form of an azimuthally symmetric magnetization configuration that tends towards the field polarized state can be found by

$$\frac{\mathbf{m}_1}{M_S} = \left[\cos\left(N\theta+\gamma\right)\sin(f(r)), \sin(N\theta+\gamma)\sin(f(r)), \cos(f(r))\right], \tag{2.34}$$

---

[1] This can be seen by the fact that $\nabla \times \mathbf{v}(x,y)$ is not required to be parallel to the z-axis.

[2] This is a choice to use an orthogonal basis, not a requirement. Also note that the dimension of the vector space spanned by possible $\mathbf{m}_\infty$'s is two: a degree of freedom has been eaten by azimuthal symmetry.

[3] In fact, as $|\mathbf{m}_\infty| = M_S$ throughout space, all that is required is that the k_i are not oscillatory, or otherwise irregularly varying, as r tends towards infinity.

where N must be an integer so that $\mathbf{m}_1(\theta + 2\pi) = \mathbf{m}_1(\theta)$.

It is now worth remarking on the properties of this ansatz. Firstly, when substituted into the energy functional in Eq. (1.3), the angular part can be directly integrated, leaving

$$\begin{aligned} E = 2\pi \int \Bigg(\frac{1}{2}(\partial_r f(r))^2 + \frac{N^2}{2r^2}\sin^2 f(r) - BM_S \cos f(r) + \\ D\frac{\sin(N\pi)\sin(\gamma + N\pi)}{N-1}\Big(\partial_r f(r) + \frac{N}{2r}\sin(2f(r))\Big)\Bigg) r dr\,. \end{aligned} \tag{2.35}$$

In Ref. [29], the authors claim that there are no stable solutions to Eq. (2.35) unless $\sin(N\pi)\sin(\gamma + N\pi)/(m-1) \neq 0$, citing the famous scaling argument in Ref. [60] inappropriately. This is incorrect due to the dimensionality of the integral in Eq. (2.35), as shown below. It will be useful to first define

$$A(f) = \frac{N^2}{r^2}\sin^2 f(r) - BM_S \cos f(r)\,, \tag{2.36}$$

$$I_1[f(r)] = \int (\partial_r f(r))^2 dr\,, \tag{2.37}$$

$$I_2[f(r)] = \int A(f) dr\,, \tag{2.38}$$

where $E = I_1 + I_2$. In order for $\mathbf{m}_1$ to be a stable solution, it is necessary that the second order variation of the energy $\delta^2 E \geq 0$. As can be verified by substitution, the following identities also hold

$$I_1[f(\lambda r)] = \lambda I_1\,, \tag{2.39}$$

$$I_2[f(\lambda r)] = I_2/\lambda\,, \tag{2.40}$$

so that $E_\lambda = \lambda I_1 + I_2/\lambda$, $dE/d\lambda = I_1 - I_2/\lambda^2$ and $d^2E/d\lambda^2 = 2I_2/\lambda^3$. Evaluating this expression for the second derivative of the energy at $\lambda = 0$ does not enforce any restriction on its sign, and so scaling arguments alone cannot be used to determine the value of N in Eq. (2.35)[1].

Instead, the value of N and γ that minimize E can be inferred by noticing that, for some $f(r)$, $I_D = \int \big[r\partial_r f(r) + N/2\sin(2f(r))\big]dr$ will be either positive or negative. Whichever sign I_D takes, the overall sign of the Dzyaloshinskii-Moriya energy can be tuned by γ; when $N = 1$ this energy contribution can be seen by inspection to be maximally negative with either $\gamma = \pi/2$ or $\gamma = -\pi/2$.

With $N = 1$, the radial Euler-Lagrange equation of Eq. (2.35) is

$$Jr\partial_r^2 f + J\partial_r f + D\sin\gamma(1-\cos 2f) - \frac{J}{2r}\sin 2f - Br\sin f = 0\,. \tag{2.41}$$

This equation has no known general solutions, so in order to make progress one must examine limits and make appropriate approximations. As $\lim_{r\to\infty} f(r) = 0$, in the large r limit, keeping only terms $\mathcal{O}(f)$, the equation simplifies to

$$r^2\partial_r^2 f + r\partial_r f - (1+\lambda^{-2}r^2)f = 0\,, \tag{2.42}$$

which is the first order modified Bessel equation, with linearly independent solutions $I_1(r/\lambda)$ and $K_1(r/\lambda)$ (where $\lambda = \sqrt{J/BM_S}$) which are the first order modified Bessel functions of the first and second kind, respectively. Using the boundary condition $\lim_{r\to\infty} f(r) = 0$, the exponentially growing Bessel function of the first kind can be disregarded, and the solution can be written as $f(r) \propto K_1(r/\lambda) \propto e^{-r/\lambda}/\sqrt{r}$ [2].

While the asymptotic behaviour is possible to understand relatively straightforwardly, the behaviour of a function f that satisfies Eq. (2.41) in the small r limit is more complicated. This has recently been solved in stereographically projected coordinates (the expression can be found in Ref. [61], Eq. 25). For the purposes

---

[1] Had the integral in Eq. (2.35) been three dimensional, then we would have had $E_\lambda = I_1/\lambda + I_2/\lambda^3$, $(dE/d\lambda)_{\lambda=1} = -I_1 - 3I_2$ and $d^2E/d\lambda^2_{\lambda=1} = 2I_1 + 12I_2$, so that $d^2E/d\lambda^2_{\lambda=1} = -2I_1$ when $f(r)$ is a solution to the E-L equations of Eq. (2.35). As $I_1 > 0$, this would mean that $\delta^2 E < 0$, as in [60].

[2] This proportionality denotes the asymptotic behaviour of $K_1(r/\lambda)$, not its behaviour for all r. This is precisely the limit in which Eq. (2.42) was derived and so the more complex general behaviour of $K_1(r/\lambda)$ will not be explored further.

of this work, the azimuthally symmetric skyrmion ansatz is treated purely as a toy model and its exact form will only be required asymptotically. The complicated expressions for the near field profile given in Ref. [61] will be bypassed by simply noting that $f(r) = \pi - kr$ solves Eq. (2.41) (although this substitution does not bound k).

It is possible to construct a toy model for the radial profile of a skyrmion by smoothly connecting the near field solution $f_N(r) = \pi - k_N r$ with the far field solution $f_F(r) = k_F e^{-r/\lambda}/\sqrt{r}$. This can be done in a particularly convenient manner by using a logistic function L, which has been modified so that $L(0) = 0$. The adjusted logistic function is given by

$$L(r) = \frac{k_F}{1 + e^{-\kappa(r-r_0)/(J/D)}} - \frac{k_F}{1 + e^{\kappa(r+r_0)/(J/D)}}\,, \tag{2.43}$$

which obeys the limits $L(r = 0) = 0$ and $\lim_{r\to\infty} L(r) = k_F$, and is a monotonically increasing function of r. The constants κ and r_0 dictate some of the properties of the radial profile; in the large κ limit, one can write $\lim_{\kappa\to\infty} L(r) = H(r - r_0)$, where $H(r - r_0)$ is the Heaviside step function. This elucidates the purpose of the parameter r_0, which provides a measure for the radius of a skyrmion by indicating the value of r beyond which the skyrmion is better described by its far field solution than its near field solution.

Using this modified logistic function, the expression for the radial profile of a skyrmion becomes

$$f(r) = \big(1 - L(r)\big)(\pi - k_N r) + L(r)\frac{e^{-r/\lambda}}{\sqrt{r}}\,, \tag{2.44}$$

or, written out in full

$$\begin{aligned} f(r) = &\left(1 - \frac{k_F}{1 + e^{-\kappa(r-r_0)/(J/D)}} - \frac{k_F}{1 + e^{\kappa(r+r_0)/(J/D)}}\right)(\pi - k_N r) + \\ &\left(\frac{k_F}{1 + e^{-\kappa(r-r_0)/(J/D)}} - \frac{k_F}{1 + e^{\kappa(r+r_0)/(J/D)}}\right)\frac{e^{-r/\lambda}}{\sqrt{r}}\,. \end{aligned} \tag{2.45}$$

Of the constants k_N, k_F, κ and r_0 that appear in this equation, k_N and r_0 can be approximated analytically by following the work of Ref. [61] (namely, ϵ in Ref. [61] becomes r_0 once stereographically projected, and k_N can be found by stereographically projecting Eq. 25 in Ref. [61] and matching coefficients of r). The constant k_F cannot be found analytically, as any value of k_F solves Eq. (2.42) – to approximate k_F, one has no choice but to solve Eq. (2.41) numerically as a boundary value problem. Finally, κ is simply a fitting parameter that dictates the size of the region in r over which the near field solution mixes with the far field solution.

Owing to the simplicity[1] of the azimuthally and translationally symmetric skyrmion ansatz given in Eq. (2.34), the radial Euler-Lagrange equation given in Eq. (2.41) has been widely studied, and many attempts have been made to approximate its solution, each differing depending on the task at hand.

When considering the properties of the core of a skyrmion, a piecewise linear model such as

$$f(r) = \begin{cases} \pi - k_N r & r < \pi/k_N \\ 0 & \text{otherwise} \end{cases} \tag{2.46}$$

has been used to calculate energetics and dissipation [58, 62]. To investigate far field behaviour, authors have neglected the linear component entirely and a first order modified Bessel function of the second kind has been used[2] [29, 57]. This approach has the issue that $K_1(r)$ diverges at $r = 0$; if one carries out a calculation using $K_1(r)$ that involves an integral, one must be very concerned about limits. Another fashionable approach is to model the radial profile using trigonometric functions

---

[1] In fact, the popularity of this ansatz is likely fuelled by a general misunderstanding of the symmetry of the micromagnetic energy density. In the famous review by Nagaosa and Tokura, this ansatz is justified by the meaningless phrase “using the symmetry of the skyrmion” [24], while Lin et al [57] and Kiselev et al [58] fail to provide any justification at all for the ansatz in their popular theoretical works.

[2] As $\lim_{r\to\infty} K_N(r) = K_0(r)$, in the context of Eq. (2.42), it is not uncommon for authors to solve Eq. (2.42) with $K_0(r/\lambda)$, or to simply neglect the $r^{-1/2}$ prefactor of the exponential term [57, 58]

[63–65], for example the function

$$f(r) = 4\tan^{-1}\left(e^{-r/\lambda}\right) \tag{2.47}$$

is fairly accurate for its simplicity and is non-divergent [64]. The major drawback of the formulation in Eq. (2.47) is that its asymptotic behaviour is out by a factor of $\sqrt{r}$; while this is an excellent model in most cases, when asymptotic accuracy is important it is far from ideal.

To better appreciate how these models relate to each other, the expressions for $f(r)$ in Eq. (2.45), Eq. (2.46), and Eq. (2.47) are compared to the numerical solution of the radial Euler-Lagrange equation in Eq. (2.41) (integrated using the bpv4c algorithm, following the procedure detailed in Ref. [66]) in Fig. 2.1.

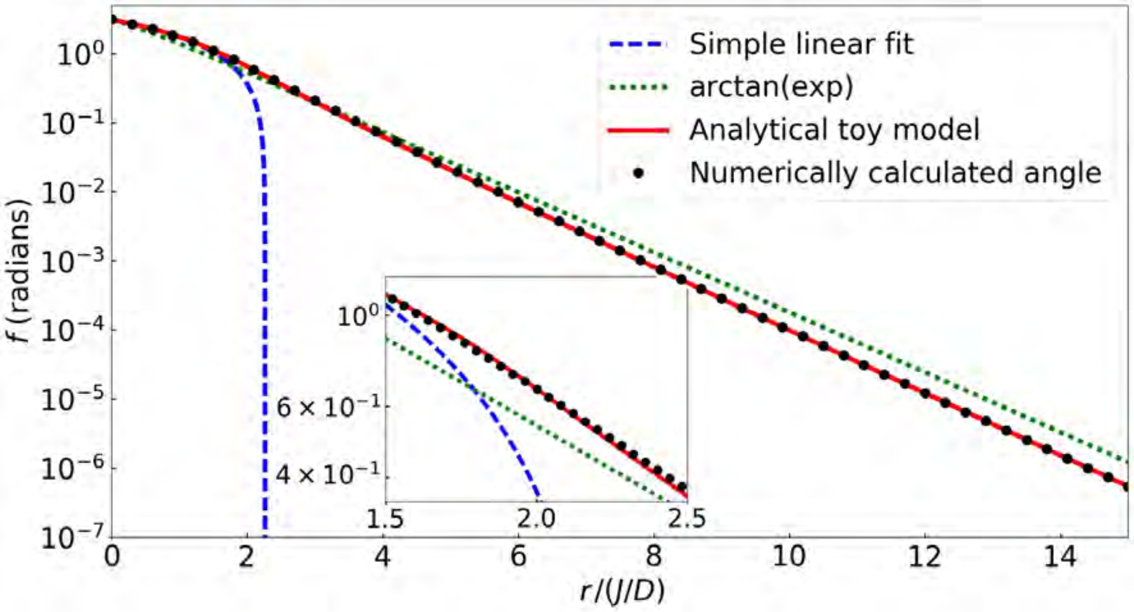

Figure 2.1: A fit of the analytical toy model described in Eq. (2.45) to the numerical solution of Eq. (2.41). In the differential equation the values of J, D, and B were taken to be 1 while choosing $\gamma = -\pi/2$. The toy-model parameters were refined to be $k_F = 6.95$, $\kappa = 5.54$, $r_0 = 1.61$, $k_N = 1.37$, and $\lambda = 1$. For comparison, the popular piecewise linear model is plotted [58, 62], as well as the model $f(r) = 4\arctan(e^{-\frac{r}{\lambda}})$ [64].

As can be seen in Fig. 2.1, the simple linear model is holds only when the angle $f(r)$ between the constituent moments of a skyrmion and the external magnetic field **B** is larger than about one radian. The arctan model given in Eq. (2.47) is fairly accurate throughout all space, but its incorrect asymptotics become clear for large r. The toy model given in Eq. (2.45) is accurate for all values of r, with only a minor deviation from the numerical value of $f(r)$ where $r \approx r_0$. While this can be attributed to the fact that four of its parameters were obtained by least squares refinement, none of these parameters will be relevant in later treatments utilizing this equation. As discussed earlier, if the parameters r_0 or k_N become relevant, they can be approximated analytically [61], and the impossibility of determining k_F plagues every radial profile model; the only fitting parameter unique to this model is κ.

Finally, with the radial profile of an azimuthally symmetric skyrmion understood to be determined by the solution to Eq. (2.41), one need simply substitute the obtained radial profile back into the ansatz in Eq. (2.34) to obtain the two dimensional, rotationally symmetric magnetization configuration of a skyrmion. The resultant magnetization field is displayed in Fig. 2.2, where the magnetization field is represented by cones which are coloured by $f(r)$. Clearly this represents a localized whirling deviation from the field polarized state in which it is contained, but one final question remains: is it topological?

As derived earlier, the topological winding number is defined by

$$W = \frac{1}{4\pi} \iint d^2x \mathbf{m} \cdot \left(\frac{\partial \mathbf{m}}{\partial x} \times \frac{\partial \mathbf{m}}{\partial y} \right) . \tag{2.48}$$

Substituting in the azimuthally symmetric ansatz in Eq. (2.34) into Eq. (2.48) yields $W = N$ after some tedious, but straightforward, algebra [24]. As it has already been found that the energy of the skyrmion configuration is minimized when $N = 1$, then the lowest energy state of the ansatz given in Eq. (2.34) corresponds to a localized, topologically nontrivial region of magnetization whose constituent moments wrap the unit sphere.

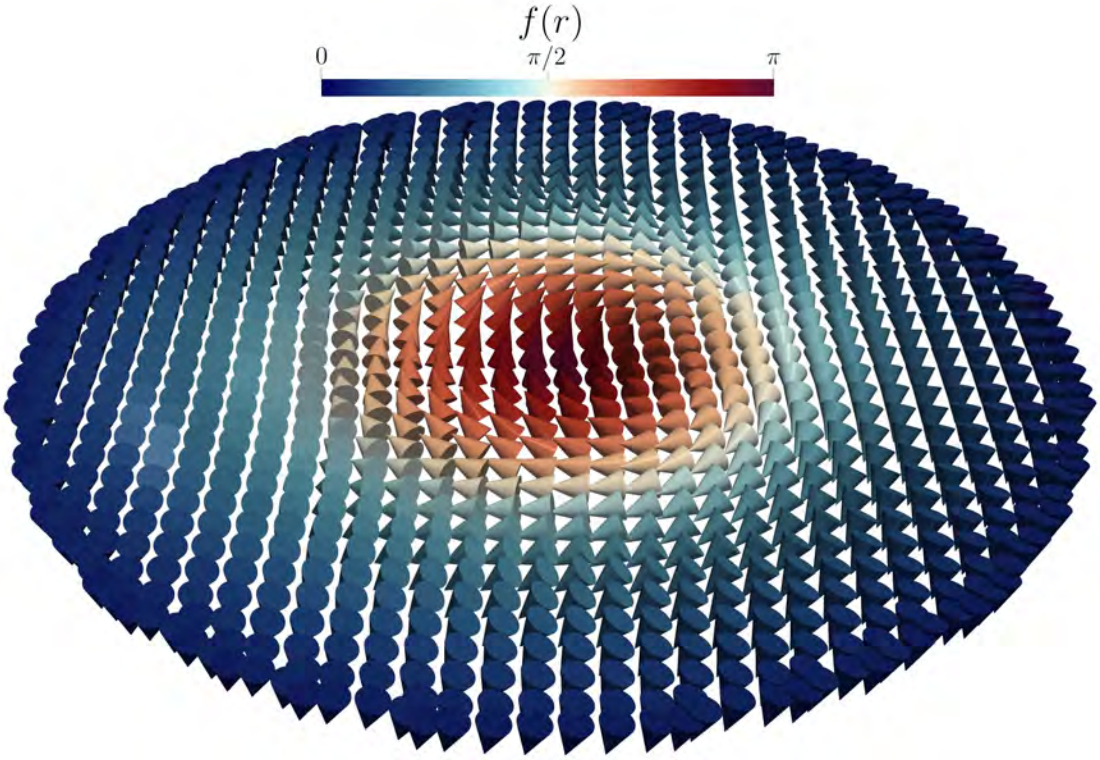

Figure 2.2: Visualization of an isolated skyrmion, obtained by substituting the numerically obtained solution to the radial Euler-Lagrange equation in Eq. (2.41) into the azimuthally symmetric skyrmion ansatz in Eq. (2.34). The orientation of the resultant magnetization configuration is represented by cones. These cones are colored by the angle between the magnetization and the direction of the out-of-plane magnetic field — this angle is referred to as $f(r)$.

2.3 Neighbouring magnetic textures

2.3.1 Helices, cones and solitons

While it has been shown that the azimuthally symmetric skyrmion ansatz is a solution to the micromagnetic energy functional in Eq. (1.3), there are many other well known magnetization fields that extremeize Eq. (1.3) that one might expect to observe in experiment. These structures may exist in the same region of parameter space as magnetic skyrmions; in order to interpret scattering data or real space images it is crucial to be able to identify each member of this magnetic family.

An ansatz for a generalized helicoidal structure (whose propagation vector has been used to orient the z-axis) can be written as

$$\mathbf{m} = \big(\cos\psi(z)\cos\chi, \sin\psi(z)\cos\chi, \sin\chi\big)\,, \tag{2.49}$$

where the angle χ denotes a tilt angle of the helicoid, while $\psi(z)$ dictates its propagation. Substituting this ansatz into the energy functional in Eq. (1.3) yields

$$E = \int dz \big(J(\partial_z\psi)^2\cos^2\chi - D\cos^2\chi\partial_z\psi - B_z M_S \sin\chi - B_x M_S \cos\psi\cos\chi\big)\,, \tag{2.50}$$

where, following the discussion above, the external magnetic field $\mathbf{B}$ has been taken to be constant. The external field $\mathbf{B}$ and helicoid propagation vector $\mathbf{k}$ span a 2D plane, without loss of generality this plane has been chosen to be the xz-plane. However, for simplicity, only three cases will be studied here: $\mathbf{B} = \mathbf{0}$, $\mathbf{B} \parallel \hat{\mathbf{x}}$ and $\mathbf{B} \parallel \hat{\mathbf{z}}$. This corresponds to the fact that, if one is imaging a plane (let this be the xy-plane), one is sensitive to k-vectors in that plane. Then the most typical experimental arrangements involve orienting the external magnetic field such that it is either in the plane ($\mathbf{B} \parallel \hat{\mathbf{x}}$) or out of the plane ($\mathbf{B} \parallel \hat{\mathbf{z}}$). Very often, experimental equipment is mechanically constrained in such a way that other orientations of the external magnetic field cannot be provided. These external magnetic field orientations will be referred to as *in-plane* and *out-of-plane*, respectively, hereafter.

First, it is simplest to consider the case when $\mathbf{B} \parallel \hat{\mathbf{z}}$. Then, the Euler-Lagrange equation for z in Eq. (2.50) becomes

$$2J\cos^2\chi\partial_z^2\psi = 0\,, \tag{2.51}$$

which has solutions $\psi(z) = k_0 + k_1 z$. Substituting this back into the helicoidal energy functional in Eq. (2.50) and evaluating the resultant indefinite integral gives

$$E = z\big(Jk_1^2\cos^2\chi - Dk_1\cos^2\chi - B_z M_S\sin\chi\big) + \text{const.}\,, \tag{2.52}$$

which can be minimized with respect to k_1 and χ by elementary means, giving $k_1 = D/2J$ and $\chi = \sin^{-1}\left(2B_z M_S J/D^2\right)$ (with saturation field $B_S = D^2/2JM_S$). These expressions also contain the solution for $B_z = 0$: $k_1 = D/2J$, $\chi = 0$. These states are referred to as the helical ($\chi = 0$) and conical ($\chi > 0$) states, and their magnetization fields are plotted in Fig. 2.3(a) and Fig. 2.3(b).

The case when $\mathbf{B} \parallel \hat{\mathbf{x}}$ becomes much more complicated algebraically, but has been widely studied theoretically [44, 59, 67–70] and more recently experimentally [71–73]. Substituting $\chi = B_z = 0$ into Eq. (2.50) leads to the functional

$$E = \int dz\big(J(d_z\psi)^2 - Dd_z\psi - B_x M_S\cos\psi\big)\,. \tag{2.53}$$

To make progress it is useful to note that the Euler-Lagrange equations of this functional in the z coordinate lead to the time independent sine-Gordon equation [59], which has solitonic solutions

$$\sin\left(\frac{\psi(z)-\pi}{2}\right) = \mathrm{sn}\left(\frac{\sqrt{\beta}}{k}z|k\right)\,, \tag{2.54}$$

where $\beta = BM_S/(\sqrt{J^2/4 + D^2})$ and $\mathrm{sn}(x|k)$ is the Jacobi elliptic function with elliptic modulus k. The energetically favourable value of k is given by the expression [44, 67, 68]

$$\frac{\pi D}{2J\sqrt{\beta}} = \frac{e(k)}{k}\,, \tag{2.55}$$

where $e(k)$ is the complete elliptic integral of the second kind. The structure of the resultant 1D magnetization field can be found in Fig. 2.3(c).

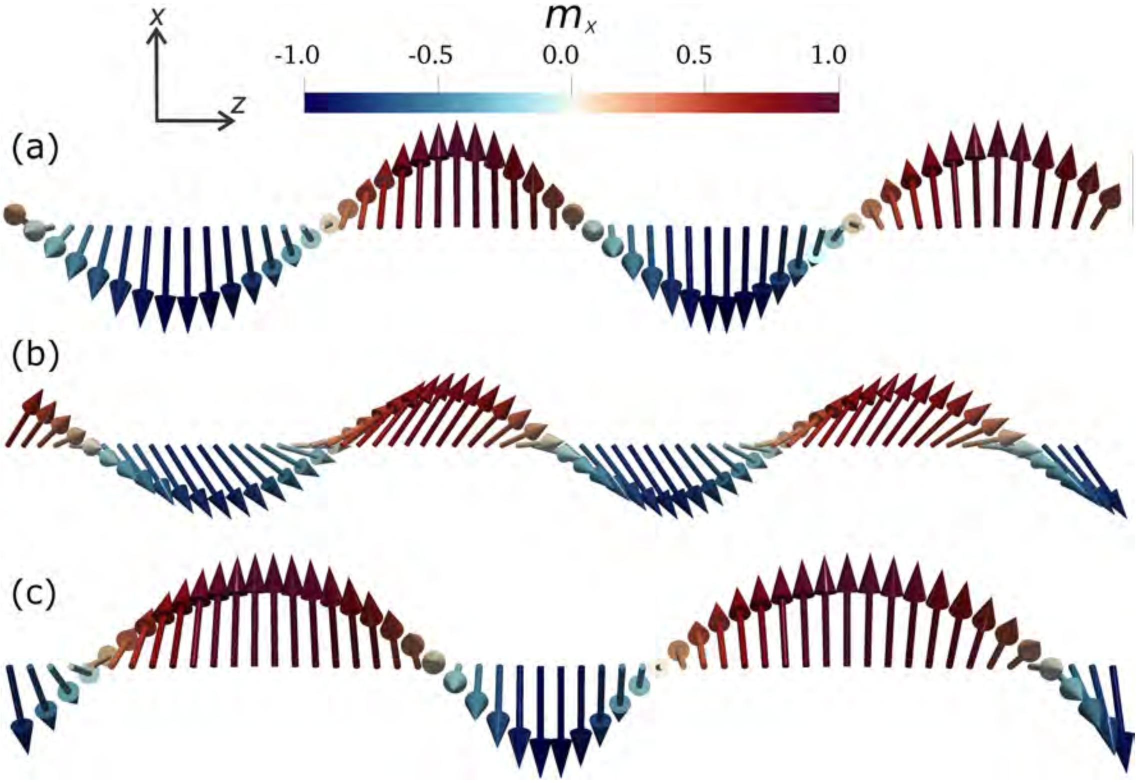

Figure 2.3: A visualization of magnetic (a) helices, (b) cones, and (c) solitons. (a) A helical magnetization structure, obtained by integration of the Landau-Lifshitz-Gilbert equation in the presence of finite bulk Dzyaloshinskii-Moriya and exchange interactions, but with $\mathbf{B} = \mathbf{0}$. Arrows indicate the local orientation of the magnetization field, coloured by their x-component. The k-vector of the helix is parallel to the z-direction. (b) As in (a), but with a finite magnetic field pointing along the positive z-direction. To minimize energy, the magnetic moments cant by an angle $\sin\chi = 2B_xM_sJ/D^2$ towards the external magnetic field. (c) As in (b), but with the external magnetic field applied along the positive x-direction. Regions in which moments are roughly parallel to $\mathbf{B}$ are extended by an amount determined by $|\mathbf{B}|$, while areas with moments pointing antiparallel to B are contracted; the overall wavelength of the periodic structure increases by an amount given by the solution of Eq. (2.55).

2.3.2 Surface twist instabilities

Recently, another state was found to exist in systems which are described by the solitonic energy functional in Eq. (2.53) [45]. These so-called surface twist instabilities are a necessary boundary condition of systems with both the Dzyaloshinskii-Moriya and exchange interactions. This can be seen by assuming that $B_z > B_S$, so that the bulk of the state is field polarized, giving $\psi(z)$ the boundary conditions $\psi(0) = \psi_0$, $\lim_{z\to\infty} = 0$. Evaluating the integral in Eq. (2.53) from 0 to ∞, its Euler-Lagrange equation in z is

$$\left(\frac{-2J}{BM_S}\right)\partial_z^2\psi = \sin\psi\,, \tag{2.56}$$

which can be directly integrated once both sides have been multiplied by $\partial_z\psi$ to arrive at the expression

$$\left(\frac{-J}{BM_S}\right)(\partial_z\psi)^2 = -\cos\psi + C_1\,, \tag{2.57}$$

where C_1 is a constant of integration. As $\lim_{z\to\infty}\psi(z) = 0$, $C_1 \overset{!}{=} 1$. After some trigonometric manipulation, Eq. (2.57) can then be integrated to give

$$\psi(z) = 4\tan^{-1}\left(C_2\exp\left(-z\frac{D}{2J}\sqrt{\frac{B}{B_S}}\right)\right)\,. \tag{2.58}$$

The value of ψ_0 that minimizes Eq. (2.53) can be found by minimizing Eq. (2.53) with respect to C_2 to arrive at [45]

$$C_2 = 2\sqrt{B/B_S} - \sqrt{4(B/B_S) - 1}\,, \tag{2.59}$$

so that $\psi(0) = \psi_0$ becomes

$$\psi_0 = 2\sin^{-1}\sqrt{B/4B_S}\,. \tag{2.60}$$

While $\psi(z)$ in Eq. (2.54) takes the form of a soliton solution to the sine-Gordon equation, $\psi(z)$ in Eq. (2.58) takes the form of a kink solution to the sine-Gordon equation [59] and is visualized in Fig. 2.4. As the boundary conditions imposed to give this kink solution simply require that the magnetization is field polarized, these surface-twists should be present at the boundary of every material that hosts skyrmions in the form specified by the azimuthally symmetric skyrmion ansatz in Eq. (2.34). This makes these surface twists immensely important in the field of skyrmionics – if skyrmions are driven down a track, or nanowire, they will be in close proximity to surface twists at all times. As a result, understanding the interaction between a skyrmion and a surface twist is essential; this topic will be discussed at length in chapter 5. An image of a skyrmion nearing the edge of a material is shown in Fig. 2.4.

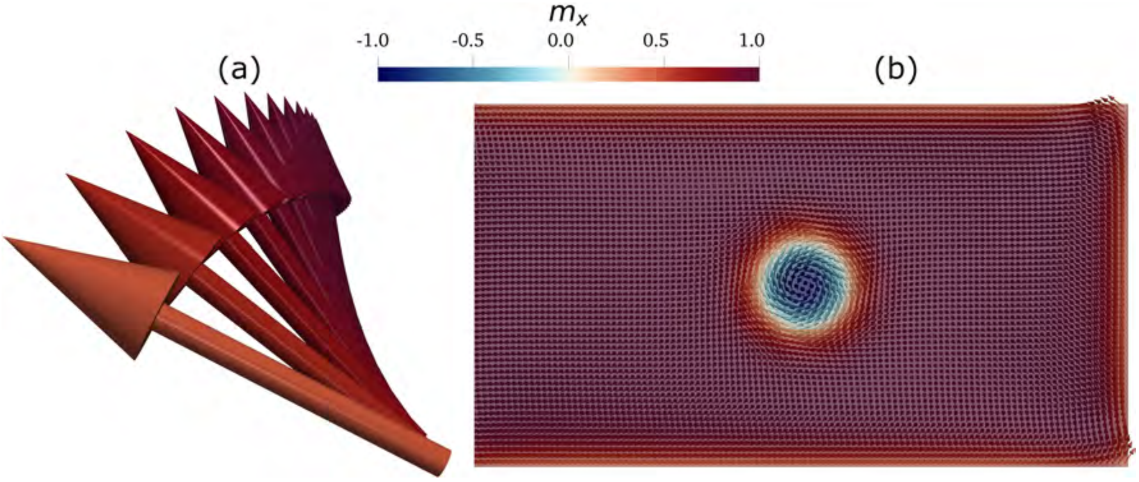

Figure 2.4: (a) Visualization of the tilting of magnetic moments at the edge of a material, with the magnetization field represented by arrows coloured by their x-component. Here, the z-axis points into the page. (b) A calculation carried out under precisely the same energetic conditions as in (a), but relaxed with a unit of topological charge at one end of a nanotrack. The resultant skyrmion configuration coexists with surface twist state, which bounds the bounds the edges of the material. Here, the x axis points into the page.

Chapter 3

Measuring 2D magnetic structures

The magnetic structures discussed in the previous section exist on length-scales determined by the relative strengths of physical constants. The only energy term favouring non-collinear magnetization structures is $\mathcal{E}_D$, the Dzyaloshinskii energy density; if this energy term is comparable in magnitude to the Zeeman energy density $\mathcal{E}_B$, or the exchange energy density $\mathcal{E}_J$, one should expect the helicoidal and skyrmion structures previously discussed to exist on a nanoscopic scale.

The magnetic structure of a material can only be truly said to be completely understood if the entire magnetization field $\mathbf{m}(\mathbf{x})$ is known. There is no technique that one can employ that unambiguously determines this vector field. Instead, it is typical to utilize a wide array of techniques to obtain clues relating to the true value of $\mathbf{m}(\mathbf{x})$. It is then the job of the researcher to propose vector fields that are not inconsistent with the clues obtained, deriving enough clues that the vector fields that the proposed vector fields can be said to be overwhelmingly likely to represent the true value of $\mathbf{m}(\mathbf{x})$.

To conduct any study of magnetic order, it is crucial to understand the experimental techniques that can be used to study a particular length-scale, and to be aware of existing studies that have been carried out using a technique on a material of interest. A table describing a simplistic overview of common techniques for the study of magnetization configurations is provided below, followed by a more detailed discussion of each method of measurement.

3.1 Studying magnetic order experimentally

Technique	Information provided	Sensitivity	Resolution
Magnetometry	Net moment	Bulk	N/A
MFM	Real space	Surface	≈10 nm
LTEM	Real space	Bulk∗	≈10 nm
X-ray holography	Real space	Bulk∗	≈1 nm
Kerr microscopy	Real space	Surface	≈200 nm
STXM	Real space	Bulk∗	≈10 nm
Neutron diffraction	Reciprocal space	Bulk	Å
REXS	Reciprocal space	Surface	Å

Bulk∗: these techniques probe the entirety of a sample, but mandate that the sample be very thin (typically <0.5 μm).

Magnetometry

Magnetometers measure magnetic fields. In the context of materials characterization, they measure the net magnetic moment of a sample. There are two prominent modes of operation for magnetometry: DC and AC. DC magnetometry involves measuring the equilibrium net moment of a sample in a wide range of temperatures and magnetic fields. Temperatures typically range from room temperature to liquid helium temperatures, while fields generated by superconducting magnets range from ±7 T with ramp rates of tens of mT per second. Magnetometers utilizing superconducting quantum interference devices (SQUIDs) can, theoretically, measure individual quanta of flux. This makes them exceptionally sensitive, appropriate for studying the net magnetization of even magnetic monolayers. The only requirement of samples is usually that they are not too large; commercial SQUIDs often require that a sample is mounted inside a weakly diamagnetic straw. Data collected can include hysteresis loops as a function of temperature, and the temperature dependence of the magnetic susceptibility can easily be investigated by DC magnetometry. An excellent reference discussing the pitfalls of commerical SQUIDs, and how to overcome them, is given in Ref. [74].

AC magnetometry is richer, yielding information on low frequency resonances and magnetization dynamics. In this mode of measurement, the externally applied magnetic field is oscillatory. For low frequencies of oscillation and small external fields oscillating about $\mathbf{H} = \mathbf{0}$, one can write [75]

$$\frac{dM}{dH} = \frac{M}{|H| \sin \omega t}, \tag{3.1}$$

so that the susceptibility $\chi(T) = dM/dH|_{H=0}(T)$. AC susceptibility measurements at low fields as a function of temperature therefore provide a convenient and sensitive indirect probe of phase transitions, as dM/dH increases at phase transitions (equivalently to the statement that materials become magnetically softer at phase transitions). In general, for larger and higher frequency external fields, the response of the magnetization should lag behind the applied field by an amount that can be used to determine dissipation in materials.

Magnetic force microscopy (MFM)

Magnetic force microscopes (MFMs) probe the stray field at the surface of a sample. This is done by measuring the deflection of a thin magnetized needle which is suspended tens of nanometres above the surface of a sample at the end of a cantilever [76]. This is a flexible, in-situ technique with a spatial resolution of tens of nanometres. However, MFMs have a series of significant drawbacks. As the MFM tip is itself magnetized, measurements cannot be made in particularly large external fields due to the risk of remagnetizing the tip. Typically, out-of-plane magnetic fields cannot exceed ≈75 mT, and in-plane magnetic fields cannot exceed ≈25 mT, but these characteristic values can vary significantly depending on the magnetic hardness of the coating of the magnetized tip. Additionally, the stray field from the tip can interact with the probed magnetization field. While this can provide interesting insight into the dynamical properties of the magnetization field of interest (it has been used to manipulate individual skyrmions in Ref. [77]), it generally hinders ones ability to determine $\mathbf{m}(\mathbf{x})$ [76].

Lorentz transmission electron microscopy (LTEM)

Lorentz transmission electron microscopes measure the average in-plane magnetic field generated by the magnetization of a sample. This is achieved very simply by firing electrons through a thin magnetic lamella, which are deflected according to the Lorentz force law and then recorded on an area detector [78]. If there is any non-uniform in-plane magnetization in the lamella, the resultant spatially varying magnetic flux density in the sample will deflect electrons by different amounts depending on their position as they pass through the sample. This leads to bright and dark patches appearing on the detector, which can be focused by adjusting the distance between the lamella and the camera. This imaging technique has excellent (≈5 nm) spatial resolution [79–81], its only downsides being that samples can only be measured if they are thin enough for electrons to penetrate and the external magnetic field must be constant to avoid additional electron deflection.

X-ray holography

Holograms constructed from resonant elastic x-ray scattering data measures the out-of-plane magnetic moment of periodic structures. This technique is an extension of REXS in transmission (discussed below), with an additional slit to allow the direct beam to hit the detector [82, 83]. The slit is included to solve the famous phase problem associated with imaging in reciprocal space – the beam that travels directly through the slit contains information on the phase of the light, while the portion of the beam that travels through the lamella contains information on the magnetic structure. Then, a Fourier transform of the collected data contains the sample-sample autocorrelation, the reference-reference autocorrelation, and the desired sample-reference convolution [82]. Obtaining the same image with the opposite polarization of the incident light will reverse the sign of the magnetic signal, but leave the structural information the same, which allows for significant contrast enhancement [83]. This technique is best suited for studying periodic structures and has a spatial resolution of $< 20\,\mathrm{nm}$, but requires that samples are thin enough for resonant soft x-rays to pierce and is sensitive only to the out-of-plane component of the magnetization.

Kerr microscopy

Kerr microscopy is sensitive to all components of the magnetization at the surface of a sample. This technique leverages the magneto-optic Kerr effect to resolve magnetic contrast in differences in intensity between images taken in an optical microscope [84, 85]. As a result, the deficiencies of a Kerr microscope are the same as those of an optical microscope; one can obtain information only near the surface of a material of interest, and, critically, one cannot resolve details that are smaller than a few hundred nanometres in size. Consequently, this technique is only suitable to study skyrmionic materials with extremely small Dzyaloshinskii-Moriya interactions [86–90].

Scanning tunnelling x-ray microscopy (STXM)

STXM is sensitive to the average of any component of the magnetization throughout a thin sample, with element specificity and the ability to distinguish between orbital and spin moments [91]. This is a scanning technique, achieving contrast at each point by focusing an x-ray beam to a small region of a thin sample and taking the difference between transmitted intensity with x-rays of different polarizations [92, 93]. The resolution of this technique is limited by the diameter of the focused x-ray beam, typically tens of nanometres [93]. As with LTEM and x-ray holography, the primary drawback of this technique is the requirement that the sample is thin enough for resonant x-rays to penetrate the sample.

Neutron diffraction

Neutron diffraction is a powerful technique, with the capability of providing a variety of different pieces of information relating to the Fourier transform of the magnetization of different magnetic structures [94, 95]. For the purpose of studying magnetization configurations that are well defined by micromagnetism (i.e. configurations that vary smoothly over length-scales more than an order of magnitude larger than the atomic spacing) a popular technique is small angle neutron scattering (SANS) [95]. SANS can provide information on the average of the Fourier transform of each component of the magnetization throughout the crystal [95]. The most noteworthy prerequisite of this technique is that samples must be large, with a greater size corresponding to more counts per second, and typically samples under 50 mg would be considered to be prohibitively small. For many crystal systems this does not pose a problem, but for the chiral crystals in which skyrmions have been observed, stabilizing massive monochiral crystals can be difficult.

Resonant elastic x-ray scattering (REXS)

Resonant elastic x-ray scattering (REXS) can provide surface-sensitive information on the Fourier transform of each component of the magnetization in a reflection geometry, and the average of the Fourier transform of the out-of-plane component of the magnetization in a transmission geometry [96]. Hereafter, to disambiguate the scattering geometries, REXS in transmission will be referred to as T-REXS[1]. Both in transmission and reflection, incident x-rays are polarized and tuned to an *L*-edge of a magnetic element in the material of interest; the short ranged nature of REXS is due to the very small penetration depth of resonant x-rays. This edge is chosen to

---

[1] In the literature, this technique is often referred to as small angle x-ray scattering (SAXS), to emphasize geometric similarities to its neutronic counterpart, SANS. In this text, T-REXS will be used throughout, because dinosaurs are more memorable than neutron scattering techniques.

excite core electrons with angular momentum into a magnetic band; the amplitude for incident x-rays of a particular polarization to excite these electrons into a magnetic band will be a function of the angular momentum state in the magnetic band. Assuming that the amplitude to scatter from wavevector $\mathbf{k}_1$ to $\mathbf{k}_2$ is proportional to the amplitude for absorption of $\mathbf{k}_1$, the scattering matrix element can be written

$$\langle \mathbf{k}_2 | \hat{V} | \mathbf{k}_1 \rangle = \iiint_{\text{All space}} e^{-\Delta\mathbf{k}\cdot\mathbf{x}} V(\mathbf{m}(\mathbf{x})) d^3\mathbf{x} \,. \tag{3.2}$$

Without finding the precise form of the potential $V(\mathbf{m})$ (which would require a rather more advanced treatment) it is clear that such an approach yields magnetic information, and it is not far-fetched to expect that this information comes out as being proportional to the Fourier transform of the magnetization. Complete derivations of the scattered intensity as a function of angle, polarization and magnetization can be found in Ref. [96] – owing to the simplicity of the final result (that one measures signal proportional to the Fourier transform of the magnetization) this involved derivation is omitted here. Additionally, such derivations provide no insight into magnetic truncation rods, which completely change the intensity one measures in a CCD camera in REXS in reflection. In place of a one-off mathematical treatment, intuition for expected scattering patterns from REXS will be built on a case-by-case basis by visualizing the intersection of magnetic peaks with the Ewald sphere.

The surface sensitivity of REXS, combined with the fact that it allows for the acquisition of the same information as SANS, make it an excellent counterpart to SANS. Many investigations of magnetic structure use SANS to probe the bulk magnetic structure, and REXS to study details of the structure at the surface. Additionally, any samples that are too small to be usable in a neutron scattering experiment can be studied by REXS and T-REXS, as only a few nanometres of magnetic material is sufficient to achieve acceptable magnetic scattering signal.

In reflection, magnetic REXS signal is convolved with structural Bragg peaks. This can be problematic; as soft x-rays are required to obtain magnetic contrast, unless the unit cell for a material of interest is particularly large, or the L-edge of a magnetic element is relatively high in energy, it may be impossible to satisfy any Bragg condition. Of the skyrmion hosting materials listed in table A.1, the only material whose (100) reflection is observable at the L_3-edge in Cu_2OSeO_3. When probed by soft x-rays, all other materials must be studied using T-REXS, where the magnetic reflections are observed about the (000) reflection (i.e. the straight beam).

For the remainder of this thesis, REXS will be used extensively to study the properties of the skyrmion lattice. The reason for this choice of specialization is simple, and is fundamentally unrelated to all previously discussed limitations. Manipulation of a magnetization configurations such as skyrmion will be discussed in detail in chapter 6, but to surmise: if one would like to deterministically manipulate skyrmions, one cannot avoid non-uniform magnetic fields. Spin-transfer and spin-orbit torques can be used to drive skyrmions, but as both of these popular techniques involve driving a current through a material, both techniques will generate a spatially varying magnetic field. Alternatively, one can exploit the direct coupling of the skyrmion lattice to external fields to drive skyrmions with non-uniform magnetic fields alone. In all cases, magnetic field gradients that would deflect neutrons and electrons are present, which is highly problematic for SANS and LTEM. In principle, one could attempt to correct for this probe particle deflection, but to do so would introduce an avoidable layer of complexity – why correct for something that can be sidestepped by choosing a probe particle that does not couple to non-uniform magnetic fields? The preference of REXS over x-ray holography and STXM will become clear in chapters 7 and 8, but is related to the fact that important signatures of dynamical motion are more naturally captured in the structure factor than they are in direct space. Additionally, in chapter 4 the surface sensitivity of REXS will be exploited to study the three-dimensional nature of skyrmion tubes pinned to the surface of materials.

3.2 REXS from helicoidal structures

As helices and cones can be written in terms of trigonometric functions, which can be described in terms of only one Fourier component, scattering from cones and helices is particularly simple. In T-REXS, one would expect to see an additional magnetic peak either side of the direct beam appearing. The situation in REXS is analogous, but greatly complicated by the region of reciprocal space one is sensitive to when sampling the outgoing beam with an area detector.

Typically, magnetic helices will lie in the plane of the sample defined by the sample's surface normal, with propagation vectors along high symmetry directions that lie within that plane. For instance, when scattering from Cu_2OSeO_3 with $\mathbf{q} \parallel (001)$, helices will often be pinned to lie along the (110) and $(1\bar{1}0)$ directions – this is represented by the stripe domains shown in Fig. 3.1(a) and Fig. 3.1(c). In reciprocal space this corresponds to two pairs of magnetic satellite peaks, where the lines connecting each pair are mutually orthogonal. For in-plane magnetic structure, these satellite peaks exist in the plane tangent to the Ewald sphere. Crucially, this is not the plane of reciprocal space sampled by an area detector. Cameras that receive intensity over a finite region span two angular axes. Area detectors are usually aligned so that the vertical axis on the detector lies parallel to rotations generated by the diffractometer's 2θ axis, and the horizontal axis on the detector lies parallel to rotations generated by the diffractometer's χ axis. Rotations about χ cut a curve through reciprocal space with constant $|q|$, while rotations about 2θ define a curve that is at all points orthogonal to χ, but that also changes $|q|$. Consequently, the surface in reciprocal space cut by an area detector should be a locus of spherical shells, each from a sphere centred on the origin of reciprocal space, with linearly increasing radius along the polar coordinate and constant radius along the azimuth[1]. As long as the radii of these spherical shells are reasonably large, one can rather more simply think of this surface as the brown translucent plane visualized in each subfigure of Fig. 3.1. This simplification is surprisingly useful, capturing the fact that azimuthally separated Friedel pairs should be visualized with the same intensity, only becoming qualitatively inaccurate when one considers multiple orders of azimuthal magnetic reflections.

As this surface in reciprocal space is not tangential to a Ewald sphere in all directions, one should expect to observe distortions in reflected magnetic intensity. If helices lie in the plane of a sample as described above, it is not possible for all helical peaks to intersect the surface sampled by an area detector. This situation is shown in Fig. 3.1(a) and Fig. 3.1(b), where only peaks corresponding to the green helical domains intersect the plane sampled by the detector, while peaks due to the blue helical domains appear to exist at different values of $|q|$. In a diffraction experiment, the magnitude of the scattering vector $|q|$ that one is sensitive to is fixed by the relative orientations of the x-ray source, sample and detector. So, if a magnetic peak does not intersect the detector's surface, one should not be able to observe diffracted intensity corresponding to that peak without changing the relative orientations of the source, sample and detector. In order to observe peaks corresponding to the blue stripe domain, one would need to scan $|q|$ (by, for instance, scanning the ω- and 2θ-axes simultaneously such that the 2θ-axis moves with twice the angular velocity of the ω-axis). In reciprocal space, a scan of $|q|$ would correspond to translations of the brown plane along the radial direction.

In real diffraction experiments, one commonly observes diffracted intensity from helical peaks that ought to appear at a $|q|$ which is not intersected by the detector's reciprocal surface. This is related to the shallow penetration depth of resonant x-rays. When scattering from a perfect infinite lattice, points in the reciprocal lattice are infinitesimal in reciprocal space. But, when a wide x-ray beam is incident on

---

[1] This picture is not quite precise, it is actually a lowest order approximation in half the angular width of the detector. As long as this width does not exceed around 20°, which would be extremely large, this picture should be accurate.

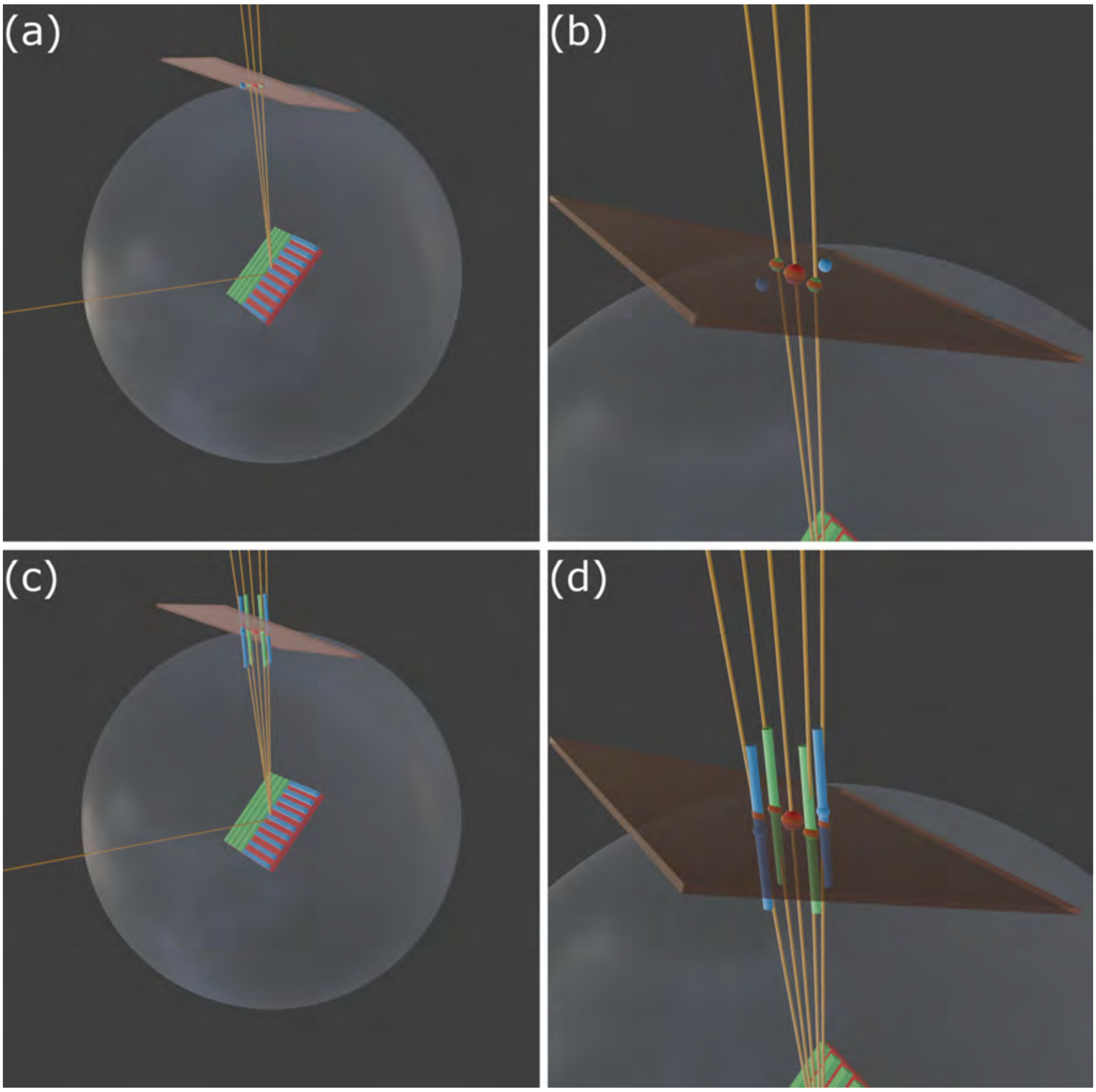

Figure 3.1: A visualization of the region of reciprocal space sampled by a rectangular camera. In each subfigure, the Bragg peak is indicated by a large red sphere, while green and blue magnetic satellites are the Fourier transforms of their respective green and blue helical domains (indicated by stripes on the sample at the centre of the Ewald sphere). The reciprocal space has been rotated towards the outgoing beam by an angle of $(\pi - 2\theta)/2$, and linearly scaled so that the outgoing wavevectors intersect the reciprocal lattice points from which they diffracted. The surface of reciprocal space sampled by the camera is indicated by a light brown translucent plane, and the Ewald sphere with the radius of the Bragg scattering vector is rendered in gray. (a) An overview of the scattering geometry, where magnetic reciprocal lattice peaks are taken to be isotropic and small. (b) A close-up of the reciprocal space plane spanned by the camera – intersections between magnetic and structural peaks with this plane are highlighted by an orange band. (c) As in (a), but replacing point-like peaks with truncation rods. (d) As in (b), but now all helical peaks are visible while the camera plane intersects the Bragg peak, as each truncation rod also passes through this plane.

the surface of a sample with a shallow penetration depth, while the sample's surface area may appear to be constructed from an infinite number of unit cells, one can no longer justify the assumption that the sample is infinitely deep. The change to the structure of the reciprocal lattice that corresponds to a finite thickness along the surface normal direction is that points on the reciprocal lattice become extended parallel to the surface normal [97–101]. The precise functional form of the extension is unimportant here, but a complete treatment can be found in the supplementary material of Ref. [101]. This extension is often referred to as a truncation rod, owing to its dependence on the truncation of a crystal at its surface, and in this work these rods will be simply represented by cylinders with an axis parallel to the radial direction at the corresponding Bragg peak.

Surrounding the spherical magnetic peaks in Fig. 3.1(a) and Fig. 3.1(b) with such cylinders gives Fig. 3.1(c) and Fig. 3.1(d). Due to the intersection of all four truncation rods with the detector's reciprocal surface, there are now five different k-vectors that outgoing light can elastically scatter to that could be detected simultaneously while diffractometer axes are aligned to the Bragg condition. In reality, one should expect to observe something between these two cases – truncation rods will not have a constant diameter in reciprocal space, and so while one might simultaneously observe diffracted signal corresponding to both green and blue domains, one would expect the peaks to have differing intensity, with the brightest peaks being determined by $|q|$.

It is now possible to appreciate the reason why T-REXS is relatively simple in comparison to its reflective counterpart. For the detector's reciprocal surface to intersect Ewald spheres at an angle, along one direction $|q|$ must be decreasing. As $|q|$ is positive definite, there must be some limit to this behaviour, some way of setting up the diffractometer such that $|q|$ can decrease no further. This is achieved when one chooses to diffract about the (000) peak, i.e. the straight beam; then, the detector's reciprocal surface is minimized (at exactly $|q| = 0$) at its central pixel.

This is the only case in which a receiving camera's intensity is symmetric[1], as in this setup the 2θ and χ axes are indistinguishable (the symmetry between them has not been broken by a sample rotation) and $|q|$ increases radially from the centre of the camera.

Helicoidal scattering data is shown in Fig. 3.2. As the detector's reciprocal surface anisotropically cuts through the Ewald sphere, labelled axes are not shown – instead, one can think of the distance between Friedel pairs of magnetic reflections as providing scale bars along the axis connecting them. This peak to peak distance has a length of 0.21 nm^{-1} for data acquired from Cu_2OSeO_3 in Fig. 3.2(a) and Fig. 3.2(d), a length of 0.10 nm^{-1} for the data acquired from $Co_8Zn_{10}Mn_2$ in Fig 3.2(b), and a length of 0.18 nm^{-1} for the data acquired from FeGe in Fig 3.2(c). These peak to peak distance scales will continue to hold for all magnetic diffraction images shown in this chapter taken from these materials. Figure 3.2(a), gathered from helical domains in a single crystal of Cu_2OSeO_3 at remanence, elucidates the importance of magnetic truncation rods. The pair of magnetic peaks at almost the same $|q|$ as the Bragg peak have roughly the same intensity as the Bragg peak itself. The vertical pair of peaks are much weaker, indicating that their magnetic truncation rods only just clip the detector's reciprocal surface. In the experimental setup used in Fig. 3.2(a) and Fig. 3.2(b), scattering at higher $|q|$ occurs lower down in the image. As the magnetic peak below the Bragg peak is brighter than its Friedel pair, one can conclude that the diffractometer must have been aligned such that the centre of the camera's reciprocal surface was at a $|q|$ slightly above that of the Bragg peak.

T-REXS patterns obtained on samples of $Co_8Zn_{10}Mn_2$ and FeGe are shown in Fig. 3.2(b) and Fig. 3.2(c), respectively. Only one helical domain is observed as a time as these samples are 36 $\mu\mathrm{m}^2$, whereas in Fig. 3.2(a) an area on the surface of the Cu_2OSeO_3 sample measuring around 40,000 $\mu\mathrm{m}^2$ was illuminated. The dif-

---

[1] This statement is not precise; backscattered light would maximize $|q|$ at the central pixel of a camera. As backscattering requires that an x-ray source is inside a detector, one cannot satisfy this geometry without building a custom camera, so this can never be seen in a typical diffractometer. Backscattering geometry is, however, extremely common in Laue diffractometers, which are used to orient crystals and characterize crystallite domains.

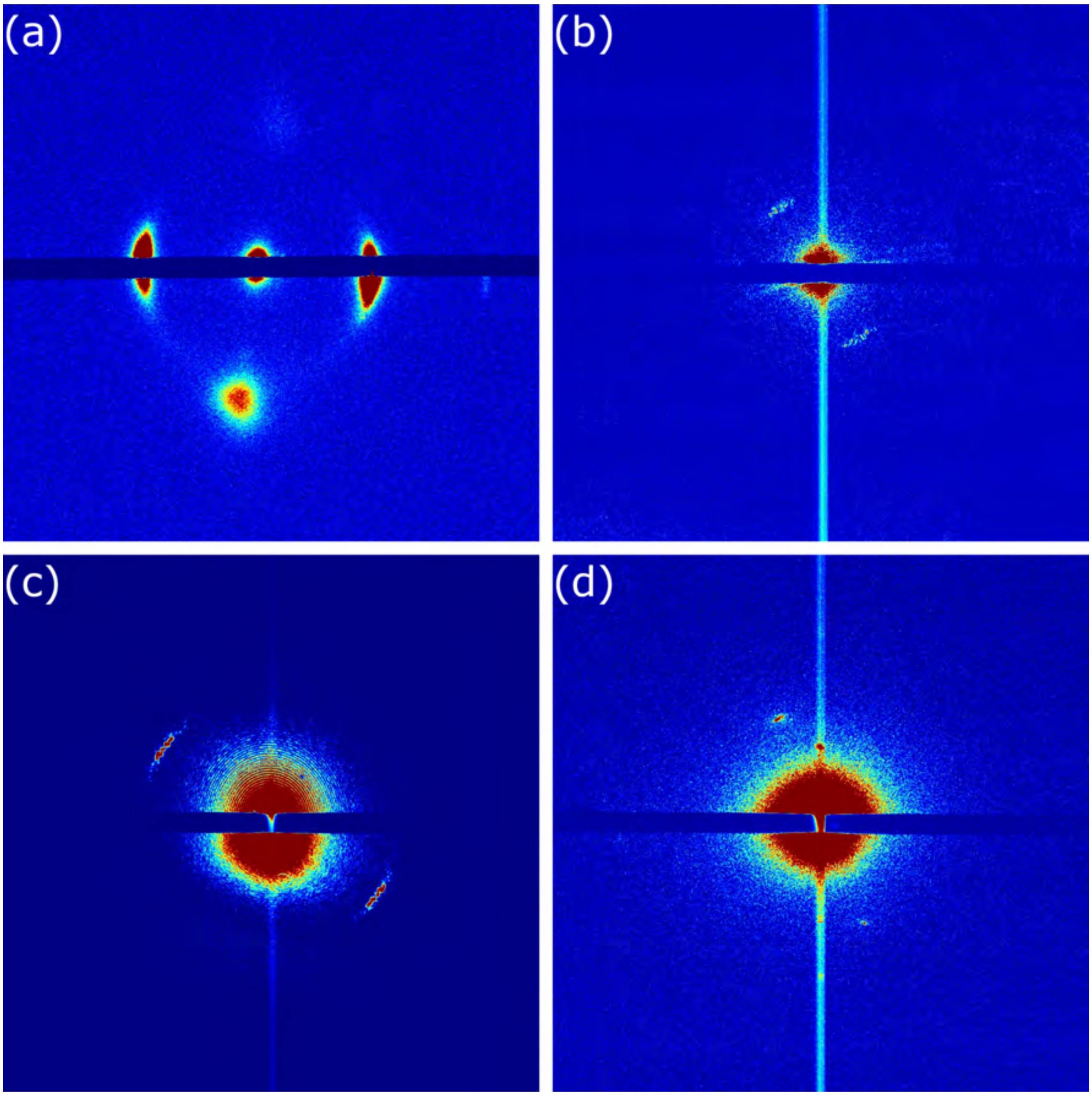

Figure 3.2: Scattering data obtained on the helical and conical states. The vertical streak of intensity present in (b)-(d) is a detector artefact and should be ignored. Axes are are not shown due the anisotropic non-linear dependence of scattering vector on pixel position. (a) A REXS pattern captured from a sample of Cu_2OSeO_3 that was zero-field-cooled to 50 K. Two orthogonal helical domains give rise to pairs of magnetic reflections either side of a central Bragg peak, which is mostly covered by a beamstop. The peaks above and below the Bragg peak are visible only because of their truncation rods, as in Fig. 3.1(d). (b) A T-REXS pattern taken from a sample of $Co_8Zn_{10}Mn_2$ at 355 K at remanence. (c) A T-REXS pattern taken from a sample of FeGe at 268 K with no external field. The bright central region consists of Airy rings due to the beam diffracting through the circular aperture behind the sample. (d) A REXS pattern from a sample of Cu_2OSeO_3 at 56 K with an in-plane field field of 27 mT. The peaks above and below the central Bragg peak are conical. As $|q|$ is optimized for the Bragg condition in this image, the conical peaks appear to be particularly weak, as only the edge of their truncation rods clip the Ewald sphere.

ference in intensity between Fig. 3.2(b) and Fig. 3.2(c) is related to the alignment of the beamline, not a property of the samples. In each case, the direct beam is masked by a horizontal beamstop, but Airy diffraction rings are visible at an intensity comparable to the magnetic intensity. This places a natural lower bound on $|q|$ values of magnetic peaks that can be easily observed using this technique. Generally speaking, a magnetic structure with a period of longer than around 200 nm would be difficult to observe using this technique[1].

In Fig. 3.2(a) there is a faintly visible second order helical scattering peak, even though helices can be described by a single trigonometric function, which have only one Fourier mode. There are two possible reasons for this deviation from expectations. Firstly, helices in reality could be reasonably expected to experience some additional perturbations that deform their internal structure slightly. Using trigonometric functions as a basis for function space, components of the helical magnetization may still be very nearly parallel to the $\cos kz$ direction, but these unaccounted perturbations give rise to a slight rotation in function space that produce additional Fourier modes in reciprocal space. Secondly, it is possible for a photon to scatter multiple times off the same scattering vector, which leads to a second peak at exactly twice the scattering vector of the first peak. It is likely that this secondary peak is primarily the result of multiple scattering, but the possibility that there are slight deformations to the helical structure that require additional Fourier modes to describe is still a realistic prospect.

Due to the rotational limitations of the magnets used in these transmission experiments, it was impossible to image the conical state in lamellae of $Co_8Zn_{10}Mn_2$ and FeGe. While it would be possible to enter the conical state by applying a large out-of-plane magnetic field, its satellite peaks would lie inside the Bragg peak. The same is true in a reflection geometry; conical peaks due to an out-of-plane magnetic field would lie directly above and below the red Bragg spot in Fig. 3.1(b)

---

[1] Although, even if magnetic signal is buried deep within Airy rings for any polarization of light, the difference between data acquired using opposite polarizations could still give excellent magnetic contrast.

and Fig. 3.1(d). The conical truncation rods intersect the detector's reciprocal surface at the same point as the Bragg peak, and would be completely masked by its intensity. When carrying out REXS experiments in reflection, it was possible to use magnets with more rotational degrees of freedom without blocking the beam. By using these magnets to apply an in-plane magnetic field, the conical state in Fig. 3.2(d) was found. This state looks identical in reciprocal space to the helical states in Fig. 3.2(a) but with only one pair of sharp peaks corresponding to cones with a k-vector parallel to $\mathbf{B}$.

3.3 Chiral soliton lattice above room temperature

While magnetic skyrmions are two-dimensional topological field configurations, the magnetic solitons discussed in the previous chapter represent a one-dimensional topological field configuration, where a single 2π twist of the spin chain cannot be smoothly deformed into the field-polarized state. As a result, they have been the subject of some interest as candidate information carriers themselves, where the state of the spin chain (either having, or not having, a twist) can represent the state of a bit of information. Unfortunately, in the presence of a sizeable external magnetic field, helimagnetic configurations tend to align their k-vectors with the field to form the more stable conical state. In fact, despite their theoretical prediction by Igor Dzyaloshinskii in 1964 [44], the magnetic soliton lattice was first observed in a sample of $\mathrm{Cr_{1/3}NbS_2}$ in 2012 [71].

The reason that these solitons are difficult to observe is intimately connected to skyrmions. In a region a phase space near T_C, when magnetic fields are applied that are sufficiently large that the Zeeman energy is comparable to the exchange and antisymmetric exchange interactions, chiral cubic magnets tend to form a skyrmion lattice state. The situation changes in $\mathrm{Cr_{1/3}NbS_2}$, which has a single helical axis in its unit cell that pins helimagnetic textures, forcing them to propagate along that direction. In ref. [71], the chiral soliton lattice was stabilized by applying a field perpendicular to the principal axis of $Cr_{1/3}NbS_2$, allowing for the state to be observed at temperatures under 127 K. The chiral soliton lattice has also been observed in single crystals of $Yb(Ni_{1-x}Cu_x)_3Al_9$ leveraging the same technique. $Yb(Ni_{1-x}Cu_x)_3Al_9$ is a monoaxial helimagnet, and by applying a magnetic field perpendicular to the helical axis, the ground state becomes that of the chiral soliton lattice under 6.5 K.

In Cu_2OSeO_3, which has a chiral cubic structure, the chiral soliton lattice has also been observed [102]. This was possible by straining the Cu_2OSeO_3 crystal uniaxially. This strain breaks the cubic symmetry and stabilizes the chiral soliton lattice with a propagation vector parallel to the strain direction. So, due to the cubic symmetry of the underlying Cu_2OSeO_3 crystal, it was necessary to break that symmetry to stabilize the chiral soliton lattice.

The sample of $Co_8Zn_{10}Mn_2$ used to obtain the helical scattering pattern in Fig. 3.2(b) was mounted to study the skyrmion lattice state. However, throughout the T-REXS experiment, in regions of out-of-plane magnetic field that would normally encourage the nucleation of the skyrmion lattice near T_C (measured to be 365 K in this sample of $Co_8Zn_10Mn_2$), no skyrmions were observed. The exploration of phase space for the skyrmion lattice state involved changing temperature and aligning at remanence (as the 36 μm^2 sample was attached to a cryostat arm that expands/shrinks on a temperature change, which causes the sample to drift out of the incident beam) and scanning the external field from 50 mT to 100 mT in steps of 2 mT. Unnoticed at the time of the experiment, the data collected at 355 K shows clear evidence for the first measurement of the chiral soliton lattice above room temperature. The fitted scattering peak profiles are shown in Fig. 3.3(a), revealing an indisputable dependence on external field. The corresponding real-space periodicities were calculated; the wavelength of the helices at remanence were found to be 120 nm, increasing to a maximum of (184 ± 7) nm at 96 mT.

This measurement is significant for a number of reasons. Firstly, this observation

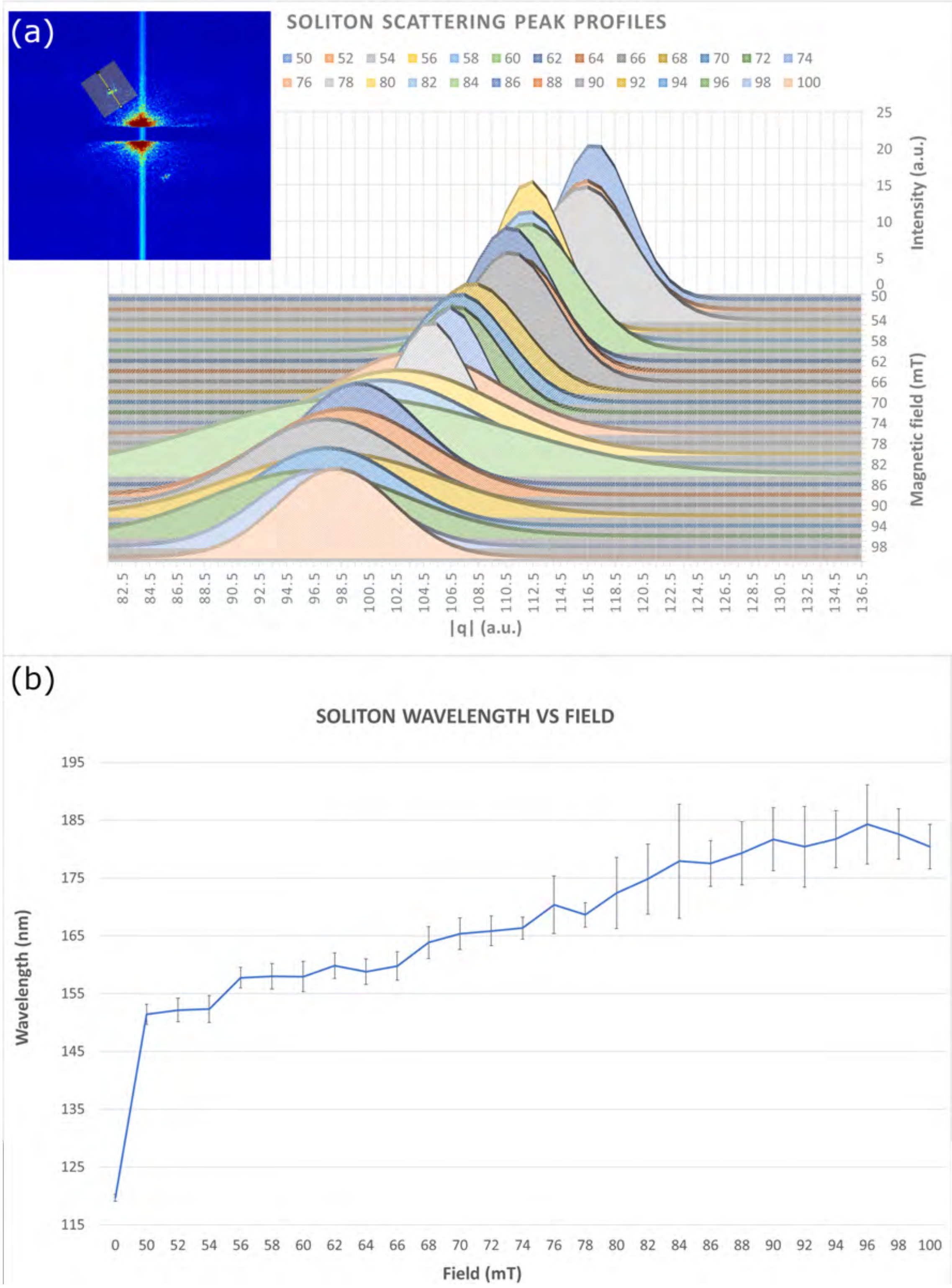

Figure 3.3: (a) Gaussians fit to soliton scattering peak profiles measured at magnetic fields ranging in strength from 50 mT to 100 mT. The inset shows the region of interest from which the raw data was extracted. (b) The wavelength of the solitons as a function of field was calculated by converting the mean $|q|$ of the Gaussians in (a) to nanometres, where error bars are propagated standard deviations. The data point at 0 mT was measured repeatedly during alignment; integration of consecutive scans gave a well defined peak profile with a lower standard deviation.

of the chiral soliton lattice was taken at a temperature of 355 K, more than 200 K warmer than any previous measurement. Above room temperature observation of the chiral soliton lattice brings the state an important step closer to its adoption in computing devices. Secondly, as $Co_8Zn_{10}Mn_2$ belongs to the $P4_132$ space group, it is not a uniaxial magnet like $Cr_{1/3}NbS_2$ and $Yb(Ni_{1-x}Cu_x)_3Al_9$. The $Co_8Zn_{10}Mn_2$ sample was mounted with the (100) direction out of plane, giving two symmetry equivalent (010) and (001) directions in the plane of the sample. This sample of $Co_8Zn_{10}Mn_2$ is a thin lamella that has been transplanted over an aperture, as is required for T-REXS experiments. It is possible that the $Co_8Zn_{10}Mn_2$ lamella has been strained by this sample preparation procedure. However, in Ref. [102], the magnitude of the helical scattering vector was significantly affected by the strain required to nucleate the chiral soliton phase. In this sample of $Co_8Zn_{10}Mn_2$ this is not the case, with the helical period at remanence of 120 nm exactly matching that of other samples.

3.4 REXS from the skyrmion crystal

So far, the mathematical description of skyrmions has been limited to a single skyrmion. One can construct a picture of a lattice of skyrmions straightforwardly from the ansatz in Eq. (2.34) by noticing that linear superpositions of well-separated skyrmions asymptotically approach solutions to the Euler-Lagrange equation in Eq. (2.41). As the skyrmion magnetization tends towards to field polarized magnetization exponentially quickly in the far field limit, the skyrmion-skyrmion separation will not need to be particularly large. Indeed, in many materials, within a certain range of field and temperature, the magnetization spontaneously crystallizes into a skyrmion lattice state. Within this pocket of phase space, typically beginning at a temperature 1-2 K below T_C with an externally applied magnetic field of tens of mT, the magnetic skyrmion lattice becomes the ground state of the magnetization.

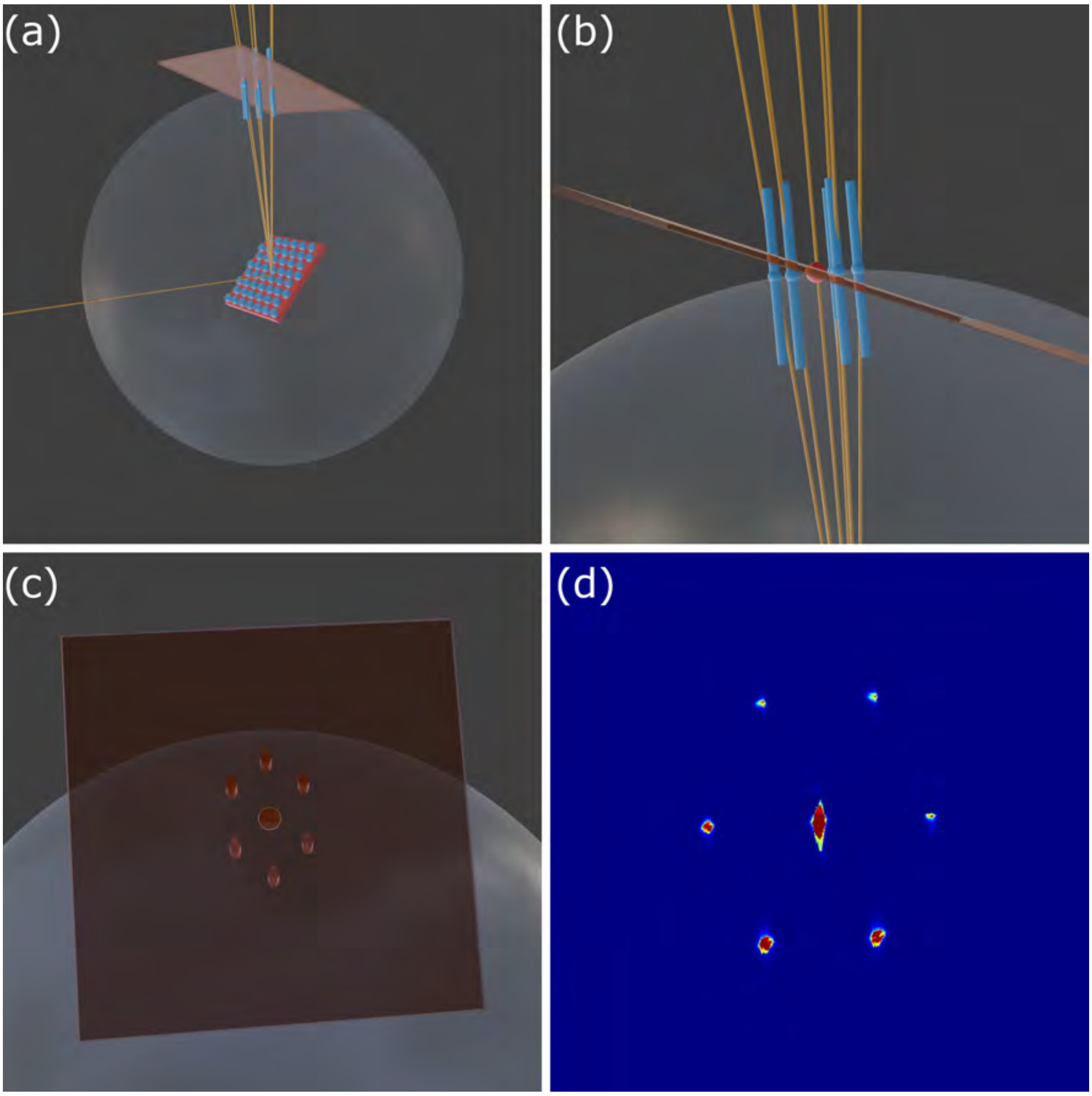

Figure 3.4: (a) A visualization of the reciprocal space surface intersected by an area detector as in Fig. 3.1, but when the sample's magnetization has frozen into a monodomain skyrmion crystal. (b) A close-up of the intersection of the skyrmion lattice magnetic truncation rods with the detector's reciprocal surface. As the detector cuts these rods at an angle, the image received by a detector will appear distorted, and the peaks could appear to have varying intensities. (c) A similar image to (b), but only rendering the Ewald sphere with the radius of the Bragg scattering vector, the detector's reciprocal surface and the intersection between peaks/truncation rods and the detector's reciprocal surface. As the detector's surface cuts the magnetic truncation rods at an angle, the scattered intensity measured becomes elliptically distorted. (d) A REXS image captured on an area detector of a monodomain skyrmion lattice state.

When a skyrmion hosting sample enters the skyrmion pocket, the symmetry of the system is spontaneously broken. While each of the individual skyrmions may be azimuthally symmetric, the most efficient way to pack these azimuthally symmetric nanoparticles into a crystal is via the hexagonally close-packed (hcp) crystal structure. But, there is still one rotational degree of freedom – the hcp crystal structure can be continuously rotated about the axis of the external magnetic field without decreasing its packing density. As a result, unless there are significant additional anisotropic contributions to the micromagnetic energy functional, several domains of magnetic skyrmions can instantaneously form.

For an out-of-plane magnetic field, the reciprocal space structure of the skyrmion lattice is entirely analogous to the reciprocal space structure of the helical state. Where the Fourier transform of sinusoidal magnetic stripes gives just one pair of peaks, the Fourier transform of a general hcp crystal gives, to lowest order, six peaks. The REXS setup for diffraction from a crystal with a similar Bragg condition as Cu_2OSeO_3 is shown in Fig. 3.4(a), and a close-up of the intersection between the detector's reciprocal surface and the skyrmion lattice magnetic truncation rods are shown in Fig. 3.4(b). As can be seen in Fig. 3.4(b), the detector's reciprocal plane intersects the skyrmion lattice's magnetic truncation rods at an angle. This has the consequences previously discussed – that different magnetic peaks can be brought into focus at different values of the ω and 2θ axes of the detector, even though they share the same $|q|$ in reciprocal space. Another repercussion of this angular intersection, difficult to spot in helical patterns but clear in some skyrmion lattice diffraction patterns, is that these peaks become elliptically distorted on the detector screen. This distortion can be seen clearly in Fig. 3.4(c). In this subfigure, the only rendered objects are the detector's reciprocal surface, Ewald sphere, and intersections between the detector's reciprocal surface and the reciprocal lattice. For comparison, a REXS pattern from a monodomain skyrmion lattice formed in a single crystal of Cu_2OSeO_3 is shown in Fig. 3.4(d).

The picture in Fig. 3.4(a) and Fig. 3.4(b) is idealized and not always accurate. When tuning incident x-rays slightly off resonance (by, say, 1 eV or less) the penetration depth of the light dramatically increases. This has the effect of shortening the magnetic truncation rods, to the point where not all six skyrmion peaks are clearly visible. As the (100) Bragg peak in Cu_2OSeO_3 is a symmetry disallowed peak only visible due to the distortion of electronic wavefunctions in the presence of resonant light, moving from resonance can improve magnetic contrast relative to the strength of the structural reflection. The resultant shrinking of magnetic truncation rods necessitates scanning the diffractometer's $|q|$ axis[1] to guarantee that the detector's reciprocal plane intersects each truncation rod. This is equivalent to sliding the plane in Fig. 3.4(b) radially, or up and down the visualized outgoing light that intersects the central Bragg peak. This effect can be seen most clearly when scattering from a multi-domain skyrmion lattice state, as there are many first order magnetic peaks for each diffractometer $|q|$. Such a multi-domain skyrmion lattice is shown in Fig. 3.5(a) and Fig. 3.5(b) at different values of the diffractometer's $|q|$ axis. It is possible to construct a high resolution magnetic image by summing the intensity gathered at different values of $|q|$; a summation of the 21 images from which Fig. 3.5(a) and Fig. 3.5(b) were taken is shown in Fig. 3.5(c).

The variation of the skyrmion lattice magnetization is by no means sinusoidal, being more accurately modelled as a superposition of magnetization configurations such as the azimuthally symmetric kind studied in the previous chapter. A crude model for the skyrmion lattice exists, known as the "triple-q model", which assumes that the skyrmion lattice takes the form of a linear superposition of helical magnetizations with k-vectors each in the same plane and rotated 60° from one another. This model has no grounding in reality, nor does it have any theoretical justification, and can be neatly disproven by looking for higher order peaks in the magnetization structure factor. As discussed above, the helical magnetization is well modelled by sinusoidal variation, allowing its reciprocal lattice to be described in terms of just

---

[1] This is a virtual axis, accessed by simultaneously scanning ω and 2θ, moving 2θ at twice the ω axis' angular speed.

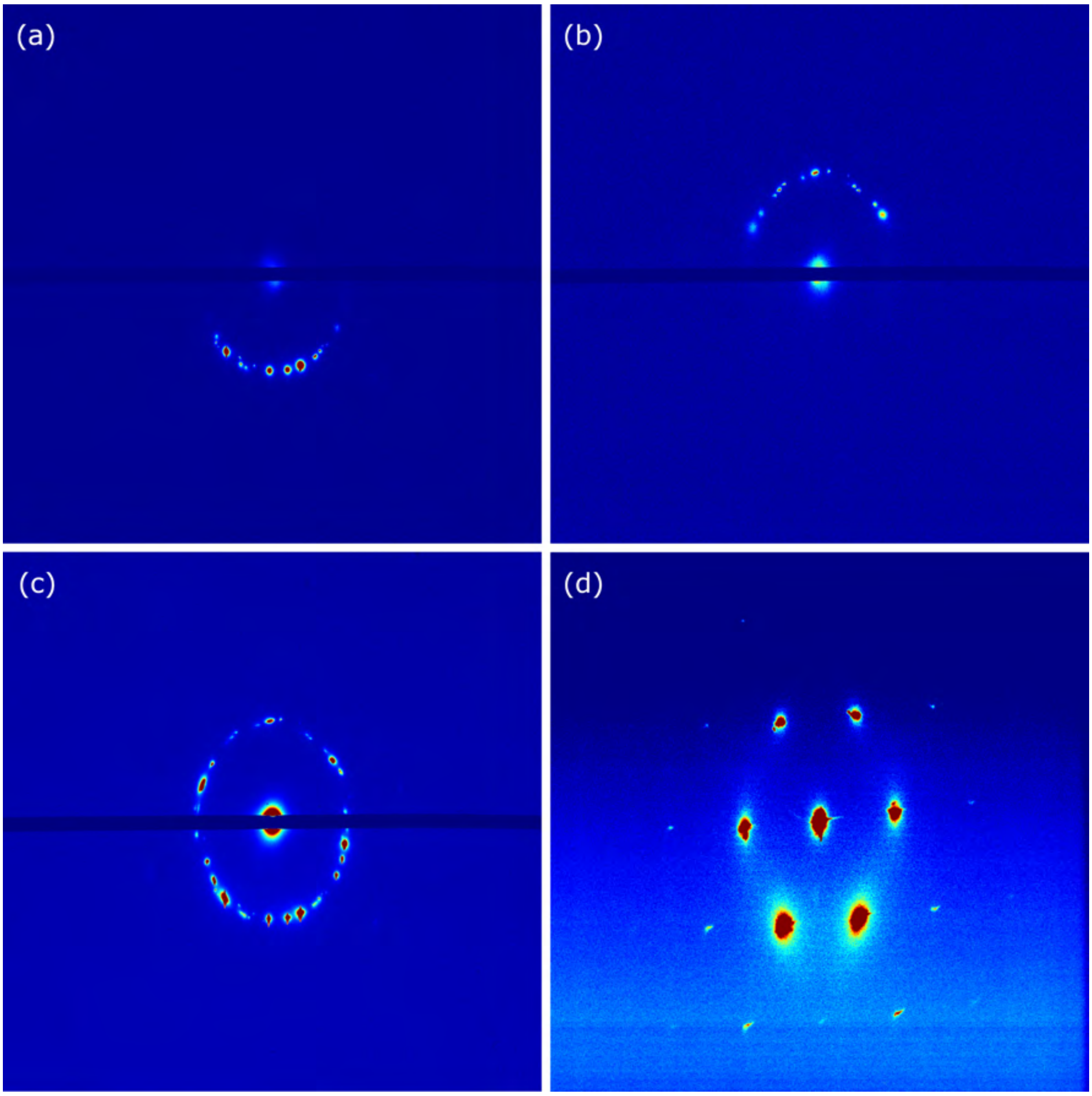

Figure 3.5: (a)-(c) A REXS pattern on a multidomain skyrmion lattice state observed in a single crystal of Cu_2OSeO_3 at an out-of-plane magnetic field of 25 mT. (a) and (b) show the REXS patterns obtained when scanning the area detector through different values of $|q|$, while (c) shows the summed intensity from the $|q|$ scan. (d) The same REXS pattern as in Fig. 3.4(d), but with contrast tuned for lower intensity regions. A large number of higher order scattering peaks are visible.

one pair of peaks. In Fig. 3.2(a), a highly intense REXS pattern for the helical state shows only one extremely faint higher order peak. A comparable REXS pattern obtained from the skyrmion lattice state from the same region of the same crystal of Cu_2OSeO_3 at 57 K is shown in Fig. 3.5(d). Without conducting any detailed analysis, it is clear at a glance that the intensity of higher order scattering peaks has significantly increased, which reflects the fact that the components of the skyrmion lattice's magnetization are highly non-trivial vectors when written in a trigonometric basis. A more detailed quantitative discussion of the REXS structure and form factors for the skyrmion lattice can be found in Ref. [103].

3.4.1 Additional phases of skyrmion ensembles

The above discussion has assumed that, within some pocket of phase space, skyrmions represent, in some sense, the most preferable configuration of magnetic moments. As shown from the scattering patterns in Fig. 3.4(d) and Fig. 3.5 that are consistent with intensity from a hcp magnetization structure, this must be the case. If this pocket exists it is usually very small, occupying tens of mT in one direction and just a few Kelvin in the other. The rest of phase space can often host skyrmions, but the resultant magnetization no longer represents a skyrmion crystal.

The state closest to the lattice state can be found by driving the skyrmion lattice in a non-uniform manner. The resultant state is smectic in structure. This state will be discussed in more detail in chapter 7, and in chapter 8 will be found to unlock the possibility of measuring the skyrmion Hall angle in the skyrmion lattice state.

In many materials, there is no pocket in which skyrmions are the most energetically preferable magnetization configuration, but the skyrmion structure is still a local minimum of the energy functional. In this case, it has been found to be possible to nucleate individual skyrmions using current pulses [104–108]. The resultant state, in which skyrmions are well separated and move mostly independently, is often referred to as the skyrmion gas phase [109, 110]. This situation is very common in magnetic multilayer systems with interfacial DMI, resulting from broken symmetry at the interface between thin layers material.

In systems containing a large number of skyrmions, but where there are not quite enough skyrmions to fill all of space, the skyrmion lattice can appear to melt. This is often measured the moment the magnetic field is increased beyond the upper critical field for the skyrmion phase pocket [102]. There is some disagreement in the literature, with some authors referring to this state as the skyrmion glass [111–113], others calling it the skyrmion liquid phase [114–116]. The main feature that would encourage one to refer to a material as a liquid as opposed to a glass would be viscosity. Amorphous solids such as glasses are “liquids that do not flow”, after all. In this text, a state with characteristic interparticle distances comparable to the skyrmion lattice phase but which exhibit structural order to such a degree that the magnetic structure factor has rotational symmetry, will be referred to as the skyrmion liquid phase. As will be shown in later chapters focused on the dynamics of skyrmion systems, magnetic skyrmions are generally highly mobile. Were it possible to measure the Reynolds number for a skyrmion fabric, it would probably be rather large[1].

The skyrmion liquid state will be understood theoretically in chapter 5 in terms of its interactions, but here the first measurement of the skyrmion liquid state away from the upper critical field of the skyrmion pocket is shown in Fig. 3.6(a). This is constructed in the same way as Fig. 3.5(c), by scanning the diffractometer’s virtual $|q|$-axis slightly off resonance and summing the resulting images. While this image is consistent with scattering from a diffuse liquid of skyrmions with a characteristic interparticle separation similar to that of the skyrmion crystal lattice parameter, it is also indistinguishable from a non-topological disordered state. It has recently been shown that the topological winding number of a state is equal to the num-

---

[1] This could be considered to be related to the relative magnitude of the components of the dissipative tensor appearing in the Thiele equation, which will be discussed in chapter 5.

ber sinusoidal periods in its x-ray magnetic circular dichroism (XMCD) signal. In ordered states such as a monodomain skyrmion lattice, this can be difficult to calculate as the dichroism signal can only be measured at six points simultaneously. In the skyrmion gas state, as there is rotationally symmetric magnetic signal, this measurement of the winding number becomes extremely clear. This measurement, proving that this rotationally symmetric magnetic state is a liquid of skyrmions, is shown in Fig. 3.6(b). A very similar scattering pattern has recently been measured from the chiral maze state at remanence in a [Ir(1)/Co(0.8)/Pt(1)]$_5$ multilayer (thicknesses in nm) [117]. As the applied field of 25 mT is around 10 mT too large to stabilize in-plane helices in Cu_2OSeO_3, it is highly unlikely that the scattering patterns shown in Fig. 3.6 are related to the chiral maze state.

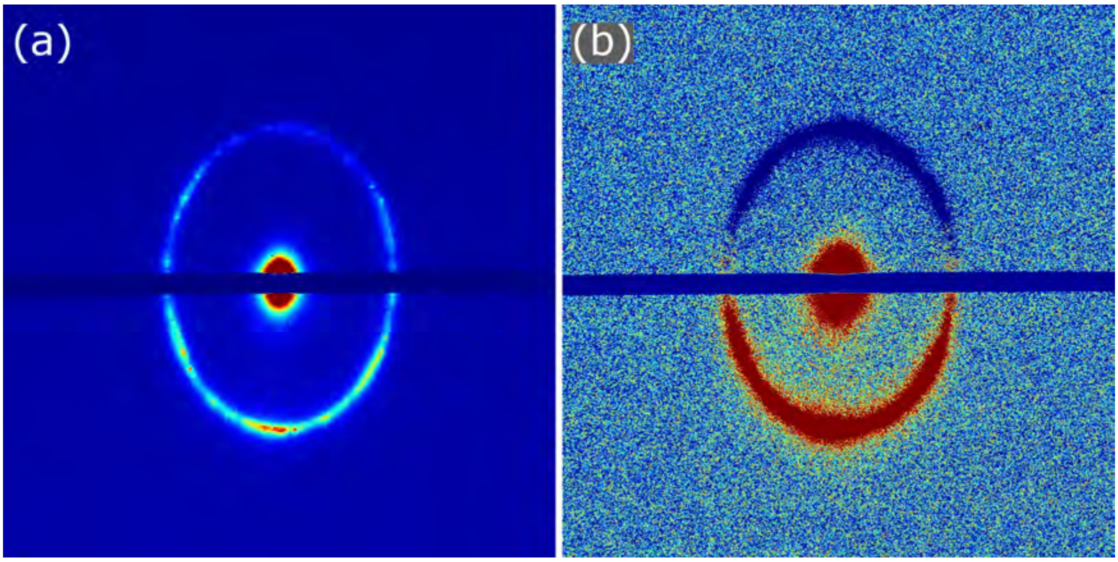

Figure 3.6: (a) A measurement of the skyrmion liquid state in a sample of Cu_2OSeO_3 at a temperature of 54 K and an applied out-of-plane field of 25 mT. While this scattering pattern is consistent with the Fourier transform of a liquid of skyrmions, it is also consistent with a disordered collection of topologically trivial objects (such as spatially separated helices with k-vectors pointing along random directions). (b) A measurement of the topological winding number of the state in (a), obtained by subtracting the image in (a), obtained with right-handed circularly polarized light, by an image obtained with left-handed circularly polarized x-rays. As the dichroic intensity is described by a single sinusoidal period, this must correspond to light scattered from a liquid of particles with winding number $N = 1$: magnetic skyrmions.

Though the two-dimensional models of a skyrmion lattice introduced in this chapter are highly idealized, the skyrmion lattice retains much of its two-dimensional character as it extends nontrivially into the third dimension. These extensions will form the topic of the following chapter.

Chapter 4

Skyrmions in three dimensions

As discussed in detail in chapter 2, the symmetry of micromagnetics is complicated and inherently three-dimensional. As a result, any information gleaned from two-dimensional models must be taken with a pinch of salt. However, even solving for the radial profile of a skyrmion with rotational symmetry about the z-axis and translational symmetry along it was a difficult task – making progress with three-dimensional comes with understandable challenges. However, by combining numerical techniques with careful analysis and experiment, it is possible to uncover some of the secrets of 3D magnetism on the nanoscale.

The content of this chapter will focus on two aspects of the three-dimensional structure of skyrmions. Firstly, a proof of the necessity of the conical modulation of skyrmions, in certain regions of phase space, will be presented. This will provide much needed context for the rotationally symmetric skyrmion ansatz used in chapter 2. Secondly, the behaviour of skyrmion strings near the surfaces of materials will be studied by computational micromagnetics. This will be combined with experimental data to paint a picture of the surface sensitivity of skyrmions in real materials.

4.1 Conically modulated skyrmion strings

The model for a two-dimensional skyrmion was derived based on the assumption that the magnetization configuration of a skyrmion is embedded within the field polarized state. In chapter 2, Eq. (2.49) provides a general description of a helicoidally modulated magnetization field. One could understandably ask the question: what happens to a skyrmion when it is embedded within a helicoidal state, as opposed to the field polarized state?

First, the definition of an embedded state should be extended to the third dimension. Assuming that the skyrmion magnetization $\mathbf{m}_1$ is a function of the axial coordinate z, the localization equation Eq. (2.31) can be simply re-expressed as

$$\lim_{r\to\infty} \mathbf{m}_1(r,\theta,z) = \mathbf{m}_\infty(r,\theta,z)\,. \tag{4.1}$$

Before diving into algebra, it is worth considering what manner of helicoid could take the place of $\mathbf{m}_\infty$ and coexist with a skyrmion. As soliton lattices are infrequently observed, the two prime candidates are helices (with propagation vector $\mathbf{k} \perp \hat{\mathbf{z}}$) and cones (with propagation vector $\mathbf{k} \parallel \hat{\mathbf{z}}$). Skyrmions tend to be separated from the conical state in temperature, while a transition from the helical to the skyrmion state typically requires an increase in external field. However, as skyrmions are topologically protected, once a skyrmion crystal has nucleated within the skyrmion pocket it is possible to field cool to a temperature that would usually host only cones without destroying the skyrmion state. Using this field-cooling procedure, it is realistic to expect that the skyrmion state $\mathbf{m}_1$ may be required to satisfy

$$\lim_{r\to\infty} \mathbf{m}_1(r,\theta,z) = \mathbf{m}_{\mathrm{Con}}(z)\,, \tag{4.2}$$

$$\mathbf{m}_{\mathrm{Con}}(z) = \big(\cos kz \sin\chi, \sin kz \sin\chi, \cos\chi\big)\,, \tag{4.3}$$

where the angle χ has been redefined to make a comparison to the single skyrmion state more straightforward. With this modified χ, one can satisfy Eq. (4.2) by constraining $f(r)$ to satisfy $\lim_{r\to\infty} f(r) = \chi$. But, as one can have two functions of different variables equal only when both functions are constant, Eq. (4.2) can hold only when $k = N = 0$. These conditions impose that both states are simply uniformly magnetized. For any cone state $\mathbf{m}_{\text{Con}}$ with finite periodicity, or any state $\mathbf{m}_1$ described by the azimuthally symmetric ansatz in Eq. (2.34) with nontrivial topology, one can never satisfy the localization equation Eq. (4.2).

To describe a valid $\mathbf{m}_1$, it is useful to express vector fields in terms of a basis that includes the conical state. Noticing that the vector

$$\mathbf{m}_\perp(z) = \big(\cos(kz)\sin(\chi), -\sin(kz)\sin(\chi), 0\big) \tag{4.4}$$

is orthogonal to $\mathbf{m}_{\text{Con}}$ in Eq. (2.49) throughout all space, a convenient orthonormal basis for vector fields is given by

$$\hat{\mathbf{e}}_1 = \mathbf{m}_{\text{Con}}(z)\,, \tag{4.5}$$

$$\hat{\mathbf{e}}_2 = \mathbf{m}_\perp(z)\,, \tag{4.6}$$

$$\hat{\mathbf{e}}_3 = \hat{\mathbf{e}}_1 \times \hat{\mathbf{e}}_2\,. \tag{4.7}$$

In this basis, any localized configuration $\mathbf{m}_1$ satisfying Eq. (4.2) can be written as

$$\mathbf{m}_1 = C_g \cos R(\mathbf{x})\hat{\mathbf{e}}_2 + S_g \cos R(\mathbf{x})\hat{\mathbf{e}}_3 + \sin R(\mathbf{x})\hat{\mathbf{e}}_1\,, \tag{4.8}$$

where $C_g = \cos g(\mathbf{x})$, $S_g = \sin g(\mathbf{x})$, $g(\mathbf{x})$ is an arbitrary function of $\mathbf{x}$ that controls the internal structure of $\mathbf{m}_1$, and $R(\mathbf{x}) = R(r,\theta,z)$ determines the projection of a state along the conical direction. Applying the limit in Eq. (4.2) to Eq. (4.8) yields the requirement

$$\lim_{r\to\infty} R(r,\theta,z) = \pi/2\,. \tag{4.9}$$

Derivatives of Eq. (4.9) give $\lim_{r\to\infty} \partial_\theta R(r,\theta,z) = \lim_{r\to\infty} \partial_z R(r,\theta,z) = 0$, so that the most general form of $R(r,\theta,z)$ is given by

$$R(r,\theta,z)=\rho_{\frac{\pi}{2}}(r)+\rho_0(r)R_{\theta,z}(\theta,z)\,, \tag{4.10}$$

where $\lim_{r\to\infty}\rho_n(r)=n$.

Now that the functional form of $R(r,\theta,z)$ has been constrained, it is instructive to use the basis to describe an unmodulated state $\mathbf{m}_{\text{NoCone}}$, for which $\partial_z\mathbf{m}_{\text{NoCone}}=0$. This will elucidate the conditions that must be met by $R(r,\theta,z)$ so that $\mathbf{m}_1$ is independent of z, and so that it is independent of its surrounding conical state. Choosing $\mathbf{m}_{\text{NoCone}}=(x_0(r,\theta),y_0(r,\theta),z_0(r,\theta))$, then solving the simultaneous equations

$$a\hat{\mathbf{e}}_1+b\hat{\mathbf{e}}_2+c\hat{\mathbf{e}}_3=x_0\hat{\mathbf{x}}+y_0\hat{\mathbf{y}}+z_0\hat{\mathbf{z}} \tag{4.11}$$

gives the expression for a (found numerically using the Gaussian elimination method)

$$a(r,\theta,z)=\frac{x_0(r,\theta)\cos kz+y_0(r,\theta)\sin kz+z_0(r,\theta)\cot\chi\cos 2kz}{\sin\chi+\cos\chi\cot\chi\cos 2kz}\,, \tag{4.12}$$

so that, if $\mathbf{m}_1$ is to be independent of the z coordinate, the function $R(r,\theta,z)$ must satisfy the equation

$$R(r,\theta,z)_{\text{NoCone}}=\sin^{-1}\left(a(r,\theta,z)\right)\,. \tag{4.13}$$

If, for some finite interval $r\in[a,b]$, $a,b\in\mathbb{R}_{>0}$, $\rho_{\frac{\pi}{2}}(r)=0$ and $\rho_0(r)R_{\theta,z}(\theta,z)=R_{\text{NoCone}}$, then it is possible, in this region, for $\mathbf{m}_1$ to be independent of z. However, as $\lim_{r\to\infty}\rho_{\frac{\pi}{2}}(r)=\pi/2$ and $\lim_{r\to\infty}\rho_0(r)=0$, if $|b-a|>\epsilon$ for any $\epsilon>0$, then the ρ_n, and by extension $R(r,\theta,z)$ and $\mathbf{m}_1$, are not analytic. Therefore, if $\mathbf{m}_1$ is an analytic vector field, it cannot be independent of the z-coordinate.

The above proof that $\mathbf{m}_1$ cannot be independent of the z-coordinate is identical to the proof that the dependence of $\mathbf{m}_1$ on the z-coordinate cannot be different than the dependence of the basis vectors on the z-coordinate. In order to show that $\mathbf{m}_1$

must not be independent of the axial coordinate, the functions $x_0(r,\theta)$, $y_0(r,\theta)$ and $z_0(r,\theta)$ were not allowed to vary with z. However, if the functions x_0, y_0 and z_0 are allowed to vary arbitrarily with z, the proof is identical, with the only changes being that $x_0(r,\theta) \to x_0(r,\theta,z)$, $y_0(r,\theta) \to y_0(r,\theta,z)$ and $z_0(r,\theta) \to z_0(r,\theta,z)$. Again it is found that the basis vectors $\hat{\mathbf{e}}_1, \hat{\mathbf{e}}_2$ and $\hat{\mathbf{e}}_3$ are incapable of simultaneously satisfying the localization constraint in Eq. (4.2) and allowing $\mathbf{m}_1 = x_0\hat{\mathbf{x}} + y_0\hat{\mathbf{y}} + z_0\hat{\mathbf{z}}$ for a finite region of r.

Therefore, if $\mathbf{m}_1$ is an analytic vector field, it must be conically modulated, i.e. periodically modulated along the z-direction with wavevector k.

This shows that a state localized within the conical state must exhibit some modulation with the periodicity of the conical state, but does not provide any information on the internal structure of such a state. To investigate this further, the Landau-Lifshitz-Gilbert equation was integrated until the magnetization field was relaxed, according to the procedure outlined in chapter 1. The magnetic field was applied roughly parallel to the z-axis[1] with J and D constants of $8.78 \times 10^{-12}\,\mathrm{Jm}^{-1}$ and $1.58 \times 10^{-3}\,\mathrm{Jm}^{-2}$, respectively, chosen to match the skyrmion hosting chiral magnet FeGe. The system was discretized into finite difference cubes each with a volume of $8\,\mathrm{nm}^3$, and the simulation geometry was periodic in the xy-plane but finite in the z-direction with a height of 252 nm. The magnitude of the external field was chosen to be 250 mT for this particular calculation, although all fields in the range 225-300 mT display the same conical modulation.

A cross-section of the yz-plane of the resultant state is shown in Fig. 4.1. In Fig. 4.1(a) the cross-section is coloured by the z-component of the magnetization. The skyrmion string can be seen to oscillate slightly as it progresses from one side of the sample to the other. The conically modulated nature of the skyrmion tube is best seen in Fig. 4.1(b), which is the same region of magnetization as Fig. 4.1(a)

---

[1] In all calculations carried out in this work, magnetic fields are never applied precisely normal to the faces of finite difference cells. This is done to ensure that the symmetry of the simulation is broken, helping prevent the system from becoming trapped in symmetric configurations that maximize the system's energy.

but allowing the y-component of the magnetization to decide the colour of the cross-section. The y-component of the magnetization at the core of the skyrmion is periodic with the same wavelength as the surrounding conical state, indicated by the colour oscillating between red and blue along the skyrmion string. The skyrmion state becomes modulated in this manner throughout its entire coexistence region with the conical state in computational hysteresis loops. The amplitude of the conical modulation of the skyrmion state is dependent on the magnitude of the external magnetic field, decreasing with increasing field in the same way as the conical state.

To determine whether such a state manifests itself in real materials, a REXS study was carried out on a single crystal of Cu_2OSeO_3. In the REXS data presented in the previous chapter, one would be unable to measure the conical state, as intensity from magnetic diffraction from conical satellite peaks would be contained within the Bragg peak. To bypass this limitation, the REXS experiment was carried out using an in-plane magnetic field. When a magnetic field is applied in-plane, the six-fold skyrmion magnetic satellites are correspondingly rotated by 90°, as shown in Fig. 4.2(a). This means that three of the skyrmion scattering peaks lie above the Bragg peak's Ewald sphere, and three lie below it. If one would have a highly idealized unmodulated skyrmion lattice state (visualized in Fig. 4.2(c1)), these six peaks would appear in the $q_z q_y$-plane, as shown in Fig. 4.2(c2). Defining $q_z = 1$ as the value of q_z at which the pair of skyrmion reflections appear at the same q_z value above the Bragg peak, if one would increase their diffractometer's q_z to this value (by increasing the value of its virtual $|q|$ axis in this geometry) one would expect to observe a pair of peaks in the $q_x q_y$-plane. In reality, the six skyrmion peaks will be significantly elongated along the q_z direction, as these peaks will become truncation rods due to the shallow penetration depth of resonant x-rays. This elongation due to truncation rods is captured in Fig. 4.2(c2), which shows REXS data from the experiment in the $q_y q_z$-plane. Thanks to these magnetic truncation rod effects, one would expect to observe a pair of peaks corresponding to diffraction from the

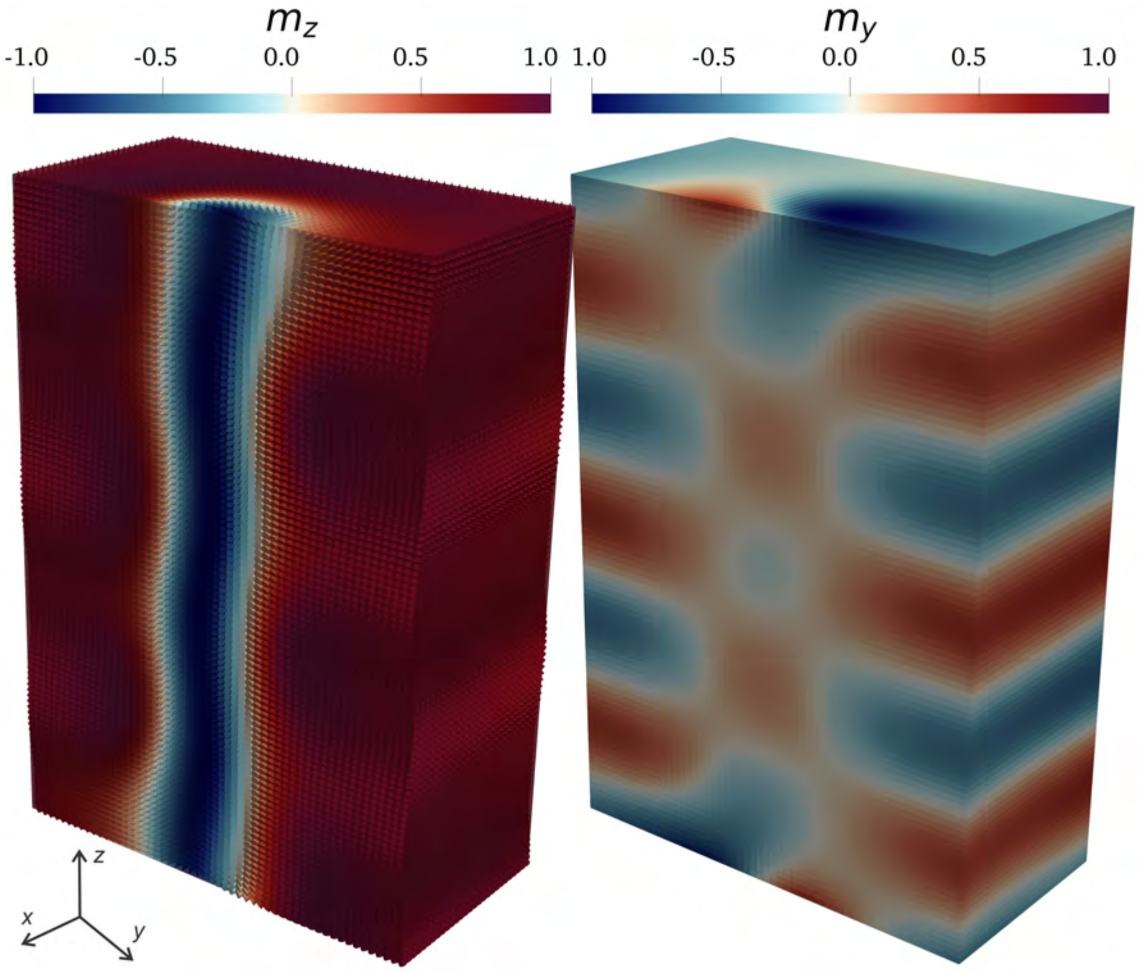

Figure 4.1: A slice (whose normal defines the x-axis) through a simulation of the conically modulated skyrmion state. (a) The skyrmion string propagates along the z-axis, shifting left and right as it progresses, represented by arrows which point along the local orientation of the magnetization and are coloured by its z-component. (b) As in (a), but in place of arrows the surface of the slice is coloured by the y-component of the magnetization. The y-component of the magnetization at the core of the skyrmion is oscillatory (π out of phase with the surrounding conical state) with the same $\mathbf{k}$-vector as the encompassing conical state.

skyrmion lattice for a wide range of values of q_z. With this in mind, the expected diffraction pattern in the $q_y q_z$- and $q_x q_y$-planes from the conical state in Fig. 4.2(e1) are shown in Fig. 4.2(e2) and Fig. 4.2(e3), respectively. Using the coordinate of the Bragg reflection as the origin of q-coordinates, no peaks would be observed in the $(0, q_y, q_z)$ plane. While one would expect no peaks to appear in the $(q_x, q_y, 1)$ plane, truncation rods from the conical peaks in the $(q_x, q_y, 0)$ plane would intersect the $(q_x, q_y, 1)$ plane. Experimental data from the $(q_x, q_y, 1)$-plane is shown in Fig. 4.2(c3), where both skyrmion and conical peaks are observed simultaneously in an area detector.

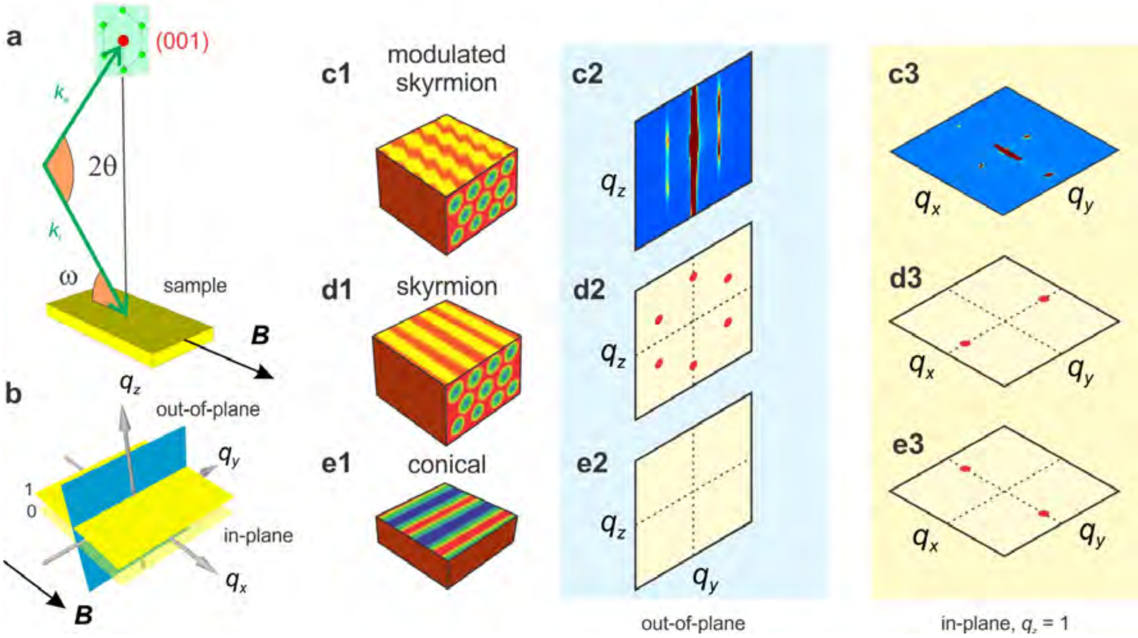

Figure 4.2: The reciprocal space geometry of a REXS experiment carried out on an in-plane conically modulated skyrmion lattice. (a) The Bragg peak scattering vector ($q = k_s - k_i$) is indicated by an arrow normal to the sample's surface. This time, as the skyrmion lattice lies in the sample plane, the six magnetic satellite peaks from the skyrmion lattice have been rotated by 90°. (b) The definition of the axes used to define the following slices through reciprocal space. (c) The conically modulated skyrmion state is shown in (c1), and its experimentally measured diffraction patterns across different slices through reciprocal space are shown in (c2) and (c3). (d) The unmodulated skyrmion state is visualized in (d1), with its theoretical scattering peaks shown in (d2). One would expect to observe peaks as shown in (d3) for many values of q_z in a real in-plane scattering experiment, because the peaks in (d2) would appear as magnetic truncation rods along the q_z direction (as shown by the experimental data in (c2)). (e) The expected diffraction pattern from a conical state visualized in (e1). There would be no peaks in the $q_y q_z$-plane, as shown in (e2), with peaks only in the $q_x q_y$-plane as in (e3).

Experimental data acquired using this technique is slightly more complicated than Fig. 4.2(c3) implies. As the detector's reciprocal surface cuts the Ewald sphere at an angle, the plane in Fig. 4.2(c3) is not quite a $q_x q_y$-plane. The value of q_z is linear in q_x with a small, but non-zero, constant of proportionality. This is why the conical peak at the bottom right of Fig. 4.2(c3) is brighter than its Friedel pair. The bottom right of the image (with smaller q_x) has a q_z closer to $q_z = 0$, where the conical satellite peaks lie, while the top left (with larger q_x) has a q_z further from $q_z = 0$. For the purposes of this technique, the presence of magnetic truncation rods make this a formality that need not be dwelled on – for the duration of this chapter, the reciprocal space surface sampled by the camera will be simply referred to as the $q_x q_y$-plane. This technicality would become important if one carried out the same experiment slightly off resonance, where the truncation rods significantly shrink in the q_z-direction as a result of significantly increased penetration depth.

Images of the $q_x q_y$-plane for the helical, skyrmion, and conical and skyrmion states when a magnetic field is applied parallel to the x-axis, are shown in Fig. 4.3(a), Fig. 4.3(b) and Fig. 4.3(c), respectively. These images are taken at $q_z = 1$, i.e. the diffractometer's $|q|$ has been aligned to the skyrmion peaks. As discussed, this means that helicoidal intensity is always greater towards the bottom of the image, owing to the weak coupling between q_z and q_x.

Using this scattering geometry, Fig. 4.3 shows that one can simultaneously image reflections from the skyrmion lattice state, and from the conical/helical states. This was exploited to map out phase diagrams of intensity in each of the regions of interest shown in Fig. 4.3(c). These phase diagrams were acquired using two hysteresis protocols. The phase diagrams in the top row of Fig. 4.4 were acquired following the field-cooling protocol, while the phase diagrams in the bottom row of Fig. 4.4 were acquired using the zero-field-cooling protocol. With the zero-field-cooling protocol, the skyrmion state is completely separated from any helicoidal state (skyrmions being present only in the region enclosed by the dotted line), and higher order

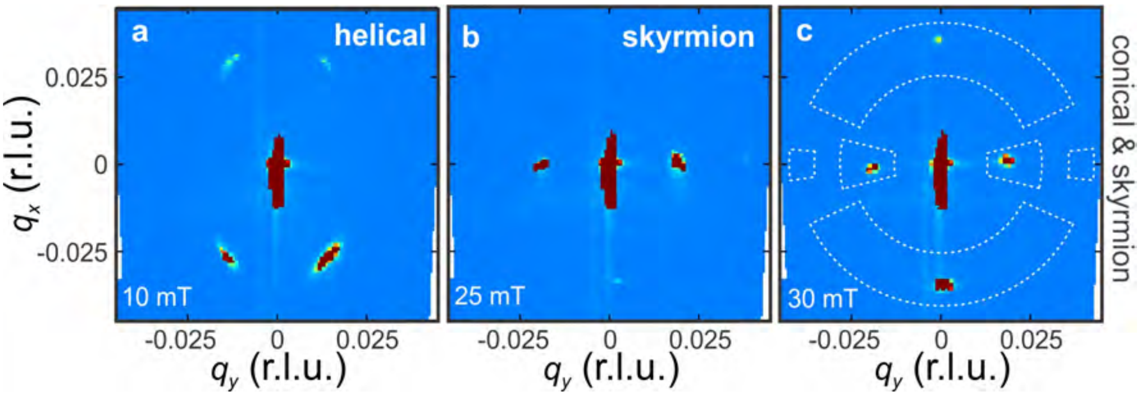

Figure 4.3: Three examples of scattered intensity from different phases in the q_xq_y-plane, with $q_z = 1$. In each panel, the magnetic field is applied along the x-direction. (a) Two helical domains, with their corresponding pairs of peaks, have rotated slightly towards the external field of 10 mT. (b) At 25 mT, the skyrmion phase has formed. First order skyrmion peaks are bright and visible along the q_y-axis. A second order skyrmion peak, and a conical peak along the q_x-axis, are faintly visible. (c) At 30 mT, the skyrmion phase is coexisting with the conical state. The regions of interest used to integrate helicoidal, first order skyrmion and second order skyrmion intensity are indicated.

skyrmion peaks were not observed. When field-cooling, skyrmions nucleate within the pocket indicated by the dotted line, but are metastable at lower temperatures due to their topological stability. In this protocol, the extended skyrmion pocket coexists with the conical/helical states for a large region of phase-space. This can be seen by looking at the parts of the intensity map in Fig. 4.4(c) that lie outside of the dashed line – any skyrmion signal outside of the dashed line was observed at the same time as non-zero intensity from the helical/conical region of interest.

Intriguingly, in areas of phase space where the skyrmion lattice and helical/conical peaks were simultaneously observed, the intensity of the second order skyrmion peaks increased. It has been proven above that, if skyrmions are embedded within the conical state, they must become conically modulated. This increase in intensity of the second order skyrmion peak is experimental verification that there is a structural transition in the skyrmion state when immersed within the helical/conical state. A change in the relative intensities of the skyrmion Fourier modes is possible only if the skyrmion lattice magnetization along the x-direction has been rotated in function space.

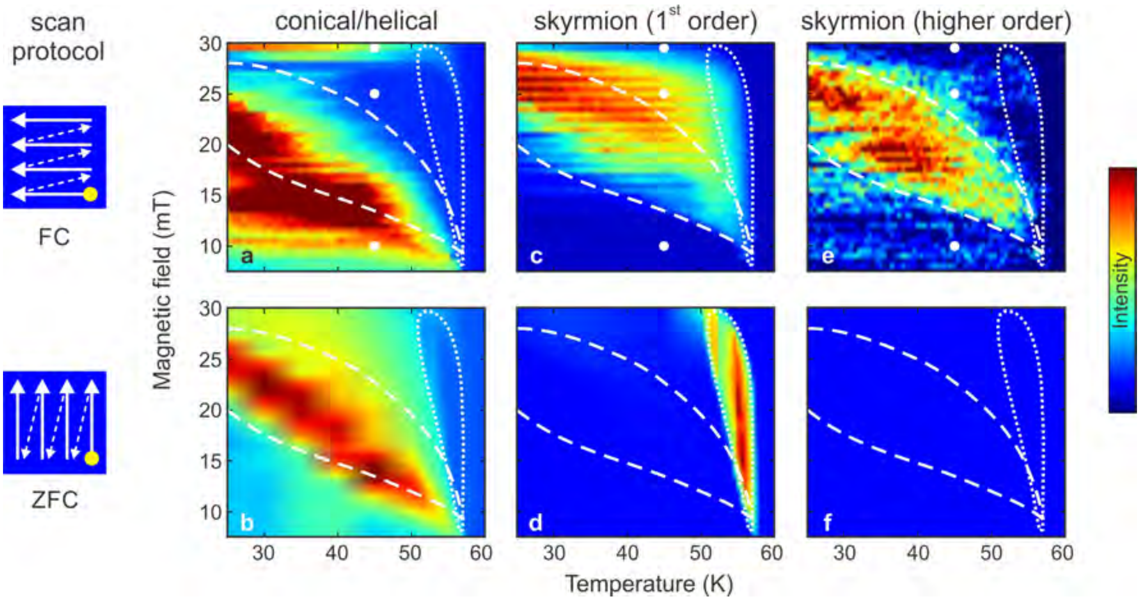

Figure 4.4: In-plane REXS phase diagrams showing the coexistence of magnetic peaks corresponding to the conical/helical state with the skyrmion state's magnetic peaks in a sample of Cu_2OSeO_3 . These peaks were disambiguated by applying an in-plane magnetic field. All panels on the top row were measured at the same time using a field-cooling protocol, while all data on the bottom row was gathered simultaneously using a zero-field-cooling protocol. The three dots in the field-cooling protocol diagrams indicate the location on the phase diagram of the three scattering patterns shown in Fig. 4.3. (a)-(b) Integrated intensity from regions of interest on the area detector that contain signal corresponding only to conical/helical peaks. (c)-(d) As in (a)-(b), but integrating intensity from regions of interest in which one would expect to observe reflections from skyrmion tubes. (e)-(f) As in (c)-(d), but placing the regions of interest at twice the radial distance from the Bragg reflection, so that only second order magnetic diffraction from the skyrmion state is integrated.

As conically modulated skyrmions are periodic along their core, one would expect conically modulated skyrmions to have an extra pair of magnetic satellites when compared to the unmodulated skyrmion lattice. These satellites would exactly overlap with where one would expect to measure conical peaks. The diffraction pattern associated with conically modulated skyrmion is shown in Fig. 4.2(c3), while Fig. 4.2(d3) and Fig. 4.2(e3) show expected scattering from unmodulated skyrmions and cones, respectively. In principle, one cannot distinguish using REXS alone between a lattice of unmodulated skyrmions spatially separated from the cone phase, and a single lattice of conically modulated skyrmions. Combining the analytical argument and micromagnetic results with evidence of a structural transition in the second order skyrmion peak, it is overwhelmingly likely that the regions in which skyrmion peaks coexist with conical peaks host conically modulated skyrmions.

To conclude, it has been shown analytically that if a skyrmion is embedded within the conical state, the skyrmion must become conically modulated. This conically modulated state has been investigated using computation micromagnetics, and a cross-section of the resultant magnetization is shown in Fig. 4.1. Experimentally, it has been found that, when field-cooling, the skyrmion lattice state can coexist with the conical state. As proven, this implies that, in this region of magnetic phase-space, skyrmions must become conically modulated. This is further evidenced by the change in intensity of the second order skyrmion reflection in this coexistence region, which results from the altered in-plane order of the skyrmion lattice. The properties of this state will be studied in the following chapter, where conically modulated skyrmions will be found to have an attractive interparticle interaction, while unmodulated skyrmions have a repulsive interparticle interaction. This attraction will become the key to understanding the skyrmion liquid phase.

4.2 Surface pinning effects

Above, the fluctuations in the internal structure of a skyrmion string have been studied as the string progresses along the axis defined by the external magnetic field, here conventionally chosen to be the z-axis. Consider now the properties of a skyrmion string which is allowed to vary spatially in another dimension as it propagates along the z-axis. Intuitively, one would not expect a skyrmion string to substantially bend or contort. The structure derived in chapter 2 should minimize the micromagnetic energy, and any deformations of this structure should lead to an increase in energy. If skyrmions become conically modulated, as discussed above, one would further anticipate that skyrmions should propagate exclusively along the k-vector of the conical state. Here, a REXS study will show that skyrmions are pinned to the surfaces of materials, preferring to propagate towards surfaces when in their vicinity. This phenomenon will be verified using computational micromagnetics, and understood in terms of a simple analytical toy model for the energy of a skyrmion string that costs more energy than the state in which it is embedded.

To study the response of the skyrmion lattice to an external field that is far from being out-of-plane or in-plane can be challenging in experiments. The well defined fields used to nucleate the skyrmion lattice in the samples of Cu_2OSeO_3 characterized so far were set up by a pair of permanent magnets. These magnets have rotational and translational freedom, which allows for magnetic fields to be freely rotated about the ω-axis at varying strengths. As the (100) Bragg reflection for Cu_2OSeO_3 is at 96° when x-rays are tuned to the Cu L_3-edge, incident light strikes the surface of the sample approximately 42° from the (100) surface normal. This 42° rotation is made about the ω-axis. The magnets and their enclosure have an angular diameter of around 20°-30°, depending on the magnitude of the field applied. Consequently, magnetic fields cannot be applied to Cu_2OSeO_3 using this set up that are rotated by around 30°-60° to the surface normal without blocking the incident/outgoing beam.

It would be possible to circumnavigate this problem by applying external magnetic fields generated by more complicated arrays of permanent magnets. However, the nature of the investigation mandates that the orientation of the external magnetic field be well defined with respect to the surface normal, which is most straightforward to achieve with a pair of well aligned rare earth magnets.

The solution found was to keep the magnets in their out-of-plane geometry, align the diffractometer to the (100) Bragg condition, and diffract from an adjacent (110) face. The angle between a (110) and a (100) face is 45°, so with the external field applied along the (100) direction, the angle between the applied field and the surface normal is 45° and no light is blocked by the magnets. One must exercise caution when using such an approach, as this technique will not always work. For example, the angle between a (100) face and an adjacent (111) face is roughly 55°. To meet the Bragg condition, outgoing light must travel 48° above the [100] planes. But, $55° > 48°$, so it is geometrically impossible to meet the (100) Bragg condition on a (111) face in some crystal orientations. As the 45° rotation between the (100) and (110) faces is smaller than the scattering ω of 48°, it is always possible for light satisfying the (100) Bragg condition to escape from a (110) face.

REXS from a face that is not parallel to the scattering q-vector has one significant additional complication: magnetic truncation rods are rotated by the angle between the q-vector and the surface normal. In the case of scattering from the (110) face with a q-vector parallel to the (100), this means that the truncation rods are rotated by 45°. As a result, even a skyrmion lattice normal to the (100) will show a highly distorted magnetic scattering pattern if truncation rods are long and propagated along the (110) direction. A graphic reciprocal space geometry of scattering from a skyrmion lattice pinned to a face that is not normal to the scattering vector is shown in Fig. 4.5(a). A close-up of the detector's reciprocal surface is shown in Fig. 4.5(b). As the skyrmion lattice in Fig. 4.5(a) is pinned to a plane that is not normal to the (100), its magnetic satellites now intersect the Ewald sphere at an angle. In Fig. 4.5(c), the reciprocal space geometry of a skyrmion lattice that is not pinned to the surface is shown. This subfigure shows the reciprocal space geometry one would expect if skyrmion tubes propagated along the direction of the applied field near the surface. The key difference in reciprocal space between the case when skyrmions are pinned to the surface (as in Fig. 4.5(b)) and when skyrmions are pinned to the magnetic field (as in Fig. 4.5(c)) is that, when skyrmions are pinned to the magnetic field, their magnetic satellites remain on the plane tangent to the Ewald sphere. If they are pinned to the surface, the plane in which the magnetic satellites lie is rotated by the angle between the scattering vector and the surface normal.

The scattering patterns one would expect to observe from skyrmions pinned to the surface is given by the intersection between the truncation rods in Fig. 4.5(b) and the detector's reciprocal surface; these intersections are shown in Fig. 4.5(d). The REXS pattern one would expect to observe from skyrmions that are ordered in the plane perpendicular to the scattering vector, but that are near a surface whose normal is not parallel to the scattering vector, is given by the intersection between the truncation rods in Fig. 4.5(c) and the detector's reciprocal surface and is shown in Fig. 4.5(e). Unfortunately, the expected patterns in Fig. 4.5(d) and Fig. 4.5(e) are very nearly identical[1].

The REXS pattern shown in Fig. 4.5(f) was obtained as described above, from a (110) face of Cu_2OSeO_3 about the (100) Bragg peak while the external field was applied parallel to the (100) direction. This pattern was acquired exactly on resonance, so the magnetic truncation rod effects were strong enough that all six skyrmion peaks could be observed simultaneously. However, in this regime where magnetic truncation rods are very long, the patterns from surface-pinned and not-surface-pinned skyrmions are almost indistinguishable. To differentiate between the surface-pinned and the not-surface-pinned scattering patterns, the synchrotron monochromator was

---

[1] Fig. 4.5(d) is ever so slightly more eccentric, and the major/minor axes of the ellipses in Fig. 4.5(d) and Fig. 4.5(e) are not quite collinear.

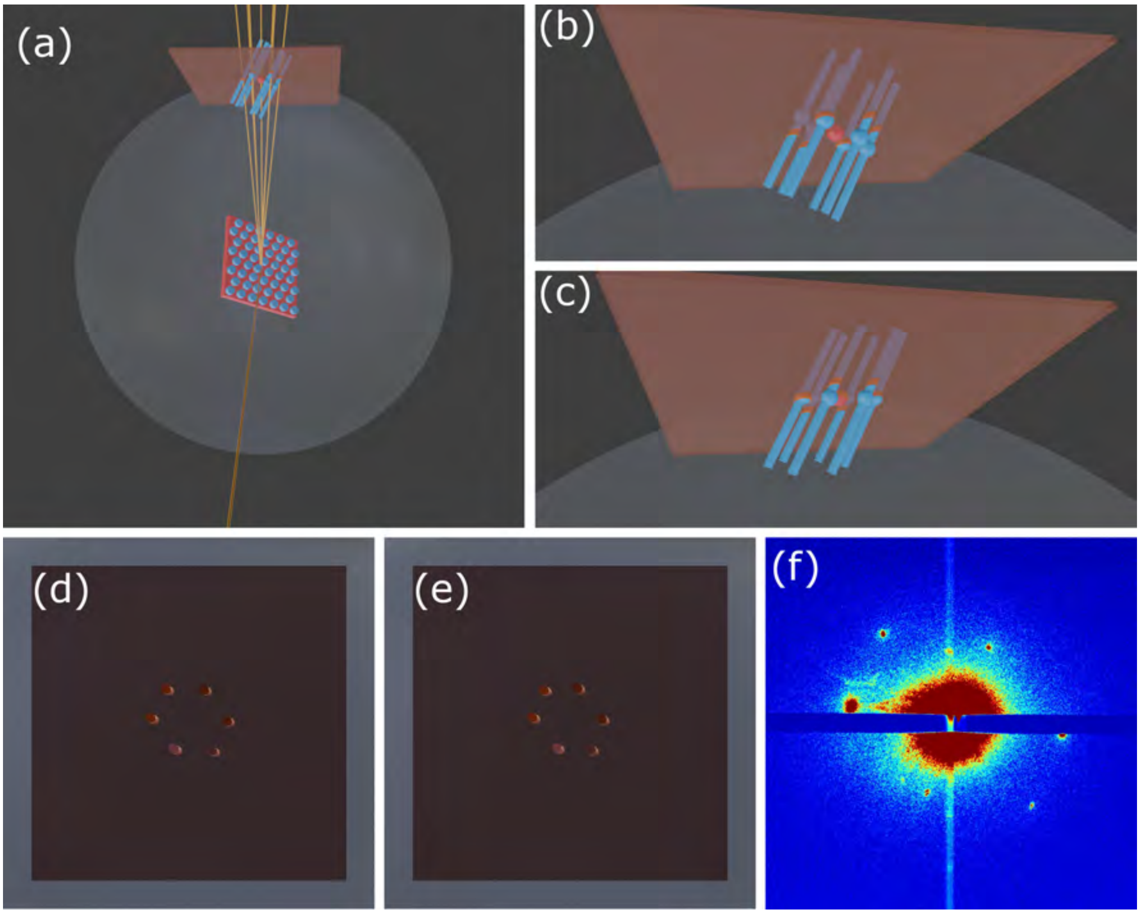

Figure 4.5: (a) Geometry of the surface pinned skyrmion scattering. The sample surface normal is not parallel to the scattering vector, or even in the scattering plane. The skyrmion lattice is taken to be pinned to the surface normal. (b) Close-up of the intersection between the detector's reciprocal surface and the truncation rods from the surface pinned skyrmion state shown in (a). (c) Close-up of the intersection between the detector's reciprocal surface and the truncation rods from a skyrmion lattice in the plane perpendicular to the scattering vector (i.e. a skyrmion lattice aligned along the external field direction). (d) The intersections in (b), showing the expected diffraction pattern from the surface pinned skyrmion state. (e) The intersections in (c), showing the expected diffraction pattern from a skyrmion lattice not pinned to the surface, that instead follows the magnetic field. Clearly, when truncation rods are present, one cannot distinguish between surface-pinned and not-surface-pinned skyrmions; this expected diffraction pattern is too similar to the one shown in (d). (f) A REXS pattern obtained from the (110) face of a crystal of Cu_2OSeO_3 where the field and scattering vectors are both aligned along the (100) direction.

detuned to 925 eV, more than 5 eV below the resonance condition. At this energy, magnetic scattering intensity was slashed, but the heightened penetration depth of x-rays abolished all magnetic truncation rod effects, and diffractometer $|q|$ scans were required to image the magnetic satellites. In this regime, the REXS patterns due to surface-pinned and not-surface-pinned skyrmions can be readily disambiguated, as the REXS pattern from the not-surface-pinned skyrmions in the untruncated limit will lie in the ellipses of intensity shown in Fig. 3.5, where diffraction patterns were also taken slightly off resonance. On the other hand, if skyrmions are pinned to the surface, the ellipse in which skyrmion satellites will lie will continue to be distorted as in Fig. 4.5, as in this case the skyrmion satellites live in the plane normal to the truncation rod axes.

Experimental data captured 5 eV below the Cu L_3-edge is shown in Fig. 4.6. Off resonance, the truncation rods were found to shrink significantly, in accordance with expectation. On resonance, a single snapshot with the diffractometer's $|q|$ aligned to the (100) Bragg condition was all that was required to capture the image in Fig. 4.5(f), as each truncation rod intersected the detector's reciprocal surface. Off resonance, single snapshots gave images such as Fig. 4.6(a) and Fig. 4.6(b), which are much more localized in reciprocal space. The aligned summation of intensity from the $|q|$ scan series from which Fig. 4.6(a) and Fig. 4.6(b) were taken is shown in Fig. 4.6(c). The vertical streaks of intensity were a trivial consequence of alignment necessary after performing the $|q|$ scan, needed when the surface from which x-rays are scattering is not quite the centre of rotation at the diffractometer, and should be ignored. Imperatively, the major axis of the ellipse on which the magnetic signal lies is not parallel to the detector vertical, which is possible only if skyrmion are pinned to the surface of their confining material – if the skyrmion tubes were parallel to the applied field at the surface, then the scattering patterns in Fig. 3.5 would have been retrieved once effects due to truncation rods were eliminated.

The surface pinning of skyrmions was then investigated using computational

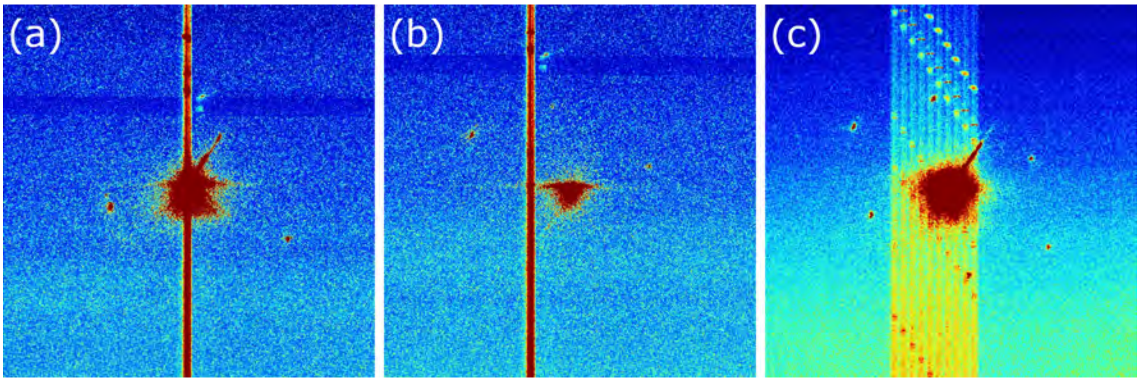

Figure 4.6: Images of the surface-pinned skyrmion state 5 eV below the Cu L_3-edge; (a) and (b) show different images captured on an area detector at different diffractometer $|q|$ values. Off the resonance energy, the penetration depth of x-rays has significantly increased, making features in reciprocal space more point-like and requiring that $|q|$ be scanned to image all six magnetic satellites. Off resonance, magnetic and structural intensities drop drastically (as the (100) reflection is a disallowed peak in Cu_2OSeO_3 visible only on resonance). Consequently, a detector artefact that is normally hidden below background is visible – a line of weakly activated pixels marking the centre of the detector. (c) The summation of the 10 images taken at different $|q|$ values from which (a) and (b) were taken. The line of damaged pixels seen in (a) and (b) is blurred across this subfigure, but it an artefact of the image alignment process and should be ignored.

micromagnetics. To emulate the geometry of the experiment on the nanoscale, a wedge was cut from a cuboid with dimensions 420 nm ×140 nm ×480 nm and finite difference cells of volume 2.5 nm ×2.5 nm ×2 nm. Setting the exchange and anti-symmetric exchange interactions, as well as the saturation magnetization, to be the values of a crystal of FeGe[1], the external field was set to 286 mT. The $(\bar{1}01)$ surface was sliced through the cuboid such that it cut both the (001) and the $(\bar{1}00)$ faces in half. The system was initialized with nine azimuthally symmetric skyrmion strings, equally spaced in the xy-plane, propagating along the (001) direction. Relaxing the system gave the magnetization shown in Fig. 4.7, which shows that the minimum energy configuration for skyrmions incident on a tilted surface is reached when the skyrmions cant towards the surface.

---

[1] All micromagnetic calculations in this work make use of the Fidimag package, using the parameters for FeGe even when the corresponding experiments are carried out on different materials. Changing the ratio of J/D only affects characteristic length-scales, and the magnitude of $\mathbf{B}$ required to induce phase transitions, in computational micromagnetics. By standardizing simulation parameters, one can avoid repeating computationally expensive energy density calculations per parameter set.

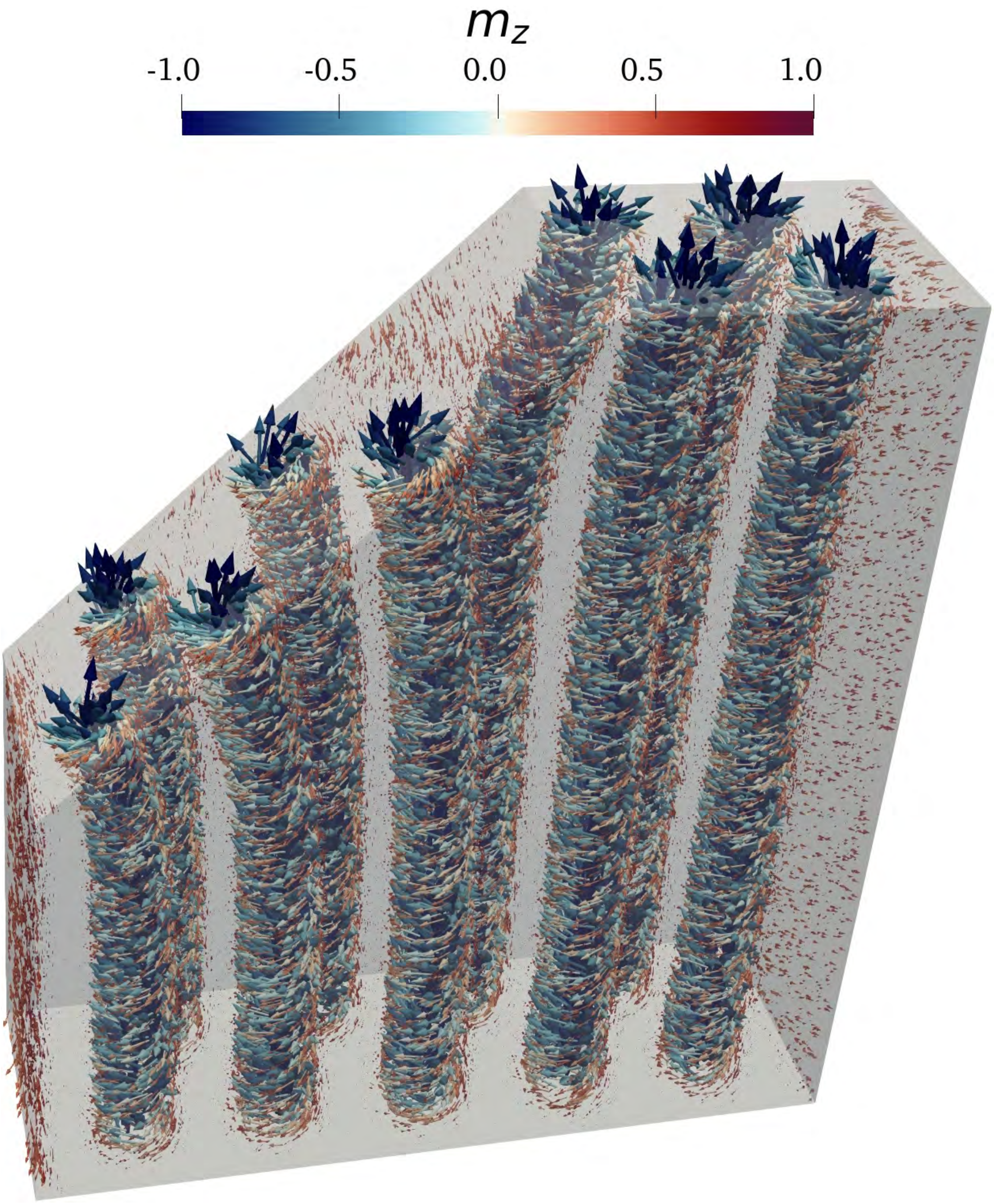

Figure 4.7: A micromagnetic simulation of skyrmion tubes near a tilted surface. Approximately one in four finite difference cells were randomly selected to be rendered, with the cell's magnetization represented by an arrow whose length is scaled by the magnetization's z-component (with $m_z = 1$ having length 0, and $m_z = -1$ having maximal length). Scaling in this fashion allows skyrmion tubes to be visualized that would otherwise be lost in the bulk.

The skyrmions found in the relaxation that yielded the state in Fig. 4.7 are all azimuthally symmetric, immersed in the field-polarized state. One could attribute this tilting of the skyrmion strings to an energetic preference of the system for the field polarized state over the skyrmion tubes. As skyrmions are topologically protected, to deform a skyrmion tube into the field-polarized state would cost a significant amount of energy. Since Fig. 4.7, along with all other micromagnetic calculations carried out in this work, was carried out at a temperature of 0 K, it would be impossible for the system to source the energy required overcome the energy barrier to annihilate a skyrmion. This would frustrate the magnetic system – the energy would decrease if skyrmion tubes disappeared, but destroying them comes with a prohibitive energy cost. A natural compromise would be that the skyrmion tubes would make themselves as short as possible, by bending towards the nearest surface.

There are two problems with such a model. Firstly, labelling skyrmions in Fig. 4.7 from left to right, the sixth skyrmion has distorted itself in such a way as to increase its length, moving towards the fifth skyrmion in the bulk, then clustering next to the seventh skyrmion at the surface. Secondly, the value of the external magnetic field used during this calculation, 286 mT, may appear oddly specific. This value was not chosen accidentally, and will be derived numerically in the following chapter. In short, using the material parameters for FeGe in a micromagnetic calculation, an unmodulated skyrmion has exactly the same energy as the field-polarized state. At this field value, there is absolutely no preference for the system to be in either the field-polarized state or the skyrmion state, and yet the surface pinning effects persist.

As can be seen by the path traversed by the sixth skyrmion in Fig. 4.7, this pinning occurs only at the surface, with skyrmions behaving unusually even in the bulk. This behaviour is related to the content of the following chapter, the interactions between skyrmions and their environment. There are three magnetization configurations coexisting in Fig. 4.7: skyrmions, the field polarized state, and surface twist instabilities. As axis-symmetric skyrmions have repulsive interparticle interactions, in the bulk where the energetics of the surface twist state can be neglected, the skyrmion strings will be repulsive. At the surface, as again will be found numerically in the following chapter, skyrmions have a much higher energy density than the surface twist state. The result is that skyrmions cluster tightly at the surface, balancing the increase in energy due to their interactions with the decrease in energy due to a higher surface area covered by the surface twist state. It is precisely this phenomenon, of skyrmion tubes being forced to cluster on the surface of materials, that was observed in experiment. So, the pinning of the skyrmion lattice to their nearest surface should not be thought of as being the result of skyrmions literally being pinned, instead this is a consequence of skyrmions clustering on the surfaces of their confining materials (where the most efficient method of clustering is, as usual, to form a hcp lattice) to maximize the surface area of the energetically preferable surface twist state.

To conclude, the first experimental measurement of surface pinned skyrmions has been made by REXS. This state has been shown to be stable in micromagnetic simulations, and has been understood in terms of the energy preference of the system for surface twists over skyrmions at the surface of materials.

Chapter 5

Interactions in micromagnetism

The previous chapter ended with a presentation of a magnetic state, the surface pinned skyrmion state, whose structure was dependent on the interactions between skyrmions and their environment. For understanding the magnetic structure of physical systems, this is an important topic. Further, for the simulation of devices in which skyrmions act as a logic unit, integration of the Landau-Lifshitz-Gilbert equation quickly becomes a prohibitively computationally expensive method of study. In this chapter, a more efficient equation of motion for the centre of mass of a skyrmion will be presented, following the approach developed by Thiele to describe the motion of magnetic bubble domains [118]. A major downside of this approach is that it requires that one understands the interactions between a localized, robust magnetic texture, and that texture's surroundings. To mitigate this problem, a general technique for the calculation of repulsive interaction potentials will be derived and benchmarked. This testing procedure will involve understanding of the energetic balance between micromagnetic states, which will solidify the assumptions made in the discussion of the surface pinned skyrmion state in the previous chapter.

While axis-symmetric skyrmions will be have been known for some time to have a repulsive interparticle interaction, the interaction between conically modulated skyrmions is less well documented. These will be found numerically to have an attractive interaction, forming a bound state whose structure is determined by the geometry of their host material. This interaction will be combined with the phase diagrams shown in Fig. 4.4 to explain the physical mechanism behind the formation of the skyrmion liquid state.

5.1 Thiele's equation

So far, the time evolution of a region of magnetization has been studied solely using by Eq. (1.10), the Landau-Lifshitz-Gilbert equation. Consider a region of magnetization whose internal structure is unchanging, moving at a constant velocity $\mathbf{v}$, $\mathbf{m}(\mathbf{x}, t) = \mathbf{m}(\mathbf{x} - \mathbf{v}t)$. This allows the time derivative of the magnetization to be written as $\dot{\mathbf{m}} = \mathbf{v} \cdot \nabla \mathbf{m}$, so that the Landau-Lifshitz-Gilbert equation becomes

$$\mathbf{v} \cdot \nabla \mathbf{m} = -\gamma \mathbf{m} \times \mathbf{H}_{\text{eff}} + \alpha \mathbf{m} \times (\mathbf{v} \cdot \nabla \mathbf{m}) \,. \tag{5.1}$$

The Thiele equation can be obtained by integrating over Eq. (5.1) after premultiplying both sides of with $\mathbf{m}\times$, using $\mathbf{m} \cdot \dot{\mathbf{m}} = 0$ to simplify a resulting vector triple product, and multiplying the result with $\partial_i \mathbf{m}$. An excellent, step-by-step derivation can be found in Ref. [119], but alternative derivations can be found in Refs. [57, 118, 120–124]. As this derivation is lengthy, it will be omitted here in favour of a discussion of the final result, which can be written as

$$\mathbf{G} \times \mathbf{v} - \alpha \mathbf{v} = -\nabla U \,, \tag{5.2}$$

where U is the potential energy landscape of the magnetization configuration[1]. The vector $\mathbf{G} = \pm 2\pi N \hat{z}$ is the gyrocoupling vector, whose sign and direction is set by the orientation of the external magnetic field when dealing with skyrmions [24]. The

---

[1] This is not the same as the micromagnetic energy functional E, which is the total magnetostatic contribution to the Helmholtz free energy. This is the fraction of E that can be considered to result from the interactions between one particular localized magnetization configuration and its environment.

appearance of the topological winding number N in this equation of motion is an incredible coincidence of nature, implying that topological magnetization configurations acquire a component of their velocity that is not parallel to the direction of an applied force $\mathbf{F} = -\nabla U$. The $\alpha\mathbf{v}$ term is the dissipative term, with the damping tensor α dictating the energy dissipation experienced by the region of magnetization being described. In many publications, the damping tensor is written as $\alpha = \alpha_G \mathcal{D}$, where α_G is the Gibbs damping coefficient and $\mathcal{D}$ is a dissipative tensor with components [42, 62, 125–133]

$$\mathcal{D}_{ij} = \frac{1}{4\pi} \iint_S \partial_i \mathbf{m} \cdot \partial_j \mathbf{m} \, dx \, dy \, , \tag{5.3}$$

where the integral is to be taken over the smallest region S within which the localized magnetization configuration is fully defined (for a skyrmion, this could be set to the surface S_{Sk} within which the winding number integral over the magnetization of a skyrmion $\mathbf{m}_{\mathrm{Sk}}$ returns 1). This picture of damping assumes that Gilbert damping is the primary source of dissipation for a moving skyrmion. In metallic materials, this is not a justifiable assumption, as dissipation due to a moving skyrmion coupling to the electron gas has been shown to be the primary source of a skyrmion's energy loss [134]. In general, the damping tensor should be written as $\alpha = \alpha_G \mathcal{D} + \alpha' \eta'$, where α' is linear in sample conductivity and the shape factor η' can be expressed as [134]

$$\eta' = \frac{1}{4\pi} \iint_S \left(\mathbf{m} \cdot (\partial_x \mathbf{m} \times \partial_y \mathbf{m}) \right)^2 dx \, dy \, . \tag{5.4}$$

The origin of η', as well as the functional form of α' are related to the spin-transfer torque effect and will be discussed in more detail in the following chapter. Physically, this term is a result of the emergent electric field of a moving skyrmion driving a dissipative current, and is finite in any skyrmion-hosting sample whose conductivity $\sigma \neq 0$.

Thiele's equation, the equation of motion given in Eq. (5.2), provides an incredibly simplified description of the behaviour of a skyrmion when compared to integration of the Landau-Lifshitz-Gilbert equation. Considering the motion of skyrmions in two dimensions down a 1 μm long wire with width 200 nm, a finite differences integration of the Landau-Lifshitz-Gilbert equation that uses finite difference cells with dimensions 2 nm $\times$2 nm $\times$2 nm would be discretized over 50,000 cells. So, to study the motion of a single skyrmion through an idealized two-dimensional wire, one would need to integrate 50000 coupled first order differential equations per timestep. Using Thiele's approach, only one differential equation needs to be integrated to provide the same information – the position of the centre of a skyrmion as a function of time. Thiele's equation becomes even more advantageous when one would need to consider three-dimensional finite differences grids to integrate the Landau-Lifshitz-Gilbert equation for a geometry of interest – for example, more than two million finite differences cells were needed to produce Fig. 4.7, which contains information on just nine skyrmions[1].

The main downside of Thiele's equation for describing the dynamics of skyrmions appears to be a serious one: for each new magnetic environment or applied force, one must determine ∇U, the gradient of the potential energy environment in the vicinity of the skyrmion. For example, when two skyrmions move near to each other, one would expect that they exert some sort of a force on each other. To study a system of multiple skyrmions using computational micromagnetics, one simply needs to initialize two skyrmions near to each other, and keep integrating the Landau-Lifshitz-Gilbert equation until the average angular velocity of the magnetic moments decreases below a cutoff value. The simulation will have automatically calculated the interaction between the two skyrmions by considering the interactions between all neighbouring magnetic moments in the system, making computational micromagnetics software easy to use. To simulate the motion of these two skyrmions using Thiele's equation, one must know the functional form of the skyrmion-skyrmion interaction *a priori* and add the gradient of the skyrmion-skyrmion interaction potential to the RHS of Eq. (5.2). This makes Thiele's approach generally more laborious,

---

[1] Although, Fig. 4.7 was used to study the detailed three-dimensional structure of skyrmions, which would not have been possible using Thiele's approach, as it treats skyrmions as point particles.

as studying any new magnetic landscape requires a physical investigation.

On the flip side, the fact that the skyrmion-skyrmion interaction is being recalculated from scratch in computational micromagnetics is precisely the reason why Thiele's approach promises such an increase in efficiency. Studying the behaviour of just three nearby skyrmions using computational micromagnetics introduces redundancy into the calculation. The mutual repulsion of each of the three pairs of skyrmions will be fundamentally the same, but will be recalculated from the ground up for each pair. The reason why large systems of skyrmions cannot be studied using computational micromagnetics is that, for each nearest neighbour pair, the simulation will need to constantly recalculate the skyrmion-skyrmion interaction. Thiele's approach is equivalent to noticing this redundancy in micromagnetism and choosing to properly understand the relevant interactions and forces in a system before running a simulation, so its prerequisite that one has an *a priori* understanding the potential energy landscape of a magnetization configuration is both its strength and its limiting factor.

5.2 Calculating micromagnetic interaction potentials

As the integrating the Thiele equation promises such significant speedups over computational micromagnetics, the topic of understanding the interactions between skyrmions has received some interest in the literature in recent years. In 2013, Lin et al. first conjectured that the skyrmion-skyrmion interaction potential could be exponentially decaying with interparticle separation, using their intuition from previously conducted research on the dynamics of magnetic flux vortices in type-II superconductors [57]. After fitting the exponential to simple micromagnetic simulations, they continued their work with Thiele's equation with the understanding that their interaction model was reasonable, without looking into their interaction model in too much detail. This exponentially decaying interparticle interaction soon became accepted, and in 2019, Foster et al. provided the first complete derivation of the skyrmion-skyrmion interaction potential, showing that it should indeed decay exponentially quickly asymptotically [29]. In the time since that work, some more advanced discussions of skyrmion-skyrmion interactions have been published, reaffirming the same asymptotic result [135, 136].

While these papers are accurate, the techniques they present are tailored to the calculation of the skyrmion-skyrmion interaction. No general form of an interaction potential between two magnetization configurations is given, and all calculations are dependent on the form of the micromagnetic energy functional. The issue caused by this lack of generality shows in attempts to calculate the interaction between skyrmions and surface twists in the literature. The first attempt to derive an analytical form of the interaction potential between a skyrmion and a surface twist was in the article that first discussed them, where Meynell et al. expected that the interaction potential should be exponentially decaying, but the argument of the exponential they derive leads to a poor fit to micromagnetics [45]. In the article proposing that skyrmions can be used as a key component in stochastic computers by Pinna et al., the authors derive an accurate interaction potential by over-constraining the potential and fitting a product of six exponentials to micromagnetic data [109]. The argument of each exponential was treated as an independent fitting parameter. While overconstrained models will always provide an accurate interaction potential, sidestepping the physics of the problem leads to unwieldy algebraic results.

In the following derivation of a general form of the interaction potential between two arbitrary localized micromagnetic textures, the only assumptions applied will be the same assumptions as one makes when deriving Thiele's equation. Firstly, the textures will be assumed to be robust, so that their internal structure does not change during the interaction process. This assumption is equivalent to requiring that the textures in question, let them be called $\mathbf{m}_A(\mathbf{x})$ and $\mathbf{m}_B(\mathbf{x}-\mathbf{R})$, are each local minima of the micromagnetic energy functional. Thiele's equation treats the magnetization configurations whose equation of motion it describes as point particles. As a result, there is an implicit assumption in Thiele's equation that any texture whose motion it describes must be in some sense localized. For convenience, the textures will be constructed such that they are each localized about the origin (so that $\mathbf{m}_A(\mathbf{x})$ lies a distance $\mathbf{R}$ from $\mathbf{m}_B(\mathbf{x}-\mathbf{R})$). If these configurations are localized, then using the notation introduced in chapter 2 and chapter 4, it must be possible to write

$$\lim_{x_j \to \infty} \mathbf{m}_i(\mathbf{x}) = \mathbf{m}_\infty(\mathbf{x}) \,, \tag{5.5}$$

where x_j is one or more of the coordinates in $\mathbf{x}$, and $i \in \{A, B\}$.

It will first be proven that if these magnetization configurations locally minimize the energy functional, and if these magnetization configurations are analytic, then their interparticle interaction must be repulsive. The condition for these textures to minimize the energy functional can be written

$$\lim_{\Delta \to 0} E[\mathbf{m}_i(\mathbf{x}) + \Delta \mathbf{f}(\mathbf{x})] > E[\mathbf{m}_i(\mathbf{x})] \,, \tag{5.6}$$

where $\mathbf{f}$ is an arbitrary vector valued function on the coordinates $\mathbf{x}$ and, again, $i \in \{A, B\}$. If the separation $\mathbf{R}$ between $\mathbf{m}_A$ and $\mathbf{m}_B$ becomes small, then the tail of $\mathbf{m}_A$ will overlap with the tail of $\mathbf{m}_B$, and vice versa. The idea of an overlap region can be formalized by using the fact that Eq. (5.5) also implies that

$$\lim_{x_j \to \infty} \partial_k \mathbf{m}_i(\mathbf{x}) = \partial_k \mathbf{m}_\infty(\mathbf{x}) \,, \tag{5.7}$$

where derivatives are taken with respect to the kth component of $\mathbf{x}$, the x_j are the one or more components of $\mathbf{x}$ for which Eq. (5.5) hold, and $i \in \{A, B\}$. This gives the sensible definition of an overlap region as being the set of coordinates $\{\mathbf{x}_O\}$ that satisfy both $\partial_k \mathbf{m}_A(\mathbf{x}_O) \neq \partial_k \mathbf{m}_\infty(\mathbf{x})$ and $\partial_k \mathbf{m}_B(\mathbf{x}_O - \mathbf{R}) \neq \partial_k \mathbf{m}_\infty(\mathbf{x})$. As a consequence of this overlap, the textures $\mathbf{m}_i$ could change. According to Eq. (5.6), this would necessitate an increase in energy, and an increase in energy as a result of close proximity would give rise to a repulsive interaction. The alternative is that the $\mathbf{m}_i$ do not change, in which case the energy of the system does not change when the textures overlap and they do not interact. Intuitively, one would expect that jamming two magnetization textures next to each other would likely affect at least the structure of the tails of the respective configurations, which would necessarily give rise to a repulsive interaction, but it is worth bounding this analytically before proceeding.

Writing the possibly changed textures as $\mathbf{m}'_i$, throughout this overlap region $\mathbf{x}_O$ the following identity must hold

$$\mathbf{m}'_A(\mathbf{x} \in \mathbf{x}_O) = \mathbf{m}'_B(\mathbf{x} \in \mathbf{x}_O - \mathbf{R})\,. \tag{5.8}$$

The condition for the vectors to remain unchanged can be written as $\mathbf{m}'_i - \mathbf{m}_i = 0$, to which applying Eq. (5.8) gives the following conditions for the interaction between the $\mathbf{m}_i$ to not be repulsive

$$\mathbf{m}'_B(\mathbf{x} \in \mathbf{x}_O - \mathbf{R}) = \mathbf{m}_A(\mathbf{x} \in \mathbf{x}_O)\,, \tag{5.9}$$

$$\mathbf{m}_B(\mathbf{x} \in \mathbf{x}_O - \mathbf{R}) = \mathbf{m}'_A(\mathbf{x} \in \mathbf{x}_O)\,. \tag{5.10}$$

As the separation $\mathbf{R}$ can take any value, the above equalities can hold only if $\partial_k \mathbf{m}_i(\mathbf{x} \in \mathbf{x}_O) = 0$. This can hold throughout the finite region of points $\mathbf{x} \in \mathbf{x}_O$ only if all derivatives of the $\mathbf{m}_i$ vanish for all $\mathbf{x} \in \mathbf{x}_O$, implying that the $\mathbf{m}_i$ are locally flat, non-analytic functions. So, if the $\mathbf{m}_i$ are analytic (namely, if there are no extended localized uniformly magnetized regions contained within the bounds of the $\mathbf{m}_i$), then the $\mathbf{m}_i$ have a repulsive interparticle interaction.

This proof is strengthened in the special, but common, case that $\partial_k \mathbf{m}_\infty = 0$. This occurs when the $\mathbf{m}_i$ are localized within the field-polarized state. In this situation, the overlap region is defined by the region in which both $\partial_k \mathbf{m}_A(\mathbf{x}_O) \neq 0$ and

$\partial_k \mathbf{m}_B(\mathbf{x}_O - \mathbf{R}) \neq 0$, in which case neither Eq. (5.9) nor Eq. (5.10) can be satisfied for any $\mathbf{m}_i$. Therefore, any magnetization states $\mathbf{m}_i$ that minimize the micromagnetic energy functional and that are contained within a uniformly magnetized state must have a repulsive interparticle interaction. If the magnetization states minimize the micromagnetic energy functional but are localized within another state, then they have a repulsive interaction if they are analytic.

It is worth emphasizing that any smooth non-analytic functions that satisfy both Eq. (5.9) and Eq. (5.10) are highly pedantic, such as patches of uniform magnetization contained within a conical state of infinitesimal pitch. Two such equivalent patches of uniform magnetization would not interact when they overlap, but are little more than miscellaneous theoretical constructions. In reality, one should expect all magnetization configurations that minimize the micromagnetic energy functional to have a repulsive interparticle interaction.

Going forward, it will be assumed that all interactions that must be accounted for between configurations that are well described by Thiele's equation will take the form of repulsive interactions that arise in this manner – resulting from the finite overlap between two encroaching configurations pushing each other off minimal energy configurations. Instead of considering explicitly the change in the micromagnetic energy functional as a result of this overlap, the focus will be on properly parameterizing the degree of overlap between adjacent magnetization configurations. To do so, it is useful to define reduced configurations $\boldsymbol{\mu}_i$ from the $\mathbf{m}_i$ such that the magnitude of the $\boldsymbol{\mu}_i$ vanishes when the $\mathbf{m}_i$ are well described as $\mathbf{m}_\infty$. This can be accomplished using the following expression

$$\boldsymbol{\mu}_i = \mathbf{m}_i - \mathbf{m}_\infty \, . \tag{5.11}$$

Then, a measure of the overlap between $\mathbf{m}_A$ and $\mathbf{m}_B$ can be constructed as follows. Firstly, the degree of overlap at coordinate $\mathbf{x}$ when the $\mathbf{m}_i$ are separated by displacement $\mathbf{R}$ should be linear in the product of magnitudes $|\boldsymbol{\mu}_A(\mathbf{x})||\boldsymbol{\mu}_B(\mathbf{x} - \mathbf{R})|$. This ensures that the degree of overlap is small at coordinates $\mathbf{x}$ where either of the $\mathbf{m}_i$ are well described by their enclosing state, and large at a coordinate where $\mathbf{m}_A(\mathbf{x})$ and $\mathbf{m}_B(\mathbf{x}-\mathbf{R})$ both deviate from their enclosing state despite their separation. Secondly, the degree of overlap should depend on the angle between the orientations of $\mathbf{m}_A(\mathbf{x})$ and $\mathbf{m}_B(\mathbf{x}-\mathbf{R})$ that would respectively minimize the energy functional. If $\cos^{-1}(\mathbf{m}_A(\mathbf{x})\cdot\mathbf{m}_B(\mathbf{x}-\mathbf{R}))=0$, then their overlap at $\mathbf{x}$ must not cost energy, since both $\mathbf{m}_A$ and $\mathbf{m}_B$ wanted to have their moments pointing along the same direction at that point anyway. Similarly, arrangements for which $\cos^{-1}(\mathbf{m}_A(\mathbf{x})\cdot\mathbf{m}_B(\mathbf{x}-\mathbf{R}))=\pi$ and the angle between of the $\mathbf{m}_i$ and $\mathbf{m}_\infty$ is $\pi/2$ must cost the maximum possible energy. In this case, the angle between the $\mathbf{m}_i$ couldn't be greater, the plane in which they lie is normal to the state in which both textures are localized, and the angle between two $\boldsymbol{\mu}_i$ is $\pi/2$. To capture this behaviour, defining θ_{AB} as the angle between $\boldsymbol{\mu}_A$ and $\boldsymbol{\mu}_B$, a good measure for the degree of overlap between $\mathbf{m}_A$ and $\mathbf{B}$ would look like $|\boldsymbol{\mu}_A(\mathbf{x})||\boldsymbol{\mu}_B(\mathbf{x}-\mathbf{R})|\sin\theta_{AB}$. This gives an estimate of the total overlap ψ between $\mathbf{m}_A$ and $\mathbf{m}_B$

$$\psi(\mathbf{R}) = \iiint_V \Big|\boldsymbol{\mu}_1(\mathbf{x}) \times \boldsymbol{\mu}_2(\mathbf{x}-\mathbf{R})\Big| d^3x\,. \tag{5.12}$$

If the $\mathbf{m}_i$ are well separated $\psi(\mathbf{R})$ approaches zero – $\psi(\mathbf{R})$ only becomes large when the $\mathbf{m}_i$ are significantly overlapping. This makes ψ an ideal parameter with which one can describe increases in the micromagnetic energy due to interactions between neighbouring magnetic textures. Ignoring the zeroth order term, which equals the equilibrium energy of the system, the Taylor expansion for the micromagnetic energy as a function of texture separation reads

$$U(\mathbf{R}) = K\psi(\mathbf{R}) + \mathcal{O}\left(\psi^2\right)\,, \tag{5.13}$$

where K is a constant of proportionality. Where relevant, this constant can be fit to micromagnetic simulations following the procedure detailed later in this chapter. While ψ is small, Eq. (5.13) will remain an accurate gauge of the interaction potential between $\mathbf{m}_A$ and $\mathbf{m}_B$. As $\mathbf{R}$ decreases and the overlap between the adjacent textures becomes large, one will generally need higher order terms to accurately describe $U(\mathbf{R})$. But, this is precisely the limit in which Thiele's equation breaks down – no higher order terms need be considered when using these potentials with Thiele's equation. This is because $\psi(\mathbf{R})$ simultaneously estimates the strength of interparticle interactions, and the validity of Thiele's equation, by measuring magnetization overlap.

Before moving on to use Eq. (5.13) to calculate interaction potentials for skyrmions, it is important to understand when this theory will break down in practice. It is true that all well behaved local minima of Eq. (2.1) should interact in a repulsive manner, but saddle point solutions to the Euler-Lagrange equations of Eq. (2.1) could be observed in experiment. Even more serious is the fact that experiments are infrequently carried out at zero temperature – a local minimum of Eq. (2.1) that is separated from a saddle point solution by less than $k_{\mathrm{B}}T$ should consider its days numbered. The conically modulated skyrmion state discussed in the preceding chapter are saddle point solutions, as will be shown by their attractive interactions. For users of Thiele's equation, this is not necessarily an issue, as one could not use Thiele's equation to model the dynamics of such particles anyway. Instead, caution should be exercised when applying results obtained using Eq. (5.13) outside of the context of Thiele's equation.

5.2.1 The interaction between two skyrmions

The algorithm for using Eq. (5.13) to produce interaction potentials is as follows. First, analytically construct the magnetization configuration(s) of interest $\mathbf{m}_A(\mathbf{x})$ and $\mathbf{m}_B(\mathbf{x})$. Inspecting the asymptotics of the $\mathbf{m}_i$ should provide the functional form of $\mathbf{m}_\infty$ – use this to construct $\boldsymbol{\mu}_i$. Use the $\boldsymbol{\mu}_i$ to evaluate the overlap integral in Eq. (5.12), Taylor expanding the integrand as much as is necessary. The interaction potential is proportional to the integral, where the constant of proportionality can be determined numerically.

Working through this procedure for an azimuthally symmetric skyrmion is straight forward, but algebraic. Aligning the z-axis to the external field, the radial profile in Eq. (2.45) can be substituted into the rotationally symmetric skyrmion ansatz in Eq. (2.34), which yields the reduced magnetization after subtraction of the field polarized state. Then, the volume integral in Eq. (5.12) becomes an area integral by symmetry along the z-axis. The integral

$$\psi(\mathbf{R}) = \iint \big|\boldsymbol{\mu}_{\mathrm{Sk}}(\mathbf{x}) \times \boldsymbol{\mu}_{\mathrm{Sk}}(\mathbf{x}-\mathbf{R})\big| d^2x \tag{5.14}$$

can be thought of as an infinite sum of line integrals connecting the two skyrmions. The largest contribution from this sum comes from the term in which the line directly connects the two skyrmions. Changing coordinates to $\beta = r - R/2$ and defining the azimuthal angle θ such that $\theta = 0$ along this line, Taylor expanding the integrand to lowest order in $\mathbf{R}$ gives[1]

$$U_{\mathrm{SkSk}}(R) \propto e^{-\frac{R}{\lambda}} \int_{-R/2}^{R/2} d\beta \frac{L(\beta + \frac{R}{2})\big(1 - L(\beta - \frac{R}{2})\big)}{\sqrt{\frac{R^2}{4} - \beta^2}}\,, \tag{5.15}$$

where L is the modified logistic function introduced in Eq. (2.43). One could Taylor expand the integrand and integrate, but the behaviour of $U_{\mathrm{SkSk}}(R)$ will be dominated by the rapidly decaying exponential term. This leads to the well known result

$$U_{\mathrm{SkSk}}(R) \propto e^{-\frac{R}{\lambda}}\,. \tag{5.16}$$

This approach justifies (and, in fact, motivated) the analytical radial profile toy model presented in chapter 2. If one would try to directly substitute the asymptotic form of the radial profile, $f(r) \propto e^{r/\lambda}/\sqrt{r}$, the integral in Eq. (5.14) would be

---

[1] An eagle-eyed mathematician might notice that the integrand of Eq. (5.15) doesn't quite seem to match the integrand of Eq. (5.14). A trick has been played here – it has silently been assumed that the leading contribution to the integrand will come from a very small region of overlap midway between $\boldsymbol{\mu}_{\mathrm{Sk}}(\mathbf{x})$ and $\boldsymbol{\mu}_{\mathrm{Sk}}(\mathbf{x}-\mathbf{R})$ in which the angle θ between the $\boldsymbol{\mu}$'s will be roughly constant. This has been used to absorb a factor of $\cot\theta$ into the constant of proportionality.

divergent at the origin and at $\mathbf{R}$, and its integrand would be an increasing function of β. Using the toy model, before any approximations are made, the integrand of Eq. (5.14) is a strictly decreasing function of β – the region of maximal overlap between skyrmions is at the point midway between them. Additionally, none of the parameters introduced in the construction of the toy model feature in the final form of the derived skyrmion-skyrmion interaction potential. Those parameters were introduced to describe the internal structure of a skyrmion. As the region of maximal overlap between skyrmions should occur about $\beta = 0$, far from either skyrmion's core, an interaction potential containing any information on the internal structure of a skyrmion must either be incorrect, or needlessly accurate for short values of $\mathbf{R}$ which break the assumption of unperturbed internal structure in Thiele's equation. The only purpose of the additional parameters contained within $L(R)$ in the context of deriving interaction potentials, is to keep integrals finite.

5.2.2 The interaction between a skyrmion and a surface twist

Calculating the interaction between a skyrmion and a surface twist is very similar to the calculation of the interaction between two skyrmions. The reduced magnetization profile of a surface twist decorating a semi-infinite film bounded by the x-axis is

$$\boldsymbol{\mu}_{\text{Twist}} = \big(0, \sin\theta(x), \cos\theta(x)\big)\,, \tag{5.17}$$

where $\theta(x)$ takes the form derived in chapter 2, given in Eq. (2.58). More important than the full profile are the profile's asymptotics, which are given simply by $\theta(x) = e^{-x/\lambda}$. As both the rotationally symmetric skyrmion ansatz and the surface twist are independent of the z-coordinate, once again the volume integral becomes an area integral $\iint |\boldsymbol{\mu}_{\text{Twist}}(\mathbf{x}) \times \boldsymbol{\mu}_{\text{Sk}}(\mathbf{x} - \mathbf{R})| d^2x$ that yields the same result to lowest order

$$U_{\text{SkTwist}}(R) \propto e^{-x/\lambda}\,. \tag{5.18}$$

As surface twist instabilities are always lower energy than the field polarized state at the boundary of materials, this interaction should be considered whenever a skyrmion is near the walls of its confining material. In a simulation of a skyrmion in a finite geometry, one can handle this interaction by adding a force that increases exponentially quickly near the edge of the geometry to the right hand side of Thiele's equation. This result also explains why the product of exponentials used to model the skyrmion-boundary interaction in Ref. [109] – as the asymptotics of a surface twist share the asymptotic behaviour of skyrmions, the interaction between a skyrmion and boundaries must take the same form, to lowest order, as the interaction between skyrmions.

Due to this asymptotic relation, one can think of a skyrmion incident on the edge of a material as interacting with a continuum of virtual skyrmions centred on the boundary. This picture is useful for understanding how skyrmions might interact with boundaries of different geometries – a real skyrmion sees a greater density of virtual skyrmions at a concave boundary than a convex boundary, so one would expect the constant of proportionality in Eq. (5.18) to be larger for a concave boundary than for a convex.

5.2.3 Calculating interaction potentials numerically

In previous attempts to benchmark skyrmion interaction potentials, profiles topologically equivalent to a skyrmion would be initialized near to each other, and the motion of the skyrmions would be approximately tracked and fit to Thiele's equation using the force term of interest [29, 57]. When studying the force applied to a skyrmion by a surface twist, the same approach was used – an approximate skyrmion profile was initialized near the boundary of a material, and the resultant motion of the skyrmion was tracked and fit to Thiele's equation [109]. There are two major sources of error one encounters when using this procedure. Firstly, when integrating the Landau-Lifshitz-Gilbert equation, only the final relaxed state is guaranteed to be a solution to the Euler-Lagrange equations of the micromagnetic energy functional. All intermediate states are unphysical – the reason why skyrmions are repulsive in such a setup is that they have been initialized so close to each other that the system is far from a solution to the Euler-Lagrange equations, with a solution only being reached when the skyrmions are so far away from each other that they no longer overlap. This copy-pasted initialization breaks smoothness in the overlap region between the two textures. Since the interaction between magnetic textures is delicately related to this overlap region, it is crucial that the overlap region has time to relax and reach the energy-minimizing form it will have in nature when two skyrmions are pushed towards each other. Secondly, tracking the motion of skyrmions as they repel is a crude way to approximate an applied force. Errors due to discretization of time and space, as well as errors in ones skyrmion recognition algorithm, will propagate through to the force fit.

In this work, both of these sources of error are overcome by measuring the interaction potential directly. To do this, the magnetization configurations of interest can be confined in a film of length ℓ along the interparticle separation direction. One can initialize the configurations, relax the resultant state, and plug the final magnetization into the energy functional to calculate the total energy and the energy per finite difference cell. Using the case of the interaction between two skyrmions as an example, one can confine two skyrmions in a film of length L in the x-direction that is periodic along all three Cartesian axes. Any length can be used along the z-direction due to the translational symmetry of the state along it, for calculations in this work the length was simply taken to be a single finite difference cell. The length along the y-direction should be any length sufficiently large that the internal structure of the skyrmions is not affected by interactions of a skyrmion with its periodic boundary mirrors in the y-direction[1]. Writing the total energy of the field-polarized state as E_{FP} and the total energy of the two skyrmions as E_{Sk}, the total

---

[1] Of course, one could exploit the interaction between a skyrmion and its periodic mirror images to carry calculate the skyrmion-skyrmion interaction potential in a periodic system of varying length containing only one skyrmion. But, these calculations are relatively inexpensive, and the methodology is easier to appreciate when two skyrmions can be seen, such as in Fig. 5.1.

energy of the relaxed system becomes $E_{\mathrm{FP}}(\ell) + E_{\mathrm{Sk}} + U_{\mathrm{SkSk}}(\ell/2)$. The energy of the field-polarized state per finite difference cell can be calculated *a priori* and used to calculate $E_{\mathrm{FP}}(\ell)$. Assuming that the structure of a skyrmion deforms minimally as a result of the interaction, the energy contribution E_{Sk} can be taken to be a constant energy offset. As ℓ decreases, the increase in energy due to U_{SkSk} can be extracted. Typical simulations used to determine the skyrmion-skyrmion and skyrmion-surface twist interactions are shown in Fig 5.1.

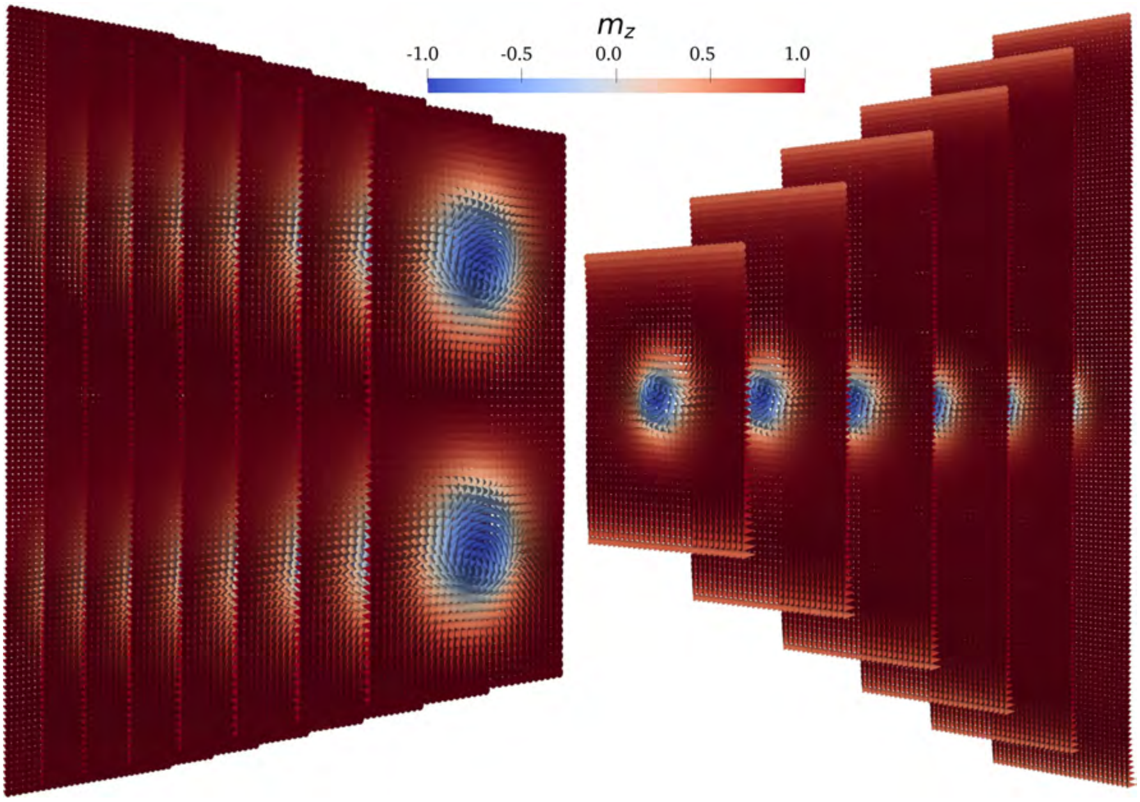

Figure 5.1: An example of the variation of the simulation geometries used in the computation of the numeric potentials in Fig. 5.3. The length ℓ of the simulation geometry along the direction of interparticle separation was varied, and for each ℓ the energy of the system was minimized by relaxing the Landau-Lifshitz-Gilbert equation numerically. The interaction energy can be derived from the energy density of these states as a function of ℓ. On the left, relaxed states from calculations used to determine the skyrmion-skyrmion interaction potential are shown. On the right, relaxed states from calculations used to determine the skyrmion-surface twist interaction potential are shown. In both cases, the magnetization is represented by cones coloured by the component of the magnetization along the direction of the applied field. The simulations used to calculate the skyrmion-surface twist interaction were carried out at larger external fields, which is why the skyrmions occupy a smaller area in those calculations.

However, this is an even simpler way to directly extract U_{SkSk} from the micromagentic energy densities extracted from simulations such as those in Fig. 5.1. The energy of the field-polarized state linearly decreases with increasing applied field. The energy of the skyrmion state is a non-linear, generally increasing function of external field (which can be seen simply by the Zeeman energy cost of the central moments that point antiparallel to the external field). There must be some value of $\mathbf{B}$ that one can apply such that $E_{\text{Sk}} = E_{\text{FP}}$. In that case, the sum $E_{\text{FP}} + E_{\text{Sk}}$ is not a function of ℓ, and all variations in the energy per finite difference cell can be attributed to U_{SkSk}. This magnetic field can be found by carrying out the above-described process as a function of magnetic field.

The data set used to determine the field at which the field-polarized state has the same energy density as the skyrmion state is shown in Fig. 5.2. For lower magnetic fields, the skyrmion state has a lower energy density than the surrounding field-polarized state. In the large separation limit, the energy density of the system asymptotically approaches the energy of the field-polarized state. So, for calculations with low magnetic fields (such as those at the top of Fig. 5.2), the total energy density decreases as the fraction of the simulation area occupied by the field-polarized state decreases and the fraction occupied by skyrmions increases. Then, as the skyrmions begin to interact, the energy increases again. For larger fields, the increase in energy at small separations has contributions both from the skyrmion-skyrmion interaction and from the increase in energy density due to a lower fraction of the system being occupied by the lower energy field-polarized state. One could use any of these data to extract the skyrmion-skyrmion interaction by first calculating the energy density of the skyrmion and field-polarized states respectively, but at 286 mT, as the energy densities of the skyrmion and field-polarized states are the same, the increase in energy density of the system is due only to the skyrmion-skyrmion interaction. The interaction potential $U_{\text{SkSk}}(R)$ can be straight-forwardly extracted from the 286 mT curve by writing $E/A = U_{\text{SkSk}}(R) + E_{\text{Const}}$ and finding E_{Const} from the curve's large separation limit.

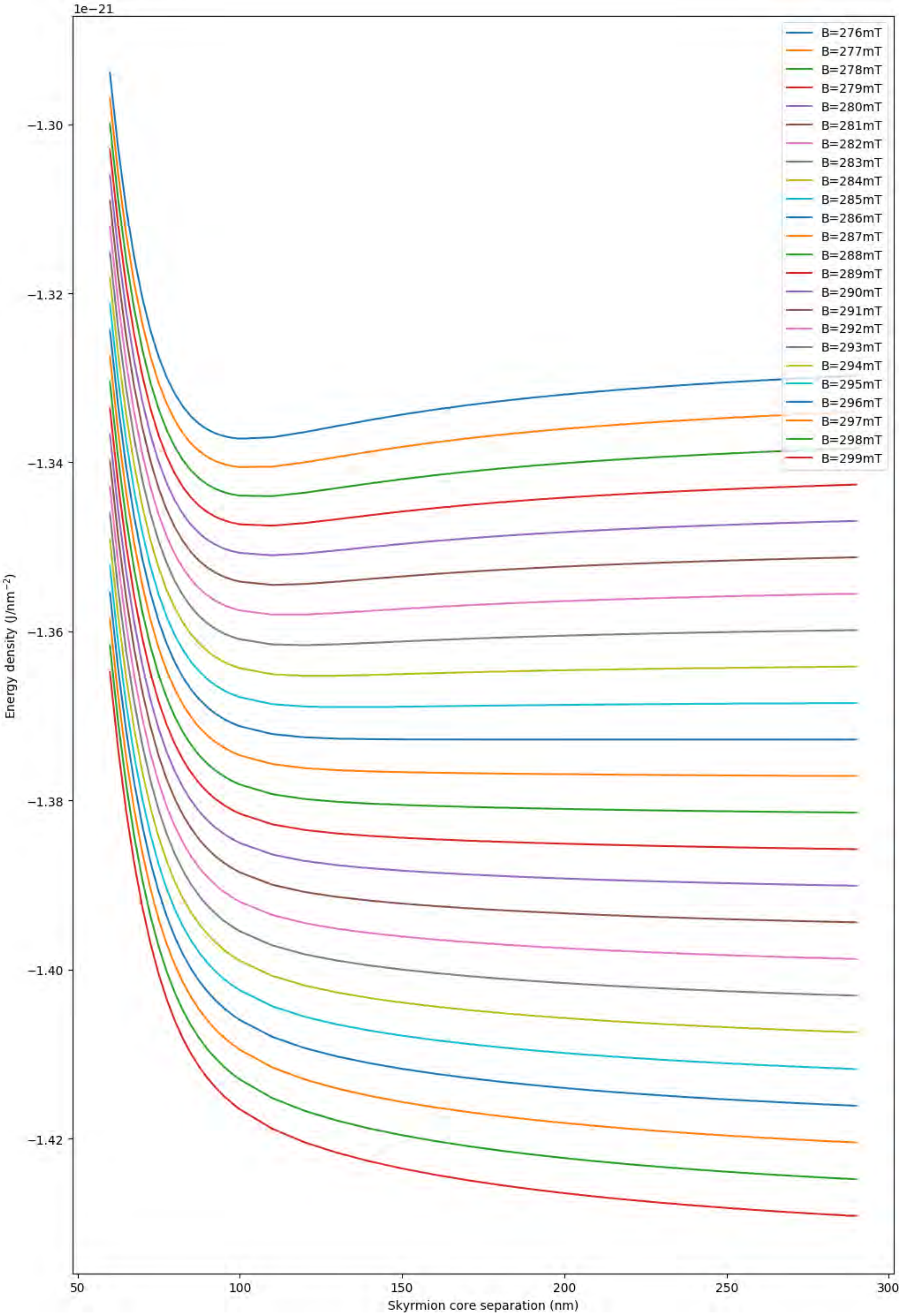

Figure 5.2: The energy density of two-skyrmion states as a function of magnetic field and skyrmion separation. Each point on each curve is the result of a micromagnetic relaxation of geometries such as those shown in Fig. 5.1.

Using the skyrmion-skyrmion interaction potential as the 286 mT curve in Fig. 5.2 less the constant energy offset, the constant of proportionality in Eq. (5.16) was fit by least squares refinement to the numeric potential. The resultant fit is shown in Fig. 5.3(a). To calculate the skyrmion-twist potential numerically, the same approach was used, with the key difference that the system was made finite in the x-direction so that surface-twists minimize the micromagnetic energy at the edges. The magnetic field that balanced the constant energy of the surface twists and the skyrmion with the length-dependent field-polarized energy in this finite geometry was found using the process outlined in Fig. 5.2 to be 463 mT. As the energy of the field-polarized state linearly decreases with external field, this increase in field required to balance energies when surface twists are included shows that the energy density of a surface twist is lower than the energy density of a skyrmion. This is precisely the reason why skyrmions were found to be pinned to surfaces in the previous chapter – to increase the volume of the magnetization that can be occupied by the energy-reducing surface twist state. Again, the constant of proportionality in Eq. (5.18) was fit to the micromagnetic data obtained at 463 mT and a comparison of the fit to the micromagnetic data is shown in Fig. 5.3(b). Also included is the functional form of the skyrmion-twist interaction potential derived in Ref. [45], where for fairness of comparison the prefactor to their exponential was also treated as a fitting parameter. The exponential that they derive has an incorrect argument, giving a very poor fit to calculation. This mistake is likely a product of their generally more complicated method of derivation, involving direct substitution of a superposition of skyrmion and surface twist magnetization into the micromagnetic energy functional, integrating and attempting to find the leading order contribution to an increase in energy.

To summarize, interactions between magnetization configurations whose equations of motion can be described using Thiele's equation have been shown to always be repulsive, and arise as a result of the overlap between neighbouring magnetic textures. To understand the interaction between these textures in an energy-functional-

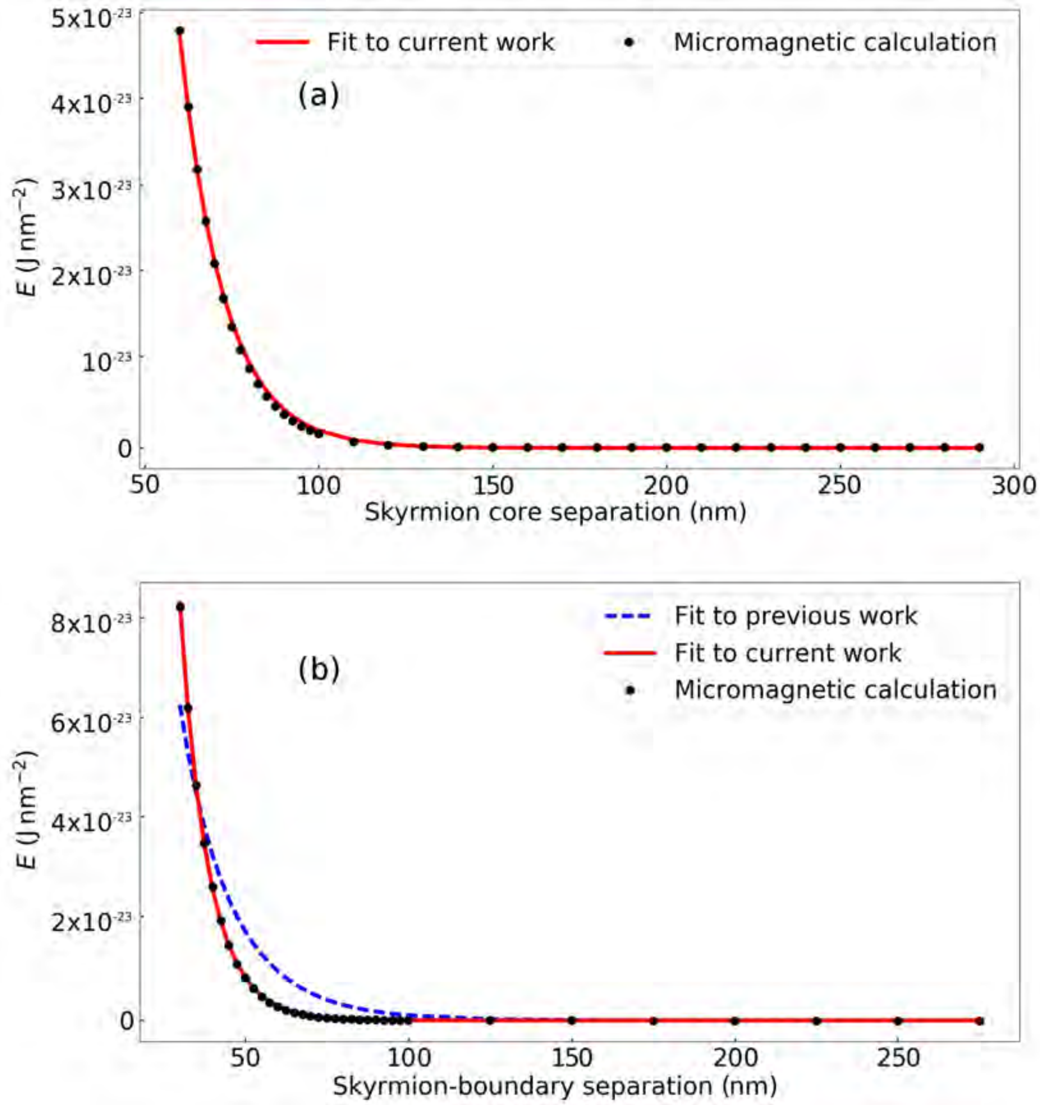

Figure 5.3: A fit (of constants of proportionality) of the analytically derived interaction potentials to the numerically obtained potentials. (a) A fit of Eq. (5.16) to the 286 mT curve shown in Fig. 5.2. (b) A fit of Eq. (5.18) to its corresponding 463 mT curve, also including a fit of the skyrmion-twist interaction potential derived in Ref. [45] for comparison.

agnostic manner, it has been hypothesized that the interaction potential between adjacent textures should be well described by a Taylor expansion in an expression for the overlap between the textures. The overlap integral provided is a functional in the textures, which was crafted to qualitatively agree with situations of overlap that one would expect to cause a large or small increase in energy. This approach was used to derive approximate forms of the skyrmion-skyrmion and skyrmion-surface twist interaction potentials, given in Eq. (5.16) and Eq. (5.18), respectively. To benchmark these potentials, a new micromagnetic technique to accurately calculate interaction potentials was developed. Fits of the derived potentials are in good agreement with the micromagnetic calculations, and in the case of the skyrmion-surface twist interaction, far outperform potentials presented in previously published literature.

5.3 Interactions between conically modulated skyrmions

While azimuthally symmetric skyrmions are local minima of the micromagnetic energy, the same cannot be said of the conically modulated skyrmions derived in the previous chapter. As can be seen in Fig. 5.4, conically modulated skyrmions must represent saddle point solutions to the energy functional as they are attractive and form a bound state Consequently, their motion cannot be modelled using Thiele's equation, as their internal structure should not be expected to be constant while they are in motion. Nevertheless, a discussion of the interactions between skyrmions is incomplete without a discussion of their interactions, and the bound states they can form.

Following the procedure identified in chapter 4, using the same FeGe J and D parameters to nucleate a pair of conically modulated skyrmions, two units of topological winding number 1 were introduced into a finite differences geometry with xyz dimensions 800 nm ×300 nm ×200 nm, respectively. The cores of the topological units were initialized 160 nm from each other, and formed a bound state with a core-to-core distance of roughly 90 nm, although the modulation of the bound state means that this value deviates substantially along the z-direction. Various slices through this state are shown in Fig. 5.4.

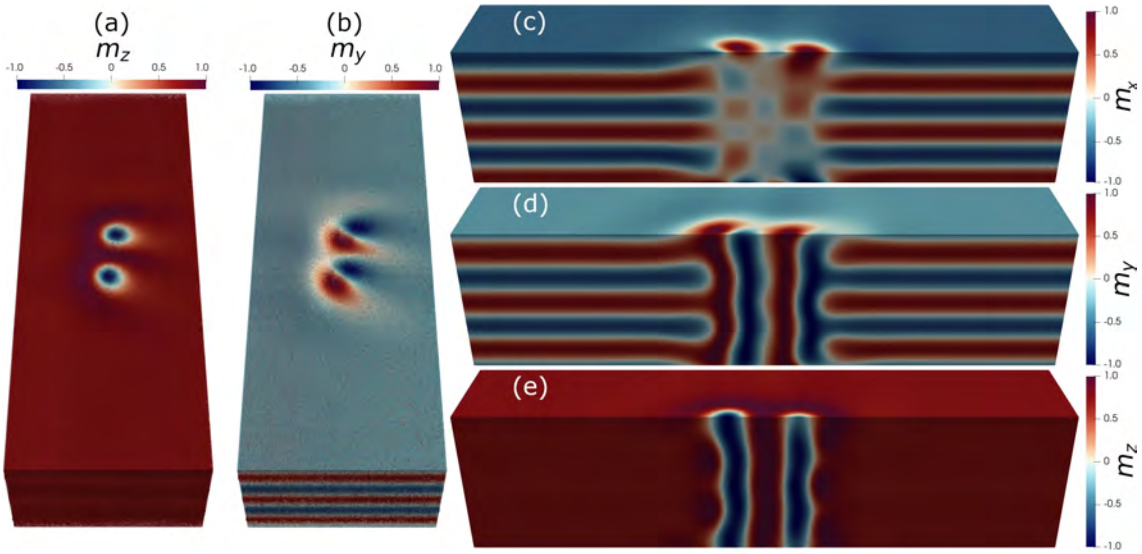

Figure 5.4: Conically modulated skyrmions in three dimensions interact attractively and form bound states. (a) An aerial view of the bound state, where the magnetization is represented by cones whose orientation is set by the magnetization where the colour is set by the z-component of the magnetization. (b) As in (a), but colouring the cones by the y-component of the magnetization. (c)-(e) A cross-section normal to the y-axis through the bound state, where the surface is coloured by the x-component of the magnetization in (c), the y-component in (d) and the z-component in (e).

As the bound state is localized within the conical state, as proven in chapter 4, the bound state must be conically modulated. This modulation is most readily visualized in Fig. 5.4(c), where the x-component of the magnetization shows oscillatory variation along the z-axis with the same period as the encompassing conical state, although side-to-side variation of contours of constant m_y are also clearly visible in Fig. 5.4(d). This idea of skyrmion bound states is not new; the relationship between conical modulation and attractive interparticle interaction was first noticed in Ref. [137], where the authors note only the weak condition that conical modulation “can” occur when skyrmions coexist with the cone phase, and do not calculate the full three-dimensional profile of conically modulated skyrmions, but the authors do show that they always have attractive interactions. At a similar time, skyrmions with a short-ranged attractive character were found numerically using an energy functional with an anisotropic exchange interaction [138]. These interactions are likely a quirk of the anisotropies present in their system; as they are not correlated with the conical phase, they will not be further considered here. Shortly after, in a magnetic field regime in which magnetic cones are typically present, attractive skyrmion clusters were observed in a sample Cu_2OSeO_3 in real space [139]. Attractive skyrmions were observed at a similar time in an LTEM experiment [138].

An important feature of attractive skyrmions is that they are necessary for the formation of the skyrmion liquid state as shown in Fig. 3.6. If skyrmions were interacting repulsively and the number density of skyrmions decreased, the minimum energy configuration of the skyrmion crystal would still be hexagonally close packed. If the number density of skyrmions decreased to a point where the interaction between neighbouring skyrmions was negligible, then a disordered state such as the one pictured in Fig. 3.6 could form. Were that the case, the $|q|$ vectors for magnetic scattering would contract towards the Bragg peak, as a longer ordering period in real space should correspond to a shorter period in reciprocal space, and the magnetic reciprocal space is convolved with the Bragg peak. So, the liquid state measured in Fig. 3.6 implies an attractive interparticle interaction. Moreover, any disordered state resulting from repulsive interparticle interactions would be gaseous in nature, as the large skyrmion-skyrmion distances required to melt a repulsive skyrmion crystal would lead to a state that is readily compressible.

Using this logic, the skyrmion liquid state shown in Fig. 5.5 was obtained by nucleating a low number density of randomly placed topological units (36 in total) in a large, $700\,\mathrm{nm} \times 700\,\mathrm{nm} \times 200\,\mathrm{nm}$ geometry, under the same conditions as those used to obtain Fig. 5.4. The interparticle distances in Fig. 5.5 are similar to those that one would expect from a skyrmion lattice, but skyrmion-skyrmion separations are randomly oriented. The diffraction pattern one would expect from such a state precisely matches the one obtained in Fig. 3.6 due to the combination of rotational disorder but fixed skyrmion-skyrmion separation.

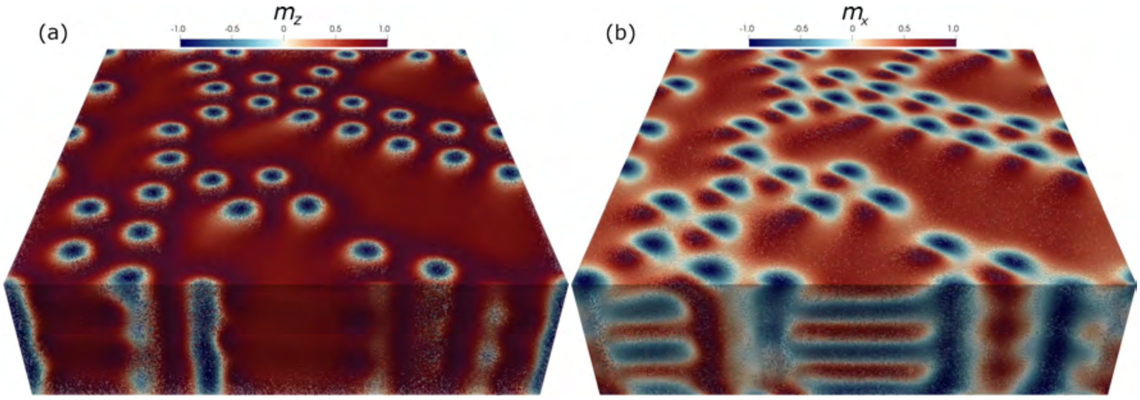

Figure 5.5: The skyrmion liquid state, constructed from randomly placed topological units in an energetic environment in which conically modulated skyrmions extremize the micromagnetic energy functional. (a) 500,000 cones were rendered at randomly selected points in the system, pointing parallel to the magnetization and coloured by its z-component. (b) As in (a), but colouring the cones by y-component of the magnetization. The oscillatory nature of this component along the z-axis in regions away from skyrmions shows that the skyrmions are immersed in the conical state, while oscillations of the skyrmion's magnetization along the z-axis confirm that the skyrmion clusters are conically modulated.

In conclusion, micromagnetic investigations reaffirm that conically modulated skyrmions have attractive interparticle interactions, where a conically modulated bound state is shown in Fig. 5.4. This attractive interaction was used to explain the liquid-like scattering pattern shown in Fig. 3.6, and to simulate the skyrmion liquid state shown in Fig. 5.5.

Chapter 6

External forces

The previous chapter discussed the interactions between skyrmions and their magnetic environment, providing a general expression for the interactions between magnetic configurations whose motion can be described by Thiele's equation. Here the functional form taken by external forces ∇U will be considered, and their effects on the resultant motion of topological objects will be understood in terms of the skyrmion Hall angle. The skyrmion Hall angle one measures in an experiment is known to be strongly affected by pinning potentials in real materials. This will be briefly reviewed, before the deflection of a skyrmion driven down a nanowire by spin-orbit torque due to the field generated by the current will be bounded.

6.1 The skyrmion Hall angle

Inspecting Thiele's equation, it can be seen that any magnetization configuration with a non-trivial topological winding number acquires a component of its velocity perpendicular both to the direction of the applied force and to the surface normal. This is a consequence of a finite gyrocoupling vector $\mathbf{G}$. The magnitude of this vector is determined by the topology of the magnetization, and cannot be substantially tuned by materials parameters. Writing $\nabla U = \mathbf{F}_{\mathrm{Ext}}$, the angle between an externally applied force $\mathbf{F}_{\mathrm{Ext}}$ and the induced velocity of a magnetization configuration defines the skyrmion Hall angle, and is given by

$$\theta_{\mathrm{SkH}} = \tan^{-1}(G/\alpha)\,, \tag{6.1}$$

where it has been assumed that α is proportional to the identity matrix. This behaviour of α is required when the magnetization configuration is rotationally symmetric, as can be seen by inspecting the elements of the dissipation tensor in Eq. (5.3). While $\mathbf{G}$ is not tunable, as α has a linear dependence on materials parameters such as conductivity and Gilbert damping, the skyrmion Hall angle will vary from material to material.

This angle is of paramount importance, completely controlling the qualitative dynamical behaviour of magnetization configurations in a system. For the purposes of device design, as the skyrmion Hall angle determines the direction in which skyrmions are driven by external forces, understanding the skyrmion Hall angle of a materials system of interest takes highest priority.

6.2 Current driven motion

The manipulation of skyrmions with electric currents provides an attractive route towards skyrmionic devices. In thin magnetic skyrmion-hosting films, large current densities can be reached with small voltages that can be switched and pulsed using conventional electronics. Depending on the design of the film, there are two different physical mechanisms that can drive skyrmions. If a spin-polarized current is passed directly through the skyrmion-hosting material, a force acts on the skyrmions proportional to the gradient of the magnetization in a skyrmion, which is governed by its radial profile. This is known as the spin-transfer torque effect in the literature, and the direction of the applied force is usually parallel to the current direction [57, 140–144]. The second process is referred to as the spin-orbit torque effect, and arises when a spin-polarized current in an adjacent layer exchange-couples to spins in the magnetic film. This is a much richer physical phenomenon, in the case of skyrmions leading to an applied force whose orientation depends on the helicity of the skyrmion [141, 145–148]. Including both spin-transfer torque and spin-orbit torque terms into the Landau-Lifshitz-Gilbert equation gives [57, 141]

$$\begin{aligned} \frac{d\mathbf{m}}{dt} =& -\gamma\big(\mathbf{m}\times\mathbf{H}_{\text{eff}} - \eta\mathbf{m}\times\frac{d\mathbf{m}}{dt}\big) - \frac{g\hbar\gamma}{4q_e L}\Phi_{\text{SH}}\mathbf{m}\times\mathbf{m}\times(\hat{z}\times\mathbf{j}_{\text{HM}}) \\ &+ \frac{\hbar\gamma}{2q_e}\Big((\mathbf{j}_{\text{Mag}}\cdot\nabla)\mathbf{m} - \beta\mathbf{m}\times(\mathbf{j}_{\text{Mag}}\cdot\nabla)\mathbf{m}\Big)\,, \end{aligned} \tag{6.2}$$

where the charge of an electron is q_e, the current density flowing through the skyrmion-hosting material is $\mathbf{j}_{\text{Mag}}$, β is the spin-torque non-adiabatic factor, the Landé g-factor is g, the spin-Hall angle of the adjacent layer with thickness L is written as Φ_{SH}, and the current density in the adjacent layer is $\mathbf{j}_{\text{HM}}$. The term with prefactor Φ_{SH} is the spin-orbit torque contribution, and terms due to spin-transfer torque are characterized by their linearity in $\mathbf{j}_{\text{Mag}}\cdot\nabla\mathbf{m}$. These contributions will be discussed independently below.

6.2.1 Spin-transfer torque

While spin-orbit torque driven motion is expected to produce the velocities required for skyrmionic devices, skyrmion lattices have been shown to respond to ultra-low spin-transfer torques. Additionally, unless the resistivity of the skyrmion-hosting sample is overwhelmingly higher than an adjacent spin-Hall layer, any voltage applied through the spin-Hall layer will undoubtedly give rise to a finite current $\mathbf{j}_{\text{Mag}}$, which could lead to velocity components perpendicular to the expected drive direction in an experiment.

An incredibly important point relating to spin-transfer torque is that it is an unavoidable effect in conductive skyrmion-hosting materials when skyrmions are not at rest with respect to the conduction electrons in the system. If one assumes that conduction electrons are strongly exchange coupled to the underlying magnetic lattice (Hund's rule coupling), the spin wavefunction $|\chi(\mathbf{x})\rangle$ of an electron at point $\mathbf{x}$ in a coordinate system centred on a rotationally symmetric skyrmion is given by

$$|\chi(\mathbf{x})\rangle = \left(\cos\frac{f(r)}{2}, e^{i(N\theta+\gamma)}\sin\frac{f(r)}{2}\right)^{\intercal} \tag{6.3}$$

when written using a basis of the Eigenspinors of the S_z operator $\chi_+^{(z)}$ and $\chi_-^{(z)}$, where $^{\intercal}$ represents the transpose operation. The form of the phase factor in the $\chi_-^{(z)}$ component can be found by projecting Eq. (6.3) onto a basis of Eigenspinors of the the S_x and S_y operators. The amplitude for an electron to hop a to a site a displacement $A\mathbf{e}_k$ from $\mathbf{x}$ can then be written

$$t(\mathbf{x}, A\mathbf{e}_k) = t\left\langle \chi(\mathbf{x}) | \chi(\mathbf{x} + A\mathbf{e}_k)\right\rangle\ , \tag{6.4}$$

where A is the lattice constant and $\mathbf{e}_k$ is the unit vector along the kth spatial dimension. This can be written $t(\mathbf{x}, A\mathbf{e}_k) = te^{ia_k(r)q_e/\hbar c}$, which takes precisely the same form as the Peierls factor for hopping in the tight-binding model in the presence of an applied magnetic field where q_e is the charge of an electron, c is the speed of light and $\hbar$ is the reduced Planck constant. This allows the factor

$$a_k(r) = \frac{\hbar c}{2q_e}(1 - \cos f(r))\partial_k N\theta \tag{6.5}$$

to be interpreted as the vector potential due to a skyrmion. Differentiating gives the following expressions for emergent magnetic and electric fields

$$B_{\mathrm{Sk},i} = \frac{\hbar c}{2q_e}\epsilon_{ijk}\mathbf{m}\cdot\left(\partial_j\mathbf{m}\times\partial_k\mathbf{m}\right), \tag{6.6}$$

$$E_{\mathrm{Sk},i} = \frac{\hbar}{2q_e}\mathbf{m}\cdot\left(\partial_i\mathbf{m}\times\frac{d\mathbf{m}}{dt}\right)\ , \tag{6.7}$$

where, interestingly, the z-component of the emergent magnetic field in Eq. (6.6) is linear in the topological charge density $\mathbf{m}\cdot(\partial_x\mathbf{m}\times\partial_y\mathbf{m})$. The time derivative in Eq. (6.7) states that an emergent electric field is an unavoidable consequence of skyrmion motion. This induces a current $\mathbf{j} = \sigma \mathbf{E}_{\mathrm{Sk}}$ in any material for which the conductivity $\sigma \neq 0$. As this current is driven directly through the magnetic layer, this leads to a finite $\mathbf{j}_{\mathrm{Mag}}$ when skyrmions are driven through a conductive material even in the absence of an externally applied voltage. The result is that skyrmions moving through a conductive medium exhibit dissipation in addition to the Gilbert damping term with a magnitude linear in the conductivity of the sample, as alluded to in the previous chapter. This damping term is nothing but dissipation due to the generation of spin-transfer torque currents by a skyrmion's finite emergent electric field. Setting $\mathbf{j}_{\mathrm{Mag}} = \sigma \mathbf{E}_{\mathrm{Sk}}$ in Eq. (6.2), assuming the resultant spin-transfer torques are adiabatic ($\beta = 0$) and following the procedure to derive Thiele's equation outlined in the previous chapter gives the contribution $\alpha'\eta'$, where the shape factor η' takes the form shown in Eq. (5.4) and $\alpha' = (\hbar/2q_e)^2\gamma\sigma$ [57, 134].

6.2.2 Spin-orbit torque and the spin Hall effect

The spin Hall effect is a phenomenon in which electrons moving through a material are segregated by spin at opposite interfaces of a material, as a result of spin-orbit scattering from the atoms in the host material. In materials with a non-zero spin Hall effect, charge currents can be thought of as giving rise to spin currents in a perpendicular direction. This perpendicular direction is selected by asymmetries in the material, which in the case of a thin film becomes the film's thickness direction [149]. If a current flows through a conductor with a large spin Hall effect that has been grown on a magnetic film, exchange coupling between the magnetization in the magnetic layer and the spin-polarized electrons at the magnetic layer-conductor interface will exert a torque on the magnetization. As the strength of spin orbit coupling scales with atomic number, the current flowing through the spin Hall layer is labelled as $\mathbf{J}_{\mathrm{HM}}$ for heavy metal. Assuming that any spin-transfer torque due to emergent electric field of a skyrmion is adiabatic and takes the form $\mathbf{j}_{\mathrm{Mag}} = \sigma \mathbf{E}_{\mathrm{Sk}}$, Thiele's equation as stated in Eq. (5.2) acquires a ∇U term including a factor [141]

$$\mathcal{H}_{ij} = \frac{1}{4\pi} \iint \left(\mathbf{m} \times \partial_i \mathbf{m}\right)_k \epsilon_{kj} \, dx \, dy \,, \tag{6.8}$$

where ϵ_{kj} is the rank-2 Levi-Civita tensor. As discussed in Ref. [141], when carried out for a single rotationally symmetric skyrmion, this can be written as $\mathcal{H}_{ij} = -IR_{z,ij}(\gamma)$, where $R_z(\gamma)$ is the rotation matrix about the z-axis with a rotation angle equal to the helicity of the skyrmion, and the integral I is given by

$$I = \frac{1}{4} \int_0^\infty \left(\sin f \cos f + r\frac{df}{dr}\right) dr \,. \tag{6.9}$$

Including this term into Thiele's equation along with its prefactors inherited from Eq. (6.2) and a change of variables gives

$$\mathbf{G} \times \mathbf{v} - (\alpha_G \mathcal{D} + \alpha' \eta')\mathbf{v} = -\pi \xi_{\mathrm{Sk}} I \frac{g\hbar\gamma}{q_e L} \Phi_{\mathrm{SH}} R_z(\gamma) \mathbf{j}_{\mathrm{HM}} \,, \tag{6.10}$$

where $\xi_{\mathrm{Sk}} = \sqrt{S_{\mathrm{Sk}}/\pi}$ is the radius of a skyrmion. This derivation followed Ref. [141], but includes also the important $\alpha'\eta'$ spin-transfer torque contribution to damping. As the authors neglected this term, the equation of motion derived in Ref. [141] is valid to describe only insulating skyrmion-hosting magnets driven by spin-orbit torque. As the only insulating skyrmion-hosting magnet currently known is $\mathrm{Cu_2OSeO_3}$, the equation of motion derived in Ref. [141] is valid only when describing the motion of skyrmions in $\mathrm{Cu_2OSeO_3}$ driven by spin-orbit torque, and one should expect significant errors in calculated skyrmion Hall angles using their equation to describe metallic magnets.

As the rotation matrix $R_z(\gamma)$ makes an appearance in Eq. (6.10), the resultant direction of motion one would expect to observe from spin-orbit torque driven skyrmions has an unusual relationship with the direction of the applied current. In the large skyrmion Hall angle limit, when one would usually expect motion perpendicular to the direction of an applied force, Bloch-type skyrmions with a helicity of $\gamma = \pi/2$ would be driven colinearly with the direction of the applied current. One should not make the mistake of assuming that this means that the skyrmion Hall angle is 0° in this case, as the skyrmion Hall angle is the angle between the direction of the applied force and the direction of the induced motion – this unusual current-velocity relationship is a consequence of the fact that the direction of the applied force due to spin-orbit torque in this case is perpendicular to the direction of the applied current[1]. Similarly, in materials with high damping in which Bloch-type skyrmions ought to have a skyrmion Hall angle approaching 0°, one would expect Bloch-type skyrmions to move perpendicularly to the direction of the applied current (but collinearly with the force due to spin-orbit torque).

The effects of the spin-orbit torque term in Eq. (6.2) can be most easily visualized when applied to large magnetic domains. In Fig. 6.1 the motion of a magnetic domain through a patterned nanowire of a Ta(3.2)/Pt(2.7)/[Pt(0.6)/CoB(0.8)/Ir(0.4)]$_X$ Pt(2.2) multilayer (thicknesses in nm) on Si_3N_4, where the stack is listed bottom-to-top and $X = 3$. This is an interfacial DMI system in which one might expect to see skyrmions, but in this sample, none were observed. The magnetization was tracked by Kerr microscopy as 5 ns 5 V current pulses were applied, driving the domain from left to right. The motion of the domain wall was reversible by reversing the sign of the voltage.

6.3 Skyrmions in non-uniform magnetic fields

As skyrmions are characterized by a radial profile for which $f(r)$, the angle between a magnetic moment and the applied field, is non-zero, skyrmions cost Zeeman energy. The Zeeman energy cost of a rotationally symmetric skyrmion can be calculated

---

[1] A point of endless confusion amongst referees.

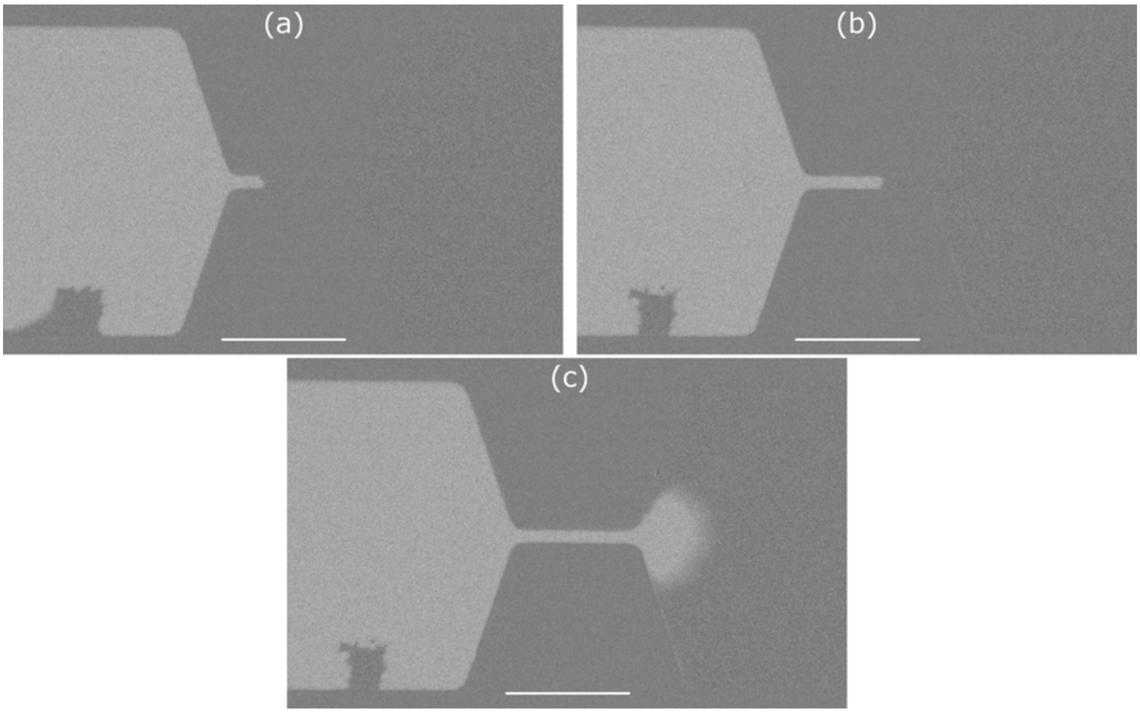

Figure 6.1: A magnetic domain wall, driven by spin-orbit torque, imaged by the wide field magneto-optic Kerr effect microscope at the EXTREMAG facility. The white bar in each subfigure indicates a distance of $20\,\mu$m. Spin-orbit torque was applied by 5 ns duration square wave current pulses with current density $1.2 \times 10^{12}\,\mathrm{Am}^{-2}$.

simply. Substituting $\mathbf{m}_{\mathrm{Sk}}$ into Eq. (2.1) gives

$$E_B[\mathbf{m}(\mathbf{x})] = -\iiint_{V_{\mathrm{Sk}}} \mathcal{E}_B(\mathbf{m}(\mathbf{x}))d^3x = -2\pi LBM_S \int_0^\infty r\cos f(r)dr\,, \tag{6.11}$$

where the thickness of the skyrmion-hosting sample is L, and the angular and axial integrals were carried out in cylindrical coordinates centred at R. As this integral is not cut off, it is always infinitely negative – the energy cost of the localized deviation from the field polarized state is perhaps more instructive and can be written

$$E_{B,\mathrm{SkCost}} = 2\pi LBM_S \int_0^\infty r\big(1-\cos f(r)\big)dr = -\mathbf{B}\cdot\iiint \boldsymbol{\mu}_{\mathrm{Sk}}\,d^3x\,. \tag{6.12}$$

This expression is now finite and positive definite, describing the increase in Zeeman energy of the system as a result of the existence of a skyrmion texture (as opposed to the field polarized state). This is conveniently expressed in terms of the reduced magnetization $\boldsymbol{\mu}_{\mathrm{Sk}}$ originally introduced to calculate interaction potentials. The boundary conditions for $f(r)$ are $f(0) = \pi$ and $\lim_{r\to\infty} f(r) = 0$, where numerical solutions to the Euler-Lagrange equation that dictates $f(r)$, Eq. (2.41), show that $f(r)$ monotonically decreases. To minimize the energy cost in Eq. (6.12), as $\mathbf{B}$ increases, $f(r)$ wants to approach 0 more and more rapidly. As a result, $f(r)$ has a weak dependence on $\mathbf{B}$, where the limited dependence on $\mathbf{B}$ comes from the fact that regions of steeper gradients of $f(r)$ cost more antisymmetric exchange energy density $\mathcal{E}_D$. The dependence of the radial profile on external field can be seen in Fig. 5.1 – the magnetic field applied to carry out the skyrmion-skyrmion interaction study was much lower than the one applied during the skyrmion-surface twist calculations, resulting in a change in size of skyrmions between the two geometries shown.

In REXS, T-REXS and neutron scattering studies, the scattering q-vectors of the skyrmion lattice are observed to be very slowly varying functions of applied field [150–152]. This indicates that, in experiments, the radial profile varies more slowly than one might expect using a simple energy functional such as Eq. (2.1). So, unless the magnitude of the applied field is varying substantially on the characteristic length-scale of a skyrmion ξ_{Sk}, writing $I_\mu = 2\pi LBM_S \int r(\cos f(r) - 1)dr$, to a good approximation one can write $E_{B,\text{SkCost}} = -B_z(\mathbf{R})I_\mu$. This leads to a force acting on a skyrmion of

$$\mathbf{F}_{\nabla\mathbf{B}} = -\nabla U = I_\mu \nabla B_z(\mathbf{R})\,. \tag{6.13}$$

This energy term can be appended to the right hand side of Thiele's equation in Eq. (5.2) to model the resultant motion of a skyrmion system immersed in a non-uniform magnetic field.

6.3.1 Perpetuum mobile

"The law that entropy always increases, holds, I think, the supreme position among the laws of Nature. If someone points out to you that your pet theory of the universe is in disagreement with Maxwell's equations — then so much the worse for

Maxwell's equations. If it is found to be contradicted by observation — well, these experimentalists do bungle things sometimes. But if your theory is found to be against the second law of thermodynamics I can give you no hope; there is nothing for it but to collapse in deepest humiliation."

-Sir Arthur Stanley Eddington, The Nature of the Physical World (1927)

A fascinating consequence of field gradient driven motion (or unfortunate, according to Sir Eddington) is uncovered in the presence of a radial magnetic field gradient. If $B_z(\mathbf{R}) = B_z(r)$ is taken to be monotonically decreasing, the energy of a central skyrmion would decrease if the skyrmion moved further $r = 0$. This leads to a force $F_{\nabla \mathbf{B}} = I_\mu \partial_r B_z(r) \hat{r}$ on the right hand side of Thiele's equation. If dissipation is small (as would be the case in Cu_2OSeO_3, the only insulating skyrmion-hosting magnet), one could write an approximate Thiele equation

$$\mathbf{G} \times \mathbf{v} = -\nabla U = I_\mu \partial_r B_z(r) \hat{r} \, . \tag{6.14}$$

The form taken by Thiele's equation in the limit of vanishing dissipation is interesting, stating that the induced skyrmion velocity $\mathbf{v}$ is parallel to contours of constant U. In the case of such a radial field gradient, this would induce concentric in-phase rotation of the skyrmion lattice. Remarkably, not only has such dynamical behaviour been observed in the past, but the required experimental set-up is simple to achieve [153]. If magnetic fields are applied by means of two permanent magnets, one either side of the sample, then the applied field is necessarily maximized about the axis of the magnets, decreasing radially.

Even accounting for finite dissipation need not halt the rotation. The topological protection exhibited by skyrmions is expected to not hold in finite-sized materials [154]. Indeed, recently, the energy barrier for the destruction of a skyrmion at the boundary of its material has been shown by Cortès-Ortuño et al. to be significantly reduced when compared to the topologically protected bulk value (which can be understood by the fact that skyrmions can be smoothly unwound at the edge of a material without introducing discontinuities into the magnetization field) [155]. The force $\mathbf{F}_{\nabla\mathbf{B}}$ could be sufficient to destroy skyrmions at these edge regions. Such destruction events will continually free up an area near $r = 0$ where, within the skyrmion pocket, more skyrmions will nucleate before spiralling out towards the confines of the geometry.

One can understand that this set-up does not allow for true perpetual motion by the fact that skyrmions cannot be nucleated at temperatures below the skyrmion pocket, as thermal fluctuations are necessary to tear the magnetization fabric and spawn new skyrmions in the central region. In experiments, the cryostat temperature is carefully maintained by the competition between a liquid helium cooled arm and an electrical heating element – unassisted the dissipation caused by any finite value of α would invariably lead to temperature decreases that would, eventually, drive an idealized system's temperature beneath the skyrmion pocket.

6.4 The motion of skyrmions through nanowires

Nanowires fabricated in exactly the same way as the wire shown in Fig. 6.1 with the multilayer stack repeated $X = 5$ times, have been shown to host skyrmions, which can be reproducibly nucleated by applying current pulses [104–108]. In this materials system, skyrmions tend to be very large (well modelled as an extended region of magnetization antiparallel to the external field terminated by a thin domain wall) with irregular sizes. As the components of the dissipative tensor in Eq. (5.3) generally scale with skyrmion size, one would expect the skyrmion Hall angle of a Néel-type skyrmion driven by spin-orbit torque to decrease as a function of radius. This was not found to be the case, and the skyrmion Hall angle was found to be independent of skyrmion diameter.

The spin-orbit torque effect involves driving a current through an adjacent layer, and that current will generate a non-uniform magnetic field. One could become understandably concerned that the preceding discussion of Thiele's equation for a skyrmion driven by spin-orbit torque is incorrect – as the force due to the magnetic field gradient would drive skyrmions towards the boundary of a wire, and the force due to spin-orbit torque on a Néel type skyrmion would drive the skyrmion along the wire, the resultant direction of motion would be completely dominated by the ratio of these forces, having little to do with dissipative effects.

Taking the RHS of Eq. (5.2) to be $\nabla U = \mathbf{F}_{\nabla \mathbf{B}} + \mathbf{F}_{\mathrm{SOT}}$, setting $\mathbf{F}_{\mathrm{SOT}} \perp \mathbf{F}_{\nabla \mathbf{B}}$, solving the resultant simultaneous equations for the components of $\mathbf{v}$ and defining θ_{SkH} as the angle between between $\mathbf{v}$ and $\mathbf{F}_{\mathrm{SOT}}$ gives

$$\theta_{\mathrm{SkH}} = \tan^{-1}\left[\left(1 + \frac{\alpha_G \mathcal{D}}{N}\frac{F_{\nabla \mathbf{B}}}{F_{\mathrm{SOT}}}\right) \Big/ \left(\frac{F_{\nabla \mathbf{B}}}{F_{\mathrm{SOT}}} - \frac{\alpha_G \mathcal{D}}{N}\right)\right] , \tag{6.15}$$

which is a function of $F_{\nabla \mathbf{B}}/F_{\mathrm{STT}}$. As Thiele's equation is first order in time, one can also write $F_{\nabla \mathbf{B}}/F_{\mathrm{STT}} = \mathbf{v}\cdot\hat{F_{\nabla \mathbf{B}}}/\mathbf{v}\cdot F_{\mathrm{STT}}$. As the speed at which skyrmions are driven by the spin-orbit torque was found to be $(6\pm1)\,\mathrm{ms}^{-1}$ experimentally, to estimate an upper bound for $F_{\nabla \mathbf{B}}/F_{\mathrm{STT}}$, it is only necessary to calculate an upper bound for the speed at which skyrmions are driven by the magnetic field gradient in the nanowire that results from the pulse. This was estimated by integrating the Biot-Savart law numerically, and found to be approximately $5\,\mathrm{mT}\,\mu\mathrm{m}^{-1}$. Using the materials parameters found in the experiment of $J = 10\,\mathrm{pJ\,m}^{-1}$, $D = (-1.1 \pm 0.1)\,\mathrm{mJ\,m}^{-2}$, $\alpha_G = 0.07$ and $M_S = (1.2 \pm 0.1)\,\mathrm{MA\,m}^{-1}$, and a uniaxial anisotropy constant of $K = 0.1\,\mathrm{MJ\,m}^{-3}$, the motion of skyrmions in a magnetic field gradient of magnitude $5\,\mathrm{mT}\,\mu\mathrm{m}^{-1}$ was investigated in out-of-plane magnetic fields ranging from 3-5 mT to match the fields used in the experiment. This was carried out by using computational micromagnetics to measure the time it took for a skyrmion nucleated using the above materials parameters in a finite differences geometry with cells of volume $2.5\,\mathrm{nm} \times 2.5\,\mathrm{nm} \times 2.5\,\mathrm{nm}$ to travel a distance of 500 nm along the direction of the field gradient.

These numerical data were used to derive a mean value of $F_{\nabla\mathbf{B}}/F_{\mathrm{STT}} = 0.0028 \pm 0.0001$. The only parameter deviating from experimental value in this investigation was the uniaxial anisotropy constant K, which was underestimated in the calculation. However, underestimations of K were found numerically to increase the speed at which skyrmions moved under a field gradient, hence the value $F_{\nabla\mathbf{B}}/F_{\mathrm{STT}} = 0.0028 \pm 0.0001$ should be taken as an upper bound. The size of this ratio indicates that $F_{\nabla\mathbf{B}}$, along with any deflection from field gradients when driving a skyrmion down a wire with spin-orbit torque, can safely be neglected.

Instead of the observed diameter independence of the skyrmion Hall angle in these nanowires being attributed to the force due to a magnetic field gradient, it was proposed that this unusual behaviour resulted from imperfections in the magnetic material itself. The multilayers from which the nanowires were fabricated for this experiment were grown by magnetron sputtering, which is an energetic deposition technique known to introduce imperfections in the resultant materials. The study of the effects of such imperfections is an active field, but it is generally agreed that, when pinning potentials attributed to material defects dominate the energy landscape of a skyrmion, one observes an effective skyrmion Hall angle that is reduced in magnitude and drive dependent. In the low-drive limit, the force due to pinning potentials dominates the RHS of Thiele's equation in Eq. (5.2), and the skyrmion Hall angle appears to approach 0° [113, 156–160]. In the large-drive limit, when the force due to pinning potentials becomes negligible, one should expect to recover the defect-free skyrmion Hall angle. Such a velocity dependence of the skyrmion Hall angle has been measured in the past [62, 126, 130, 161].

To conclude, the form of Thiele's equation for spin-orbit torque drives, including spin-transfer-torque-like damping originating from the emergent electric field of a skyrmion, has been presented in Eq. (6.10). Thiele's equation has been further extended by the force due to magnetic field gradients, whose form has been derived and is shown in Eq. (6.13). This field gradient force has been discussed in the context of its apparent indefinite resultant rotations of the skyrmion lattice. The force due to the magnetic field gradient arising from the current applied during spin-orbit torque driven motion of skyrmions has been found to be negligible, validating the form of the equation presented in Eq. (6.10).

Chapter 7

Magnetically straining the skyrmion crystal

Now that Thiele's equation has been derived including Gilbert and metallic damping terms for drives due to spin-orbit torque and magnetic field gradient driven motion, one can combine these drives with knowledge of skyrmion interactions to study the property of skyrmion crystals in a range of situations. Incorporating the preceding results relating to the Thiele equation, the equation of motion for the ith skyrmion in a skyrmion crystal immersed in a non-uniform magnetic field can be written

$$\mathbf{G} \times \mathbf{v}_i - \alpha \mathbf{v}_i = -\sum_{j \neq i} \nabla U_{\mathrm{SkSk}}(|\mathbf{x}_i - \mathbf{x}_j|) + I_\mu \nabla B_z(\mathbf{x}_i)\,, \tag{7.1}$$

where it has been assumed that the skyrmion crystal is sufficiently large that the interaction between a skyrmion and the edges of its confining material, as described by Eq. (5.18), can be neglected. This chapter will investigate numerical solutions to Eq. (7.1), focussing on the strain that develops in the skyrmion lattice when $\nabla B_z \neq 0$. This strain will be used to explain the anisotropic broadening of peaks in REXS patterns.

7.1 Numerics

As skyrmion interactions have an exponentially decaying character, it is possible to integrate Eq. 7.1 using an algorithm similar to the linked-list algorithms popular in molecular dynamics solvers – the precise procedure implemented is detailed below. The first order equation of motion in Eq. (7.1) was integrated using a second order Runge-Kutta method [162]. To optimize the integration process, a series of simplifications were made. The exponentially decaying nature of $U_{\mathrm{SkSk}}(R)$ implies that only interactions with nearby skyrmions need be considered, where the jth skyrmion was treated as being nearby to the ith skyrmion if $|\mathbf{x}_j - \mathbf{x}_i| < \Lambda$, where Λ was chosen to be just under twice the lattice parameter of the unperturbed hexagonally close packed skyrmion lattice. If there are n skyrmions in the simulation, this promises to optimize the algorithm's complexity from n^2 to ρn, where ρ is the mean number of skyrmions a skyrmion typically has a non-negligible interaction with. But, if the Boolean expression $|\mathbf{x}_j - \mathbf{x}_i| < \Lambda$ is evaluated for every possible skyrmion pair, the overall complexity of the algorithm is still n^2, even if interactions themselves are only calculated for skyrmions for which $|\mathbf{x}_j - \mathbf{x}_i| < \Lambda$ is true.

The key to successfully implementing such an algorithm is to reduce performance in memory-space. At initialization time, a rank-3 tensor of skyrmion identifiers can be stored such that the $[a, b]$th element of the tensor contains a vector of unique skyrmion identifiers for skyrmions whose coordinates $[x, y]$ satisfy $a\Lambda < x \leq (a+1)\Lambda$ and $b\Lambda < y \leq (b+1)\Lambda$. Then, it is possible to calculate which skyrmions are within a distance Λ to the ith skyrmion by computing the Boolean expression $|\mathbf{x}_j - \mathbf{x}_i| < \Lambda$ for the set of skyrmion identifiers $\{j\}$ contained within the same vector of the skyrmion identifier tensor, or any of the eight adjacent vectors. This involves computing $|\mathbf{x}_j - \mathbf{x}_i| < \Lambda$ an average of $36\rho/\pi$ times per skyrmion, or $36n\rho/\pi$ times to generate a complete list of pairs of skyrmions whose interparticle separation is less than Λ[1]. After every integration step for each skyrmion, if the floor of any of the skyrmion's $[x, y]$ coordinates have changed, one simply updates the tensor of skyrmion identifiers and the algorithm will continue to function for the following integration step.

As the form of gradients of the skyrmion-skyrmion interaction potential is constant, the performance of the simulation can be significantly improved by using a lookup table to calculate the skyrmion-skyrmion interaction force. This moves the bottleneck of the code to the calculation of the list of skyrmions that should interact with each other each timestep, generated according to the above algorithm. However, as skyrmions move only a small fraction of Λ per timestep, as is required to ensure smoothness in $-\nabla U_{\mathrm{SkSk}}$ in time, the list of interacting skyrmions is a very slowly varying function of time. To a good approximation, this interaction list can be recalculated more than an order of magnitude less frequently than the positions of the individual skyrmions. In skyrmion crystal calculations carried out in this work, a list of interacting pairs of skyrmions was calculated once every ten iterations of the second order Runge-Kutta algorithm. Both the lookup of the skyrmion-skyrmion interaction force and the calculation of the interaction list were parallelized to leverage the power of large scale computing facilities, particularly the SCARF cluster located at the Rutherford Appleton Laboratory.

7.2 Anisotropic magnetic fields

As described in Eq. (6.14), skyrmion lattices tend to rotate in the presence of radial magnetic fields. Three timestamped REXS patterns of such motion are shown in Fig. 7.1. The diffraction peaks rotate counter-clockwise in time, but at each point in time throughout the entire rotation, the peaks appear distorted. Below, this

---

[1] Massively multiplayer online video games implement this algorithm to allow thousands of players to exist in seemingly continuous worlds. Setting the distance Λ to the render distance of a client's camera, a server can calculate lists of pairs of 'interacting' users. For large worlds with low player densities, ρ approaches 1, and the optimization increases server performance by $n/\rho \approx n$.

distortion will be understood to be the result of anisotropic magnetic fields at the surface of the sample.

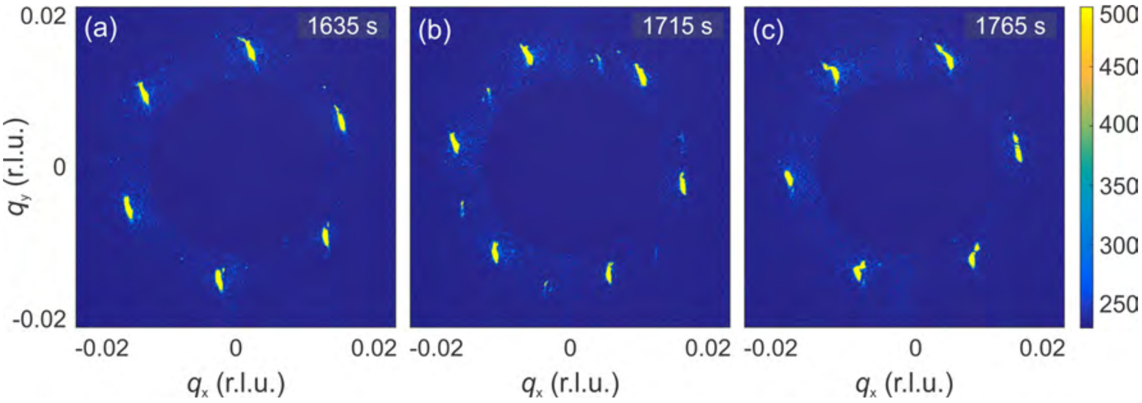

Figure 7.1: REXS data taken on the skyrmion lattice state in a sample of Cu_2OSeO_3 at a temperature of 57 K and an external field of 25 mT. These data were acquired exactly on resonance, so truncation rod effects were large enough that all six diffraction peaks can be clearly seen simultaneously. In this data set, to circumnavigate complexities arising from the REXS technique, the elliptical scattering patterns were projected onto a circle. The skyrmion lattice was immersed in an external field that was radially decaying which, as approximately described by Eq. (6.14), induces lattice rotation. This rotation was counter clockwise, and can be seen by comparing peak positions from (a)-(c), which were acquired at the same point on the same crystal over 130 s. In each of (a)-(c), the diffraction peaks are distorted uniaxially.

The Taylor expansion for the magnetic field about its maximum can be written in polar coordinates as

$$B_z(r,\theta) = B_0 - B_2 r^2 - Y(r,\theta)\,, \tag{7.2}$$

where terms of the form B_1r would break smoothness of the magnetic field at the origin – all remaining terms in the Taylor expansion are contained within $Y(r,\theta)$. In a system with $Y(r,\theta) = 0$, one would expect the skyrmion lattice to rotate in phase (with skyrmions following spiral trajectories in real space when $\alpha \neq 0$). If the magnetic field B_z is generated by means of two axially aligned permanent magnets, contours of constant B_z will be described by concentric cylinders connecting the two magnets. If the sample surface is located ideally in the plane perpendicular to the applied field, then the magnetic field profile at the sample surface will exactly follow the description given in Eq. (7.2) with $Y = 0$, and contours of constant field will be concentric circles. But, ellipses are defined in general as the intersection between planes and cylinders – if the sample's surface vector is not exactly parallel to $\mathbf{B}$, the intersection between the sample's surface and the cylinders of constant magnetic field will give ellipses of constant field on the sample's surface. As it is impossible experimentally to perfectly align the external field with a sample surface, this situation of ellipses of constant field is unavoidable.

An additional assumption required for $Y \neq Y(\theta)$ is that the magnets generating the field are perfectly aligned. As many magnet assemblies at synchrotron end-stations are reconfigurable, magnets will often be moved around, replaced, rotated and jostled when samples are loaded prior to an experiment. It would be little short of miraculous if such magnets were mounted coaxially with accuracy of within a fraction of a beam width (which, for the data in Fig. 7.1, was roughly $200\,\mu$m). A misalignment of the axes of the permanent magnets would result in a rotation of the axis of the cylinders of constant magnetic field, further increasing the likelihood that contours of constant field on the sample surface are elliptical.

Assuming that the above experimental considerations break continuous azimuthal symmetry, one can include a finite $Y(r,\theta)$ into Eq. (7.2). If one expects in a certain experimental configuration for the magnetic field to have p-fold symmetry, then terms such as $Y(r,\theta) = r^2\cos^2(p\theta/2+\phi_0)$ are allowed in the Taylor expansion of the magnetic field, where ϕ_0 is a phase factor. Considering only lowest order variation in r allows magnetic fields to be described as $B(r,\theta) = B_0 - r^2(B_2 + Y_2\cos^2(p\theta/2))$. A magnetic field taking this form with $p = 4$ is shown in Fig. 7.2.

To study the consequences of an anisotropic magnetic field at the sample surface, Thiele's equation was integrated using $\mathbf{F}_{\nabla\mathbf{B}} = -2B_2x\hat{\mathbf{y}}$. As can be seen in Fig. 7.2, regions far from the centre appear locally to have straight contours of constant force. This would also be true of a magnetic field with continuous azimuthal symmetry and $Y = 0$, but for discrete azimuthal symmetry, as $\partial_\theta B \neq 0$, there will be an angular imbalance in regions well described by these linear approximations. For example, in

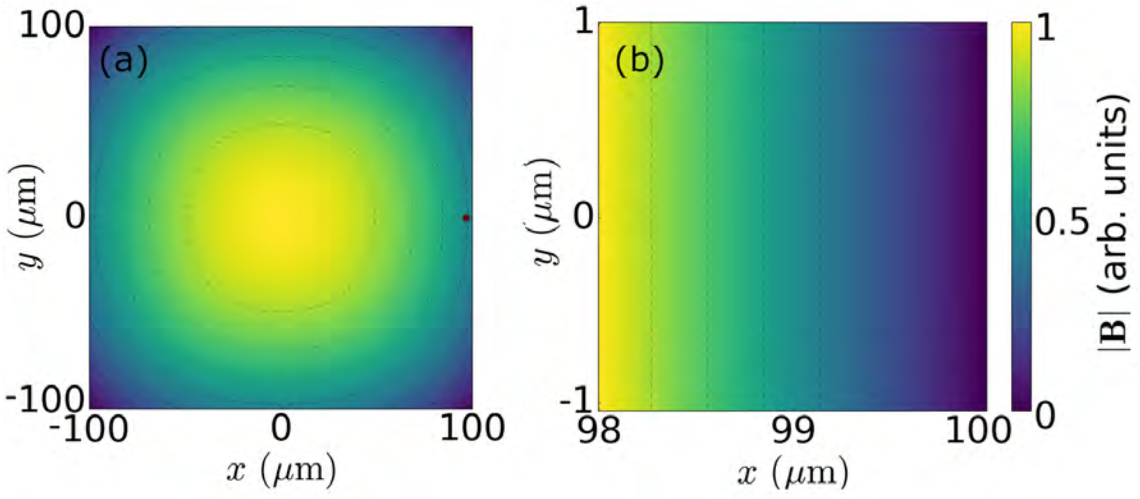

Figure 7.2: Plots of an example anisotropic magnetic field. (a) An image of how a magnetic field with a small four-fold anisotropy would look in a region with roughly the same size as the x-ray beam. A small red square towards the right of the panel indicates the area occupied by roughly 5000 skyrmions – the same number of skyrmions as used in calculations. Contours of constant magnetic field are indicated by dotted lines. (b) A magnified view of the red region in (a). Dotted lines indicate contours of constant force $F_{\nabla\mathbf{B}}$, to show that, in this region, one can write $F_{\nabla\mathbf{B}} = -2B_2x\hat{\mathbf{y}}$ with a high degree of accuracy.

Fig. 7.2(a), contours of constant field appear straightest at the sides of the square, while they bend most quickly towards the corners of the square; setting $Y = 0$ would give contours of constant field that are equally curved for all angles. For the case of $p = 2$, which was most likely to occur in the experiment, nearly straight constant field contours would move parallel to the major axis of the ellipse. While any interesting phenomena occurring in regions where $\mathbf{F}_{\nabla\mathbf{B}} \approx -2B_2x\hat{\mathbf{y}}$ would be averaged out for $Y = 0$, p-fold symmetric magnetic fields would leave p-fold signatures in the structure factor. The geometry of the simulation was periodic in 5138 skyrmions; to ensure continuity of the force, $\mathbf{F}_{\nabla\mathbf{B}} = -2B_2|x|\hat{\mathbf{y}}$ was used, so that, for a square simulation of length L, $\mathbf{F}_{\nabla\mathbf{B}}(L/2, y) = \mathbf{F}_{\nabla\mathbf{B}}(-L/2, y)$. The initial condition of the skyrmion lattice was generated by simulated annealing, which provides a good estimate of the lowest energy state of high dimensional optimization problems (which, in the case of crystal annealing, produces monodomain lattices) [163, 164]. For the calculations, as $\alpha' = 0$ in Cu_2OSeO_3, $\theta_{\mathrm{SkH}} = 85°$ was used. Although, all values of θ_{SkH} were found to produce entirely comparable results (differing only in an axis selected by the rotation of $\mathbf{F}_{\nabla\mathbf{B}}$ by the skyrmion Hall angle) and smaller values of θ_{SkH} converged much more quickly.

The simulations of the behaviour of the skyrmion lattice were carried out for a range of values of B_2, requiring only that $|F_{\nabla\mathbf{B}}(\mathbf{x}_i)| \ll |\nabla U_{\mathrm{SkSk}}(|\mathbf{x}_i - \mathbf{x}_j|)| \;\forall\; i, j$. If the force due to the field gradient was comparable to the skyrmion-skyrmion interaction force, skyrmions could be pushed near enough to each other that they would significantly overlap, breaking the assumptions used to derive Thiele's equation. In all calculations, simulation axes are rotated by the skyrmion Hall angle so that the resultant direction of motion of skyrmions acted on by the force is parallel to the y-axis of the simulation. Defining the [010] lattice vector as the lattice vector parallel to the y-axis of the simulation, the most striking effect of the applied shear force $F_{\nabla\mathbf{B}}$ is to rotate and strain any skyrmion lattice parameters not parallel to the [010] direction. This combination of rotation and strain is shown by the dotted line of values taken by the [100] vector in Fig. 7.3(a). Typical profiles of the strained skyrmion crystal are shown in Fig. 7.3(c) and Fig. 7.3(d), where the magnitude of B_2 was larger in Fig. 7.3(d). The manifestation of this strain in the structure factor of the skyrmion lattice is a uniaxial peak broadening, as can be seen in Fig. 7.3(b).

7.3 Defects and dislocations

The properties of real crystals under strain are completely determined by their defects and dislocations [165]. This is made particularly clear when one considers the magnitude of the shear stress required to plastically deform a crystal. In 1926, Frenkel showed that the shear stress that must be applied to a crystal to plastically deform it is on the order of its shear modulus [166] – this was found to overestimate the shear stress that induces plastic deformations in experiment by 4-8 orders of magnitude [167]. This stark discrepancy arises as a result of dislocations in a real crystal, which brings the shear stress required to plastically deform a lattice to

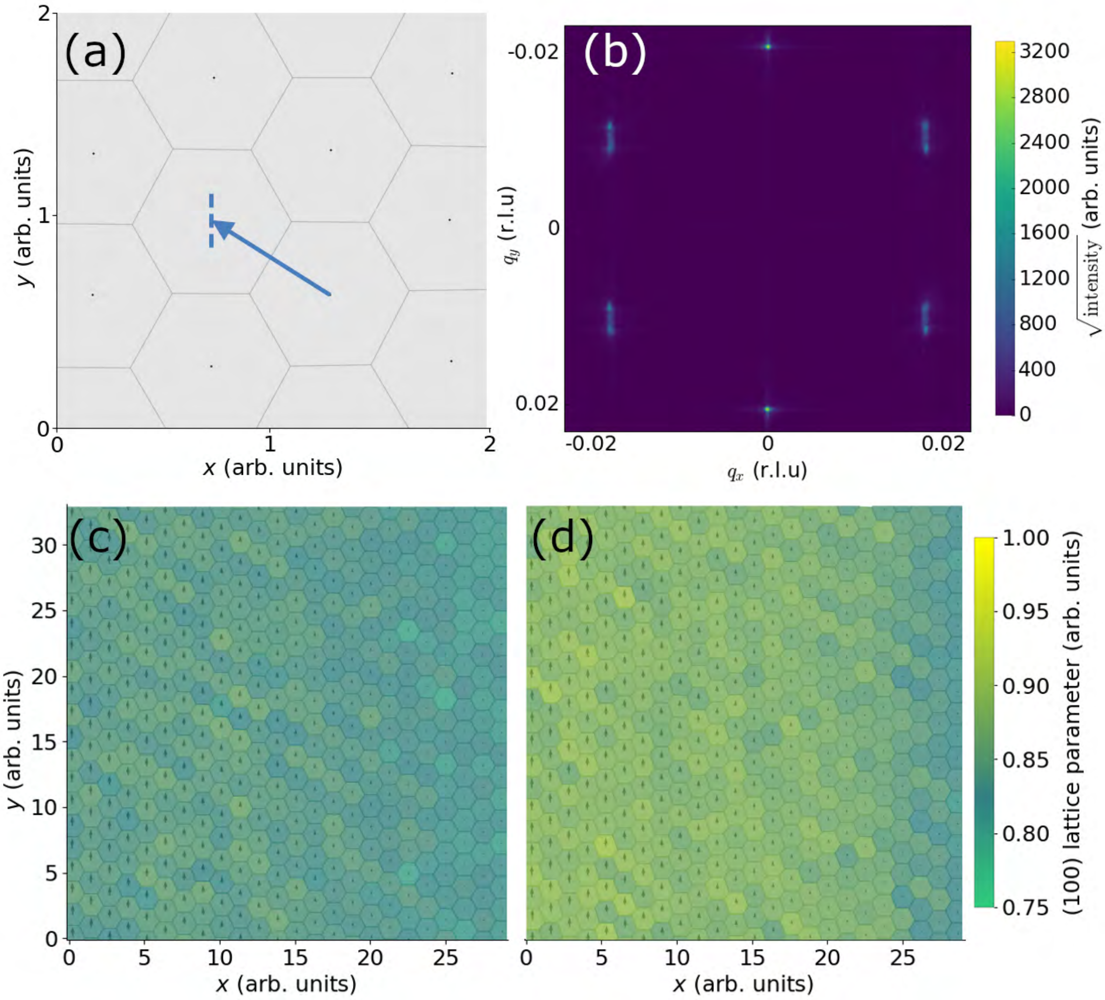

Figure 7.3: Results obtained by integrating Thiele's equation in the presence of a shearing magnetic field gradient of the kind shown in Fig. 7.2(b). (a) A triangular primitive lattice vector is shown in blue (here chosen to define the [100] direction), and the dotted line indicates the typical deviation of the strained lattice vector from its equilibrium position. Voronoi surfaces surrounding each lattice point are included as dark lines to guide the eye. (b) The absolute value of the structure factor one would expect to observe in a scattering experiment from a strained system. This structure factor has been rotated by 90°, so that uniaxial deformations of the structure factor peaks are collinear with the deformations of the real lattice vectors. (c) An image of a typical strained skyrmion crystal. Skyrmions are represented by small arrows, indicating their relative velocity, and surrounded by Voronoi surfaces. The area contained within a Voronoi cell is coloured by the strain of the [100] vector at that point. This region was used to calculate the structure factor shown in (b). (d) As in (c), subject to a slightly larger shear force. The otherwise equivalent simulation has a higher average deviation of the length of its [100] lattice vectors from the unperturbed value.

the order of the Peierls-Nabarro stress, which is the critical shear stress for the displacement of a dislocation [168].

Skyrmion lattices are well described as being two-dimensional, the only form of dislocations present in the lattice are edge dislocations – other common dislocations (such as screw or spiral dislocations) are fundamentally 3D objects [167]. In three dimensions an edge dislocation can glide along its 2D slip plane, defined by the plane spanned by its dislocation line and Burgers vector. In two dimensions, the dislocation line becomes a point, confining the gliding motion of edge dislocations to the direction of their Burgers vectors. In a hexagonal crystal, allowed Burgers vectors for edge dislocations are real lattice vectors. The length of the Burgers vector of an edge dislocation is proportional to the number of lattice planes the crystal is effectively missing on one side of the dislocation. By far the most common Burgers vector for edge dislocations in real systems are primitive lattice vectors, which correspond to edge dislocations resulting from a single missing lattice plane [169]. As such, in a two dimensional hcp crystal, if a shear stress is applied along a direction that is not parallel to one of the three primitive lattice directions, strain can only be relieved by defect motion that involves glides and climbs.

The climbing motion of defects is far more costly than glides, as each climb changes the shape of the macroscopic crystal [167]. If the direction of the shear force is misoriented from the nearest primitive lattice vector by an angle θ_0, then to uniformly dissipate strain requires that there are $\sin\theta_0$ defect climbs for ever $\cos\theta_0$ defect glides. This sets the energy cost of the displacement of a single edge dislocation to $E_{\text{Climb}}\sin\theta_0 + E_{\text{Glide}}\cos\theta_0 \approx E_{\text{Climb}}\sin\theta_0$. This energy contribution is clearly minimized when $\theta = 0°$, so, one would expect a material to reorient such that its primitive lattice vectors are parallel to the direction of an applied shear stress.

An image of an edge dislocation with a Burgers vector equal to the [010] vector is shown in Fig. 7.4(a). In hexagonal systems, dislocations whose Burgers vectors have unit length force one lattice point comprising the defect to have five nearest neighbours, and its neighbour to have seven. In the literature, these dislocations are typically referred to as 5-7 defects. The strain relieving effect of the propagation of 5-7 defects is captured by a comparison between Fig. 7.4(c) and Fig. 7.4(d), which show two snapshots of a simulation at nearby points in time. The gliding motion of the 5-7 defect substantially reduces strain in the skyrmion material. Peak splitting in the structure factor shown in Fig. 7.4(b) reflects the extremes of strain either side of the defect.

States such as the skyrmion crystal shown in Fig. 7.3(c)-(d) and Fig. 7.4(c)-(d) are typically referred to as smectic (literally meaning soapy) [170]. Smectic states are characterized by organized columns of material that can slip past each other for relatively little energy, by propagation of edge dislocations, and are often present in liquid crystals [171–173]. In Fig. 7.3, strain induced peak broadening is visible in only four out of the six peaks of the magnetic structure factor, unlike in the experimental data in Fig. 7.1, where broadening is visible in all six peaks. This is a consequence of the fact that these calculations account only for a shear force field, and to minimize the energy cost of immersion in this shear force field, as argued above, the skyrmion lattice reorients along the direction of the shear. This reorientation results in a perfect smectic state, where no strain develops along the [010] direction.

In the experiment, these effects appear as a perturbation on top of the rotating lattice. Skyrmions in magnetic field regions such as the one shown in Fig. 7.2(b) will have their lattice parameter locally distorted by the development of uniaxial strain resulting from the local shear stress applied to the skyrmion lattice. As the skyrmion lattice is constrained to rotate in-phase macroscopically, it is unable to rotate locally to minimize the energy cost of the shear in these regions. The fingerprint of the shear stress still appears in the structure factor of the skyrmion material as a broadening of peaks, but the skyrmion lattice's inability to rotate in this case results in the broadening of all six peaks. As the contours of constant field

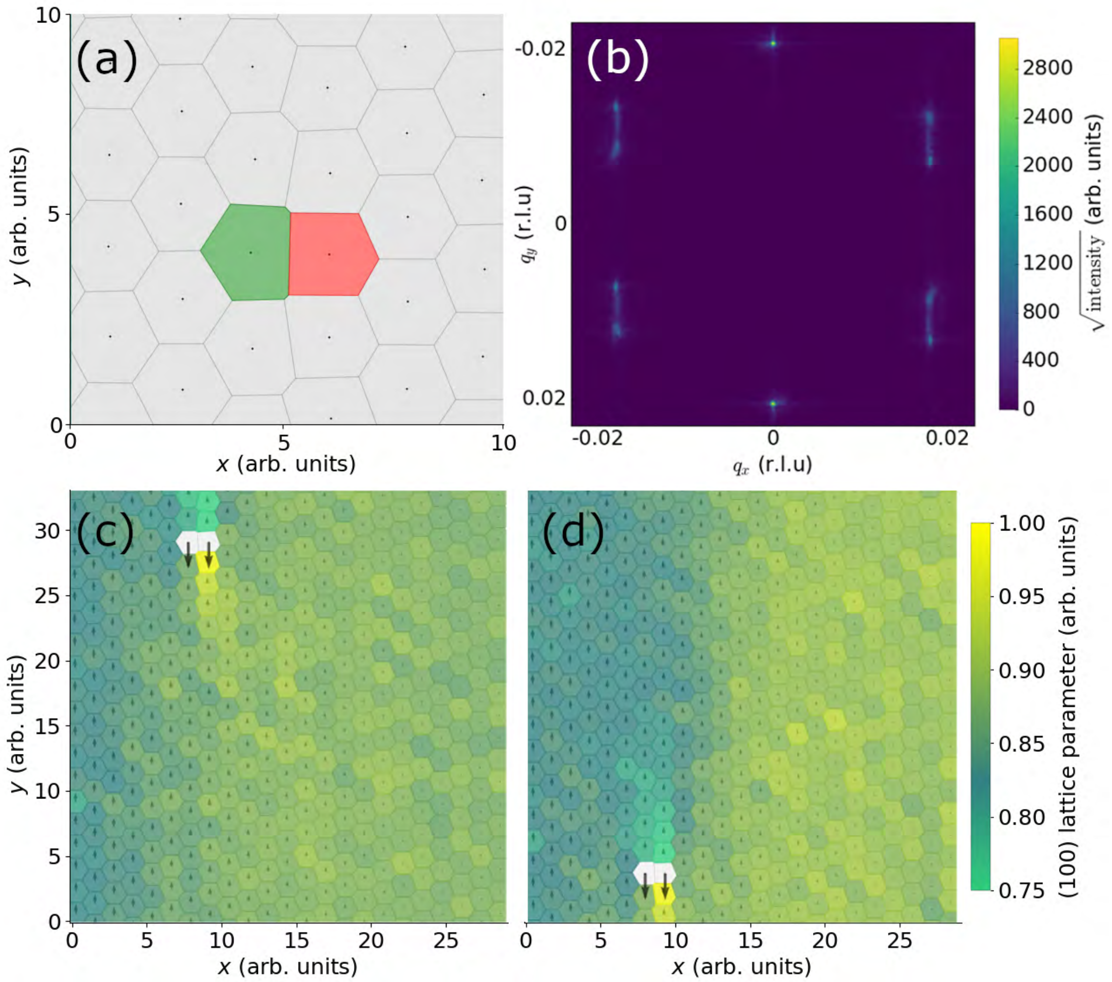

Figure 7.4: Illustrative example of the role played by 5-7 defects in the smectic state. (a) A visualization of a 5-7 defect, where the skyrmion with 7 nearest neighbours' Voronoi cell is coloured green, and the skyrmion with 5 nearest neighbours' Voronoi cell is filled in red. (b) An example of a structure factor generated in the presence of a 5-7 defects, rotated by 90° for comparison with Fig. 7.3(b), which exhibited comparatively less peak splitting. (c) A 5-7 defect glides through a strained skyrmion lattice to relieve strain. The 5-7 defect is coloured white, and its direction of motion is indicated by arrows whose magnitude is scaled relative to the velocity arrows of neighbouring skyrmions. (d) As in (c), further evolved in time. The 5-7 defect has propagated through the skyrmion crystal, resulting in a substantial relief of strain.

at the surface of the sample have two-fold azimuthal symmetry, the ideally point-like peaks broaden into lines – if the magnetic field profile at the surface of the sample somehow had the symmetry shown in Fig. 7.2(a), the structure factor peaks would manifest as crosses with four-fold symmetry. As argued, this distortion of peaks is not unique to rotation (which occurs only when B_2 is particularly large) and has since been observed independently in otherwise static skyrmion lattice states [152].

In conclusion, the uniaxial broadening of magnetic structure factor peaks has been investigated by integrating Thiele's equation in the presence of a quadratically varying magnetic field gradient. It has been argued that, in the REXS experiment shown in Fig. 7.1, a two-fold anisotropy in the applied field was unavoidable, which leads to extended regions in which the skyrmion crystal is well described as being immersed under a quadratically varying magnetic field gradient. For a skyrmion lattice with a large skyrmion Hall angle, this gives rise to an almost pure shear force, as can be seen by the velocity profiles in Fig. 7.3(c)-(d). The behaviour of the simulation was found to be dictated by the dynamics of topological defects in the skyrmion crystal; their strain relieving effects are captured in Fig. 7.4(c)-(d). The broadening of magnetic structure factor peaks observed in the experiment was found to be consistent with the effects one would expect from an applied field with a two-fold anisotropy.

Chapter 8

Measuring the skyrmion Hall angle

The skyrmion Hall angle θ_{SkH}, the angle between the direction of an applied force and the induced motion of a skyrmion, has complete control over the qualitative dynamical properties of skyrmions in a material. While a skyrmion with a skyrmion Hall angle of 90° travels exclusively along contours of constant energy, a skyrmion for which $\theta_{\mathrm{SkH}} = 0^\circ$ cuts contours of constant energy at right angles. An excellent example of this is given in Ref. [57], where skyrmions with skyrmion Hall angles approaching 90° are shown to glide around potential wells, while skyrmions with a skyrmion Hall angle nearer to 0° would be trapped by the same potential well. Skyrmions with a large skyrmion Hall angle have a much lower depinning threshold for applied forces, while skyrmions with lower skyrmion Hall angles have force-velocity relationships that may be more conducive to device development.

As the skyrmion Hall angle is a complicated parameter whose behaviour must be known exactly before one can design a device, there has been a significant movement in the community to search for materials in which the skyrmion Hall angle is vanishing. In particular, to utilize the popular racetrack memory schematic, in which skyrmions are driven down a long, straight wire, it would be useful for skyrmions to stay true to their path. Finite skyrmion Hall angles would propel skyrmions towards the boundaries of the wire, where they can be trapped and where their topological protection is rendered insubstantial [155]. This led to a surge of recent interest in skyrmions in antiferromagnetic, synthetic antiferromagnetic and compensated ferrimagnetic materials, which have a skyrmion Hall angle of 0° These $\theta_{\mathrm{SkH}} = 0°$ skyrmion systems may simplify the device design process, but were it possible to easily and reliably characterize the skyrmion Hall angle of a material, the increased mobility of high skyrmion Hall angle systems could be leveraged to make devices more efficient and reliable [113].

Owing to the importance of this parameter, experimental attempts to quantify its magnitude have become an important focus of the skyrmionics community. Recently, the skyrmion Hall angle was measured accurately for the first time in a material that hosts sparsely distributed skyrmions with a diameter of approximately $1\,\mu$m [62, 126][1]. While this seminal work represents an exciting advance in the understanding of the properties of skyrmions, their approach of tracking the motion of individual, large skyrmions in real space with an optical Kerr microscope cannot be applied to the lattices composed of nanoscale skyrmions that are commonly found in single crystals. While it is possible to go beyond the diffraction limit of optical light with x-ray imaging techniques (such as STXM or x-ray holography), these methods lack the time resolution required to capture the motion of skyrmions without imaging stroboscopically. The random nature of the initial state frozen into by the skyrmion lattice makes stroboscopic measurements impossible; to use such techniques, the initial configuration of the magnetic state must be reset deterministically (as in Ref. [126]).

The approach presented in this chapter surpasses the above-mentioned limitations by considering the mechanical properties of a sheared lattice of skyrmions, using the connection developed in the previous chapter between skyrmions to the

---

[1] Refs [62, 126] were published in the same volume of Nature Physics, both reporting the first observation of the skyrmion Hall effect.

physics of crystal defects. The combination of the reorientation of the skyrmion lattice with the strain that develops in the structure factor allows for an unambiguous measurement of the shear direction in reciprocal space. This can be combined with the fact that the stray field from a current carrying wire exerts a force on a lattice of skyrmions such that it is sheared along its direction of motion. As the shear direction is the motion direction, and the shear direction can be resolved in the structure factor, there is a signature of real-space motion in reciprocal space. This allows for the measurement of the skyrmion Hall angle with scattering techniques.

8.1 Deriving the skyrmion Hall angle from skyrmion lattice dynamics

As discussed in the previous chapter, in the presence of a shear stress, the energy cost required to relieve strain takes the form

$$E_{\mathrm{Defects}}(\theta_0) = E_{\mathrm{Climb}} \sin\theta_0 + E_{\mathrm{Glide}} \cos\theta_0 \,, \tag{8.1}$$

where θ_0 is the smallest angle between a primitive triangular lattice vector and the direction of the shear, and $E_{\mathrm{Climb}} \gg E_{\mathrm{Glide}}$. The energy in Eq. (8.1) is minimized when the skyrmion lattice reorients itself along the direction of the shear. This can be understood from Fig. 8.1 – the case $\theta_0 = 0^\circ$ in Eq. (8.1) corresponds to a vertical shear in Fig. 8.1(a), in which case the resultant stress could be dissipated for a small energy $E_{\mathrm{Defects}} \propto E_{\mathrm{Glide}}$ by the gliding of the visualized 5-7 defect along its Burgers vector. Using the calculations from the previous chapter, one would expect the resultant structure factor to take the form shown in Fig. 8.1(b).

To shear the skyrmion lattice state, the sample was subject to a magnetic field of varying magnitude. This was set up by means of permanent magnets with a field profile of the previously discussed form given in Eq. (7.2). On top of this, a

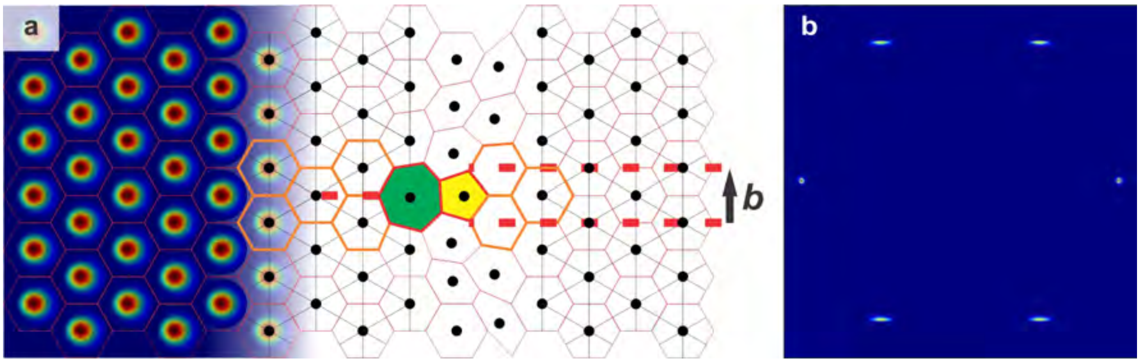

Figure 8.1: (a) An idealized visualization of a 5-7 defect in a skyrmion crystal. The red dotted lines indicate the lattice plane that is destroyed at the 5-7 defect, coloured so that the skyrmion with 5 nearest neighbours' Voronoi cell is yellow, while the skyrmion with 7 nearest neighbours' Voronoi cell is green. The missing lattice plane defines the Burgers vector, shown by the vector **b**. Were a shear stress applied vertically in this image, the defect could glide parallel to **b** to relieve strain for very little energy. (b) An example structure factor that one would expect to observe from (a).

perturbative field was generated from a current carrying wire mounted in the plane of the sample surface less than 1 mm from the sample. Assuming that the wire lies along the x-axis, the overall field profile can be written

$$B_z(y, r, \theta) = B_0 + B_1/y + B_2 r^2 + T(r, \theta)\,, \tag{8.2}$$

where a mix of Cartesian and polar coordinates have been used. The factor B_1 determines the strength of the field due to the wire, while B_2 arises due to the finite spatial extent of the permanent magnets and $T(r, \theta)$ contains both terms higher order in r, and angular terms resulting from a finite angle between the surface normal and the axis of the permanent magnets. If any sizeable current is applied through the adjacent wire, terms arising as a result of small imperfections in the experimental setup will become completely negligible, and the field at the surface of the sample will be well described by $B_z(y, r, \theta) = B_0 + B_1/y$. In the experiment, 11 A were applied through the wire – its resultant field completely masks the comparatively small $\mathcal{O}(r^2)$ terms that gave rise to the dynamics studied in the previous chapter. This leads to a force $F_y = I_\mu B_1 \hat{\mathbf{y}}/y^2$ acting on skyrmions at a position y, so that the Thiele equation becomes

$$\mathbf{G} \times \mathbf{v}_i - \alpha \mathbf{v}_i = -\nabla \sum_{j \neq i} U_{\mathrm{SkSk}} + I_\mu B_1 \hat{\mathbf{y}} / y^2 \,, \tag{8.3}$$

where the damping, velocity and gyrocoupling vector are represented by their usual symbols. Velocity fields one would expect to obtain from solutions to Eq. (8.3) are shown in 8.2 as a function of the skyrmion Hall angle.

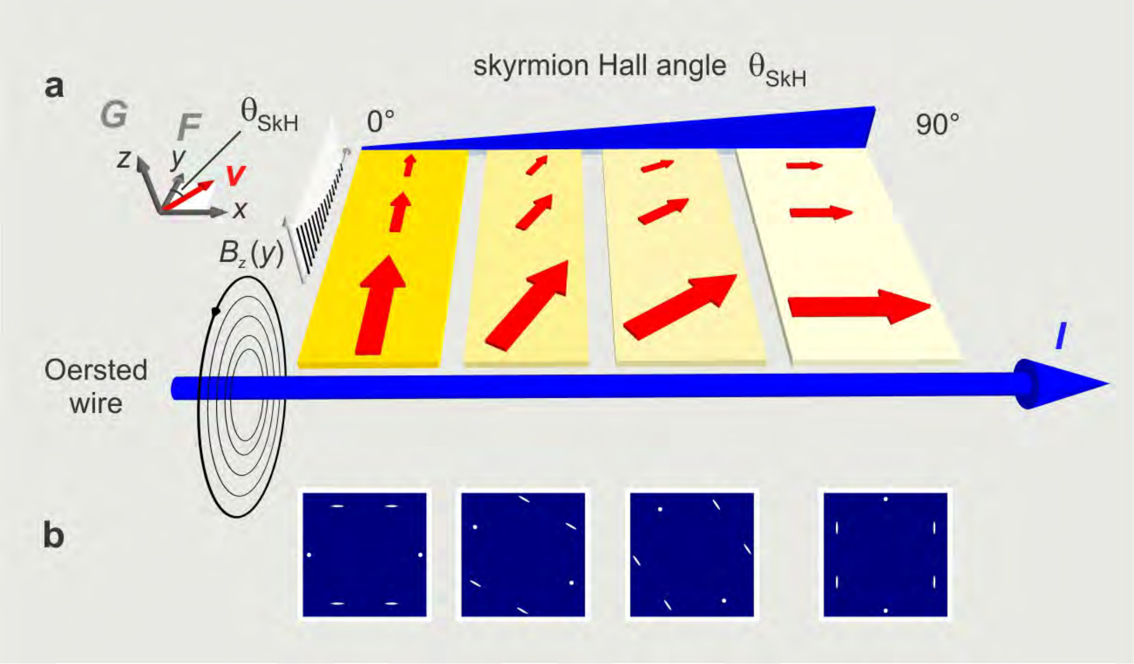

Figure 8.2: (a) The skyrmion velocity fields one would expect to observe by integrating Eq. (8.3) in the presence of a current carrying wire are indicated by red arrows. These arrows are shown on four different regions, each representing a sample with a skyrmion Hall angle in $[0°, 90°]$. For any $\theta_{\mathrm{SkH}} > 0°$, the skyrmion lattice is sheared along its direction of motion. Idealized visualizations of the scattering structure factors one would expect from skyrmion lattices affected by such a shear are shown in (b), each matching its corresponding sample's skyrmion Hall angle. The difference between these structure factors leave a fingerprint of the skyrmion Hall angle in diffraction patterns obtained on skyrmion lattices sheared by the field gradient from a current-carrying wire.

For clarity, it is worth carefully considering at this point the nature of the shear force acting on the skyrmion lattice due to the perturbative Oersted field. If skyrmions were topologically trivial (or if damping were infinite), $\theta_{\mathrm{SkH}} = \tan^{-1}(G/\alpha) = 0°$, meaning that topologically trivial objects would simply be driven along the y-axis, away from the wire, by the Oersted field gradient. The velocity field induced in this case is shear-free and is visualized at the $\theta_{\mathrm{SkH}} = 0^\circ$ extreme of Fig. 8.2. Conversely, in a fictitious material without damping, skyrmions would be subject to pure shear motion along the x-axis, which is pictured at the opposite side of Fig. 8.2. In all real materials, the induced motion is some combination of these two cases: both the direction of motion and the magnitude of the shear on the skyrmion lattice are dictated by the skyrmion Hall angle. This is captured by all intermediate values of θ_{SkH} in Fig. 8.2. Idealized structure factors one would expect to observe in each case are shown below the velocity fields, where the $\theta_{\mathrm{SkH}} = 0^\circ$ structure factor would only be found to rotate and exhibit broadened peaks were the skyrmion Hall angle slightly non-zero. Similarly, in a real experiment, one would also expect the magnitude of the peak broadening observed in an experiment to increase for increasing skyrmion Hall angle.

8.2 The skyrmion Hall angle in FeGe

In order to use this approach to measure the skyrmion Hall angle experimentally, T-REXS was performed on a 400 nm thick, $10\times10\,\mu\mathrm{m}^2$-sized FeGe lamella [174]. This sample is the FeGe lamella shown in Appendix A.2, Fig. A.1(c). To protect the camera from exposure to the straight beam, a horizontal beamstop was used. Nevertheless, as the hole through which the beam passes as very small, the scattered beam forms very bright Airy rings at low scattering $|q|$ values. These rings, as well as contributions from the beam directly passing through adjacent (but not directly illuminated) gaps in the sample holder, are masked in subsequent images to emphasize magnetic contrast. To provide the magnetic field, a single turn of 600-μm-diameter Kapton-insulated Cu wire was used. An out-of-plane magnetic field gradient of $\sim 1\,\mathrm{mT\,mm^{-1}}$ a distance of 1 mm from the sample was mapped out with a Hall probe from the 11 A current driven through the wire. The wire was thermally anchored far from the sample and the experiment was performed under ultra-high vacuum conditions, which allowed the experiment to be carried out in the absence of a perturbative temperature gradient. The maximum temperature fluctuations at the sample were observed immediately after applying the current before the cryostat's PID controller could respond; these temperature fluctuations did not exceed 0.1 K.

Entering the skyrmion pocket by field sweeping from the helical state, a skyrmion lattice with a roughly random orientation was obtained. Due to the nature of the small $10{\times}10\,\mu\text{m}^2$ FeGe samples (prepared by focused-ion-beam milling) there were preferential orientations for the skyrmion lattice in the absence of a driving force (this could be in response to, e.g., a strong shape anisotropy). An average over all REXS diffraction pattern obtained immediately after entering the skyrmion pocket is shown in Fig. 8.3(a). As a result of this energetic anisotropy, minor natural reorientation of the skyrmion lattice was observed for 1-2 min upon entering the skyrmion pocket, in the absence of any external drive. To control for this intrinsic reorientation, T-REXS intensity was measured for 15 min prior to application of the field gradient. An average over all final diffraction patterns obtained just before the field gradient was applied is shown in Fig. 8.3(b). The field gradient was applied after this 15 min waiting period – once the current was turned on, lattice reorientation was measured for a further 15 min. This procedure was repeated 15 times at 268 K on a sample of FeGe with a measured T_C of 273 K. Four of these repetitions were at an out-of-plane magnetic field of 55 mT, four were at 50 mT, four were at 45 mT and three repetitions were at 60 mT. The skyrmion lattice reorientation in response to the shearing Oersted field was extremely significant in every experiment, where the average over the final state of all 15 repetitions is shown in Fig. 8.3(c).

While the reorientation effects in FeGe were highly pronounced at 268 K, the skyrmion Hall angle could only be determined modulo 60° due to the sixfold symmetry of the diffraction pattern. The three real space velocity directions that would give rise to the observed scattering patterns are indicated in Fig. 8.3(c). To infer the direction of motion, it was necessary to allow more strain to be generated in the

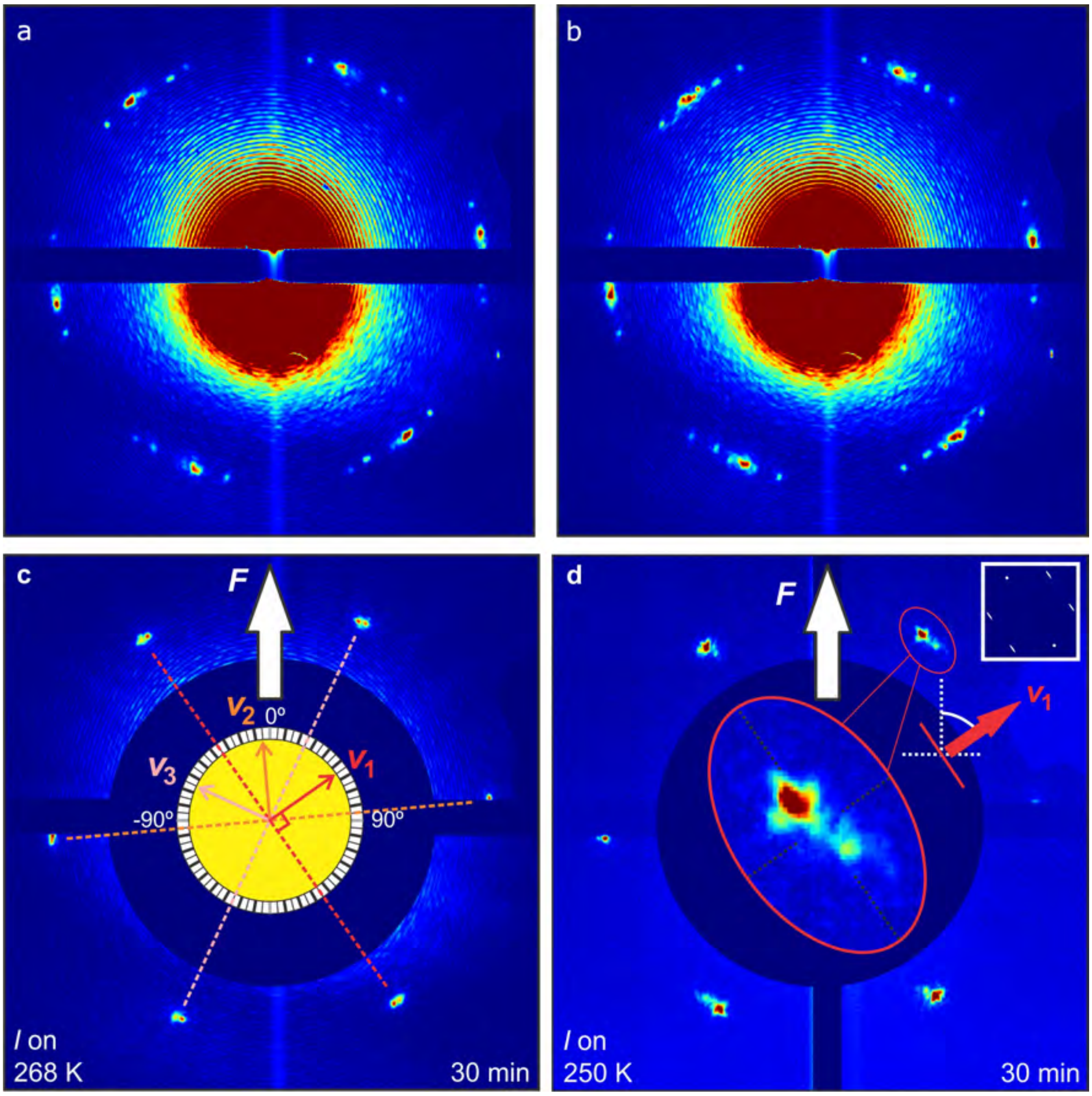

Figure 8.3: Average T-REXS diffraction patterns obtained from an FeGe lamella at 268 K for (a)-(c) and 250 K in (d). (a) Average over all 15 diffraction patterns obtained immediately after entering the skyrmion pocket at 268 K. Multiple peaks are present as the skyrmion lattice froze into several different initial orientations throughout the 15 experiments. (b) The diffraction patterns in (a), obtained after waiting 15 minutes without applying any external forces. The slight differences between (a) and (b) indicate that a small amount of reorientation was occurring in the absence of any external drives. The skyrmion states shown in (b) were exposed to a perturbative magnetic field gradient for 15 min – the average over all 15 T-REXS patterns after this 15 minute drive are shown in (c). Due to the six-fold symmetry of the pattern, this could be the result of any of three directions of motion: $\mathbf{v}_1$ due to a $\theta_{\mathrm{SkH}} = 55°$, $\mathbf{v}_2$ due to a $\theta_{\mathrm{SkH}} = -5°$, and $\mathbf{v}_3$ due to a $\theta_{\mathrm{SkH}} = -65°$. (d) As in (c), but the result of an identical experiment carried out at 250 K. Further from T_{C}, the skyrmion lattice is less magnetically soft; the skyrmion lattice was unable to dissipate strain as rapidly at 250 K, resulting in symmetry breaking uniaxial peak broadening (c). This pattern is consistent with $\mathbf{v}_1$, for which one would expect to measure diffracted intensity similar to the inset in the top right, and was used to derive a skyrmion Hall angle of 55°.

lattice along the direction of motion [175]. Leveraging the reduction in magnetic softness further from T_C, the same experiment was performed at 250 K. While the full reorientation effects were present at this temperature, much more peak broadening was observed and lattice reorientation occurred over a longer timescale. Indeed, further experiments below 200 K showed a greatly reduced response to the perturbing field gradient, with measurements on the skyrmion lattice at 100 K showing almost no response at all. This evidences that the true energy source for field gradient motion is thermal in nature, consistent with the expectation that one cannot drive skyrmions with a static field gradient at 0 K in perpetuity. An average over the final frames obtained after application of the magnetic field gradient for 15 min at 250 K is given in Fig. 8.3(d), with the anisotropic peak broadening indicating the rough direction of motion. This experiment was repeated 24 times, 8 times each at external magnetic fields of 65, 60, and 55 mT. Using the anisotropic peak broadening to match the obtained pattern with the expected patterns shown in Fig. 8.2, and measuring the angle between the direction of motion and the direction of the applied force, the skyrmion Hall angle in FeGe was determined to be $55^\circ \pm 2^\circ$, where the uncertainty is half the angular width of the average of all 15 final peak orientations measured in Fig. 8.3(c).

While this angle is larger than any previously reported skyrmion Hall angle found in magnetic multilayer systems, this is still far from the theoretical limit of 90°. As the primary damping mechanism for skyrmions moving through a metal occurs via conduction electron coupling, the insulating skyrmion-hosting material Cu_2OSeO_3 may have a skyrmion Hall angle much closer to the 90° limit. The skyrmion Hall angle in candidate low-dissipation materials such as Cu_2OSeO_3, where nanoscale skyrmions appear in the skyrmion lattice state, can be measured using the presented technique. This could unlock the possibility of the development of ultra-high mobility devices which take advantage of this unique motion [113, 153, 157].

As previously discussed, pinning potentials in real materials should make the skyrmion Hall angle a function of skyrmion velocity, and in turn a function of the magnitude of an applied force. The skyrmion Hall angle's value of $\tan^{-1}(G/\alpha)$ should really be considered the large drive limit [113, 157]. This hypothesis has been supported by experimental evidence, obtained on the skyrmions found in sputtered magnetic multilayers [62]. Due to the highly energetic nature of magnetron sputtering, these systems are expected to contain particularly high pinning potential densities [62]. The FeGe lamella used in this experiment was extracted from a high quality single crystal, which one would expect to contain a far lower density of pinning potentials (cut from the same crystal as used in Ref. [174]). As a result, it is expected that the skyrmion Hall angle of $55^\circ \pm 2^\circ$ measured in this experiment should be considered a lower bound that is close to the theoretical value. A detailed study of the drive dependence of the skyrmion Hall angle in lamellae of FeGe would make for an interesting topic of future research.

This technique also opens the prospect of studying the skyrmion Hall angle as a function of chemical composition. Both zinc and nickel doped Cu_2OSeO_3 samples have been studied recently, with doped samples having interesting properties such as enhanced metastability lifetimes [176]. The relationship between the skyrmion Hall angle and doping could provide information on how to chemically tune this parameter. The series of skyrmion lattice hosting magnets $Co_xZn_yMn_z$ have significantly varying Curie temperatures and helical wavelengths – the dependence of the skyrmion Hall angle on their chemistry would also make for a fascinating and topical future study.

In conclusion, a novel technique for the straightforward determination of the skyrmion Hall angle from the skyrmion lattice state has been presented. This technique was successfully benchmarked by measuring the skyrmion Hall angle in a lamella of FeGe. The mechanism underpinning this technique demonstrates that even the physics of a complex system of topological whirls of magnetization are fundamentally determined by defects and dislocations. The value of the skyrmion Hall angle measured in FeGe of 55° is larger than any previously observed skyrmion Hall angle, which provides verification for previous theoretical studies, and could open the door to ultra-low dissipation skyrmionic devices [177]. Most importantly, the presented technique allows for the methodical study of the skyrmion Hall angle in materials systems in which this parameter was previously impossible to measure.

Chapter 9

Summary and outlook

To summarize, in chapter 2, the general constraints for a magnetization field to leave the micromagnetic free energy invariant under translations and rotations are derived, and an accurate analytic toy model for a skyrmion is provided. The symmetry equations, and their accompanying discussions, provide much needed context for the rotationally symmetric skyrmion ansatz often used in the literature, and also justify the need for the three dimensional treatments given in chapter 4. The toy model gives the community a convenient tool with which to study the properties of skyrmions, which is asymptotically precise. In chapter 3, the first measurement of the magnetic soliton lattice above room temperature is presented, catapulting forward the prospects of using magnetic solitons in computing schemes. Additionally, the first unambiguous measurement of the skyrmion liquid phase is shown, evidencing that it is possible to melt the skyrmion lattice typically observed in chiral cubic magnets.

Chapter 4 is split into two parts. Skyrmion strings are found to be pinned to surfaces of their host materials, both in experiment and micromagnetic simulation. This can be understood by skyrmions costing more energy than surface twists at the edge of materials, and so skyrmions bend towards surfaces to increase the area occupied by these surface twists. It is also proven that states embedded in the conical state must become conically modulated. This is applied to the skyrmion phase, where skyrmions are found to exhibit modulation with the same periodicity of the encompassing conical state when immersed within it. In chapter 5, the importance of this finding becomes clear, where it is shown that conically modulated skyrmions have an attractive interparticle interaction. This implies that they are saddle point solutions of the Euler-Lagrange equations of the micromagnetic free energy, and so they cannot be modelled using Thiele's equation – an essential finding for the modelling community.

Also in chapter 5, a general form of the repulsive interparticle interactions obeyed by any magnetization configuration that can be described by Thiele's equation is discussed and benchmarked, and the simple analytic formulae derived from it are found to fit well to numerically derived interaction potentials. This vastly increases the cases in which Thiele's equation can be used to model the dynamics of magnetic structures. Prior to this work, no accurate analytic model for the interaction between skyrmions and the boundaries of their materials was known; the derivation of the interaction between a skyrmion and a surface-twist opens the door to simulations of many skyrmion systems in finite geometries on length-scales that were previously computationally inaccessible.

In chapter 6, the form the force applied to a skyrmion by a magnetic field gradient is derived, and used to show that skyrmions are negligibly deflected by this force when driven by spin-orbit torque down a nanowire, validating the design of popular racetrack memory schematics. This force is used further in chapter 7 to explain the anisotropic peak broadening one can observe in REXS experiments on the skyrmion lattice state.

Finally, in chapter 8, the first technique that can be used to determine the skyrmion Hall angle from the skyrmion lattice state is presented. As discussed above, this unlocks the possibility of studying the skyrmion Hall angle, the parameter that completely dictates the dynamical properties of skyrmion systems, in a whole range of materials in which it could not previously be measured.

Appendix A

Appendix

A.1 Details of skyrmion hosting materials

Material	T_C (K)	λ_H (nm)	Conduction	Type
FeGe [151, 174, 178]	270-280	70	Metal	Bloch
MnSi [150, 179, 180]	28-30	18	Metal	Bloch
$Fe_{1-x}Co_xSi$ [181–184]	2-50	30-230	Semiconductor	Bloch
$Mn_{1-x}Fe_xGe$ [185]	150-220	5-220	Metal	Bloch
Cu_2OSeO_3 [103, 151]	56-58	60-62	Insulator	Bloch
$Co_xZn_yMn_z$ [186]	150-500	120-200	Metal	Bloch
GaV_4S_8 [187, 188]	9-13	17-18	Semiconductor	Néel
GaV_4Se_8 [189, 190]	18	19-24	Semiconductor	Néel

Table A.1: A comparison of the Curie temperatures T_C, helical wavelengths λ_H, conductivities and types (i.e. Bloch- or Néel-type) of some known skyrmion-hosting single crystalline materials.

A.2 Sample details

Throughout this work, data has been acquired on two different samples of Cu_2OSeO_3, one sample of $Co_8Zn_{10}Mn_2$ and one sample of FeGe. These samples are shown in Fig. A.1. The samples of Cu_2OSeO_3 were synthesized by chemical vapour deposition by Dr. Haghighirad at the Karlsruhe Institute of Technology, and characterized and prepared at the University of Oxford and Diamond Light Source. Single crystals of $Co_8Zn_{10}Mn_2$ and FeGe were grown by Prof. Balakrishnan's group at the University of Warwick, and the lamellae were prepared by Luke Turnbull at the University of Durham.

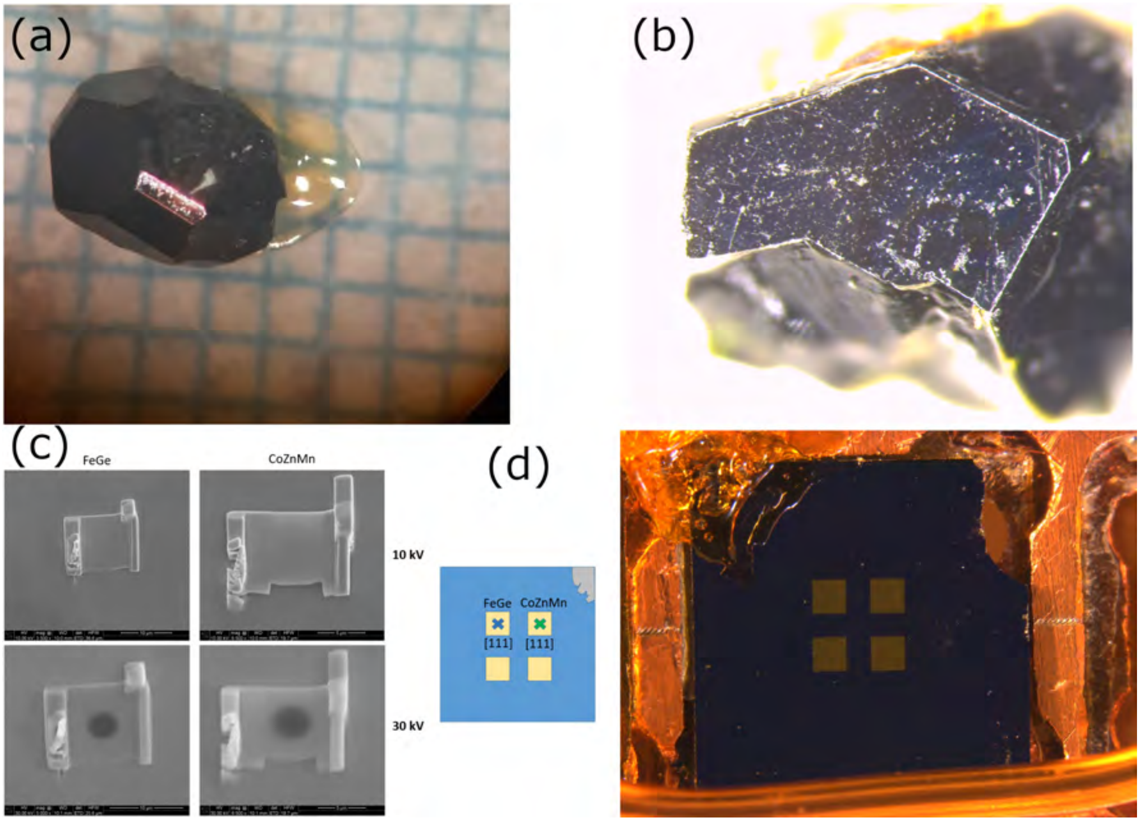

Figure A.1: Samples used to acquire the experimental data shown in this thesis. (a)-(b) Samples of Cu_2OSeO_3 used in REXS experiments, oriented so that the (100) faces are facing the camera. (c) The FeGe and $Co_8Zn_{10}Mn_2$ lamellae used in the T-REXS experiments, imaged under an electron microscope at different energies. The 10 kV image shows the details of the sample's surface, while the 30 kV electrons can penetrate the sample, allowing for the visualization of the hole through which x-rays transmit. This hole had a 6 μm diameter, and can be used as a scale bar for the images. (d) The lamellae in (c) were mounted on a slip, here shown mounted to a sample holder, fixed by GE varnish. Four gold coated windows are visible – at the direct centre of the top left window lies the FeGe lamella, and the lamella of $Co_8Zn_{10}Mn_2$ is situated in the middle of the top right window.

List of Figures

1.1 Examples of knots. (a) The two knots on the left of this panel are topologically equivalent, as they can be smoothly deformed into each other. The trefoil knot on the right is topologically distinct from the simple loops on the left, and can only be turned into a loop by cutting and retying. (b) A series of knots that cannot be smoothly deformed into one another. These are the (p, q) torus knots, with $p = 2$ and $q = 2n + 1$ for $n = 1, ..., 7$ [2]. 2

2.1 A fit of the analytical toy model described in Eq. (2.45) to the numerical solution of Eq. (2.41). In the differential equation the values of J, D, and B were taken to be 1 while choosing $\gamma = -\pi/2$. The toy-model parameters were refined to be $k_F = 6.95$, $\kappa = 5.54$, $r_0 = 1.61$, $k_N = 1.37$, and $\lambda = 1$. For comparison, the popular piecewise linear model is plotted [58, 62], as well as the model $f(r) = 4\arctan(e^{-\frac{r}{\lambda}})$ [64]. 32

2.2 Visualization of an isolated skyrmion, obtained by substituting the numerically obtained solution to the radial Euler-Lagrange equation in Eq. (2.41) into the azimuthally symmetric skyrmion ansatz in Eq. (2.34). The orientation of the resultant magnetization configuration is represented by cones. These cones are colored by the angle between the magnetization and the direction of the out-of-plane magnetic field — this angle is referred to as $f(r)$. 34

2.3 A visualization of magnetic (a) helices, (b) cones, and (c) solitons. (a) A helical magnetization structure, obtained by integration of the Landau-Lifshitz-Gilbert equation in the presence of finite bulk Dzyaloshinskii-Moriya and exchange interactions, but with $\mathbf{B} = \mathbf{0}$. Arrows indicate the local orientation of the magnetization field, coloured by their x-component. The k-vector of the helix is parallel to the z-direction. (b) As in (a), but with a finite magnetic field pointing along the positive z-direction. To minimize energy, the magnetic moments cant by an angle $\sin\chi = 2B_xM_sJ/D^2$ towards the external magnetic field. (c) As in (b), but with the external magnetic field applied along the positive x-direction. Regions in which moments are roughly parallel to $\mathbf{B}$ are extended by an amount determined by $|\mathbf{B}|$, while areas with moments pointing antiparallel to B are contracted; the overall wavelength of the periodic structure increases by an amount given by the solution of Eq. (2.55). 37

2.4 (a) Visualization of the tilting of magnetic moments at the edge of a material, with the magnetization field represented by arrows coloured by their x-component. Here, the z-axis points into the page. (b) A calculation carried out under precisely the same energetic conditions as in (a), but relaxed with a unit of topological charge at one end of a nanotrack. The resultant skyrmion configuration coexists with surface twist state, which bounds the bounds the edges of the material. Here, the x axis points into the page. 39

3.1 A visualization of the region of reciprocal space sampled by a rectangular camera. In each subfigure, the Bragg peak is indicated by a large red sphere, while green and blue magnetic satellites are the Fourier transforms of their respective green and blue helical domains (indicated by stripes on the sample at the centre of the Ewald sphere). The reciprocal space has been rotated towards the outgoing beam by an angle of $(\pi - 2\theta)/2$, and linearly scaled so that the outgoing wavevectors intersect the reciprocal lattice points from which they diffracted. The surface of reciprocal space sampled by the camera is indicated by a light brown translucent plane, and the Ewald sphere with the radius of the Bragg scattering vector is rendered in gray. (a) An overview of the scattering geometry, where magnetic reciprocal lattice peaks are taken to be isotropic and small. (b) A close-up of the reciprocal space plane spanned by the camera – intersections between magnetic and structural peaks with this plane are highlighted by an orange band. (c) As in (a), but replacing point-like peaks with truncation rods. (d) As in (b), but now all helical peaks are visible while the camera plane intersects the Bragg peak, as each truncation rod also passes through this plane. 50

3.2 Scattering data obtained on the helical and conical states. The vertical streak of intensity present in (b)-(d) is a detector artefact and should be ignored. Axes are are not shown due the anisotropic non-linear dependence of scattering vector on pixel position. (a) A REXS pattern captured from a sample of Cu_2OSeO_3 that was zero-field-cooled to 50 K. Two orthogonal helical domains give rise to pairs of magnetic reflections either side of a central Bragg peak, which is mostly covered by a beamstop. The peaks above and below the Bragg peak are visible only because of their truncation rods, as in Fig. 3.1(d). (b) A T-REXS pattern taken from a sample of $Co_8Zn_{10}Mn_2$ at 355 K at remanence. (c) A T-REXS pattern taken from a sample of FeGe at 268 K with no external field. The bright central region consists of Airy rings due to the beam diffracting through the circular aperture behind the sample. (d) A REXS pattern from a sample of Cu_2OSeO_3 at 56 K with an in-plane field field of 27 mT. The peaks above and below the central Bragg peak are conical. As $|q|$ is optimized for the Bragg condition in this image, the conical peaks appear to be particularly weak, as only the edge of their truncation rods clip the Ewald sphere. 53

3.3 (a) Gaussians fit to soliton scattering peak profiles measured at magnetic fields ranging in strength from 50 mT to 100 mT. The inset shows the region of interest from which the raw data was extracted. (b) The wavelength of the solitons as a function of field was calculated by converting the mean $|q|$ of the Gaussians in (a) to nanometres, where error bars are propagated standard deviations. The data point at 0 mT was measured repeatedly during alignment; integration of consecutive scans gave a well defined peak profile with a lower standard deviation. 57

3.4 (a) A visualization of the reciprocal space surface intersected by an area detector as in Fig. 3.1, but when the sample's magnetization has frozen into a monodomain skyrmion crystal. (b) A close-up of the intersection of the skyrmion lattice magnetic truncation rods with the detector's reciprocal surface. As the detector cuts these rods at an angle, the image received by a detector will appear distorted, and the peaks could appear to have varying intensities. (c) A similar image to (b), but only rendering the Ewald sphere with the radius of the Bragg scattering vector, the detector's reciprocal surface and the intersection between peaks/truncation rods and the detector's reciprocal surface. As the detector's surface cuts the magnetic truncation rods at an angle, the scattered intensity measured becomes elliptically distorted. (d) A REXS image captured on an area detector of a monodomain skyrmion lattice state. 59

3.5 (a)-(c) A REXS pattern on a multidomain skyrmion lattice state observed in a single crystal of Cu_2OSeO_3 at an out-of-plane magnetic field of 25 mT. (a) and (b) show the REXS patterns obtained when scanning the area detector through different values of $|q|$, while (c) shows the summed intensity from the $|q|$ scan. (d) The same REXS pattern as in Fig. 3.4(d), but with contrast tuned for lower intensity regions. A large number of higher order scattering peaks are visible. 62

3.6 (a) A measurement of the skyrmion liquid state in a sample of Cu_2OSeO_3 at a temperature of 54 K and an applied out-of-plane field of 25 mT. While this scattering pattern is consistent with the Fourier transform of a liquid of skyrmions, it is also consistent with a disordered collection of topologically trivial objects (such as spatially separated helices with k-vectors pointing along random directions). (b) A measurement of the topological winding number of the state in (a), obtained by subtracting the image in (a), obtained with right-handed circularly polarized light, by an image obtained with left-handed circularly polarized x-rays. As the dichroic intensity is described by a single sinusoidal period, this must correspond to light scattered from a liquid of particles with winding number $N = 1$: magnetic skyrmions. 65

4.1 A slice (whose normal defines the x-axis) through a simulation of the conically modulated skyrmion state. (a) The skyrmion string propagates along the z-axis, shifting left and right as it progresses, represented by arrows which point along the local orientation of the magnetization and are coloured by its z-component. (b) As in (a), but in place of arrows the surface of the slice is coloured by the y-component of the magnetization. The y-component of the magnetization at the core of the skyrmion is oscillatory (π out of phase with the surrounding conical state) with the same $\mathbf{k}$-vector as the encompassing conical state. 73

4.2 The reciprocal space geometry of a REXS experiment carried out on an in-plane conically modulated skyrmion lattice. (a) The Bragg peak scattering vector ($q = k_s - k_i$) is indicated by an arrow normal to the sample's surface. This time, as the skyrmion lattice lies in the sample plane, the six magnetic satellite peaks from the skyrmion lattice have been rotated by 90°. (b) The definition of the axes used to define the following slices through reciprocal space. (c) The conically modulated skyrmion state is shown in (c1), and its experimentally measured diffraction patterns across different slices through reciprocal space are shown in (c2) and (c3). (d) The unmodulated skyrmion state is visualized in (d1), with its theoretical scattering peaks shown in (d2). One would expect to observe peaks as shown in (d3) for many values of q_z in a real in-plane scattering experiment, because the peaks in (d2) would appear as magnetic truncation rods along the q_z direction (as shown by the experimental data in (c2)). (e) The expected diffraction pattern from a conical state visualized in (e1). There would be no peaks in the q_yq_z-plane, as shown in (e2), with peaks only in the q_xq_y-plane as in (e3). 74

4.3 Three examples of scattered intensity from different phases in the q_xq_y-plane, with $q_z = 1$. In each panel, the magnetic field is applied along the x-direction. (a) Two helical domains, with their corresponding pairs of peaks, have rotated slightly towards the external field of 10 mT. (b) At 25 mT, the skyrmion phase has formed. First order skyrmion peaks are bright and visible along the q_y-axis. A second order skyrmion peak, and a conical peak along the q_x-axis, are faintly visible. (c) At 30 mT, the skyrmion phase is coexisting with the conical state. The regions of interest used to integrate helicoidal, first order skyrmion and second order skyrmion intensity are indicated. . 76

4.4 In-plane REXS phase diagrams showing the coexistence of magnetic peaks corresponding to the conical/helical state with the skyrmion state's magnetic peaks in a sample of Cu_2OSeO_3 . These peaks were disambiguated by applying an in-plane magnetic field. All panels on the top row were measured at the same time using a field-cooling protocol, while all data on the bottom row was gathered simultaneously using a zero-field-cooling protocol. The three dots in the field-cooling protocol diagrams indicate the location on the phase diagram of the three scattering patterns shown in Fig. 4.3. (a)-(b) Integrated intensity from regions of interest on the area detector that contain signal corresponding only to conical/helical peaks. (c)-(d) As in (a)-(b), but integrating intensity from regions of interest in which one would expect to observe reflections from skyrmion tubes. (e)-(f) As in (c)-(d), but placing the regions of interest at twice the radial distance from the Bragg reflection, so that only second order magnetic diffraction from the skyrmion state is integrated. 77

4.5 (a) Geometry of the surface pinned skyrmion scattering. The sample surface normal is not parallel to the scattering vector, or even in the scattering plane. The skyrmion lattice is taken to be pinned to the surface normal. (b) Close-up of the intersection between the detector's reciprocal surface and the truncation rods from the surface pinned skyrmion state shown in (a). (c) Close-up of the intersection between the detector's reciprocal surface and the truncation rods from a skyrmion lattice in the plane perpendicular to the scattering vector (i.e. a skyrmion lattice aligned along the external field direction). (d) The intersections in (b), showing the expected diffraction pattern from the surface pinned skyrmion state. (e) The intersections in (c), showing the expected diffraction pattern from a skyrmion lattice not pinned to the surface, that instead follows the magnetic field. Clearly, when truncation rods are present, one cannot distinguish between surface-pinned and not-surface-pinned skyrmions; this expected diffraction pattern is too similar to the one shown in (d). (f) A REXS pattern obtained from the (110) face of a crystal of Cu_2OSeO_3 where the field and scattering vectors are both aligned along the (100) direction. 82

4.6 Images of the surface-pinned skyrmion state 5 eV below the Cu L_3-edge; (a) and (b) show different images captured on an area detector at different diffractometer $|q|$ values. Off the resonance energy, the penetration depth of x-rays has significantly increased, making features in reciprocal space more point-like and requiring that $|q|$ be scanned to image all six magnetic satellites. Off resonance, magnetic and structural intensities drop drastically (as the (100) reflection is a disallowed peak in Cu_2OSeO_3 visible only on resonance). Consequently, a detector artefact that is normally hidden below background is visible – a line of weakly activated pixels marking the centre of the detector. (c) The summation of the 10 images taken at different $|q|$ values from which (a) and (b) were taken. The line of damaged pixels seen in (a) and (b) is blurred across this subfigure, but it an artefact of the image alignment process and should be ignored. 84

4.7 A micromagnetic simulation of skyrmion tubes near a tilted surface. Approximately one in four finite difference cells were randomly selected to be rendered, with the cell's magnetization represented by an arrow whose length is scaled by the magnetization's z-component (with $m_z = 1$ having length 0, and $m_z = -1$ having maximal length). Scaling in this fashion allows skyrmion tubes to be visualized that would otherwise be lost in the bulk. 85

5.1 An example of the variation of the simulation geometries used in the computation of the numeric potentials in Fig. 5.3. The length ℓ of the simulation geometry along the direction of interparticle separation was varied, and for each ℓ the energy of the system was minimized by relaxing the Landau-Lifshitz-Gilbert equation numerically. The interaction energy can be derived from the energy density of these states as a function of ℓ. On the left, relaxed states from calculations used to determine the skyrmion-skyrmion interaction potential are shown. On the right, relaxed states from calculations used to determine the skyrmion-surface twist interaction potential are shown. In both cases, the magnetization is represented by cones coloured by the component of the magnetization along the direction of the applied field. The simulations used to calculate the skyrmion-surface twist interaction were carried out at larger external fields, which is why the skyrmions occupy a smaller area in those calculations. . . . 103

5.2 The energy density of two-skyrmion states as a function of magnetic field and skyrmion separation. Each point on each curve is the result of a micromagnetic relaxation of geometries such as those shown in Fig. 5.1. 105

5.3 A fit (of constants of proportionality) of the analytically derived interaction potentials to the numerically obtained potentials. (a) A fit of Eq. (5.16) to the 286 mT curve shown in Fig. 5.2. (b) A fit of Eq. (5.18) to its corresponding 463 mT curve, also including a fit of the skyrmion-twist interaction potential derived in Ref. [45] for comparison. 107

5.4 Conically modulated skyrmions in three dimensions interact attractively and form bound states. (a) An aerial view of the bound state, where the magnetization is represented by cones whose orientation is set by the magnetization where the colour is set by the z-component of the magnetization. (b) As in (a), but colouring the cones by the y-component of the magnetization. (c)-(e) A cross-section normal to the y-axis through the bound state, where the surface is coloured by the x-component of the magnetization in (c), the y-component in (d) and the z-component in (e). 109

5.5 The skyrmion liquid state, constructed from randomly placed topological units in an energetic environment in which conically modulated skyrmions extremize the micromagnetic energy functional. (a) 500,000 cones were rendered at randomly selected points in the system, pointing parallel to the magnetization and coloured by its z-component. (b) As in (a), but colouring the cones by y-component of the magnetization. The oscillatory nature of this component along the z-axis in regions away from skyrmions shows that the skyrmions are immersed in the conical state, while oscillations of the skyrmion's magnetization along the z-axis confirm that the skyrmion clusters are conically modulated. 111

6.1 A magnetic domain wall, driven by spin-orbit torque, imaged by the wide field magneto-optic Kerr effect microscope at the EXTREMAG facility. The white bar in each subfigure indicates a distance of 20 μm. Spin-orbit torque was applied by 5 ns duration square wave current pulses with current density 1.2×10^{12} Am^{-2}. 119

7.1 REXS data taken on the skyrmion lattice state in a sample of Cu_2OSeO_3 at a temperature of 57 K and an external field of 25 mT. These data were acquired exactly on resonance, so truncation rod effects were large enough that all six diffraction peaks can be clearly seen simultaneously. In this data set, to circumnavigate complexities arising from the REXS technique, the elliptical scattering patterns were projected onto a circle. The skyrmion lattice was immersed in an external field that was radially decaying which, as approximately described by Eq. (6.14), induces lattice rotation. This rotation was counter clockwise, and can be seen by comparing peak positions from (a)-(c), which were acquired at the same point on the same crystal over 130 s. In each of (a)-(c), the diffraction peaks are distorted uniaxially. 129

7.2 Plots of an example anisotropic magnetic field. (a) An image of how a magnetic field with a small four-fold anisotropy would look in a region with roughly the same size as the x-ray beam. A small red square towards the right of the panel indicates the area occupied by roughly 5000 skyrmions – the same number of skyrmions as used in calculations. Contours of constant magnetic field are indicated by dotted lines. (b) A magnified view of the red region in (a). Dotted lines indicate contours of constant force $F_{\nabla \mathbf{B}}$, to show that, in this region, one can write $F_{\nabla \mathbf{B}} = -2B_2 x\hat{\mathbf{y}}$ with a high degree of accuracy. 131

7.3 Results obtained by integrating Thiele's equation in the presence of a shearing magnetic field gradient of the kind shown in Fig. 7.2(b). (a) A triangular primitive lattice vector is shown in blue (here chosen to define the [100] direction), and the dotted line indicates the typical deviation of the strained lattice vector from its equilibrium position. Voronoi surfaces surrounding each lattice point are included as dark lines to guide the eye. (b) The absolute value of the structure factor one would expect to observe in a scattering experiment from a strained system. This structure factor has been rotated by 90°, so that uniaxial deformations of the structure factor peaks are collinear with the deformations of the real lattice vectors. (c) An image of a typical strained skyrmion crystal. Skyrmions are represented by small arrows, indicating their relative velocity, and surrounded by Voronoi surfaces. The area contained within a Voronoi cell is coloured by the strain of the [100] vector at that point. This region was used to calculate the structure factor shown in (b). (d) As in (c), subject to a slightly larger shear force. The otherwise equivalent simulation has a higher average deviation of the length of its [100] lattice vectors from the unperturbed value. 133

7.4 Illustrative example of the role played by 5-7 defects in the smectic state. (a) A visualization of a 5-7 defect, where the skyrmion with 7 nearest neighbours' Voronoi cell is coloured green, and the skyrmion with 5 nearest neighbours' Voronoi cell is filled in red. (b) An example of a structure factor generated in the presence of a 5-7 defects, rotated by 90° for comparison with Fig. 7.3(b), which exhibited comparatively less peak splitting. (c) A 5-7 defect glides through a strained skyrmion lattice to relieve strain. The 5-7 defect is coloured white, and its direction of motion is indicated by arrows whose magnitude is scaled relative to the velocity arrows of neighbouring skyrmions. (d) As in (c), further evolved in time. The 5-7 defect has propagated through the skyrmion crystal, resulting in a substantial relief of strain. 136

8.1 (a) An idealized visualization of a 5-7 defect in a skyrmion crystal. The red dotted lines indicate the lattice plane that is destroyed at the 5-7 defect, coloured so that the skyrmion with 5 nearest neighbours' Voronoi cell is yellow, while the skyrmion with 7 nearest neighbours' Voronoi cell is green. The missing lattice plane defines the Burgers vector, shown by the vector **b**. Were a shear stress applied vertically in this image, the defect could glide parallel to **b** to relieve strain for very little energy. (b) An example structure factor that one would expect to observe from (a). 141

8.2 (a) The skyrmion velocity fields one would expect to observe by integrating Eq. (8.3) in the presence of a current carrying wire are indicated by red arrows. These arrows are shown on four different regions, each representing a sample with a skyrmion Hall angle in $[0°, 90°]$. For any $\theta_{\mathrm{SkH}} > 0°$, the skyrmion lattice is sheared along its direction of motion. Idealized visualizations of the scattering structure factors one would expect from skyrmion lattices affected by such a shear are shown in (b), each matching its corresponding sample's skyrmion Hall angle. The difference between these structure factors leave a fingerprint of the skyrmion Hall angle in diffraction patterns obtained on skyrmion lattices sheared by the field gradient from a current-carrying wire. 142

8.3 Average T-REXS diffraction patterns obtained from an FeGe lamella at 268 K for (a)-(c) and 250 K in (d). (a) Average over all 15 diffraction patterns obtained immediately after entering the skyrmion pocket at 268 K. Multiple peaks are present as the skyrmion lattice froze into several different initial orientations throughout the 15 experiments. (b) The diffraction patterns in (a), obtained after waiting 15 minutes without applying any external forces. The slight differences between (a) and (b) indicate that a small amount of reorientation was occurring in the absence of any external drives. The skyrmion states shown in (b) were exposed to a perturbative magnetic field gradient for 15 min – the average over all 15 T-REXS patterns after this 15 minute drive are shown in (c). Due to the six-fold symmetry of the pattern, this could be the result of any of three directions of motion: $\mathbf{v}_1$ due to a $\theta_{\mathrm{SkH}} = 55°$, $\mathbf{v}_2$ due to a $\theta_{\mathrm{SkH}} = -5°$, and $\mathbf{v}_3$ due to a $\theta_{\mathrm{SkH}} = -65°$. (d) As in (c), but the result of an identical experiment carried out at 250 K. Further from T_{C}, the skyrmion lattice is less magnetically soft; the skyrmion lattice was unable to dissipate strain as rapidly at 250 K, resulting in symmetry breaking uniaxial peak broadening (c). This pattern is consistent with $\mathbf{v}_1$, for which one would expect to measure diffracted intensity similar to the inset in the top right, and was used to derive a skyrmion Hall angle of 55°. 145

A.1 Samples used to acquire the experimental data shown in this thesis. (a)-(b) Samples of Cu_2OSeO_3 used in REXS experiments, oriented so that the (100) faces are facing the camera. (c) The FeGe and $Co_8Zn_{10}Mn_2$ lamellae used in the T-REXS experiments, imaged under an electron microscope at different energies. The 10 kV image shows the details of the sample's surface, while the 30 kV electrons can penetrate the sample, allowing for the visualization of the hole through which x-rays transmit. This hole had a 6 μm diameter, and can be used as a scale bar for the images. (d) The lamellae in (c) were mounted on a slip, here shown mounted to a sample holder, fixed by GE varnish. Four gold coated windows are visible – at the direct centre of the top left window lies the FeGe lamella, and the lamella of $Co_8Zn_{10}Mn_2$ is situated in the middle of the top right window. . . 153

Bibliography

[1] V. F. R. Jones. "A polynomial invariant for knots via von Neumann algebras". In: *Bull. Am. Math. Soc.* 12 (1985), pp. 103–111.

[2] C. C. Adams. *The knot book*. American Mathematical Soc., 1994.

[3] W. S. Massey. *A basic course in algebraic topology*. Vol. 127. Springer, 2019.

[4] T. H. R. Skyrme. "A unified field theory of mesons and baryons". In: *Nuclear Physics* 31 (1962), pp. 556–569.

[5] J.-i. Fukuda and S. Žumer. "Quasi-two-dimensional Skyrmion lattices in a chiral nematic liquid crystal". In: *Nat. Commun.* 2 (2011), p. 246.

[6] U. Al Khawaja and H. Stoof. "Skyrmions in a ferromagnetic Bose–Einstein condensate". In: *Nature* 411 (2001), pp. 918–920.

[7] L. Leslie et al. "Creation and detection of skyrmions in a Bose-Einstein condensate". In: *Phys. Rev. Lett.* 103 (2009), p. 250401.

[8] D.-H. Lee and C. L. Kane. "Boson-vortex-Skyrmion duality, spin-singlet fractional quantum Hall effect, and spin-1/2 anyon superconductivity". In: *Phys. Rev. Lett.* 64 (1990), p. 1313.

[9] S. Mühlbauer et al. "Skyrmion lattice in a chiral magnet". In: *Science* 323 (2009), pp. 915–919.

[10] R. J. Forbes. *Studies in ancient technology*. Vol. 1. Brill Archive, 1957.

[11] S. A. Barney et al. *The etymologies of Isidore of Seville*. Cambridge University Press, 2006.

[12] H. Frith and W. Stepney Rawson. *Coil and Current; Or the Triumphs of Electricity.* Vol. 1. Ward, Lock and Company, 1896.

[13] A. Feldman. “Thoughts on Thales”. In: *Class. J.* 41 (1945), pp. 4–6.

[14] W. Heisenberg. “Multi-body problem and resonance in quantum mechanics”. In: *Magazine for Physics* 38 (1926), pp. 411–426.

[15] C. S. Henshilwood et al. “Emergence of modern human behavior: Middle Stone Age engravings from South Africa”. In: *Science* 295 (2002), pp. 1278–1280.

[16] B. Barbara. “Louis Néel: His multifaceted seminal work in magnetism”. In: *C. R. Phys.* 20 (2019), pp. 631–649.

[17] P. Weiss. “L’hypothèse du champ moléculaire et la propriété ferromagnétique”. In: *J. Phys. Theor. Appl.* 6 (1907), pp. 661–690.

[18] C. G. Shull, W. Strauser, and E. Wollan. “Neutron diffraction by paramagnetic and antiferromagnetic substances”. In: *Phys. Rev.* 83 (1951), p. 333.

[19] I. Dzyaloshinsky. “A thermodynamic theory of “weak” ferromagnetism of antiferromagnetics”. In: *J. Phys. Chem. Solids.* 4 (1958), pp. 241–255.

[20] T. Moriya. “Anisotropic superexchange interaction and weak ferromagnetism”. In: *Phys. Rev.* 120 (1960), p. 91.

[21] A. Yoshimori. “A new type of antiferromagnetic structure in the rutile type crystal”. In: *J. Phys. Soc. Japan* 14 (1959), pp. 807–821.

[22] X. Yu et al. “Real-space observation of a two-dimensional skyrmion crystal”. In: *Nature* 465 (2010), pp. 901–904.

[23] X. Yu et al. “Skyrmion flow near room temperature in an ultralow current density”. In: *Nat. Commun.* 3 (2012), p. 988.

[24] N. Nagaosa and Y. Tokura. “Topological properties and dynamics of magnetic skyrmions”. In: *Nat. Nanotechnol.* 8 (2013), pp. 899–911.

[25] A. K. Nayak et al. “Magnetic antiskyrmions above room temperature in tetragonal Heusler materials”. In: *Nature* 548 (2017), pp. 561–566.

[26] X. Zhang, Y. Zhou, and M. Ezawa. “Antiferromagnetic skyrmion: stability, creation and manipulation”. In: *Sci. Rep.* 6 (2016), p. 24795.

[27] X. Yu et al. “Biskyrmion states and their current-driven motion in a layered manganite”. In: *Nat. Commun.* 5 (2014), p. 3198.

[28] L. Peng et al. “Real-space observation of nonvolatile zero-field biskyrmion lattice generation in MnNiGa magnet”. In: *Nano Lett.* 17 (2017), pp. 7075–7079.

[29] D. Foster et al. “Two-dimensional skyrmion bags in liquid crystals and ferromagnets”. In: *Nat. Phys.* 15 (2019), pp. 655–659.

[30] C. Kind, S. Friedemann, and D. Read. “Existence and stability of skyrmion bags in thin magnetic films”. In: *Appl. Phys. Lett.* 116 (2020), p. 022413.

[31] S. Zhang et al. “Real-space observation of skyrmionium in a ferromagnet-magnetic topological insulator heterostructure”. In: *Nano Lett.* 18 (2018), pp. 1057–1063.

[32] X. Zhang et al. “Control and manipulation of a magnetic skyrmionium in nanostructures”. In: *Phys. Rev. B* 94 (2016), p. 094420.

[33] F. P. Chmiel et al. “Observation of magnetic vortex pairs at room temperature in a planar α-Fe 2 O 3/Co heterostructure”. In: *Nat. Mater.* 17 (2018), pp. 581–585.

[34] M. Ezawa. “Compact merons and skyrmions in thin chiral magnetic films”. In: *Phys. Rev. B* 83 (2011), p. 100408.

[35] H. Jani et al. “Antiferromagnetic half-skyrmions and bimerons at room temperature”. In: *Nature* 590 (2021), pp. 74–79.

[36] P. Sutcliffe. “Hopfions in chiral magnets”. In: *J. Phys. A* 51 (2018), p. 375401.

[37] Y. Liu, R. K. Lake, and J. Zang. “Binding a hopfion in a chiral magnet nanodisk”. In: *Phys. Rev. B* 98 (2018), p. 174437.

[38] X. Wang, A. Qaiumzadeh, and A. Brataas. “Current-driven dynamics of magnetic hopfions”. In: *Phys. Rev. Lett.* 123 (2019), p. 147203.

[39] N. Kent et al. “Creation and observation of Hopfions in magnetic multilayer systems”. In: *Nat. Commun.* 12 (2021), p. 1562.

[40] J. C. Loudon et al. “Do Images of Biskyrmions Show Type-II Bubbles?” In: *Adv. Mater.* 31 (2019), p. 1806598.

[41] J. Loudon. “Do Images of Antiskyrmions Show Type-II Magnetic Bubbles?” Skyrmion project winter conference. 2021.

[42] T. Dohi et al. “Formation and current-induced motion of synthetic antiferromagnetic skyrmion bubbles”. In: *Nat. Commun.* 10 (2019), p. 5153.

[43] H. Kronmüller and M. Fähnle. *Micromagnetism and the microstructure of ferromagnetic solids.* Cambridge University Press, 2003.

[44] I. Dzyaloshinskii. “Theory of helicoidal structures in antiferromagnets. I. Nonmetals”. In: *Sov. Phys. JETP* 19 (1964), pp. 960–971.

[45] S. Meynell et al. “Surface twist instabilities and skyrmion states in chiral ferromagnets”. In: *Phys. Rev. B* 90 (2014), p. 014406.

[46] P. Bak and M. H. Jensen. “Theory of helical magnetic structures and phase transitions in MnSi and FeGe”. In: *J. Phys. C* 13 (1980), p. L881.

[47] L. Landau and E. Lifshitz. *Statistical Physics Part 2 (Course of Theoretical Physics, Volume 9).* 1981.

[48] R. Joseph and E. Schlömann. “Demagnetizing field in nonellipsoidal bodies”. In: *J. Appl. Phys.* 36 (1965), pp. 1579–1593.

[49] G. Bowden, G. Stenning, and G. Van der Laan. “Inter and intra macro-cell model for point dipole–dipole energy calculations”. In: *J. Phys. Condens. Matter* 28 (2016), p. 066001.

[50] G. Bowden, G. Stenning, and G. van der Laan. “Asymptotic behavior of local dipolar fields in thin films”. In: *J. Magn. Magn. Mater.* 416 (2016), pp. 449–456.

[51] L. Landau and E. Lifshitz. “On the theory of magnetic permeability dispersion in ferromagnetic solids”. In: *Sov. Phys* 8 (1935), pp. 153–166.

[52] M. Lakshmanan. “The fascinating world of the Landau–Lifshitz–Gilbert equation: an overview”. In: *Philos. Trans. A Math. Phys. Eng. Sci.* 369 (2011), pp. 1280–1300.

[53] T. L. Gilbert. “A phenomenological theory of damping in ferromagnetic materials”. In: *IEEE Trans. Magn.* 40 (2004), pp. 3443–3449.

[54] S. J. Blundell and K. M. Blundell. *Concepts in thermal physics.* OUP Oxford, 2009.

[55] M.-A. Bisotti et al. “Fidimag–a finite difference atomistic and micromagnetic simulation package”. In: *arXiv preprint arXiv:2002.04318* (2020).

[56] J. Zang, V. Cros, and A. Hoffmann. *Topology in Magnetism.* Vol. 192. Springer, 2018.

[57] S.-Z. Lin et al. “Particle model for skyrmions in metallic chiral magnets: Dynamics, pinning, and creep”. In: *Phys. Rev. B* 87 (2013), p. 214419.

[58] N. Kiselev et al. “Chiral skyrmions in thin magnetic films: new objects for magnetic storage technologies?” In: *J. Phys. D Appl. Phys.* 44 (2011), p. 392001.

[59] J. Rubinstein. “Sine-Gordon Equation”. In: *J. Math. Phys.* 11 (1970), pp. 258–266.

[60] G. Derrick. “Comments on nonlinear wave equations as models for elementary particles”. In: *J. Math. Phys.* 5 (1964), pp. 1252–1254.

[61] S. Komineas, C. Melcher, and S. Venakides. “The profile of chiral skyrmions of small radius”. In: *Nonlinearity* 33 (2020), p. 3395.

[62] W. Jiang et al. "Direct observation of the skyrmion Hall effect". In: *Nat. Phys.* 13 (2017), pp. 162–169.

[63] N. Romming et al. "Field-dependent size and shape of single magnetic skyrmions". In: *Phys. Rev. Lett.* 114 (2015), p. 177203.

[64] A. Leonov et al. "The properties of isolated chiral skyrmions in thin magnetic films". In: *New J. Phys.* 18 (2016), p. 065003.

[65] X. S. Wang, H. Y. Yuan, and X. R. Wang. "A theory on skyrmion size". In: *Commun. Phys.* 1 (2018), p. 31.

[66] J. Kierzenka and L. F. Shampine. "A BVP solver based on residual control and the Maltab PSE". In: *ACM Trans. Math. Softw.* 27 (2001), pp. 299–316.

[67] J.-i. Kishine, K. Inoue, and Y. Yoshida. "Synthesis, structure and magnetic properties of chiral molecule-based magnets". In: *Prog. Theor. Phys., Suppl.* 159 (2005), pp. 82–95.

[68] P. De Gennes. "Calcul de la distorsion d'une structure cholesterique par un champ magnetique". In: *Solid State Commun.* 6 (1968), pp. 163–165.

[69] I. Bostrem, J.-i. Kishine, and A. Ovchinnikov. "Theory of spin current in chiral helimagnets". In: *Phys. Rev. B* 78 (2008), p. 064425.

[70] M. J. Ablowitz et al. "Method for solving the sine-Gordon equation". In: *Phys. Rev. Lett.* 30 (1973), p. 1262.

[71] Y. Togawa et al. "Chiral magnetic soliton lattice on a chiral helimagnet". In: *Phys. Rev. Lett.* 108 (2012), p. 107202.

[72] Y. Togawa et al. "Interlayer magnetoresistance due to chiral soliton lattice formation in hexagonal chiral magnet CrNb 3 S 6". In: *Phys. Rev. Lett.* 111 (2013), p. 197204.

[73] T. Honda et al. "Topological metastability supported by thermal fluctuation upon formation of chiral soliton lattice in $CrNb_3S_6$". In: *Sci. Rep.* 10 (2020), p. 18596.

[74] M. Sawicki, W. Stefanowicz, and A. Ney. “Sensitive SQUID magnetometry for studying nanomagnetism”. In: *Semicond. Sci. Technol.* 26 (2011), p. 064006.

[75] A. Bauer and C. Pfleiderer. “Magnetic phase diagram of MnSi inferred from magnetization and ac susceptibility”. In: *Phys. Rev. B* 85 (2012), p. 214418.

[76] U. Hartmann. “Magnetic force microscopy”. In: *Annu. Rev. Mater. Sci.* 29 (1999), pp. 53–87.

[77] A. Casiraghi et al. “Individual skyrmion manipulation by local magnetic field gradients”. In: *Commun. Phys.* 2 (2019), pp. 1–9.

[78] P. J. Grundy and R. S. Tebble. “Lorentz electron microscopy”. In: *Adv. Phys.* 17 (1968), pp. 153–242.

[79] A. Petford-Long and M. De Graef. “Lorentz microscopy”. In: *Mater. Charact.* (2002), pp. 1–15.

[80] V. Volkov and Y. Zhu. “Lorentz phase microscopy of magnetic materials”. In: *Ultramicroscopy* 98 (2004), pp. 271–281.

[81] S. D. Pollard et al. “Observation of stable Néel skyrmions in cobalt/palladium multilayers with Lorentz transmission electron microscopy”. In: *Nat. Commun.* 8 (2017), p. 14761.

[82] S. Eisebitt et al. “Lensless imaging of magnetic nanostructures by X-ray spectro-holography”. In: *Nature* 432 (2004), pp. 885–888.

[83] T. A. Duckworth et al. “Magnetic imaging by x-ray holography using extended references”. In: *Opt. Express* 19 (2011), pp. 16223–16228.

[84] J. Kerr. “On rotation of the plane of polarization by reflection from the pole of a magnet”. In: *London Edinburgh Philos. Mag. J. Sci.* 3 (1877), pp. 321–343.

[85] P. N. Argyres. “Theory of the Faraday and Kerr effects in ferromagnetics”. In: *Phys. Rev.* 97 (1955), p. 334.

[86] J. Zázvorka et al. “Thermal skyrmion diffusion used in a reshuffler device”. In: *Nat. Nanotechnol.* 14 (2019), pp. 658–661.

[87] B. Miao et al. “Experimental realization of two-dimensional artificial skyrmion crystals at room temperature”. In: *Phys. Rev. B* 90 (2014), p. 174411.

[88] T. Srivastava et al. “Large-voltage tuning of Dzyaloshinskii–Moriya interactions: A route toward dynamic control of skyrmion chirality”. In: *Nano Lett.* 18 (2018), pp. 4871–4877.

[89] L. Caretta et al. “Fast current-driven domain walls and small skyrmions in a compensated ferrimagnet”. In: *Nat. Nanotechnol.* 13 (2018), pp. 1154–1160.

[90] G. Yu et al. “Room-temperature skyrmion shift device for memory application”. In: *Nano Lett.* 17 (2017), pp. 261–268.

[91] B. Thole et al. “X-ray circular dichroism as a probe of orbital magnetization”. In: *Phys. Rev. Lett.* 68 (1992), p. 1943.

[92] P. Fischer et al. “Soft X-ray microscopy of nanomagnetism”. In: *Mater. Today* 9 (2006), pp. 26–33.

[93] G. Van der Laan. “Applications of soft x-ray magnetic dichroism”. In: *J. Phys. Conf. Ser.* Vol. 430. IOP Publishing. 2013, p. 012127.

[94] G. Felcher. “Neutron reflection as a probe of surface magnetism”. In: *Phys. Rev. B* 24 (1981), p. 1595.

[95] S. Mühlbauer et al. “Magnetic small-angle neutron scattering”. In: *Rev. Mod. Phys.* 91 (2019), p. 015004.

[96] G. van der Laan. “Soft x-ray resonant magnetic scattering of magnetic nanostructures”. In: *C. R. Phys.* 9 (2008), pp. 570–584.

[97] I. K. Robinson. “Crystal truncation rods and surface roughness”. In: *Phys. Rev. B* 33 (1986), p. 3830.

[98] G. Watson et al. “X-Ray Scattering Study of the Magnetic Structure near the (001) Surface of UO_2”. In: *Phys. Rev. Lett.* 77 (1996), p. 751.

[99] G. Watson et al. “Resonant x-ray scattering studies of the magnetic structure near the surface of an antiferromagnet”. In: *Phys. Rev. B* 61 (2000), p. 8966.

[100] O. Robach et al. “Magnetic anisotropy of ultrathin cobalt films on Pt (111) investigated with x-ray diffraction: Effect of atomic mixing at the interface”. In: *Phys. Rev. B* 65 (2002), p. 054423.

[101] K. Ran et al. “Creation of a Chiral Bobber Lattice in Helimagnet-Multilayer Heterostructures”. In: *Phys. Rev. Lett.* 126 (2021), p. 017204.

[102] Y. Okamura et al. “Emergence and magnetic-field variation of chiral-soliton lattice and skyrmion lattice in the strained helimagnet Cu_2OSeO_3”. In: *Phys. Rev. B* 96 (2017), p. 174417.

[103] S. Zhang et al. “Multidomain skyrmion lattice state in Cu_2OSeO_3”. In: *Nano Lett.* 16 (2016), pp. 3285–3291.

[104] J. Sampaio et al. “Nucleation, stability and current-induced motion of isolated magnetic skyrmions in nanostructures”. In: *Nat. Nanotechnol.* 8 (2013), p. 839.

[105] S. Woo et al. “Deterministic creation and deletion of a single magnetic skyrmion observed by direct time-resolved X-ray microscopy”. In: *Nat. Electron.* 1 (2018), pp. 288–296.

[106] A. Hrabec et al. “Current-induced skyrmion generation and dynamics in symmetric bilayers”. In: *Nat. Commun.* 8 (2017), p. 15765.

[107] W. Jiang et al. “Blowing magnetic skyrmion bubbles”. In: *Science* 349 (2015), pp. 283–286.

[108] K. Zeissler et al. “Diameter-independent skyrmion Hall angle observed in chiral magnetic multilayers”. In: *Nat. Commun.* 11 (2020), p. 428.

[109] D. Pinna et al. “Skyrmion gas manipulation for probabilistic computing”. In: *Phys. Rev. Appl.* 9 (2018), p. 064018.

[110] C. Schütte and M. Garst. “Magnon-skyrmion scattering in chiral magnets”. In: *Phys. Rev. B* 90 (2014), p. 094423.

[111] S. Hoshino and N. Nagaosa. “Theory of the magnetic skyrmion glass”. In: *Phys. Rev. B* 97 (2018), p. 024413.

[112] E. Chudnovsky and D. Garanin. “Skyrmion glass in a 2D Heisenberg ferromagnet with quenched disorder”. In: *New J. Phys.* 20 (2018), p. 033006.

[113] C. Reichhardt, D. Ray, and C. O. Reichhardt. “Collective transport properties of driven skyrmions with random disorder”. In: *Phys. Rev. Lett.* 114 (2015), p. 217202.

[114] P. Huang et al. “Melting of a skyrmion lattice to a skyrmion liquid via a hexatic phase”. In: *Nat. Nanotechnol.* 15 (2020), pp. 761–767.

[115] Y. Chai et al. “Observation of Skyrmion liquid in a chiral magnet”. In: *arXiv preprint arXiv:1811.01555* (2018).

[116] M. Kläui. “Freezing and melting skyrmions in 2D”. In: *Nat. Nanotechnol.* 15 (2020), pp. 726–727.

[117] J.-Y. Chauleau et al. “Chirality in magnetic multilayers probed by the symmetry and the amplitude of dichroism in x-ray resonant magnetic scattering”. In: *Phys. Rev. Lett.* 120 (2018), p. 037202.

[118] A. Thiele. “Steady-state motion of magnetic domains”. In: *Phys. Rev. Lett.* 30 (1973), p. 230.

[119] B. Krüger. “Current-driven magnetization dynamics: analytical modeling and numerical simulation”. PhD thesis. Staats-und Universitätsbibliothek Hamburg Carl von Ossietzky, 2011.

[120] Ø. Johansen. “Electric Control of Skyrmion Dynamics and Spin Torque Oscillators in Magnetic Materials with Inversion Asymmetry”. MA thesis. Norges teknisk-naturvitenskaplige universitet, 2016.

[121] A. Pozzi. “A Study of Current-Induced Motion of Magnetic Skyrmions”. MA thesis. University of Groningen, 2014.

[122] X. Zhang. “Dynamics of magnetic skyrmions in nanostructures and their applications”. PhD thesis. Shinshu University, 2018.

[123] R. Juge. "Exploring different facets of magnetic skyrmion nucleation and dynamics in ultra-thin films". PhD thesis. Université Grenoble Alpes, 2020.

[124] S. A. Diaz Santiago. "Toward Magnetic Skyrmion Manipulation". PhD thesis. UC San Diego, 2017.

[125] X. Zhang, Y. Zhou, and M. Ezawa. "Magnetic bilayer-skyrmions without skyrmion Hall effect". In: *Nat. Commun.* 7 (2016), p. 10293.

[126] K. Litzius et al. "Skyrmion Hall effect revealed by direct time-resolved X-ray microscopy". In: *Nat. Phys.* 13 (2017), pp. 170–175.

[127] S. Woo et al. "Current-driven dynamics and inhibition of the skyrmion Hall effect of ferrimagnetic skyrmions in GdFeCo films". In: *Nat. Commun.* 9 (2018), p. 959.

[128] Y. Hirata et al. "Vanishing skyrmion Hall effect at the angular momentum compensation temperature of a ferrimagnet". In: *Nat. Nanotechnol.* 14 (2019), pp. 232–236.

[129] A. G. Kolesnikov et al. "Skyrmionium–high velocity without the skyrmion Hall effect". In: *Sci. Rep.* 8 (2018), p. 16966.

[130] R. Juge et al. "Current-driven skyrmion dynamics and drive-dependent skyrmion Hall effect in an ultrathin film". In: *Phys. Rev. Appl.* 12 (2019), p. 044007.

[131] Y. Zhang et al. "Magnetic skyrmions without the skyrmion Hall effect in a magnetic nanotrack with perpendicular anisotropy". In: *Nanoscale* 9 (2017), pp. 10212–10218.

[132] B. Göbel et al. "Overcoming the speed limit in skyrmion racetrack devices by suppressing the skyrmion Hall effect". In: *Phys. Rev. B* 99 (2019), p. 020405.

[133] C. Song et al. "Skyrmion-based multi-channel racetrack". In: *Appl. Phys. Lett.* 111 (2017), p. 192413.

[134] J. Zang et al. "Dynamics of skyrmion crystals in metallic thin films". In: *Phys. Rev. Lett.* 107 (2011), p. 136804.

[135] D. Capic, D. A. Garanin, and E. M. Chudnovsky. “Skyrmion–skyrmion interaction in a magnetic film”. In: *J. Phys. Condens. Matter* 32 (2020), p. 415803.

[136] C. Ross, N. Sakai, and M. Nitta. “Skyrmion interactions and lattices in chiral magnets: analytical results”. In: *J. High Energy Phys.* 2021 (2021), p. 95.

[137] A. Leonov et al. “Three-dimensional chiral skyrmions with attractive interparticle interactions”. In: *J. Phys. Condens. Matter* 28 (2016), 35LT01.

[138] L. Rózsa et al. “Skyrmions with attractive interactions in an ultrathin magnetic film”. In: *Phys. Rev. Lett.* 117 (2016), p. 157205.

[139] J. Loudon et al. “Direct observation of attractive skyrmions and skyrmion clusters in the cubic helimagnet Cu_2OSeO_3”. In: *Phys. Rev. B* 97 (2018), p. 134403.

[140] M. D. Stiles and A. Zangwill. “Anatomy of spin-transfer torque”. In: *Phys. Rev. B* 66 (2002), p. 014407.

[141] R. Tomasello et al. “A strategy for the design of skyrmion racetrack memories”. In: *Sci. Rep.* 4 (2014), p. 6784.

[142] J. Iwasaki, M. Mochizuki, and N. Nagaosa. “Universal current-velocity relation of skyrmion motion in chiral magnets”. In: *Nat. Commun.* 4 (2013), p. 1463.

[143] J. Iwasaki, W. Koshibae, and N. Nagaosa. “Colossal spin transfer torque effect on skyrmion along the edge”. In: *Nano Lett.* 14 (2014), pp. 4432–4437.

[144] W. Koshibae and N. Nagaosa. “Theory of skyrmions in bilayer systems”. In: *Sci. Rep.* 7 (2017), p. 42645.

[145] G. Yu et al. “Room-temperature creation and spin–orbit torque manipulation of skyrmions in thin films with engineered asymmetry”. In: *Nano Lett.* 16 (2016), pp. 1981–1988.

[146] S. Woo et al. “Spin-orbit torque-driven skyrmion dynamics revealed by time-resolved X-ray microscopy”. In: *Nat. Commun.* 8 (2017), p. 15573.

[147] J. Xia et al. “Dynamics of an elliptical ferromagnetic skyrmion driven by the spin–orbit torque”. In: *Appl. Phys. Lett.* 116 (2020), p. 022407.

[148] Z. Zeng et al. “Dynamics of skyrmion bags driven by the spin–orbit torque”. In: *Appl. Phys. Lett.* 117 (2020), p. 172404.

[149] A. Manchon et al. “New perspectives for Rashba spin–orbit coupling”. In: *Nat. Mater.* 14 (2015), pp. 871–882.

[150] T. Nakajima et al. “Skyrmion lattice structural transition in MnSi”. In: *Sci. Adv.* 3 (2017), e1602562.

[151] D. M. Burn et al. “Field and temperature dependence of the skyrmion lattice phase in chiral magnet membranes”. In: *Phys. Rev. B* 101 (2020), p. 014446.

[152] M. Wilson et al. “Stability and metastability of skyrmions in thin lamellae of Cu_2OSeO_3”. In: *Phys. Rev. Res.* 2 (2020), p. 013096.

[153] S. Zhang et al. “Manipulation of skyrmion motion by magnetic field gradients”. In: *Nat. Commun.* 9 (2018), p. 2115.

[154] R. Streubel et al. “Manipulating topological states by imprinting non-collinear spin textures”. In: *Sci. Rep.* 5 (2015), p. 8787.

[155] D. Cortés-Ortuño et al. “Thermal stability and topological protection of skyrmions in nanotracks”. In: *Sci. Rep.* 7 (2017), p. 4060.

[156] J.-V. Kim and M.-W. Yoo. “Current-driven skyrmion dynamics in disordered films”. In: *Appl. Phys. Lett.* 110 (2017), p. 132404.

[157] C. Reichhardt and C. O. Reichhardt. “Noise fluctuations and drive dependence of the skyrmion Hall effect in disordered systems”. In: *New J. Phys.* 18 (2016), p. 095005.

[158] C. Reichhardt and C. Reichhardt. “Thermal creep and the skyrmion Hall angle in driven skyrmion crystals”. In: *J. Phys. Condens. Matter* 31 (2018), 07LT01.

[159] C. Reichhardt, D. Ray, and C. O. Reichhardt. “Quantized transport for a skyrmion moving on a two-dimensional periodic substrate”. In: *Phys. Rev. B* 91 (2015), p. 104426.

[160] S. A. Diaz et al. “Fluctuations and noise signatures of driven magnetic skyrmions”. In: *Phys. Rev. B* 96 (2017), p. 085106.

[161] K. Litzius et al. “The role of temperature and drive current in skyrmion dynamics”. In: *Nat. Electron.* 3 (2020), pp. 30–36.

[162] J. C. Butcher. “A history of Runge-Kutta methods”. In: *Appl. Numer. Math.* 20 (1996), pp. 247–260.

[163] P. J. Van Laarhoven and E. H. Aarts. “Simulated annealing”. In: *Simulated annealing: Theory and applications*. Springer, 1987, pp. 7–15.

[164] K. A. Dowsland and J. Thompson. “Simulated annealing”. In: *Nat. Comput.* (2012), pp. 1623–1655.

[165] S. E. Prameela and T. P. Weihs. “A defect determines strength”. In: *Nat. Phys.* 16 (2020), pp. 816–816.

[166] A. Kelly. *Strong solids*. Oxford: Oxford University Press, 1973.

[167] D. Hull and D. J. Bacon. *Introduction to dislocations*. Amsterdam: Butterworth-Heinemann, 2001.

[168] F. R. N. Nabarro. “Fifty-year study of the Peierls-Nabarro stress”. In: *Mater. Sci. Eng. A* 234 (1997), pp. 67–76.

[169] S. Pöllath et al. “Dynamical defects in rotating magnetic skyrmion lattices”. In: *Phys. Rev. Lett.* 118 (2017), p. 207205.

[170] C. Reichhardt and C. O. Reichhardt. “Magnus-induced dynamics of driven skyrmions on a quasi-one-dimensional periodic substrate”. In: *Phys. Rev. B* 94 (2016), p. 094413.

[171] W. L. McMillan. “Simple molecular model for the smectic A phase of liquid crystals”. In: *Phys. Rev. A* 4 (1971), p. 1238.

[172] A. Fukuda et al. “Antiferroelectric chiral smectic liquid crystals”. In: *J. Mater. Chem.* 4 (1994), pp. 997–1016.

[173] T. Niori et al. “Distinct ferroelectric smectic liquid crystals consisting of banana shaped achiral molecules”. In: *J. Mater. Chem.* 6 (1996), pp. 1231–1233.

[174] M. Birch et al. “Real-space imaging of confined magnetic skyrmion tubes”. In: *Nat. Commun.* 11 (2020), p. 1726.

[175] R. Brearton et al. “Skyrmions in anisotropic magnetic fields: strain and defect driven dynamics”. In: *MRS Adv.* 4 (2019), pp. 643–650.

[176] M. Birch et al. “Increased lifetime of metastable skyrmions by controlled doping”. In: *Phys. Rev. B* 100 (2019), p. 014425.

[177] F. Büttner, I. Lemesh, and G. S. Beach. “Theory of isolated magnetic skyrmions: From fundamentals to room temperature applications”. In: *Sci. Rep.* 8 (2018), p. 4464.

[178] X. Yu et al. “Near room-temperature formation of a skyrmion crystal in thin-films of the helimagnet FeGe”. In: *Nat. Mater.* 10 (2011), pp. 106–109.

[179] A. Tonomura et al. “Real-space observation of skyrmion lattice in helimagnet MnSi thin samples”. In: *Nano Lett.* 12 (2012), pp. 1673–1677.

[180] A. Bauer, M. Garst, and C. Pfleiderer. “Specific heat of the skyrmion lattice phase and field-induced tricritical point in MnSi”. In: *Phys. Rev. Lett.* 110 (2013), p. 177207.

[181] M. Ishida et al. “Crystal chirality and helicity of the helical spin density wave in MnSi. II. Polarized neutron diffraction”. In: *J. Phys. Soc. Japan* 54 (1985), pp. 2975–2982.

[182] J. Beille et al. “Helimagnetic structure of the $\mathrm{Fe}_{1-x}\mathrm{Co}_x\mathrm{Si}$”. In: *J, Phys. F Met.* 11 (1981), p. 2153.

[183] L. Bannenberg et al. “Extended skyrmion lattice scattering and long-time memory in the chiral magnet $\mathrm{Fe}_{1-x}\mathrm{Co}_x\mathrm{Si}$”. In: *Phys. Rev. B* 94 (2016), p. 104406.

[184] A. Bauer, M. Garst, and C. Pfleiderer. “History dependence of the magnetic properties of single-crystal $\mathrm{Fe}_{1-x}\mathrm{Co}_x\mathrm{Si}$”. In: *Phys. Rev. B* 93 (2016), p. 235144.

[185] K. Shibata et al. “Towards control of the size and helicity of skyrmions in helimagnetic alloys by spin–orbit coupling”. In: *Nat. Nanotechnol.* 8 (2013), pp. 723–728.

[186] Y. Tokunaga et al. “A new class of chiral materials hosting magnetic skyrmions beyond room temperature”. In: *Nat. Commun.* 6 (2015), pp. 1–7.

[187] E. Ruff et al. “Multiferroicity and skyrmions carrying electric polarization in GaV4S8”. In: *Sci. Adv.* 1 (2015), e1500916.

[188] J. S. White et al. “Direct evidence for cycloidal modulations in the thermal-fluctuation-stabilized spin spiral and skyrmion states of $\mathrm{GaV}_4\mathrm{S}_8$”. In: *Phys. Rev. B* 97 (2018), p. 020401.

[189] S. Bordács et al. “Equilibrium skyrmion lattice ground state in a polar easy-plane magnet”. In: *Scientific reports* 7 (2017), pp. 1–11.

[190] B. Gross et al. “Stability of Néel-type skyrmion lattice against oblique magnetic fields in $\mathrm{GaV}_4\mathrm{S}_8$ and $\mathrm{GaV}_4\mathrm{Se}_8$”. In: *Phys. Rev. B* 102 (2020), p. 104407.